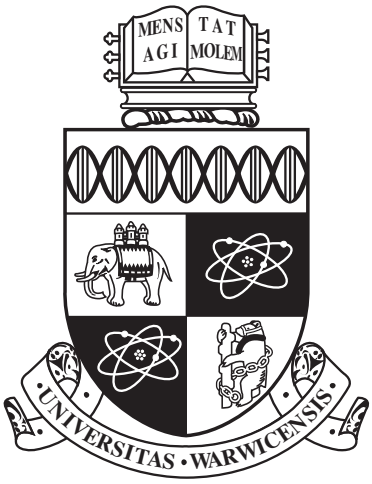

Neutron scattering studies of the geometrically frustrated $SrLn_2O_4$ materials

by

Simon Xavier Marie Riberolles

Thesis

Submitted to the University of Warwick

for the degree of

Doctor of Philosophy

Physics

March 2019

THE UNIVERSITY OF
WARWICK

Contents

Acknowledgments

Above all, I would like to thank both my supervisors Oleg A. Petrenko and Navid Qureshi. I am very grateful for their guidance and support throughout the PhD project.

I would also like to thank the members of the S & M group at Warwick that provided me with precious help. In particlar, Monica Ciomaga Hatnean and Geetha Balakrishnan for their help with the sample synthesis and single crystal growths, but also Martin Lees for his support with the bulk measurements performed on my samples.

I am also very grateful for the help of the ILL instrument scientists, Andrew Wildes, Bachir Ouladdiaf, Henry Fischer, Oscar Fabelo, Clemens Ritter and Navid Qureshi, with whom I have worked for countless hours measuring and treating neutron scattering data. My special recognition going to Navid whom supervised all my ILL experiments as well as my progress over the two years spent at the ILL. My recognition also goes to the ISIS instrument scientists Pascal Manuel and Dmitri Khalyavin as well as to Sylvain Petit at the LLB.

I also would like to thank my fellow PhD students at Warwick and at the ILL for the great time spent together

Finally, I would like to thank my fiancée and soul mate Ana Carolina Lopes Selvati for her every day love and support.

Declarations

Unless specified in the next paragraph, the experimental work presented in this thesis was performed between October 2015 and March 2019 within the frame of a partnership involving the University of Warwick and the Institut Laue-Langevin (ILL). The sample synthesis and characterisation work was carried out at Warwick while most of the neutron scattering experimental investigation was made at the ILL. Additional experiments have been performed at the ISIS and LLB facilities. All data treatments and analyses were performed by myself with the advise and support of the instrument scientists and in particular of Navid Qureshi.

The preparation of single crystal samples of the $SrEr_2O_4$ material was performed prior the start of my PhD by Geetha Balakrishnan and T. Hayes at Warwick. Also, the single crystal WISH experiment performed on the $SrEr_2O_4$ material with a magnetic field H applied parallel to the crystallographic a axis of the sample (see section 7.3.2) was carried out by T. Hayes, O. A. Petrenko and P. Manuel. The treatment and interpretation of the corresponding data was however entirely performed by myself.

This thesis has been entirely composed by myself and no part has been submitted for examination at any other institute.

Part of the work presented in this thesis has been presented under the form of poster presentations at the following conferences:

- 2016-18 UK Neutron and Muon Science and User Meeting (NMSUM), Coventry, U.K.
- 2017 International Conference on Neutron Scattering, Daejon, South Korea

And as oral presentations at the following conferences or seminar series:

- 2018 International Conference on Magnetism, 15min oral presentation, San Franciso, USA
- 2018 Participation to the ILL graduate school student seminar series, 45 min oral presentation, Grenoble, France.
- 2018 Participation to the ILL diffraction group seminar series, 45 min oral presentation, Grenoble, France
- 2019 UK Neutron and Muon Science and User Meeting (NMSUM), 30 min oral presentation, Coventry, U.K.

Abstract

Geometrical frustration in condensed matter is a phenomenon induced by competing magnetic interactions being in a situation of incompatibly with the crystal lattice geometry. In highly frustrated magnets, the competition can be such that a unique magnetic ground state cannot be stabilised, even at the lowest temperatures. Such a situation of instability is known to give rise to unusual and novel properties stimulating our interest for this class of materials. The members of the $SrLn_2O_4$ (Ln = Nd, Gd, Tb, Dy, Ho, Er, Tm, Yb) crystalline family, present the characteristics of highly frustrated systems. The magnetic sublattice of these materials consists of interconnected triangular ladders forming a three dimensional distorted honey-comb lattice. This lattice is also bipartite, in a sense that the Ln^{3+} magnetic ions are hosted by two crystallographically inequivalent sites, resulting in the presence of two different types of magnetic ladders in the system. Many different types of triangular structures are thus combined within these materials, resulting in the strong frustration of the antiferromagnetic Ln^{3+} exchange interactions.

This thesis presents an investigation of the low temperature magnetic properties of the Nd, Gd and Er variants of the $SrLn_2O_4$ family. The use of neutron scattering techniques in the determination of the different magnetic orders stabilised by these systems stands as a central aspect of this work. In fact, the structural characteristics of the orders have revealed fundamental aspects of the magnetic properties of this family of material. Of particular interest, it was understood that strong dipolar interaction can stabilise up-down-up-down (udud) Néel orders progressing along the ladders in $SrLn_2O_4$ systems containing the Ln^{3+} ions bearing the larger magnetic moments. On the other hand, near neighbour antiferromagnetic exchange interactions have the possibility to stabilise right-left-right-left (rlrl) Néel or (rrll) double Néel orders along the ladders, the moments lying within the $a - b$ plane of the materials. An investigation of the low temperature field induced properties of the $SrEr_2O_4$ material is moreover proposed in this thesis.

List of Figures

List of Tables

Chapter 1

Introduction

Magnetism is an intriguing physical phenomena that has attracted the interests of scientists and philosophers over the past three millenia. Natural ores such as the lodestone, a magnetised form of magnetite (Fe_2O_3) that attracts iron or other lodestone fragments, were the first magnetic materials to be discovered and reported by both ancient Greek and Chinese civilisations. The earliest descriptions of magnetised lodestone are attributed to the Chinese writer Guanzhong who died in 645 BC and to the Greek philosopher Thales (∼625-545 BC), as reported by Aristotle. In Greece, the lodestone ores employed to produced the first magnets were found at mount Sipylus, close to a town known as Magnesia ad Sipylum. The name of this town being at the origin of the actual English word "magnetism". Following this discovery, magnetic materials have been employed in the conception of various religious or mystical objects, such as the magnetic dagger found in the tomb of Tutankhamon or the magnetic flagstone that paves the throne room of Minos. The first advanced practical uses of magnetic materials however happened significantly later, with the invention of the compass employed by Chinese sailors for navigation. Particular spoon shaped pieces of lodestone were first utilised for this purpose. Placed in equilibrium on the surface of a plate these spoons will always point there handles towards the south direction. We should then consider significantly more recent times to find the first European publications scientifically detailing the properties of magnetism. The first of this kind being the work of Pierre Pelerin de Maricourt who introduced the notion of magnetic poles in 1269 [3]. In the 18^{th} and 19^{th} centuries, the work of Coulomb [4], Oersted [5], Ampere [6], Farraday [7] and Maxwell [8] resulted in the theoretical founding of the physics of electromagnetism. Of great interest, it was at the time theoretically introduced that magnetism and electricity are inextricably connected phenomena. The modern understanding of magnetism subsequently

arrived with the work of P. Curie [9] and Weiss [10] and later with the advent of quantum mechanic models proposed by Ising and Heisenberg [11]. Nowadays, magnetism and magnetic materials are extensively exploited by the recent technologies offering multiple applications largely influencing our every day lives.

The study of magnetism in condensed matter is nevertheless still of great interest in current research activities focusing principally on both collective and single ion aspects of the phenomenon. Single ion (single molecule) properties are extensively investigated through the studies of single molecular magnets [12], having the ability to remember the direction of externally applied fields over relatively long periods of time on experimental time scales [13]. It is nevertheless the collective aspect of magnetism that is principally under interest within the frame of this thesis. In fact, macroscopic systems have the ability to involve their microscopic constituents in cooperative manners, resulting in the observation of properties being drastically different from these of the microscopic constituents considered individually. These particular properties are often related with a phenomenon known as magnetic frustration. This characteristic of condensed matter magnetism results from the simultaneous action over the spins, of several magnetic interactions having different geometrical characteristics. Consequently, there exists no possible orientation for the spins to simultaneously satisfy each interactions.

Furthermore, the frustration effects can be maximised by the geometry of particular crystal lattices, placing the different magnetic interactions in direct situations of competition. This type of magnetic frustration being known as geometrical frustration is easily encountered in material hosting the magnetic ions within triangular geometries. The pyrochlores [14, 15], kagomé [16] and garnets [17] lattices being famous examples of this kind. In these materials, the geometrical frustration often results in the stabilisation of complex magnetic phases stabilised at temperatures being significantly lower than the predicted Curie-Weiss temperatures. To a certain degree, the frustration can also prevent any type of ordering to take place, resulting in the stabilisation of spin liquid quantum states [18]. Other type of exotic ground states such as the spin ice configurations [19] can also be stabilised, illustrating the large potential of the geometrical frustration phenomenon to induce unusual and fascinating physics in condensed matter.

Extensive investigations of these materials were carried out over the last decades resulting in the production of substential scientific results, and in a perfection of the experimental probes and techniques. The number of newly synthesised material affected by geometrical frustration being continuously growing, the search for novel properties continues to attract the interest of scientists.

In this thesis, I present a study of the $SrNd_2O_4$, $SrGd_2O_4$ and $SrEr_2O_4$ variants of the geometrically frustrated $SrLn_2O_4$ (Ln = Nd, Gd, Tb, Dy, Ho, Er, Tm, Yb) family of materials. The magnetic sublattice of these materials can be viewed as triangular ladders propagating along the c axis of the material. The interconnection of neighbouring ladders resulting in a peculiar distorted honey-comb structure in 3-dimensional space. The many combinations of triangular interactions contained within the honey-comb sublattice place the strong Ln^{3+} antiferromagnetic exchange interactions in a situation of strong competition, being responsible for the observation of interesting magnetic properties in the low temperature studies of these materials.

Following this introductory section, the plan of this thesis consists of two theoretical chapters, number 2 and 3, aiming to provide the reader with the necessary theoretical background for the understanding of my results. Chapter 2 is dedicated to a presentation of the concepts of magnetism and magnetic frustrations encountered in this thesis. This chapter terminates with a presentation of the $SrLn_2O_4$ 3-dimensional honey-comb lattice and reviews the principal results obtained from previous investigations of these materials. The use of diffraction techniques and principally of neutron diffraction techniques being central in this work, the physics employed by these techniques is detailed in chapter 3.

A presentation of the different experimental techniques and instruments used in this research project is then given in chapter 4. The techniques employed for single crystal growth and bulk characterisation measurements are first detailed and followed by the presentation of a large collection of neutron diffractometers and diffraction techniques.

The core of the thesis is then constituted of three results chapters numbered from 5 to 7, being respectively dedicated to the presentation of my studies of the $SrNd_2O_4$, $SrGd_2O_4$ and $SrEr_2O_4$ materials. The layout of these chapters first considers introductory sections, directly followed by a section dedicated to summaries of previously published results on the subject if existing. My experimental results are then successively presented in progressive orders forming the bulk of the chapters. These results sections are however being organised differently due to different degrees of involvements considered in the investigation of each of the systems. The result chapters are finally terminated by summaries and discussions sections where my theoretical understanding of the systems are detailed.

Chapter 5 is dedicated to the investigation of the $SrNd_2O_4$ material. It first contains my results concerning the material synthesis under polycrystalline form, followed by bulk measurement characterisations results and by the results of neu-

tron powder diffraction (NPD) low temperature investigations. The organisation of chapter 6, dedicated to the investigation of the $SrGd_2O_4$ material is relatively close to the organisation adopted in chapter 5. In that sense, results concerning the neutron scattering investigation of the material are preceded by a section detailing the material sample syntheses and bulk characterisations. My involvement in the investigation of this material however constitutes a continuation of previously published sample synthesis and bulk characterisation investigations of the material. In that respect, a preliminary section is dedicated to a presentation of the previously published results, standing as a base for my results. The sample synthesis results are then presented along with a few characterisation measurements uniquely aiming to verify the magnetic properties of the samples, not to repeat already published results. A detailed low temperature neutron scattering investigation of the material employing both powder and single crystal techniques is subsequently detailed and forms the core of this chapter. Chapter 7 the last result chapter, is dedicated to an investigation of the $SrEr_2O_4$ material. This chapter is a rather different from chapters 5 and 6, since it focuses on the low temperature field-induced properties of the $SrEr_2O_4$ system. In fact, considerable published work was already existing on the subject prior the start of this thesis project. My involvement thus constitutes a complement to these results, aiming to provide a better understanding of the system and confirm the previous results and predictions.

A conclusion chapter is finally proposed summarising the principal results of these magnetic investigations. A presentation of my understanding of the magnetic properties of these systems and more generally of the $SrLn_2O_4$ family as a whole, based on both recent and previously published results ultimately concludes this thesis.

Chapter 2

Magnetism, magnetic frustration, and the $SrLn_2O_4$ 3-D honeycomb lattice

In this chapter, I provide the reader with a brief theoretical introduction to magnetism focusing on the physics involved in the result sections of this thesis. I will start by detailing the ground state magnetic properties of isolated atoms employing elementary classical and quantum mechanical considerations. Magnetism in condensed matter being however a collective phenomenon, the effect of the direct surrounding on a particular magnetic moments will then be treated. Both exchange and dipolar types of magnetic interactions will there be introduced along with the lattice crystal field effects. I will then focus on concepts of magnetic frustration and introduce the $SrLn_2O_4$ magnetic lattices. Furthermore, ordering models associated to the different types of magnetic interactions acting over the $SrLn_2O_4$ systems will be presented along with a review of the recurrent types of magnetic orders stabilised by these materials at low temperature. Finally, the field-induced properties predicted by theoretical ordering models will be discussed.

This chapter only aims to provide a general introduction to the magnetic concepts considered in this thesis work. The reader searching for further advanced and complete material, is thus directed towards more exhaustive references such as Ref. [1, 14, 20, 21].

2.1 Magnetism

2.1.1 Magnetic moment and magnetic ground state

Considered at the atomic scale, magnetism is a purely quantum phenomenon induced by the presence of unpaired electrons on partially filled orbitals. A classical approach can however be used to describe magnetism in term of electrons orbiting around an atom nucleus. In these conditions, by approximating the circulating electrons as a current loop of area equal to the norm of the surface vector **dS**, the most fundamental object in magnetism, i.e. the magnetic moment μ can be defined according to:

$$\mu \;=\; \int d\mu \;=\; I \int d\mathbf{S} \;. \tag{2.1}$$

The magnetic moment has thus the units of A m^2, however it is convenient to use the moment magnitude defined in the case of a single electron orbiting around a hydrogen nucleus as a unit of reference. This unit of magnetic moment magnitude is referred as the Bohr magneton, μ_B, and is given by:

$$\mu_B \;=\; \frac{e\hbar}{2m_e} \;=\; 9.274 \;\times\; 10^{-24}\mathrm{Am}^2 \;. \tag{2.2}$$

As electrons have a mass, orbital motion of masses are involved within the current loop. Consequently, the magnetic moment is connected with the angular momentum **L**. In the simple case of an electron bunch of total mass m and total charge q orbiting on a circular pass, μ can be defined in terms of angular moment by:

$$\boldsymbol{\mu}_B \;=\; \frac{q}{2m}\mathbf{L} \;=\; \gamma\,\mathbf{L}\;, \tag{2.3}$$

where γ is a constant known as the gyromagnetic ratio.

These classical concepts are however not sufficient to describe the magnetic properties of real atoms and a quantum mechanical approach must be considered. In fact, in real atoms the electronic angular momentum is defined as the orbital angular momentum, and depends on the electronic state occupied by the orbiting electrons. In this condition the magnitude of the orbital angular momentum **L** is given by $\sqrt{l(l+1)}\;\hbar$, where l is the orbital quantum number (l = 0,1,2,...) and $\hbar$ is the reduced Planck constant equal to 1.055×10^{34} Js. The magnitude of the total dipole moment is then given by $\sqrt{l(l+1)}\;\mu_B$. The situation further complicates with the introduction to the model of the intrinsic angular momentum of electrons

called the spin, **S**. Similarly to the orbital quantum number, a spin quantum number is defined and takes a unique value equal to $\frac{1}{2}$. The magnitude of the spin angular momentum of an electron is then given by $\sqrt{s(s+1)}\ \hbar = \frac{\sqrt{3}\hbar}{2}$. The magnetic moment associated to the spin angular momentum in turn takes the magnitude $\sqrt{s(s+1)}\ g\ \mu_B = \frac{\sqrt{3}\ g\ \mu_B}{2}$. The constant g known as the g-factor takes a value of $\sim$2, hence the z-component of the electron intrinsic magnetic moment's magnitude has a value of $\sim\pm\mu_B$.

In atoms, the electrons are methodically filling up electronic shells according to the Pauli principle. In these conditions, entirely occupied shells will result with no net angular momentum. A partially filled shell may however exist. The orbital and spin angular momenta of the electrons occupying this particular shell will combine separately, resulting in a total angular momentum $\hbar\mathbf{L}$ and a total spin angular momentum $\hbar\mathbf{S}$. Atomic states are obtained by summation of these two components, resulting in the total angular momentum $\hbar\mathbf{J}$. The effective magnitude of the magnetic moment considered along z is then given by $p = \sqrt{J(J+1)}\ g_J$, in units of Bohr magnetons ($p = \mu_{eff}/\mu_B$). The normalisation factor g_J is known as the Landé g-value and is given by:

$$g_J \approx \frac{3}{2} + \frac{S\,(S\,+\,1)\,-\,L\,(L\,+\,1)}{2\,J\,(J\,+\,1)}\,. \tag{2.4}$$

These atomic orbital and spin angular momenta do however weakly combine via the spin-orbit interaction which slightly perturbs the model. Due to this perturbation only the total angular momentum $\mathbf{J} = \mathbf{L} + \mathbf{S}$ is conserved resulting in the splitting of the atomic (L and S) states in several J sub-levels. **J** can range between $|L - S|$ and $|L + S|$, resulting in many possible combinations. This splitting is known as the fine structure. In order to find the combination of angular momentum that will minimise the energy and provide the atomic ground state, a set of three empirical rules established by Hund can be employed respecting the listing order. These rules are:

1. Maximise S - The Pauli exclusion principle forbids two electrons having parallel spins to be on the same orbital. The electrostatic repulsion between electrons is thus reduced in a state where electrons in the same spin state occupy different orbitals.

2. Maximise L - Maximising L can also be seen as a way to reduce the Coulomb repulsion by imagining that it is easier for electrons circulating all in the same direction to avoid each other.

Ion	shell	S	L	J	p	p_{exp}
Nd^{3+}	$4f^3$	3/2	6	9/2	3.62	3.3-3.7
Gd^{3+}	$4f^7$	7/2	0	7/2	7.94	7.98
Er^{3+}	$4f^{11}$	3/2	6	15/2	9.59	9.5

Table 2.1: Electronic shell configuration, predicted ground state quantum numbers and magnetic moments magnitude of ions Nd^{3+}, Gd^{3+} and Er^{3+}. The experimentally determined magnetic moments values are added to the table for comparison. Table adapted from Ref. [1]

3. The value taken by J is found using $J = |L - S|$ if the shell is less than half full, and alternatively $J = |L + S|$ if the shell is more than half full. This rule relying on spin-orbit coupling considerations.

It should however be borne in mind that Hund's rules are only applicable to predict atomic ground states. Furthermore, the third rule relying on the spin-orbit coupling effect is only accurate in the case of rare earth ions. This rule is actually disobeyed by transition metal ions, being more affected by crystal field interactions generally inducing situations of orbital quenching. In the particular case of rare earth ions, the situation is different since the partially occupied $4f$ shells are well embedded beneath the fully occupied $5s$ and $5p$ shells. In these conditions, the crystal field effects are largely annihilated and the spin-orbit coupling is significant, resulting in accurate predictions of Hund's rules. The predicted values of S, L and J corresponding to the ground states of the Ln^{3+} ions of interest in this thesis are listed in Table 2.1, along with the shell configurations and both predicted and experimental magnetic moment values given in Bohr magnetons.

2.1.2 Magnetic moment subjected to an applied magnetic field

In magnetic solids, large numbers of magnetic ions bearing a magnetic moment are concentrated in restricted volumes. In such conditions, the magnetic moment per unit volume of material is defined as the magnetisation **M**. This physical quantity is directly related to the degree of magnetic order in solids, and consequently to both temperature and applied magnetic field conditions. Accounting for the non-zero magnetic permeability of free space ($\mu_0 = 4\pi \times 10^{-7}$ Hm^{-1}), a magnetic field propagating in vacuum is defined by two vector fields **B** and **H**, through the linear relation $\mathbf{B} = \mu_0 \mathbf{H}$. In magnetic solids however, a more complex relation including the solids magnetisation **M** is needed to relate the two vector fields **B** and **H**. This relation is given by:

$$\mathbf{B} \;=\; \mu_0 \,(\mathbf{H} \;+\; \mathbf{M}) \;. \tag{2.5}$$

In some specific cases, the magnetisation is found to be linearly proportional to the field propagating through the material. Such solids are called linear and the relation of proportionality is written as:

$$\mathbf{M} \;=\; \chi \,\mathbf{H} \;. \tag{2.6}$$

The proportionality constant χ is dimensionless and known as the magnetic susceptibility. In these conditions, equation. 2.5 is rewritten as:

$$\mathbf{B} \;=\; \mu_0(1 \;+\; \chi)\mathbf{H} \;=\; \mu_0 \,\mu_r \,\mathbf{H} \;, \tag{2.7}$$

with $\mu_r = 1 + \chi$ the material's relative permeability.

Consequently, by applying a low value of **B** on a solid and by measuring **H** at a temperature T, the magnetic susceptibility of the material can be monitored to characterised the magnetic state of the solid. I note that the magnetic susceptibility measurements $\chi(T)$ presented in this thesis consider molar magnetic susceptibilities. More precisely, the normalisation is made per single Ln^{3+} ions. In such conditions, the susceptibility is defined as the magnitude of an average Ln^{3+} moment induced by a field **H**, per unit of volume corresponding to the space occupied by a single Ln^{3+} ion within the unit cell of the material.

In diamagnetic materials, susceptibility measurements return negative values. In fact, when subjected to the applied field **H**, these materials that originally had no net magnetic moments respond by the stabilisation of an internal field that opposes **H**. This induced magnetic field render such materials impermeable to externally applied magnetic fields, a property that can be use to levitate diamagnetic solids above magnets. Considering a diamagnetic solid of volume V containing N ions, each having z electrons of mass m_e, the diamagnetic susceptibility is given by:

$$\chi_{dia} \;=\; -\,\frac{N}{V}\,\frac{e^2\mu_0}{6m_e}\sum_{i=1}^{z}\langle r_i^2\rangle \;, \tag{2.8}$$

where r is the atomic radius implying a spherical distribution of the electrons.

Alternatively, if the measured susceptibility is positive the material can either be in a paramagnetic or in an ordered state. Paramagnetic materials contain atoms bearing randomly ordered magnetic moments created by unpaired electrons. The application of a field **B**, induces a magnetisation of the system by aligning the moments parallel to its direction of propagation resulting in a positive value of χ.

The magnetisation of the system will be written as

$$M \;=\; M_S B_j(y)\;, \tag{2.9}$$

where

$$y \;=\; g_j \mu_B \frac{JB}{k_B T}\;, \tag{2.10}$$

and M_S is the saturation value of magnetisation given by

$$M_s \;=\; n g_J \mu_B J\;, \tag{2.11}$$

with n the number of magnetic moments per unit volume, k_B the Boltzmann constant and $B_J(y)$ the Brillouin function defined as

$$B_j(y) \;=\; \frac{2J+1}{2J}\coth\Big(\frac{2J+1}{2J}y\Big) - \frac{1}{2J}\coth\frac{y}{2J}\;. \tag{2.12}$$

The Brillouin function reduces to the Langevin L(y) = coth(y)-1/y function or to a tanh function respectively for the two limiting cases J = ∞ and J = 1/2.

Employing the Maclaurin coth expansion for small values of y, the Brillouin function can be rewritten as

$$B_j(y) \;=\; (J+1)\frac{y}{3J} + O(y^3)\;. \tag{2.13}$$

The magnetic susceptibility of a paramagnetic system can then be approximated by

$$\chi_{para} \;=\; \frac{M}{H} \;\approx\; \frac{\mu_0 M}{B} \;=\; \frac{n\mu_0\mu_B^2}{k_B T}\;. \tag{2.14}$$

The magnetic susceptibility of magnetically ordered states such as ferromagnetism and antiferromagnetism will be treated in section 2.1.5.

2.1.3 Crystalline electric field

Within magnetic solids, the influence of the local environments on the properties of the magnetic atoms have so far been neglected in my reasoning. However for many materials, these interactions significantly influence the magnetic properties at the atomic level. In crystalline materials, the magnetic ions are embedded in closed local environments which are often not spherically symmetric. Furthermore, despite the spherical s orbitals, most electronic orbitals possess a strong angular dependence that provides them with individual symmetry properties. Consequently, in

crystalline materials close degrees of proximity between orbitals belonging to neighbouring atoms can induce strong conditions of electrostatic repulsion. In particular the orbitals of the magnetic ions are affected with different energy cost. In rare earth materials, the $4f$ orbitals are well embedded beneath the $5s$ and $5p$ shells, hence the local environments will only have a reduced effect in comparison with the case of transition metals. The strong condition of repulsion between the external shells and the close surrounding however, results in the induction of an electric field known as the crystalline electric field. This electric field propagates through the material and splits the J levels of rare earth magnetic ions in up to $2J+1$ sub-levels. In the case of rare earth ions having odd numbers of unpaired $4f$ electrons (the Kramers ions), the ground state must remain a doublet. In fact, as a consequence of Kramers theorem, the J sub-levels must at least keep a two fold degeneracy when subjected to an electric field. In these conditions, the ground state of Kramers ions can be assigned an effective spin 1/2, since it resembles a spin one half state.

In the particular case of the members of the $SrLn_2O_4$ crystaline family investigated within the frame of this thesis, all Nd^{3+}, Gd^{3+} and Er^{3+} have odd numbers of unpaired $4f$ electrons. These ions being embedded within distorted octahedral environments, the influence of the crystal field environment is expected to be significant. In the case of Neodymium $J = 9/2$, I thus expect a splitting of the ground state into five Kramers doublets. Similarly, for the Erbium $J = 15/2$, the ground state should thus be splitted into eight sub-levels. The case of the Gadolinium is however largely different. In fact, in this particular ion L equals zero and J only results from the spin angular momentum of the $4f$ electrons. The ground state of this ion is thus not expected to by split by crystal field interactions.

As a result, both $SrNd_2O_4$ and $SrEr_2O_4$ systems will be affected by large single ion anisotropy properties, inducing preferable alignments of the magnetic spins according to particular crystallographic directions of the lattice. The $SrGd_2O_4$ system on the other hand, should not reveal such properties.

2.1.4 Magnetic interactions

It is now time to consider the influence of neighbouring magnetic interactions in my reasoning. In fact, in condensed matter different types of magnetic interactions exist between neighbouring magnetic ions. These interactions create a lattice of connections within magnetic materials and in some cases may induce long range orders.

The first type of magnetic interaction that I introduce is the magnetic dipolar interaction. This particular type of interaction is rather weak and will only be in a

position to significantly influence the ordering of a magnetic system at temperatures of a few Kelvins. The dipolar energy of the simplest system consisting of two magnetic dipoles μ_1 and μ_2 separated by a distance r, is given by:

$$E \;=\; \frac{\mu_0}{4\pi\; r^3}[\boldsymbol{\mu_1}\cdot\;\boldsymbol{\mu_2}\;-\;\frac{3}{r^2}(\boldsymbol{\mu_1}\cdot\;\boldsymbol{r})(\boldsymbol{\mu_2}\cdot\;\boldsymbol{r})]\;. \tag{2.15}$$

Thus the dipolar energy depends and the magnitude of the spin, on their relative distance and on the degree of mutual alignment. Within the frame of the $SrLn_2O_4$ systems, the dipolar interactions are suspected to induce long range magnetic orderings at temperatures of very few Kelvins.

The second type of magnetic interactions that is usually the strongest in magnetic systems, is known as the exchange interaction and is a purely quantum mechanical phenomenon. This property of matter lies in the fact that the overall wave function of two electrons considered in a joint state must be antisymmetric. So alternatively the spin part of the wave function can be an antisymmetric singlet state ($S = 0$) and the spatial part symmetric, or the spin part can be a symmetric triplet state ($S = 1$) and the spatial part antisymmetric. Then considering arguments that are beyond the level of complexity of my reasoning, it can be shown that the energy difference between triplet and singlet states ($E_T - E_S$) can be parametrized using $\mathbf{S}_1 \cdot \mathbf{S}_2$, and an effective Hamiltonian of the system can be written as:

$$\hat{H} \;=\; \frac{1}{4}(E_S \;+\; 3E_T) - (E_S - E_T)\;\mathbf{S_1}\cdot\;\mathbf{S_2}\;. \tag{2.16}$$

This relation is the sum of a constant and of a term that includes the dot product of the two spins. While the first terms can be relocated among other constants, the second term is used to define a constant $J = \frac{E_S - E_T}{2}$ known as the exchange constant. Thus the spin dependent term of the effective Hamiltonian can be written as:

$$\hat{H}^{spin} \;=\; -\,2J\;\mathbf{S_1}\cdot\;\mathbf{S_2}\;. \tag{2.17}$$

According to this relation, if J is positive then the triplet state ($S = 1$) is favoured, and alternatively if J is negative the singlet ($S = 0$) is favoured. Due to the relative ordering of the two spins considered, the triplet state results in ferromagnetic ordering while the singlet state results in antiferromagnetic ordering. An adaptation of this effective Hamiltonian to a many-body system is given by:

$$\hat{H} \;=\; -\,2\sum_{i>j} J_{ij}\;\mathbf{S_i}\cdot\;\mathbf{S_j}\;. \tag{2.18}$$

This Hamiltonian is known as the Heisenberg Hamiltonian and J_{ij} is the exchange constant between the i^{th} and the j^{th} spins.

Considered between two neighbouring magnetic spins contained within a material, this interaction is known as the direct exchange interaction. However, direct exchange interactions are in reality restricted in solid state materials by inter-ionic distances being too large to allow for good magnetic orbital overlapping. This fact is particularly true in the case of rare earth elements where the $4f$ orbitals being well embedded beneath fully occupied shells do usually not extend further than a tenth of inter-ionic distances. Nevertheless, exchange interactions can be mediated by the orbitals of non-magnetic ions forming the lattice of crystalline materials. These types of exchange interactions usually being at the origin of magnetic ordering phenomena, are referred as indirect exchange or superexchange interactions. In the following however, close neighbours exchange interactions would be only referred as exchange interactions for simplicity.

2.1.5 Magnetic ordering

In some paramagnetic materials, a spontaneous magnetisation resulting in long range orderings can be induced as an effect of temperature reduction in the absence of externally applied field. These orderings result from the action of the strong close neighbours magnetic interactions previously described (see subsection 2.1.4). In the particular case of exchange interactions, the Heisenberg Hamiltonian (see eqn. 2.18) reveals that the energy of magnetic systems will be reduced by aligning neighbouring moments either parallel (J>0) or anti-parallel (J<0). In a situation where neighbouring exchange interactions are strong enough to overcome thermal fluctuations, ferromagnetic or antiferromagnetic orders can then propagate through the materials resulting in the phenomena of long range ordering. At this point, it is also interesting to define the notion of internal molecular magnetic field. In fact, magnetic orderings can also be seen as resulting from the action of an internal molecular field $\mathbf{B}_{mf}$. This field is induced by ordered spins and propagates through the paramagnetic materials in turn inducing more order. If the temperature of a particular paramagnetic system is lower than a critical value, long range ordering will be established by the molecular field. I note that this interpretation results is a kind of "chicken-and-egg" scenario since the molecular field inducing the ordering, is induced by magnetic order in the first place.

In these conditions, a Zeeman term accounting for the molecular field ($\mathbf{B}_{mf}$) effects should be included in the effective Hamiltonian (see eqn. 2.18) that can be re-written as:

$$\hat{H} \;=\; g\mu_B \sum_i \mathbf{S}_i \;\cdot\; \mathbf{B}_{mf} \;. \tag{2.19}$$

This new way of expressing the effective Hamiltonian reveals that it is possible to consider the magnetic system as a paramagnet subjected to an external field.

$\mathbf{B}_{mf}$ can thus now be related to the magnetisation $\mathbf{M}$ of paramagnetic materials according to the relation:

$$\mathbf{B}_{mf} \;=\; \lambda \mathbf{M} \;, \tag{2.20}$$

where λ is a proportionality constant between the molecular field and the magnetisation. In the case of ferromagnets, λ is positive resulting in consequent values of molecular fields. In the case of antiferromagnets, the situation can be seen as two interpenetrating ferromagnetic lattices in mutual opposition. Hence, similarly to the purely ferromagnetic case, partial molecular fields and magnetisations can be attributed to each sublattices. By labelling one of these two sublattices as "+" and the other one as "-", the relationships between molecular field and magnetisation on each sublattice are given by:

$$\begin{aligned} \mathbf{B}_+ \;&=\; -\,|\lambda| \mathbf{M}_- \\ \mathbf{B}_- \;&=\; -\,|\lambda| \mathbf{M}_+ \;, \end{aligned} \tag{2.21}$$

where λ is now negative.

In both ferromagnetic and antiferromagnetic systems, when reaching a critical temperature the molecular field will start to vanish and the magnetic orders will be destroyed. Relatively for antiferromagnets and ferromagnets these critical temperatures are known as Néel and Curie temperatures and are defined as:

$$\begin{aligned} T_C \;&=\; \frac{n\lambda\mu_{eff}^2}{3k_B} \\ T_N \;&=\; \frac{n|\lambda|\mu_{eff}^2}{3k_B} \;. \end{aligned} \tag{2.22}$$

Implying these two critical temperatures, the magnetic susceptibility of both ferromagnets and antiferromagnets can be fitted to Curie Weiss dependencies.

$$\chi \propto \frac{1}{T - T_C} \text{ for ferromagnets}$$
$$\text{and} \tag{2.23}$$
$$\chi \propto \frac{1}{T + T_N} \text{ for antiferromagnets}$$

A combination of these two relations in a unique model is given by:

$$\chi = \frac{C}{T - \theta} , \tag{2.24}$$

where C is the Curie constant, and $\theta = \frac{\lambda C}{\mu_0}$ the Curie Weiss temperature. Considering equations 2.23 and 2.24, it can directly be seen that the determination of θ provides with direct information regarding the nature of the magnetic system under investigation. In fact, if $\theta = 0$ the system is a paramagnet. If θ is positive, the system will be a ferromagnet and $\theta = \mathrm{T}_C$. If θ is negative, the system is an antiferromagnet and $\theta = \text{-}\mathrm{T}_N$. A graphical illustration of these considerations is displayed in Fig. 2.1, where the inverse susceptibilities of paramagnetic, ferromagnetic and antiferromagnetic systems are fitted to Curie Weiss dependencies.

In real antiferromagnets however, phenomena such as magnetic frustration can significantly reduce the value of T_N in comparison to the fitted value of θ. Large differences between T_N and $|\theta|$ are in fact an indicator of strong degrees of frustration in magnetic materials, as will be detailed in the following subsection.

The nature of the different type of magnetic orders stabilised by the $SrLn_2O_4$ materials will be detailed in subsection 2.2.2, after having defined the geometrical properties of the crystalline lattice.

2.1.6 Magnetic frustration

In real magnetic systems, a situation of competition is often set between the close neighbour magnetic interactions due to the geometry of the crystalline lattice. This phenomenon is known as geometrical frustration and often leads to the observation of interesting and unusual magnetic properties. To illustrate this situation of incompatibility between on one hand the geometry of the crystalline lattice and on the other hand, the nature of the magnetic interactions acting between neighbouring magnetic moments. One can consider a situation implying three Ising magnetic moments interacting via antiferromagnetic exchange interactions on a triangular lattice, see Fig. 2.2. As it can easily be understood, it is impossible to order the

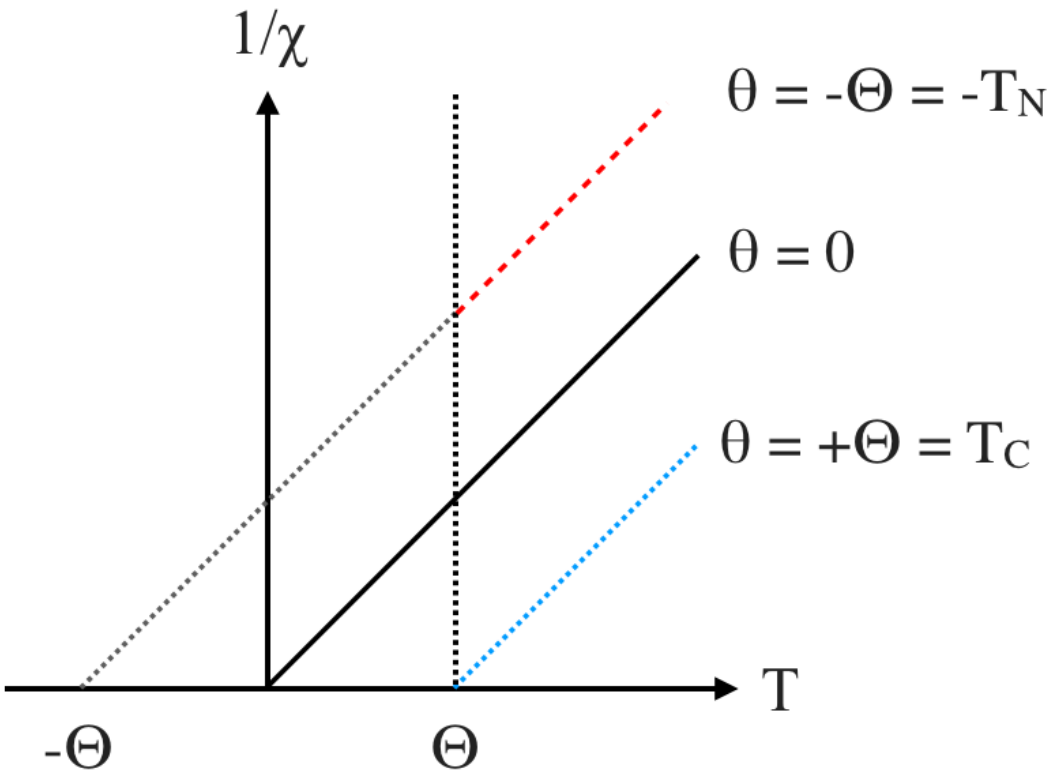

Figure 2.1: Graphical illustration of the Curie Weiss law. The inverse susceptibility trends of an antiferromagnet (red), a ferromagnet (blue) and of a paramagnet (black) are fitted to Curie Weiss dependencies. The corresponding values of θ are given by the intercepts of the linear trends with the temperature axis.

spins in a way that will simultaneously fully satisfy all the three antiferromagnetic interactions. A situation of competition is thus set and the interactions will not be in a position to entirely reduce the energy of the system resulting in six frustrated possible combinations of up and down spins. Real lattices can present rather complex combinations of such triangles resulting in situations where the number of low energy spin configurations is such that single magnetic ground states are lacking. It is then possible to externally favour the stabilisation of a particular ground state spin configuration, by means of externally applied magnetic fields or particular thermal treatments. Furthermore, frustrated systems will show a strong dependence on magnetic and thermal history.

In two-dimensional space, a few particularly famous examples of frustrated magnetic lattices are the simple edge-sharing triangular, the honeycomb lattices [22] and the kagomé lattices [16]. The structure of the kagomé lattice consists of hexagons being surrounded by equilateral triangles. In turn the triangles are also surrounded

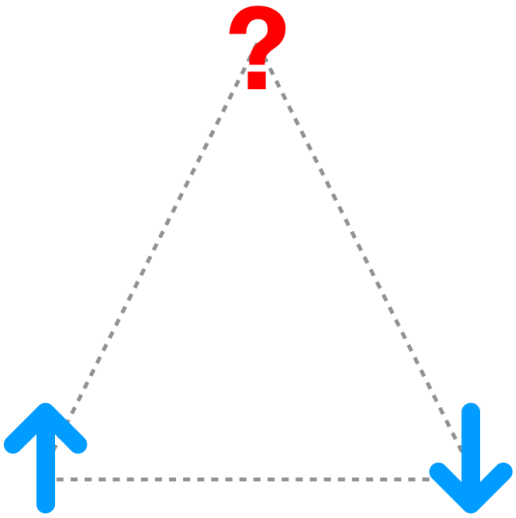

Figure 2.2: Schematic of a frustrated triangle. The magnetic spins considered interact via antiferromagnetic interactions resulting in a situation of strong competition.

by hexagons, resulting in a pavement offering many combinations of interpenetrating triangular interactions, see Fig. 2.3 a). The honeycomb lattice consists of an edge sharing pavement of hexagons, see Fig. 2.3 b). In this geometry, first neighbours antiferromagnetic interactions are not frustrated and second neighbours should be considered to result in a situation of competition. The geometrical frustration of these magnetic systems often results in the stabilisation of complicated magnetic structures at temperatures being significantly lower than the predicted Curie Weiss temperatures. Alternatively situations of short range ordering can also be stabilised by these systems keeping a significant degree of disorder down to the lowest temperatures.

In three dimensional space many frustrated lattices also exist, such as the garnets [17] or the face centered cubic structures e.g. double perovskites [23], but also the $SrLn_2O_4$ materials [24]. The most famous systems however, are known as the pyrochlores [14, 15], and consists in lattices of corner sharing tetrahedra, see Fig. 2.3 c). In pyrochlore materials frustration effects are usually very strong and prevents for long range ordering of the spins to take place in these systems down to the lowest temperatures. A resulting spin ice behaviours is exhibited by these systems being a particularly novel and strongly investigated phenomena in current research.

The $SrLn_2O_4$ family members are also strongly frustrated systems, but none of them was shown to exhibit a spin ice behaviour when cooled down to dilution

fridge temperatures. A description of the physics of spin ice systems is thus out of the scope of this thesis work and I advise interested readers to alternatively consult the following references [14, 15]. Very interesting magnetic properties induced by the frustration of the $SrLn_2O_4$ lattices are however expected and will be described in the following section 2.2.1.

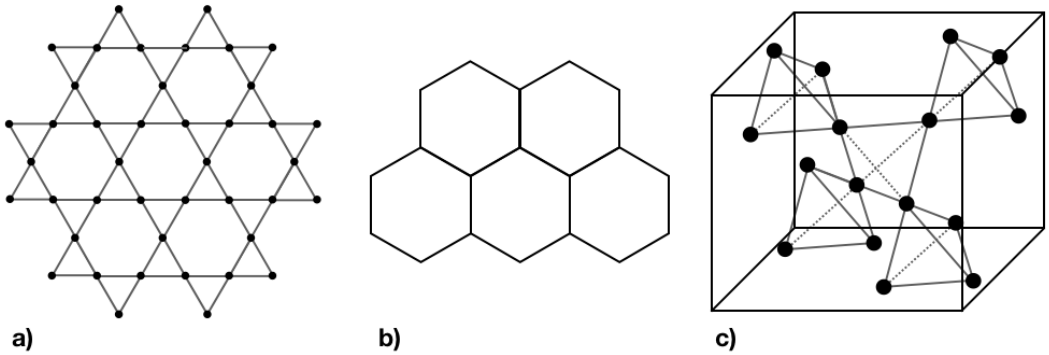

Figure 2.3: Examples of frustrated lattices. a) Kagomé, b) honeycomb and c) pyrochlore.

2.2 The $SrLn_2O_4$ systems

The $SrLn_2O_4$ crystalline family (Ln = Lanthanide) was discovered about fifteen years ago by the group of Karunadasa [24]. The magnetic sublattice of these materials consists of interconnected triangular ladders forming a distorted honeycomb structure in three dimensional space. Such a crystalline geometry offers many combinations of triangular interactions as well as honeycomb lattice characteristics, resulting in strongly frustrated properties revealed as quite interesting by the preliminary investigations performed by Karunadasa *et al.*. Following this initial work, extensive studies have been dedicated to the magnetic property investigations of various members of the family. In particular, significant progress was achieved in the determination and understanding of the magnetic properties of the $SrDy_2O_4$ [25–28], $SrHo_2O_4$ [29, 30], $SrEr_2O_4$ [31–34] and $SrYb_2O_4$ [35] variants. The most advanced results of these investigations, as well as more general features of the $SrLn_2O_4$ systems will be detailed in the next coming subsections. These results will then be used as a background for the development of my understanding of the magnetic properties exhibited by the particular variants of the family investigated within the frame of this thesis, i.e. $SrNd_2O_4$, $SrGd_2O_4$ and $SrEr_2O_4$.

2.2.1 Crystalline lattice of $SrLn_2O_4$ materials

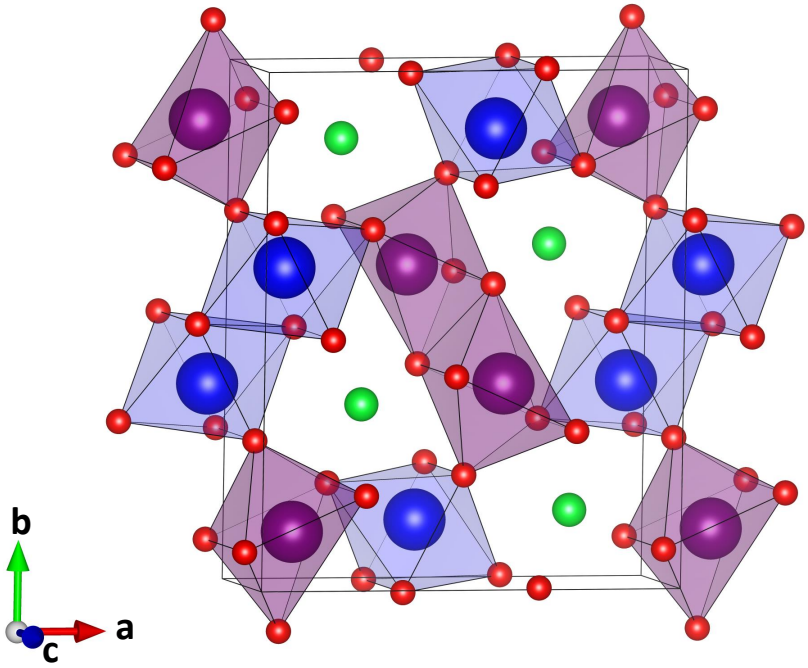

Figure 2.4: Schematic of the crystallographic unit cell of $SrLn_2O_4$ materials as seen within the $a-b$ plane. Sr, O, Ln1 and Ln2 ions are represented as green, red, blue and purple spheres, respectively. The distorted oxygen octahedral environments hosting both Ln1 and Ln2 ions and forming the distorted hexagonal lattice within the $a-b$ plane are displayed with shaded colours for clarity. This representation corresponds to the $SrNd_2O_4$ structure determined from Rietveld refinement of NPD data collected at room temperature.

The $SrLn_2O_4$ family of materials crystallises under the form of calcium ferrite [36], according to the orthorombic space group Pnam(62) [24]. I note that this space group notation is not the standard according to the international Hermann-Mauguin notation, however it has so far been used in every publication concerning the investigation of $SrLn_2O_4$ materials and should thus be kept to avoid confusion. According to this setting, the a and b axes of the unit cell have similar lengths and are significantly longer than c, the third axis. Within the frame of this thesis, the c direction will eventually be labelled as the vertical direction of the crystalline structure, while a and b define the horizontal plane. The unit cell contains 28 ions, all sitting at the Wyckoff $4c$(x,y,0.25) positions. They are split into seven groups, each of them containing four crystallographically inequivalent λ types of ions, with λ = Sr, Ln1, Ln2, O1, O2, O3 and O4. Hence the crystalline structure of these materials is hosting the lanthanides ions within two crystallographically inequivalent

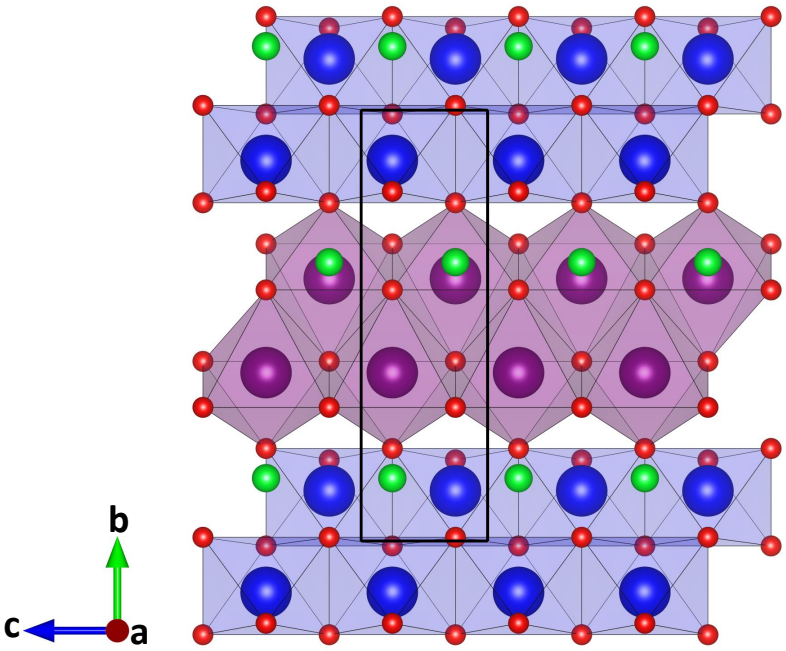

Figure 2.5: Representation of the $SrLn_2O_4$ crystalline lattice as seen within the $b-c$ plane. A single layer of ions is considered along the a axis on this representation for clarity reasons. This view of the structure allows to appreciate both Ln1 and Ln2 types of triangular ladders propagating along c, as well as the one dimensionality of the ladders' legs.

sites referred as Ln1 and Ln2. At these two positions the Ln ions are sitting within distorted oxygen octahedral environments, see Fig. 2.4. Within the horizontal plane of the structure, neighbouring octahedra corresponding to the same type of Ln site connect by sharing a particular edge, while close neighbours corresponding to different Ln sites are only sharing a corner. These connections result in distorted planes of edge sharing hexagons lying within the horizontal plane of the unit cell. Seen within the $b-c$ plane, the structure consists in two dimensional triangular ladders of Ln1 and Ln2 ions propagating along the c axis. The one dimensionality of the ladders' legs, consisting of Ln ions chains is also nicely appreciated within the $b-c$ plane, see Fig. 2.5. Moreover, as a result of different octahedral connections (i.e. edge or corner sharing interactions), the distances separating neighbouring ions sitting on two different types of ladders are longer than the distances implied within the ladders. For instance within the $SrNd_2O_4$ hexagonal planes at room temperature, Nd1-Nd1 = 3.639(5) Å and Nd2-Nd2 = 3.724(5) Å, while Nd1-Nd2 = 3.884(4) and 4.123(4) Å. Thus, dominating magnetic interactions are expected to be established within the ladders frames, while only weaker inter-ladders interactions could be in

a position to influence the $SrLn_2O_4$ systems. The triangular ladders consequently stand out as the principal features of the $SrLn_2O_4$ magnetic sublattice, their magnetic properties are thus expected to lead the general properties of these systems. Furthermore, taking into consideration both Ln1 and Ln2 site symmetry inequivalences, one can predict the observation of different magnetic behaviours for both type of ladders. In fact, the different degrees of distortions affecting both types of octahedra will have major implications on the crystal field parameters of each Ln site. Consequently, strong single ion anisotropic properties are expected to be revealed by the $SrLn_2O_4$ systems.

It is subsequently interesting to consider a representation solely displaying the magnetic ions. Furthermore, adding the close neighbours inter-ionic bonds as colour lines to the figure reveals the honeycomb geometry of the $SrLn_2O_4$ magnetic sublattice, consisting in many different combinations of neighbouring triangular interactions, see Fig. 2.6. Both Ln1 and Ln2 types of triangular ladders are particularly well evidenced by this representation. Focusing on the magnetic ladders, it should be mentioned that the distances separating two ions along the ladders' legs are equal on both types of ladders (e.g. 3.57070(6) Å in the $SrNd_2O_4$ case). However the distances corresponding to the rungs are different (e.g. Nd1-Nd1 = 3.639(5) Å and Nd2-Nd2 = 3.724(5) Å). Thus, in addition to crystallographically inequivalent sites hosting the magnetic ions, inequalities in the rungs lengths are expected to favour the stabilisation of contrasting magnetic behaviours for the two types of ladders.

Considering the honeycomb lattice, as previously mentioned magnetic frustration only arises while considering second neighbour antiferromagnetic interactions. Within the frame of the $SrLn_2O_4$ lattice, such distances are considerable for rare-earth type of exchange interactions. Effects resulting from the frustration of the honeycomb lattice are thus not expected to compete with the effects resulting from the strong frustration of the triangular ladders. However, the relative orientation of magnetic orders stabilised by neighbouring ladders could be influenced by the geometry of the honeycomb lattice.

Overall, the $SrLn_2O_4$ crystalline structure is hosting a bipartite magnetic sublattice consisting of interconnected triangular ladders propagating along the c axis, and positioned in an hexagonal geometry resulting in a three dimensional honeycomb structure. The inter-ionic distances involved within the ladders are shorter than other distances in the lattice. Thus, the ladders can be considered as the principal features of the $SrLn_2O_4$ magnetic lattice and only weak connections with the immediate surrounding should influence their magnetic properties.

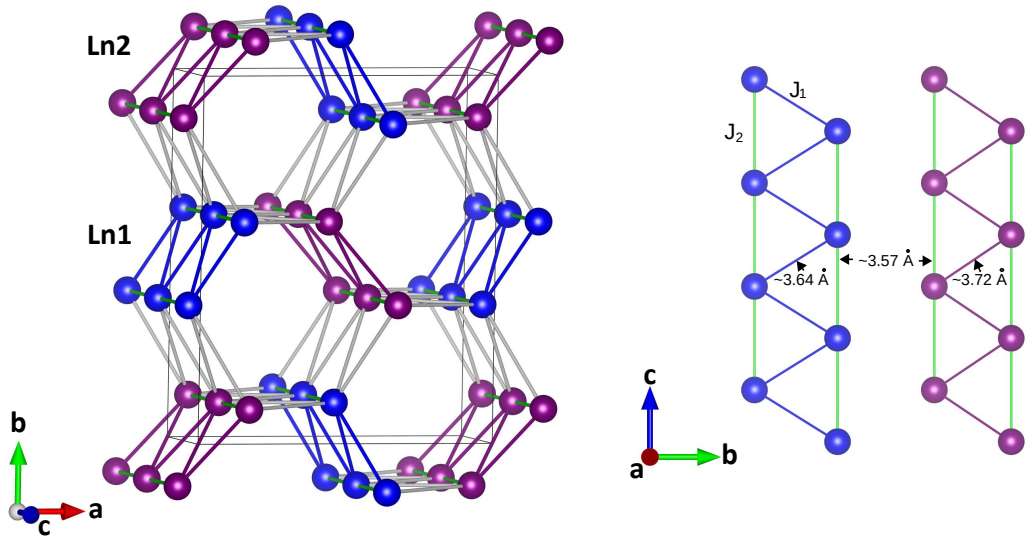

Figure 2.6: Schematic of the $SrLn_2O_4$ magnetic sublattice. Left: Three dimensional representation within the frame of the crystallographic unit cell of the material. The rungs of Ln1 and Ln2 magnetic ladders having unequal lengths are displayed in blue and purple, respectively. The legs of the ladders on the other hand, being equal on both types of ladders are represented using the same colour, i.e. in green. Inter-ladder distances being significantly longer than the ladders distances are represented in pale grey. Right: Two dimensional representation of the two different types of triangular ladders. Exchange interactions acting along the legs and rungs of the ladders are referred as J_1 and J_2, respectively.

2.2.2 General magnetic properties of $SrLn_2O_4$ systems

The recent investigations of several members of the $SrLn_2O_4$ family have revealed the recurrent stabilisation of two particular types of magnetic orders stabilised on the triangular ladders. The first type consists in ferromagnetic chains running along the c axis of the materials, while two adjacent chains are paired antiferromagnetically. This order, is stabilised by $SrEr_2O_4$ [31, 34, 37] and $SrHo_2O_4$ [29, 30] materials involving a single type of Ln site. This spin configuration is referred as a Néel order or as the up-down-up-down (ududd) order, considering the succession of up and down spins progressing along the ladders direction of propagation. Focusing on the particular $SrEr_2O_4$ case, the structural characteristics of this order were recently understood by theorists to result from the stabilisation of first and second neighbour dipolar interactions on the triangular ladder frame [31]. In fact, considering equation 2.15, it is understood that first neighbour interactions are stabilised ferromagnetically while second neighbour interactions involving larger distances will be

stabilised antiferromagnetically. Thus the dipolar interaction will not be frustrated when stabilising a udud order on the triangular ladder geometry. Furthermore, the $SrGd_2O_4$ system investigated within the frame of this thesis (see chapter 6) also stabilises a udud order. In this particular case however, the moments of both magnetic sites are involved, resulting in an up-down alternation of spins circulating around the distorted hexagon frame. Consistently with the $SrEr_2O_4$ understanding, the $SrGd_2O_4$ udud structure had previously been evidenced via Monte Carlo simulations considering a purely dipolar Hamiltonian for the system [38]. It is also important to mention that udud orders are stabilised by $SrLn_2O_4$ materials at temperatures approaching zero Kelvin, as expected for the stabilisation of dipolar interactions being significantly weaker than exchange interactions. Moreover, udud orders have uniquely been observed to be hosted by $SrLn_2O_4$ variants containing the Ln^{3+} ions bearing the largest magnetic moments. The strength of dipolar forces being strongly dependent on the magnitudes of the magnetic moments involved in the interactions is thought to be a direct consequence of this trend.

Another understanding has however been proposed to explain the stabilisation of the udud orders and is presented in a series of recent publications by various authors [33, 34, 39–41]. This understanding lies on a model considering the competition of first and second neighbours exchange type of interactions within the ladder frame. This model is known as the J_1-J_2 model, J_1 (legs) and J_2 (rungs) corresponding to first and second neighbours interactions, respectively [42–44]. Of particular interest, within the frame of this model it is understood that the triangular ladders of $SrLn_2O_4$ systems are magnetically equivalent to frustrated one dimensional spin chains with antiferromagnetic first and second neighbour interactions [33]. Thus, the J_1-J_2 model becomes equivalent to the well known (ANNNI) anisotropic next-nearest neighbours Ising model [21] and can be described by a simple effective Hamiltonian given by [43, 44]:

$$\hat{H} \;=\; \sum_i J_1 \mathbf{S_i}^x \cdot \mathbf{S}^x{}_{\mathbf{i+2}} \;+\; J_2 \mathbf{S_i}^x \cdot \mathbf{S}^x{}_{\mathbf{i+1}} - H\mathbf{S_i}^x \tag{2.25}$$

I note that in this particular case it is considered that the spins point perpendicular to the chains directions of propagation being z. This configuration will help the understanding of further discussions and is fully equivalent to the situation where the spins are aligned along the chains. Regarding the characteristic of the effective Hamiltonian it is easily understood that in the absence of externally applied field, the stabilisation of two different types of order can be stabilised as a function of J_1 and J_2 relative strengths. In fact, in the strong J_1 limit, a right-right-left-left

(rrll) double Néel configuration will be stabilised on the ladders. On the other hand, in the strong J_2 limit, a rlrl simple Néel order will be more stable, see Fig. 2.7. A critical point between the two phases was found at a J_1/J_2 ratio of 1/2.

On the triangular ladder frame, rlrl and rrll orders are respectively equivalent to the udud Néel and uudd double Néel orders previously described. It is thus also possible to explain the stabilisation of the $SrGd_2O_4$, $SrHo_2O_4$ and $SrEr_2O_4$ Néel udud orders as being stabilised by frustrated J_1 and J_2 exchange interactions on the triangular ladders frame. However, considering the results presented in this thesis and in particular these obtained through the $SrGd_2O_4$ investigation, I have strong reasons to believe that the stabilisation of udud orders are the work of dipolar forces. I also note that uudd double Néel order that would be stabilised in the strong J_1 limit have so far never been reported from $SrLn_2O_4$ systems investigations.

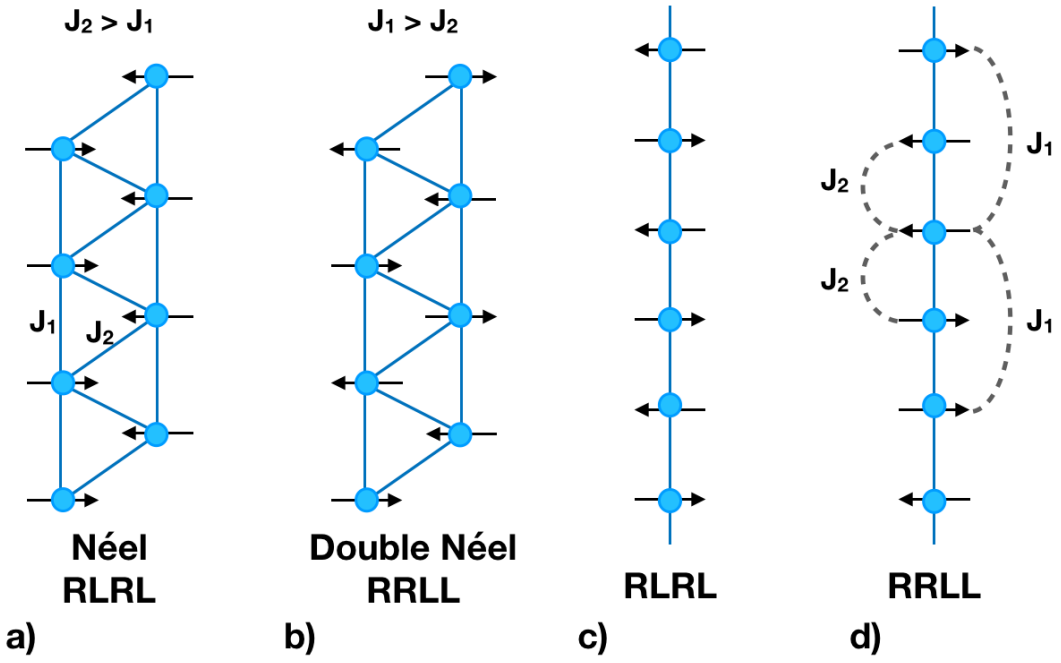

Figure 2.7: Schematic of the different J_1-J_2 spin ordering configurations. The configurations a) and b) are magnetically equivalent to the one dimensional spin chains configurations c) and d). In fact, considering a stretching of the triangular ladders by pulling on the extremities will result in one dimensional chains where J_1 and J_2 interactions now correspond to second and first neighbours interactions.

On the other hand, both rrll and rlrl magnetic orders involving ordered magnetic moments being relatively smaller than these involved in the udud orders are stabilised by several variants of the family and correspond to the second recurrent type of order stabilised by $SrLn_2O_4$ materials. For instance, $SrEr_2O_4$ [31, 33],

$SrHo_2O_4$ [30], $SrNd_2O_4$ (see chapter 5) but also the equivalent system $BaNd_2O_4$ [39], do stabilise a rrll double Néel order involving a single type of Ln site. Moreover, the $SrYb_2O_4$ system was reported to stabilise a rlrl order involving both Yb sites. These observations are thus perfectly consistent with the J_1-J_2 predictions. I thus consider the stabilisations of magnetic orders involving an alignment of the moments within the $a-b$ plane of the $SrLn_2O_4$ materials to result from the competitions of first and second neighbours exchange interactions on the triangular ladder frame. I note that the theorists that reported the udud ordering of a particular $SrEr_2O_4$ site, also reported the rrll ordering of the second site as resulting from the competition of strong antiferromagnetic exchange interactions corresponding to my description of J_1 and J_2. Moreover, it was determined within the frame of this thesis that $SrGd_2O_4$ stabilises a second magnetic phase superimposed to the udud dipolar order at low temperatures. This additional phase also involve both Gd sites and consists of a modulation of rrll and rlrl orders. I believe the stabilisation of this phase to be induced by competing J_1 and J_2 acting over the system independently from the dipolar forces. Moreover, I note that this particular modulated order has not been predicted from the J_1-J_2 model but is understood as being induced by a situation where the J_1/J_2 ratio stands in the vicinity of the critical 1/2 point.

On another aspect of the recurrent properties of these systems, strong single ion properties of anisotropy have been reported from most publications. In fact, it is often the case that a single type of Ln site hosts a long range ordered magnetic phase while the second Ln site remains in a short range ordered state, e.g. $SrEr_2O_4$ and $SrNd_2O_4$. In a few cases, it has even be found that both Ln sites remain in short range ordered states down to the lowest temperatures, e.g. $SrHo_2O_4$ and $SrDy_2O_4$ [25–28]. As an explanation, the crystal field effects induced by the distorted octahedra are believed to prevent for long range ordering transitions to proceed on these particular Ln sites.

Overall, the actions of two different types of magnetic interactions stabilising two classes of magnetic orders dominate the magnetic properties of the $SrLn_2O_4$ systems. As previously mentioned, the two different types of magnetic ladders hosted by these materials are believed to be responsible for this bipartite aspect. In fact, the crystal field environments hosting the magnetic ions as well as the rungs distances are different on the two types of ladders. These two structural characteristics are thus believed to be the fundamental reason inducing the bipartite properties of the $SrLn_2O_4$ systems.

2.2.3 Field-induced magnetic properties of $SrLn_2O_4$ systems

Frustrated systems subjected to external magnetic fields are known to often stabilise exotic magnetic phases [45, 46]. Also, prior to reaching a full polarised state several intermediate phases can be successively stabilised while progressively increasing the applied field magnitude. In the particular case of the $SrLn_2O_4$ systems, the bipartite and often Ising like nature of the low temperature magnetic properties should strongly influence the characteristic of the field-induced properties.

I first detail the case where the field is applied along the c axis of variants of the family hosting a Néel udud order stabilised by dipolar forces. In this configuration, the udud triangular ladders are subjected to a field applied parallel to the spins of one leg and anti-parallel to the spins of the other leg. From Monte Carlo simulations, the M(H) phase diagram of dipolar Ising antiferromagnets subjected to a magnetic field applied according to the antiferromagnetic chains directions has previously been determined by Ref. [47], revealing the occurrence of a metamagnetic transition, i.e. a first order type of field-induced transition characterised by a change from a state of low magnetisation to a state of high magnetisation [48]. In fact on the phase diagram, the antiferromagnetic state is predicted to remain stable under field magnitudes smaller than a lower boundary, while the ferromagnetic state is predicted to be stabilised by a field magnitude higher than an upper boundary. The intermediate region comprised between the two boundaries corresponds with a metastable mixed state, where ferromagnetic domains coexist in an antiferromagnetic matrix.

A second important applied field configuration corresponds to the case where the magnetic field is aligned with the spin directions of the rrll and rlrl orders, lying in the horizontal plane of the materials. As previously detailed, rrll and rlrl orders are believed to be stabilised by the frustrated J_1 and J_2 antiferromagnetic exchange interactions on the $SrLn_2O_4$ triangular ladder frame. The field-induced magnetic properties observed in this particular applied field configuration should thus contrast with the observations made in the $H//c$ configuration. Of great interest for this study, the M(H) phase diagram of $\mathbf{S} = 1/2$, J_1-J_2 triangular spin chains has been predicted as a function of the J_1/J_2 ratio by Ref [43, 44], see Fig. 2.8. As a main result, a large intermediate field-induced region is defined on the predicted phase diagram, and corresponds with the stabilisation of a two up one down (uud) spin configuration aligned according to the field direction. I note that in the particular case of the $SrLn_2O_4$ systems, this phase should be called rrl since the spins are lying within the horizontal plane of the crystalline lattices. However, many publications originally labelled this phase as a uud order, I have thus decided to keep this notation

through the thesis to remain coherent with earlier work. This field-induced phase is then predicted to remain stable over a significant range of field magnitudes, and to finally disappear in the high field region of the diagram resulting in a fully field polarised state. According to the predictions, I note that the stabilisation of a field-induced intermediate uud phase would be visible as a plateau on the magnetisation curve of these systems. Furthermore, the plateau should lie at a value being equal to a third of the high field asymptotic trend induced by the full polarisation of the system.

I note that a direct transition from a rlrl order to the fully polarised phase is only predicted by this model in the extreme case where J_1 equals zero. This situation being however largely improbable, the stabilisation of a field-induced intermediate state is therefore expected in the low temperatures M(H) phase diagrams of $SrLn_2O_4$ systems, when applying the field according to the spin directions of rrll or rlrl orders. These predictions are in very good agreements with published low temperature single crystal magnetisation measurements performed on the $SrDy_2O_4$, $SrHo_2O_4$ and $SrEr_2O_4$ variants [32], as well as with my understanding of the $SrLn_2O_4$ systems.

Overall, I expect to observe contrasting magnetic phenomena relying on different physics by applying magnetic fields according to the different crystallographic axes of single crystal samples of $SrLn_2O_4$ materials. These rather unusual properties being a direct consequence of magnetic frustration induced by the crystalline lattice of these materials.

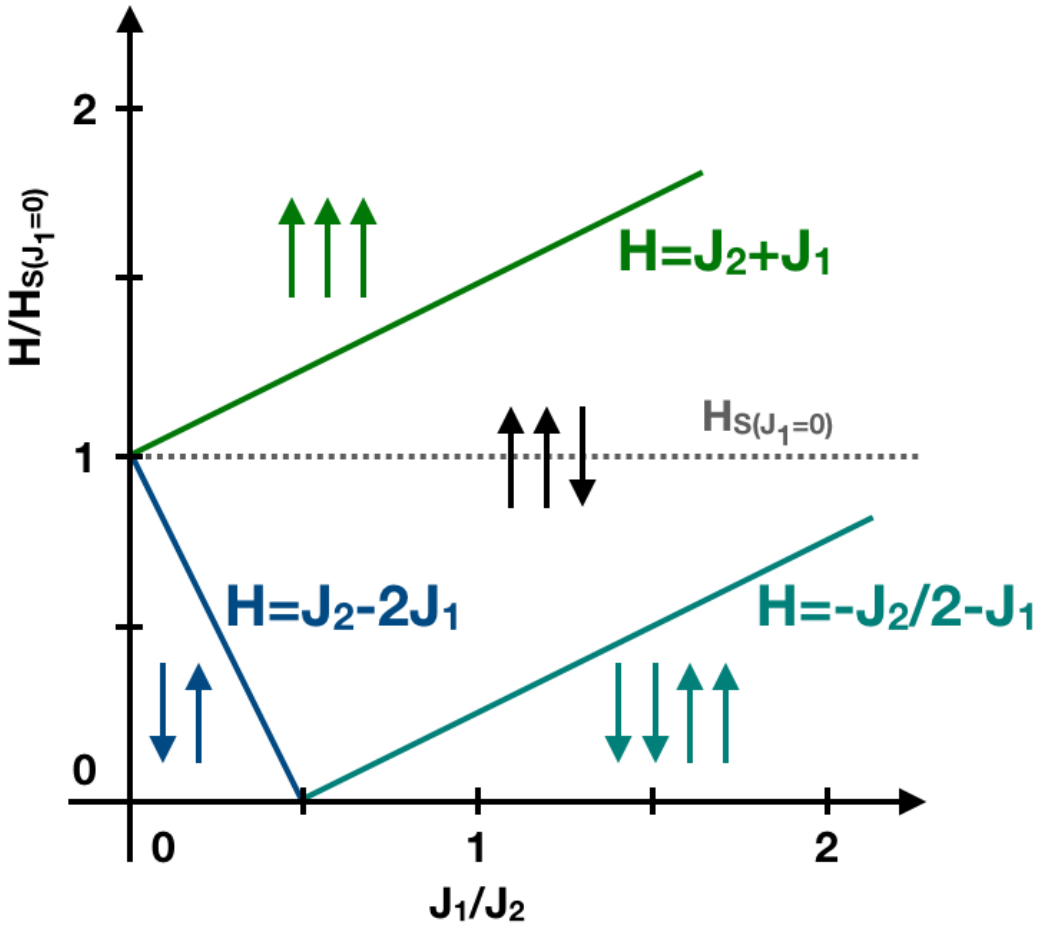

Figure 2.8: M(H) phase diagram of $\mathbf{S} = 1/2$ J_1-J_2 triangular spin chains as a function of the J_1/J_2 strength ratio. The stabilisation of a large intermediate uud phase is predicted by the model prior the stabilisation of a fully polarised state. Figure adapted from Ref. [43, 44]

Chapter 3

Magnetic neutron scattering

The investigation of the low temperatures magnetic properties of the $SrLn_2O_4$ materials and in particular of the magnetic orders presented in this thesis principally rely on the use of neutron scattering techniques. Exhaustive and more basic treatments of the principles of neutron scattering are developed in several text books or publications and the interested reader is invited to consult them [2, 20, 49–51]. In this chapter, I present a summarised overview of the neutron scattering theory to provide the reader with the necessary background to understand the physics involved in my measurements. This theoretical description will start with a brief description of basic properties of the neutrons followed by a general presentation of the physics involved in the neutron scattering process. I will subsequently separately introduce the physics of both nuclear and magnetic processes and then consider these two scattering phenomena involved within the frame of crystalline materials. Let's note that I will restrict the description of magnetic scattering by crystalline materials to the elastic case, inelastic scattering results being absent from this thesis work.

3.1 Properties of the neutrons

The basic properties of neutrons are reported in table 3.1. Of great interest, the neutron mass equals $1.674928(1) \times 10^{-24}$ g, resulting in de Broglie wavelengths for thermal neutrons (10-100 meV) ranging between ∼2.86 and ∼0.90 Å and thus matching with inter-ionic distances in condensed matter. Interference effects are thus possible when interacting with crystalline materials, disclosing structural information. Furthermore, the range of energy covered by "thermal" and "cold" neutrons matches with the energies of elementary excitations in condensed matter. This enables neutrons to probe the internal dynamics of materials at the microscopic

Neutron properties	**Corresponding values**
Mass	$1.674928(1) \times 10^{-24}$ g
Cold Neutrons En.	0.0-10 meV
Thermal Neutrons En.	10-100 meV
Hot Neutrons En.	100-500 meV
Charge	0
Magnetic Moment	-1.9130427(5) μ_N
β-decay life time	$885.8 \pm 0.9s$

Table 3.1: Basic properties of the neutron, making this particle a valuable prob to investigate the microscopic properties of condensed matter. μ_N is the nuclear magneton and is equal to $5.0507866(17) \times 10^{-}27$ JT^{-1}. Table adapted from Ref. [2].

level. Also, neutron are chargeless particles, thus unlike x-rays they will be able to deeply penetrate in matter returning information from the bulk of investigated systems. Last but not least, neutrons bear a spin that enables them to interact with magnetic moments. Consequently, neutrons can be used as a sensitive probe to magnetism in condensed matter disclosing information about magnetic orders as well as about the dynamics of spin systems.

3.2 Neutron sources

The neutrons are produced by two different types of sources that rely on two different physical processes. The first type of sources are nuclear reactors that exploit the fission of ^{235}U atoms in chain reactions, releasing free neutrons in the process. A share of the free neutrons produced can then escape the reactor medium through a set of evacuated tubes that are directly surrounding the reaction chamber. The second type of sources are known as spallation sources and produce neutrons by colliding a high energy proton beam onto a heavy metal target, e.g. lead, tantalum, tungsten, depleted uranium, or lead/bismuth. The produced neutrons are expelled in all directions surrounding the targets and collected by tubes as when produced by a reactor.

In both types of sources however, the produced neutrons are of very high energy (epithermal neutrons) and must be slowed down by a moderator to the energy range being useful for the investigation of the microscopic properties of condensed matter. Heavy water or graphite are often used as moderators. The probability of moderating the neutrons speeds within an interval $v + dv$ is controlled by the Maxwell-Boltzmann probability distribution that depends on the moderators temperatures. It is thus possible to link the neutron energy with the temperature of

the moderator, as well as with their travelling speeds and wavelengths according to a simple relation:

$$E \;=\; 0.08617\;T \;=\; 5.227\;v^2 \;=\; \frac{81.81}{\lambda^2} \tag{3.1}$$

With E in meV, T in K, λ in Å and v in km.s^{-1}. Considering the energy range of the moderated neutrons, a classification is made employing the terms "cold", "thermal" and "hot" neutrons, see table 3.1.

It is also important to mention that in spallation sources, the protons are accelerated in bunches by synchrotrons, thus spallation sources produce pulsed neutron beams. Pulsed sources are of great interest to exploit the time-of-flight techniques that take advantage of the possibility to determine the neutrons energies by monitoring their travelling time between the target and the detectors. On the other hand, reactor sources produce a constant flux of neutrons being very useful for diffraction experiments. The neutron fluxes produced by reactors are also usually significantly more intense than the average flux of spallation sources offering more possibilities of measurements.

The neutron sources exploited for the measurements presented in this thesis are the Institut Laue-Langevin high flux reactor (Grenoble), the ISIS spallation source (Didcot) and the Léon Brillouin reactor (Saclay).

3.3 Neutron scattering

In condensed matter, neutrons are scattered by nuclei as well as by the magnetic field-induced by unpaired electrons. These two phenomena being individually referred as nuclear and magnetic scattering, the scattering of neutrons by magnetic materials will result in the superposition of the two effects. It is thus essential to understand the physics of each effect in order to separately extract both nuclear and magnetic information from the scattered intensities.

3.3.1 Scattering cross-section

To define the scattering power of a crystalline material, a physical quantity known as the scattering cross-section is employed. Considering the scattering of a neutron beam with incident flux Φ by a crystalline sample containing N scatterers, a count rate C will be measured by a detector of efficiency η subtending a solid angle $\Delta\Omega$, located in a direction defined by θ and ϕ angles (see Fig. 3.1). In these conditions, a differential cross-section is obtained given by:

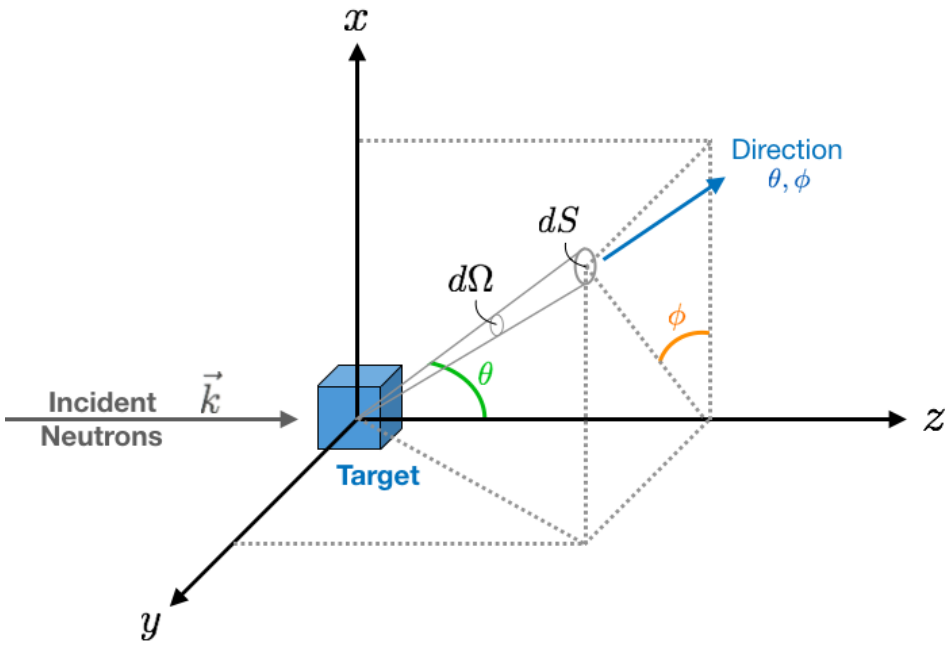

Figure 3.1: Schematic representation of a scattering experiment.

$$\frac{\mathrm{d}\sigma}{\mathrm{d}\Omega} = \frac{C}{\eta\Phi N\Delta\Omega} \ . \tag{3.2}$$

If in addition, a range of energy ΔE exchanged in the process is considered, I obtain a double differential cross-section given by:

$$\frac{\mathrm{d}^2\sigma}{\mathrm{d}\Omega\mathrm{d}E} = \frac{C}{\eta\Phi N\Delta\Omega\Delta E} \ . \tag{3.3}$$

Hence, if the total number of neutrons scattered in all space directions having energies comprised in the ΔE range are monitored, the total scattering cross-section of a particular sample is given by:

$$\sigma_{tot} \ = \ \frac{C}{\eta\Phi N} \ . \tag{3.4}$$

3.3.2 The master equation

The scattering of neutrons by scattering centers in condensed matter can also be defined by the change of scattering vector ($\mathbf{k} \mapsto \mathbf{k}$') and spin state ($\sigma \mapsto \sigma$') undergone by the neutrons, as well as by the change of state ($\lambda \mapsto \lambda$') undergone by the scattering centers. This situation is illustrated in Fig. 3.2 using simple geometry

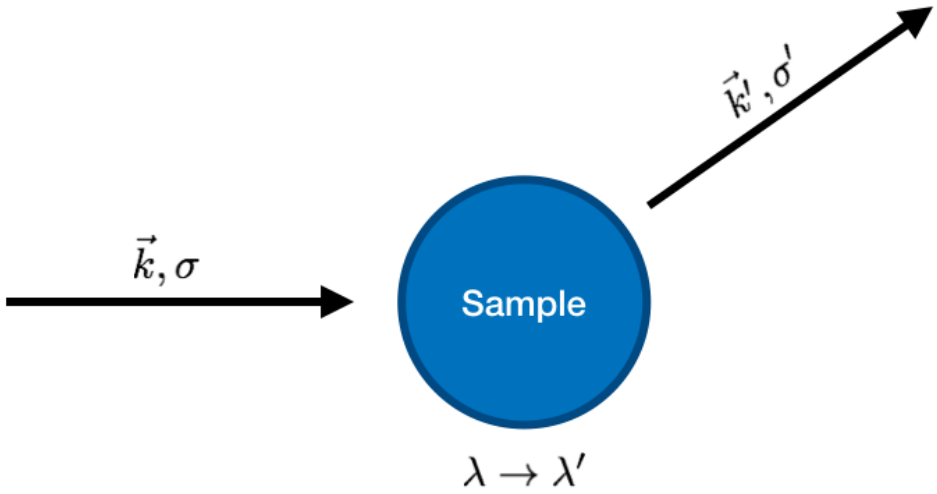

Figure 3.2: Schematic representation of a neutron being scattered by a condensed matter sample. In the initial state the neutron has a propagation vector $\mathbf{k}$ and a spin state σ, while the sample is in the state λ. After the scattering events the systems is in the states $\mathbf{k}$', σ' and λ'. Figure adapted from Ref. [50]

considerations.

The expression of the differential cross-section can thus be rewritten as:

$$\frac{\mathrm{d}\sigma}{\mathrm{d}\Omega}_{\mathbf{k},\sigma,\lambda\mapsto\mathbf{k}',\sigma',\lambda'} = \frac{1}{N\Phi d\Omega}\sum_{k'} W_{\mathbf{k},\sigma,\lambda\mapsto\mathbf{k},\sigma',\lambda'} \ , \tag{3.5}$$

where $\mathrm{W}_{\mathbf{k},\sigma,\lambda\mapsto\mathbf{k},\sigma',\lambda'}$ corresponds to the number of transitions per seconds from the initial states defined by $\mathbf{k}, \sigma, \lambda$ to the final state defined by $\mathbf{k}', \sigma', \lambda'$. The summation being considered over all the final $\mathbf{k}'$ vector states contained in the solid angle $d\Omega$.

The right hand side of the equation can be defined employing Fermi's Golden rule: a full derivation of this rule goes beyond the objective of this theoretical review. However, it can simply be understood that the golden rules rely on the validity of the first-order perturbation theory which is valid in the case of both nuclear and magnetic scattering processes. In fact, nuclear scattering is short range and the scatterers are point like centers, but also only s-shape scattering proceeds due to the spherical shape of nuclei. In the case of magnetic scattering, the scattering centers are not point like but the interactions being weak, the first-order perturbation theory remains valid. In this condition $\mathrm{W}_{\mathbf{k},\sigma,\lambda\mapsto\mathbf{k},\sigma',\lambda'}$ can be expressed as:

$$W_{\mathbf{k},\sigma,\lambda\mapsto\mathbf{k},\sigma',\lambda'} = \frac{2\pi}{\hbar}|\langle\mathbf{k}'\sigma'\lambda'|V|\mathbf{k}\sigma\lambda\rangle|^2\rho_{\mathbf{k}'\sigma'(E')} \ , \tag{3.6}$$

where the matrix element is a quantum mechanical description of the scattering event induced by the interaction potential V, and $\rho_{\mathbf{k}'\sigma'(E')}$ corresponds to the density of final states for the whole system per unit intervals of energy. This density of final state can be described using known results of quantum mechanics, allowing to rewrite the expression of the differential cross-section as:

$$\frac{\mathrm{d}\sigma}{\mathrm{d}\Omega}_{\mathbf{k},\sigma,\lambda\mapsto\mathbf{k}',\sigma',\lambda'} = \frac{1}{N}\frac{k'}{k}\left(\frac{m}{2\pi\hbar^2}\right)^2 |\langle\mathbf{k}'\sigma'\lambda'|V|\mathbf{k}\sigma\lambda\rangle|^2 \ , \tag{3.7}$$

where m is the neutron mass.

Implying this result within the expression of the double differential cross-section (see eqn. 3.3) then results in:

$$\frac{\mathrm{d}^2\sigma}{\mathrm{d}\Omega\mathrm{d}E}_{\mathbf{k},\sigma,\lambda\mapsto\mathbf{k}',\sigma',\lambda'} = \frac{1}{N}\frac{k'}{k}\left(\frac{m}{2\pi\hbar^2}\right)^2 |\langle\mathbf{k}'\sigma'\lambda'|V|\mathbf{k}\sigma\lambda\rangle|^2\delta(E+E_\lambda-E'_\lambda) \ , \tag{3.8}$$

where the Kronecker delta guarantees the law of energy conservation in the scattering process, i.e. the energy E exchanged in the scattering process equals:

$$E = E_{\lambda'} - E_\lambda \ . \tag{3.9}$$

By then summing over all final states of both neutrons and scatterers, and averaging over all the initial states having occurring probabilities p_λ and p_σ, I obtain the general formula:

$$\frac{\mathrm{d}^2\sigma}{\mathrm{d}\Omega\mathrm{d}E}_{\mathbf{k},\sigma,\lambda\mapsto\mathbf{k}',\sigma',\lambda'} = \frac{1}{N}\frac{k'}{k}\left(\frac{m}{2\pi\hbar^2}\right)^2 \sum_{\lambda\sigma} p_\lambda p_\sigma \sum_{\lambda'\sigma'} |\langle\mathbf{k}'\sigma'\lambda'|V|\mathbf{k}\sigma\lambda\rangle|^2\delta(E+E_\lambda-E'_\lambda) \tag{3.10}$$

This formula is known as the master formula of neutron scattering since it rules every possible condensed matter neutron scattering process.

3.4 Nuclear scattering

3.4.1 Scattering from a single nucleus

The scattering of neutrons by nuclei is caused by the nuclear forces being at the origin of the interaction potential $V(\mathbf{r})$. The range of interaction of this potential being point like, in comparison with the wavelength of thermal neutrons being in the order of magnitudes of lattice distances in condensed matter, the scattered waves

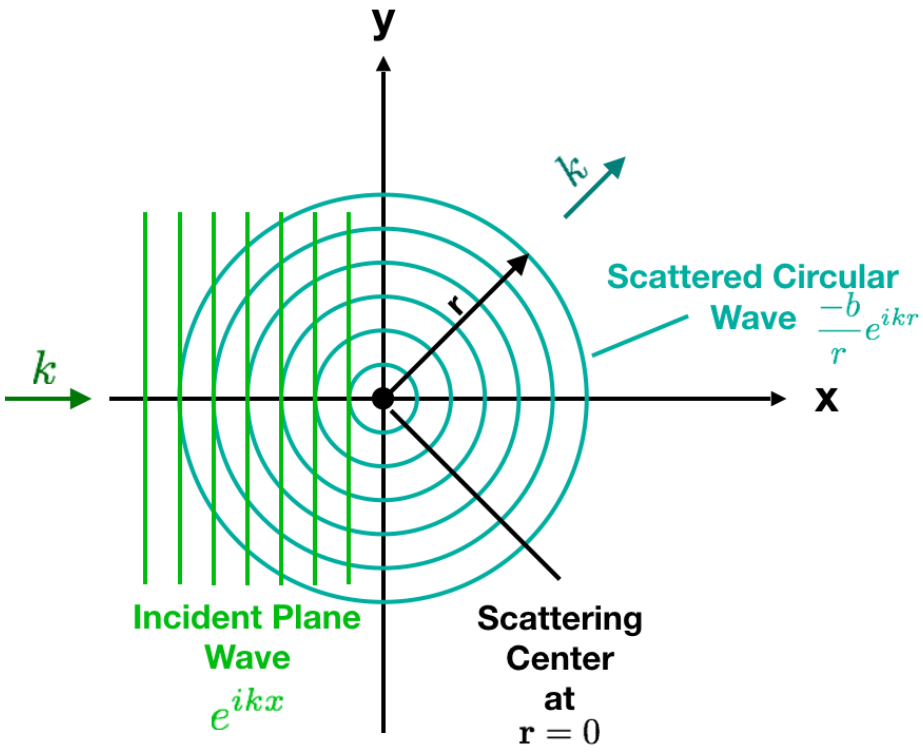

Figure 3.3: Schematic representation of a plane wave scattered elastically by a single nuclei. Due to the large difference existing between the scattering potential and the wavelength dimensions, the scattered waves are spherically symmetrical. Figure adapted from Ref. [51]

will be spherical. Thus considering an incident plane wave of the form:

$$\psi_{inc} \;=\; e^{ikx} \;, \tag{3.11}$$

travelling in the x direction (the wave fronts are perpendicular to the x axis), see Fig 3.3. The elastically scattered wave will be of the form:

$$\psi_{sc} \;=\; -\frac{b}{r}e^{ikr} \;, \tag{3.12}$$

Where r defines the distance of the scattered wave front from the scattering center (i.e. the nucleus). The prefactor b/r defines the amplitude of the wave. b is a constant having the unit of a length and is defined as the scattering length. It defines a measure of the strength of the neutron-nucleus interaction. The minus sign on the b/r prefactor of the wave function means that b is positive in the case of a repulsive scattering potential. Since both the scattering length and the previously

defined cross-section are two physical quantities defining the strength of a scattering event, a relationship exists between the two. In fact, the cross-section has the unit of an area and can be considered as the flat surface of the nucleus seen by the neutron. The scattering length having the unit of a length, these two quantities are linked by:

$$\sigma \;=\; 4\pi b^2 \;, \tag{3.13}$$

as if the scattering length was corresponding to half the radius of the nuclei seen by the neutron.

The scattering length is in reality often a complex quantity given by:

$$b \;=\; b_0 + b' + ib" \;, \tag{3.14}$$

Where b_0 is the actual scattering length associated with the interaction potential, while b' and b" are associated to a type of scattering known as resonance scattering. For instance, the imaginary component of the scattering length define the absorbing properties of the nucleus. In certain cases, this quantity is large and the neutron will be absorbed in the scattering process. An example of a strong absorber considered within the frame of this thesis is the ^{157}Gd isotope having an absorption cross-section of 259000 barn (1barn = 10^{-24} cm^2).

An important point to make about both scattering length and cross-section is that they are associated with the isotopic nature of the scattering nuclei. In fact, a rather irregular dependence exists between the scattering lengths and atomic numbers. Thus, completely different neutron scattering properties can be observed between two isotopes of the same elements. But also, nuclei with small atomic numbers may have large scattering potentials and vice-versa. These two physical quantities are moreover highly dependent on the neutron wavelength, hence properties such as strong absorption could be reduced to manageable figures by changing the wavelength of the neutron beam.

Due to this irregular isotopic dependence of the nuclei scattering lengths, the interference effects will be reduced in crystalline materials giving rise to scattering processes referred to as incoherent. Incoherent scattering is sensitive to individual properties of the nuclei such as nuclear excitations but are also sensitive to crystal field excitations. On the other hand, regular scattering processes of neutrons by nuclei still occur with strong probabilities for many elements and are referred as the coherent scattering processes. For instance, Bragg scattering or inelastic scattering of phonons are largely exploited nuclear scattering phenomena in experimental

neutron science.

3.4.2 Scattering from the crystalline lattice

I have so far restricted the reasoning to the case of a neutron being scattered by a single nucleus, and will now focus on the case of a neutron beam being scattered by an ordered assembly of nuclei. In these conditions, the interaction potential $V(r)$ becomes a three dimensional function that depends on the periodicity of the crystalline lattice. It is thus necessary to recall here a few fundamentals of crystallography prior detailing the scattering concepts.

In crystalline materials, atoms and consequently nuclei are ordered in three dimensional space. Such orders respect sets of symmetry operations, resulting in the creation of long range ordered atomic structures. At the microscopic scale, crystalline structures can be described as a periodic repetition in three dimensional space of a small volume entity containing the overall symmetry of the crystals. This small building block is known as the unit cell and its volume and shape characteristics are defined by three vectors, **a**, **b** and **c**, pointing from a point defined as the origin of the cell. Through the periodic repetition of the unit cell, a three dimensional crystalline lattice is build up. By then arbitrarily defining the origin of a particular unit cell as the lattice space origin, the position of any unit cell would be given in respect with the lattice origin by a vector $\mathbf{R}_l$ defined as:

$$\mathbf{R}_l \;=\; U\mathbf{a} + V\mathbf{b} + W\mathbf{c}\ , \tag{3.15}$$

where U, V and W are constants equal to integers.

Atomic positions are then defined within the unit cell by a vector $\mathbf{r}_d$ defined as:

$$\mathbf{r}_d \;=\; x\mathbf{a} + y\mathbf{b} + z\mathbf{c}\ , \tag{3.16}$$

where x, y and z are the fractional coordinates of each atoms d, in the unit cell.

By then combining equations 3.15 and 3.16, atomic positions $\mathbf{R}_i$ are defined in the lattice referential by:

$$\mathbf{R}_i \;=\; \mathbf{R}_l + \mathbf{r}_d\ . \tag{3.17}$$

In diffraction experiments, measurements return reciprocal space pictures of the crystalline lattices structural characteristics. It is thus useful to define the

reciprocal space unit cell vectors $\mathbf{a}^*$, $\mathbf{b}^*$ and $\mathbf{c}^*$, to facilitate the interpretation of the data. These vectors are expressed as:

$$\mathbf{a}^* = 2\pi\frac{b \times c}{a \cdot (b \times c)},\ \mathbf{b}^* = 2\pi\frac{c \times a}{a \cdot (b \times c)},\ \mathbf{c}^* = 2\pi\frac{a \times b}{a \cdot (b \times c)} . \quad (3.18)$$

And the reciprocal lattice vector $\mathbf{H}$ is defined as:

$$\mathbf{H} = h\mathbf{a}^* + k\mathbf{b}^* + l\mathbf{c}^* , \quad (3.19)$$

where the coefficients h, k and l known as the Miller indices, define the different atomic planes of crystalline structures. Generally, unit cells contain several atoms located at different crystallography positions defined by symmetry operations applied within the frame of the unit cells. Sets of symmetry operations that can be applied according to the geometrical characteristics of a particular unit cell are determined by the group theory [52, 53], and are referred as space groups. A list of all existing space groups and of their corresponding symmetry operations can be found in the International Tables for Crystallography [54].

I are now in a position to define the nuclear scattering potential of a particular crystal as:

$$V(\mathbf{r}) = \frac{2\pi\hbar^2}{m}\sum_{\mathbf{R}_i} b_{\mathbf{R}i}\delta(\mathbf{r} - \mathbf{R}_i) \quad (3.20)$$

where $b_{\mathbf{R}i}$ is the scattering length of the nucleus sitting at site $\mathbf{R}_i$, the summation going over the lattice sites of the whole system. The Kronecker delta ensures for the function to be non-zero only at the nuclei positions.

Considering the scattering to be elastic, the expression for the scattering cross-section for the crystal is given by:

$$\frac{\mathrm{d}\sigma}{\mathrm{d}\Omega} = |\int d\mathbf{r}\sum_{\mathbf{R}_i} b_{\mathbf{R}_i}\delta(\mathbf{r} - \mathbf{R}_i)\exp i\mathbf{Q}\cdot\mathbf{r}|^2 = |\sum_{\mathbf{R}_i} b_{\mathbf{R}_i}\exp i\mathbf{Q}\cdot\mathbf{R}_i|^2 , \quad (3.21)$$

where $\mathbf{Q}$ is the scattering vector defined as:

$$\mathbf{Q} = \mathbf{k}' - \mathbf{k} . \quad (3.22)$$

For most values of $\mathbf{Q}$, the value of the scattering cross-section is very small because the neutrons are scattered by the different nuclei in an out of phase con-

figuration, hence the amplitudes of the scattered waves cancel out. However, if the condition $\mathbf{Q} = \mathbf{H}$ is respected for a particular set of Miller indices (see eqn. 3.19), the neutrons will be scattered in phase by the different nuclei of the lattice. Thus, the value of the scattering cross-section will be large due to constructive interference, resulting in the observation of a high intensity peak. This particular scattering condition is known as the von Laue's scattering condition. If considered in real space this type of scattering will however be referred as Bragg's scattering and would be referred as such by experimenters.

The expression of the scattering cross-section can then be rewritten as:

$$\frac{\mathrm{d}\sigma}{\mathrm{d}\Omega} \;=\; b^2 \frac{N(2\pi)^3}{\nu_0} \sum_{\mathbf{H}} \delta(\mathbf{Q} - \mathbf{H}) \;, \tag{3.23}$$

where the summation is over all existing reciprocal space vectors $\mathbf{H}$, and the presence of the Kronecker delta function guaranties the necessary conditions for constructive interference. I also note that this expression implies that all scattering nuclei are identical. Furthermore, N is the number of scattering nuclei and ν_0 is the volume of the unit cell.

If the unit cells contain several atoms, the expression of the cross-section becomes:

$$\frac{\mathrm{d}\sigma}{\mathrm{d}\Omega} \;=\; N \frac{(2\pi)^3}{\nu_0} \sum_{\mathbf{H}} \delta(\mathbf{Q} - \mathbf{H}) |F_N(\mathbf{Q})|^2 \;, \tag{3.24}$$

with:

$$F_N(\mathbf{Q}) \;=\; \sum_d b_d \exp i\mathbf{Q} \cdot \mathbf{r}_d \;, \tag{3.25}$$

defined as the nuclear structure factor. This function rules the interference process of scattered neutrons in crystalline structure, as a function of the scattering vector $\mathbf{Q}$.

It is now interesting to graphically represent the real space geometry of a scattering experiment in Bragg scattering conditions (see Fig. 3.5), as well as a simple vector construction comparing the different scattering vectors involved in the process (see Fig. 3.4). From these two constructions, simple relations can be deduced, i.e.:

$$\mathbf{Q} \;=\; \frac{4\pi \sin(\theta)}{\lambda} \;=\; \frac{2\pi N}{d} \;, \tag{3.26}$$

with N a positive integer. This relation leads to the most famous result of

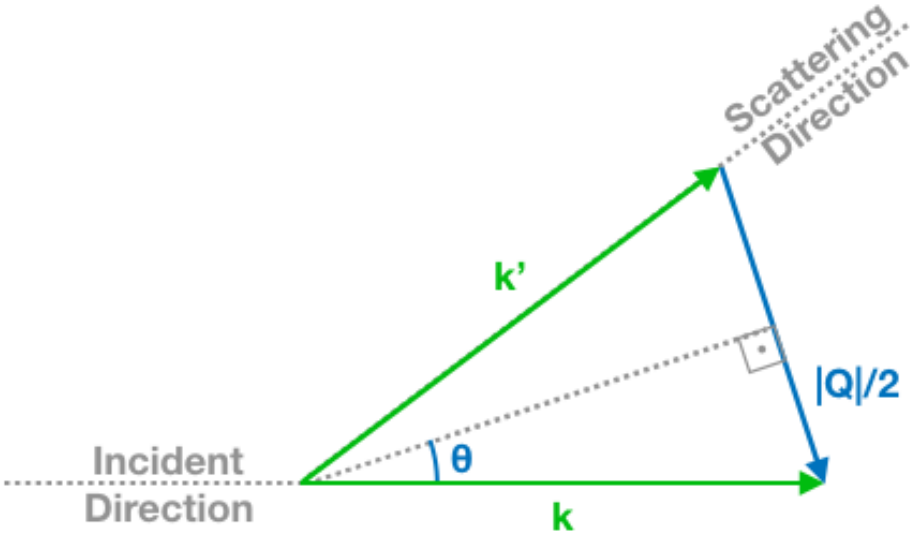

Figure 3.4: Scattering vector diagram for elastic scattering.

scattering theory:

$$2d\sin(\theta) \;=\; N\lambda \;, \tag{3.27}$$

known as Bragg's law.

3.5 Magnetic scattering

3.5.1 Scattering from unpaired electrons

As previously mentioned, neutrons do bear a spin that interacts with the magnetic field **H** produced by unpaired electrons in a magnetic type of scattering process. I first focus on a simple case where a single incident neutron interacts with the field of a moving unpaired electron having a velocity $\mathbf{v_e}$. Before interacting, the neutron is in spin state $\boldsymbol{\sigma}$ and has a magnetic moment defined as $\boldsymbol{\mu_n}$ = -γ μ_N $\boldsymbol{\sigma}$, while the electron has spin and momentum **s** and **p** inducing a magnetic moment $\boldsymbol{\mu_e}$ = -2μ_B**s**. The magnetic scattering interaction potential is defined as:

$$\mathbf{V}(\mathbf{r}) \;=\; -\,\mu_n \times \mathbf{H} \;=\; -\,\gamma\mu_N 2\mu_B\sigma \cdot \left[\mathrm{curl}\left(\frac{\mathbf{s}\times\hat{\mathbf{R}}}{R^2}\right) + \frac{1}{\hbar}\frac{\mathbf{p}\times\hat{\mathbf{R}}}{R^2}\right] , \tag{3.28}$$

with the magnetic field **H** defined as:

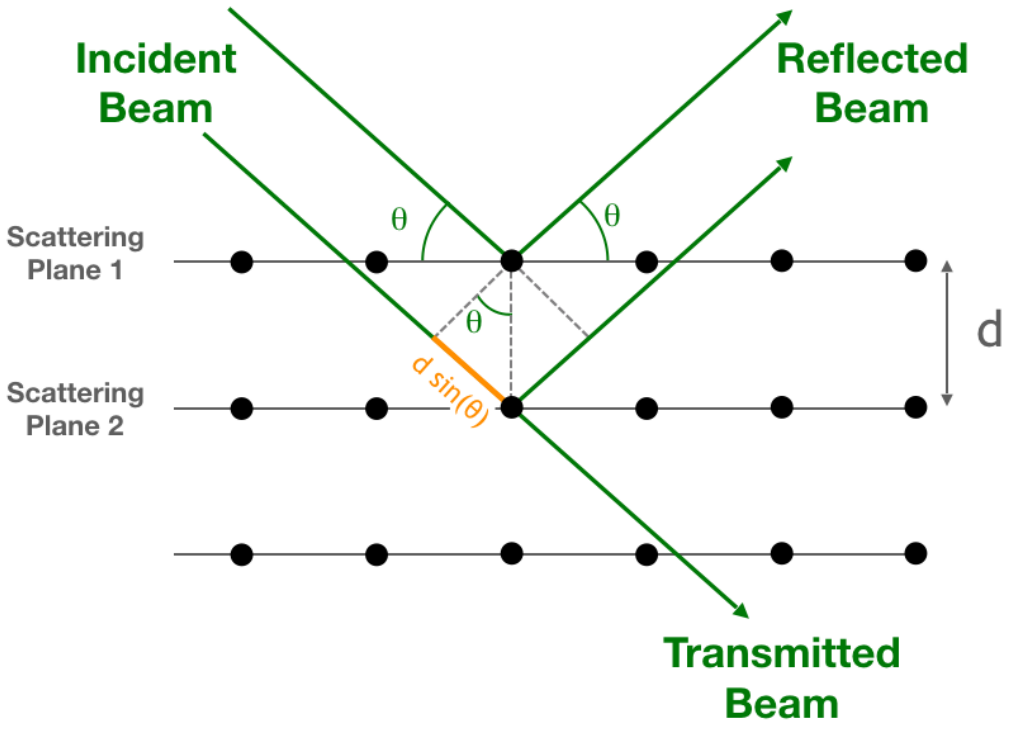

Figure 3.5: Schematic of a Bragg diffraction setup where the scattering is made by a set of regularly spaced parallel planes.

$$\mathbf{H} \;=\; \mathrm{curl}\left(\frac{\boldsymbol{\mu_e}\times\hat{\mathbf{R}}}{R^3}\right)+\frac{-e}{c}\frac{\mathbf{v_e}\times\hat{\mathbf{R}}}{R^3}\;, \tag{3.29}$$

and $\hat{\mathbf{R}}$ is the rotational invariance operator. The first term in the square braces of equation 3.28 is due to the interaction of the neutron with the electron spin and the second with the electron angular momentum, revealing the occurrence of two distinct interaction processes.

Now considering the interaction of a neutron with a sample containing several unpaired electrons, the matrix element representing the change of the neutron wave vector induced by the scattering process is defined as (see eqn. 3.10):

$$\sum_i \langle \mathbf{k}'|V|\mathbf{k}\rangle \;=\; 4\pi\gamma\mu_N 2\mu_B\sigma\cdot\mathbf{D}_\perp(\mathbf{k}-\mathbf{k}')\;, \tag{3.30}$$

where $\mathbf{D}_\perp$ is the magnetic interaction operator given by:

$$\mathbf{D}_\perp \;=\; \sum_i \left[\hat{\mathbf{Q}} \times (\mathbf{s}_i \times \hat{\mathbf{Q}}) + \frac{i}{\hbar Q}(\mathbf{p}_i \times \hat{\mathbf{Q}})\right] \exp(i\mathbf{Q}\cdot\mathbf{r}_i)\ , \tag{3.31}$$

with $\hat{\mathbf{Q}}$ the unit vector of $\mathbf{Q}$.
$\mathbf{D}_\perp$ is related to $\mathbf{D}$ by:

$$\mathbf{D}_\perp \;=\; \hat{\mathbf{Q}} \times (\mathbf{D} \times \hat{\mathbf{Q}})\ . \tag{3.32}$$

Hence $\mathbf{D}_\perp$ is the projection of $\mathbf{D}$ on the scattering plane. $\mathbf{D}$ is in turn related to the magnetisation operator of the scattering system by the relation:

$$\mathbf{D} \;=\; -\frac{1}{2\mu_B}\mathbf{M}(\mathbf{Q})\ . \tag{3.33}$$

It should also be noted that the operator $\mathbf{D}$ is the sum of $\mathbf{D}_S$ and $\mathbf{D}_L$, accounting for the separate action of the spin and orbital momentum characteristics of the electrons over the scattering process, in agreement with the expression of the scattering potential, see eqn. 3.28. Similarly, the expression of $\mathbf{M}(\mathbf{Q})$ can also be decomposed in both spin and orbital momentum parts. It can in addition be re-written as a function of the unpaired electrons positions by Fourier transformation, giving:

$$\mathbf{M}(r) \;=\; \mathbf{M}_S(r) + \mathbf{M}_L(r)\ . \tag{3.34}$$

The magnetic interaction operator $\mathbf{D}$ is thus equal to the Fourier transform of $\mathbf{M}$(r), being the real space magnetisation of the system.

3.5.2 Magnetic Scattering from crystalline lattice

In magnetic crystalline materials, unpaired electrons are located on the magnetic ions, thus their spatial distribution follows the periodicity of the crystal lattice. In a system containing only identical magnetic ions bearing unpaired orbiting electrons, the magnetic interaction operator becomes a three dimensional function of the time dependent electrons positions. It is given by:

$$\mathbf{D}(\mathbf{Q},t) \;=\; \sum_i f_i(\mathbf{Q})\mu_i(t) \exp i\mathbf{Q}\cdot\mathbf{R}_{i(t)}\ , \tag{3.35}$$

where $\boldsymbol{\mu}_i$ is the magnetic moment associated with an unpaired electron i sitting at site $\mathbf{R}_i$.

As in the case of x-ray scattering from the electronic clouds of atoms, the

$f_i(\mathbf{Q})$ factor is called the atomic form factor and account for the fact that electrons are not point like scattering centers in condensed matter. The expression of $f_i(\mathbf{Q})$ is given by:

$$f(\mathbf{Q}) \;=\; \frac{g_s}{g}\bar{j}_0(\mathbf{Q}) + \frac{g_L}{g}[\bar{j}_0(\mathbf{Q}) + \bar{j}_2(\mathbf{Q})] \;, \tag{3.36}$$

where the g constants are gyromagnetic ratios (see chapter 2), and the j_n known as the Bessel functions account for the spherical distribution of the atomic wave functions.

Furthermore, as the magnetic interaction operator $\mathbf{D}$ is linked to the magnetisation of the system by Fourier transformation, it is evident that magnetic scattering strongly depends on the spin correlations in the system. Thus, low temperature long range orderings of the spins result in the magnetic correlations becoming time independent and in the scattering to be purely elastic. In these conditions, the atomic form factor would be re-considered as a magnetic unit cell structure factor given by:

$$F_M(\mathbf{Q}) \;=\; \gamma r_0 \sum_d f_d(\mathbf{Q})\langle\mu_d\rangle \exp(i\mathbf{Q}\cdot\mathbf{r}_d)\exp(-W_d(\mathbf{Q})) \;, \tag{3.37}$$

where $\exp(-W_d(\mathbf{Q}))$ is known as the Debye-Waller factor accounting for the effect of atomic thermal motions onto the scattering and $r_0 = e^2/(m_e c^2)$ is the classical radius of the electron.

The elastic magnetic cross-section of the system can then be defined as:

$$\left(\frac{\mathrm{d}\sigma}{\mathrm{d}\Omega}\right)_{el} \;=\; \frac{1}{N_M}\frac{2\pi^3}{\nu_0}\sum_{\tau_M}\delta(\mathbf{Q}-\tau_M)|F_{M\perp}(\tau_M)|^2 \;, \tag{3.38}$$

where

$$F_{M\perp} \;=\; \hat{\mathbf{Q}}\times\mathbf{F}_M\times\hat{\mathbf{Q}} \;, \tag{3.39}$$

is known as the magnetic structure factor, accounting for the sensibility of the magnetic scattering process to the component of the magnetic moment being perpendicular to the scattering vector. $\boldsymbol{\tau}_M$ is the reciprocal lattice vector of the magnetic structure that is related to the reciprocal nuclear lattice vector by a propagation vector $\mathbf{k}$, thus $\boldsymbol{\tau}_M = \boldsymbol{\tau} \pm \mathbf{k}$. Magnetic Bragg scattering thus occurs similarly to nuclear Bragg scattering of neutrons, resulting in the measurement of strong intensity peaks if the condition $\mathbf{Q} = \boldsymbol{\tau}_M$ is satisfied.

3.6 Least square refinement analysis

The least square analysis technique consists of both Rietveld and single crystal refinement procedures allowing for the determination of crystalline and long range ordered magnetic structures from x-ray and neutron Bragg intensities. The Rietveld method is used for the analysis of polycrystalline type of diffraction data and consists in minimising the intensity differences between experimental data and simulated intensity profiles through the weight square difference X^2 given by [55]:

$$X^2 \;=\; \sum_i w_i \{y_i^{mes} - y_i^{calc}\}^2 \;, \tag{3.40}$$

where y_i^{mes} and y_i^{calc} are the measured and calculated scattering intensity profiles for each point i of a particular diffractogram. The w_i factor is the statistical weight of the intensity differences squared.

The expression of the simulated intensity profile is given by:

$$y_i^{calc} \;=\; S \sum_{hkl} C L_{hkl} |F_{hkl}|^2 \Omega(\theta) + b_i \;, \tag{3.41}$$

where F_{hkl} is the structure factor that accounts for the addition of both nuclear (see eqn. 3.25) and magnetic (see eqn. 3.37) structure factors in the particular case of neutron data collected on crystalline magnetic materials. S is the scale factor, b_i account for the experimental background and L_{hkL} is the Lorentz correction. The $\Omega(\theta)$ function accounts for the peak shape of the profile depending on both the diffractometer resolution and sample crystallinity. Typically, Lorentzian and Gaussian functions are used for this purpose but more specific functions such as the back-to-back exponential [56] might be required to account for neutron spallation source asymmetric peak shapes. Furthermore, the prefactor C stands for often needed corrections to the model such as the sample absorption and preferential orientations of the powder crystal grains.

The single crystal refinement method consists in directly adjusting the calculated $|F_{hkl}|^2_{calc}$ of a model to the measured $|F_{hkl}|^2_{mes}$ values obtained from integrated Bragg peaks intensities in reciprocal space. Correction factors will here also be needed. For instance, absorption issues are significant in single crystal neutron scattering experiments operated in transmission mode since every individual reflection will travel a particular pass length through the sample. Absorption correction can be performed directly on the measured sets of Bragg intensities through accurate modelling of the sample shape employing software such as Mag2Pole [57] or datap [58, 59]. I note that it is important to select rather small crystals (a few

cubic millimeters) to reduce this effect when collecting single crystal data to be employed for accurate structural determination. Another important correction not to be neglected is the sample extinction induced by multiple interactions between the incoming and scattered beam, as well as due to additional scattering of the beam by the lattice plane when exiting the sample. A correction for this effect is implemented in the FullProf [55] refinement routine and consists in refining a set of four parameters known as the extinction parameters, accounting for the degree of non perfect crystallinity of single crystal samples. Perfect single crystals do actually not exist but instead single crystal samples consist of several grains being slightly misoriented one with respect to an other. This property result in certain degrees of mosaicity being different for every sample. As a matter of fact, only crystals with significant degrees of mosaicity do properly scatter since strong multiple scattering effects will be largely reduced. A proper determination of the extinction parameters in thus essential in the refinement procedure of single crystal scattering data.

In practice to refine a set of Bragg scattering data employing the FullProf suite program, the symmetry of the material is described in an input file allowing for the software to calculate both crystalline and eventual magnetic structure factors for a given material. FullProf symmetry input files are referred as .pcr files, and a few examples adapted to both structural and magnetic symmetry of $SrLn_2O_4$ materials can be found in the thesis appendix. To define the crystalline symmetry, the space group must be specified according to the Hermann-Mauguin notation as well as the symmetry operations defining the Wyckoff positions occupied by the ions as specified in the International Table for Crystallography [54]. The ions coordinates within the unit cell should in addition be provided. All this structural information can for instance be found in online databases such as The Cambridge Structural Data base (CSD) [60] or The Materials Project [61]. The later being particularly well designed and documented, it allows to find the required information by simply specifying the chemical formula of a given compound followed by the platform name on the search bar of an internet browser. Structural lattice and atomic positions parameters should be refined to improve the quality of the model as well as the several different parameters previously detailed. Regarding the calculation of magnetic structure factors, the magnetic symmetries of a given material must be specified on the .pcr file according to the crystalline symmetry of the lattice. For this purpose, a set of basis vectors defining the magnetic order symmetry on the crystalline lattice base must be specified and is referred to as the irreducible representation Γ. The basis vectors have real as well as imaginary components, the later are needed for instance to define modulated magnetic orders. A propagation vector referred to as

k is also requested to specify the periodicity of the magnetic order according to this of the crystalline lattice and is to be specified on the pcr file. The Γ models that are compatible with a given crystalline structure and a propagation vector **k** can be obtained using the BasIreps program within the FullProf suite [55]. Examples of BasIreps output files containing the Irreps (Γ) characteristics corresponding to magnetic phases stabilised by the $SrLn_2O_4$ compounds investigated in this thesis project are presented in the appendix. The different Γ models returned by BasIreps must all be tried though successive refinements attempts in order to determine the magnetic order symmetry. The magnitude of the magnetic moments components can then be refined improving the quality of the fit. The FullProff software also provides a structure display program known as Studio, where both magnetic and crystalline structures can be visualised. Finally, the quality of the fits reflecting the degree of agreement between both calculated and experimental intensity profiles is defined as the *R*-Bragg factor in the FullProf program [55] and should be minimised as much as possible. The expression of the *R*-Bragg factor is defined as:

$$R_{Bragg} = 100\frac{\sum_i |y_i^{mes} - y_i^{calc}|}{\sum_i |y_i^{mes}|}, \tag{3.42}$$

in the FullProf user manual [55].

3.7 Polarised neutron scattering

Both nuclear and magnetic contributions to the scattering signal are often superimposed in the collected intensities of diffraction experiments performed on crystalline magnetic materials. However, the scattering dependence on the relative orientation of both the neutron spin and the scattering vector can be exploited to separate nuclear and magnetic intensities.

In the case where the elastic scattering signal is measured using simultaneously several detectors and collecting scattered neutrons corresponding to many different scattering vectors **Q** such as in neutron powder diffraction (NPD) experiments, the *xyz*-polarisation method is the tool of choice. This method compares the spin flip (SF) and non-spin flip (NSF) intensities for three orthogonal directions of polarisation in the lab reference frame. The *z*-direction is set vertically while x and y are orthogonally oriented within the horizontal plane. The nuclear and magnetic contributions of the scattered signal are then individually obtained by applying the following relations [49, 62]:

$$\left(\frac{\mathrm{d}\sigma}{\mathrm{d}\Omega}\right)_{nuc} = \frac{1}{6}\left[2\left(\frac{\mathrm{d}\sigma}{\mathrm{d}\Omega}\right)_{Tot.\ NSF} - \left(\frac{\mathrm{d}\sigma}{\mathrm{d}\Omega}\right)_{Tot.\ SF}\right] \tag{3.43}$$

$$\left(\frac{\mathrm{d}\sigma}{\mathrm{d}\Omega}\right)_{mag} = 2\left(\frac{\mathrm{d}\sigma}{\mathrm{d}\Omega}\right)^{x}_{SF} + 2\left(\frac{\mathrm{d}\sigma}{\mathrm{d}\Omega}\right)^{y}_{SF} - 4\left(\frac{\mathrm{d}\sigma}{\mathrm{d}\Omega}\right)^{z}_{SF} \tag{3.44}$$

$$\left(\frac{\mathrm{d}\sigma}{\mathrm{d}\Omega}\right)_{mag} = 4\left(\frac{\mathrm{d}\sigma}{\mathrm{d}\Omega}\right)^{z}_{NSF} - 2\left(\frac{\mathrm{d}\sigma}{\mathrm{d}\Omega}\right)^{x}_{NSF} - 2\left(\frac{\mathrm{d}\sigma}{\mathrm{d}\Omega}\right)^{z}_{NSF} \tag{3.45}$$

The two possibilities for the extraction of the magnetic cross-sections are equivalent.

Chapter 4

Experimental techniques

In this chapter I present the different techniques and instrumentation employed for the samples synthesis, the bulk property measurements and neutron scattering investigations presented within this thesis.

4.1 Sample synthesis preparation and characterisation

All samples employed for the measurements presented in this thesis manuscript were prepared at the University of Warwick.

4.1.1 Polycrystalline sample synthesis

Polycrystalline samples of $SrLn_2O_4$ materials are prepared employing solid state diffusion techniques, as first reported by Karunadasa *et al.* [24]. The synthesis method consists in homogeneously mixing together high purity powders of $SrCO_3$ and Ln_2O_3 in stoichiometric conditions, and to then bake the mixture at high temperature for the chemical diffusion to proceed. Concerning the synthesis of a few $SrLn_2O_4$ variants, the use of a small excess of $SrCO_3$ powder implying an off-stoichiometric ratio $1 : 0.875$ has been found to improve the chemical purity of the resulting samples. In fact, the strontium high volatility causes a depletion of this element in the reaction mixture after having proceeded to the powder mixing. The baking procedure consists in heat treating the reacting mixture being slightly pressed in an alumina crucible employing a box furnace. The optimal high temperature heat treatment has a duration of 48 hours and is performed in air and under ambient pressure. The baking temperature itself depends on the $SrLn_2O_4$ material considered. In fact, for the $SrEr_2O_4$ and $SrGd_2O_4$ materials a temperature of 1350°C is found to be optimal [63, 64], however in the $SrNd_2O_4$ case it should be reduced to 1300°C due

to high temperature chemical instabilities. I also recommend to use the starting components in quantities being larger than single grams to optimise the ionic diffusion process. Furthermore, the synthesised $SrLn_2O_4$ powders are getting altered by moisture, contact with air should thus be avoided and the samples must be stored under vacuum or in Ar atmosphere.

4.1.2 Chemical composition and structural analyses

To investigate the crystallographic structure as well as the chemical nature and purity of the synthesised samples, powder x-ray diffraction (XRD) technique was used. The measurements were performed on diffractometers Brucker D5005 and Panalytical X'Pert Pro Multipurpose employing monochromated Cu K_α (λ = 1.5418 Å) x-ray beams. The data were then exploited via Rietveld refinement analysis techniques using the FullProf software suite [55]. An example of FullProf input .pcr file to be used for the refinement analysis of Panalytical XRD data collected on a polycrystalline sample of the $SrNd_2O_4$ material can be found in the thesis appendix, see subsection A.1.1.

4.1.3 Single crystal growth

The single crystal samples of $SrGd_2O_4$ employed for the measurements presented in this thesis were grown by the floating zone technique using a two mirrors halogen furnace (Canon Machinery SC1-MDH 11020), see Fig. 4.1. This growth method first consists in melting the tip of a pressed and sintered powder rod of the material to grow, together with the tip of a single crystal seed of the same material. For this purpose, the powder rod is suspended vertically above the seed and the tips of both objects are brought in close contact at the position of the hot spot created by two halogen lamps and a focusing set of mirrors. The melting induced by the high temperature creates a stable molten zone between the seed and feed, that are both counter rotated one with respect to another to keep homogeneity and stability in the molten material. Both objects are then slowly translated downward permitting for the molten zone to progress vertically along the seed rod, leaving a crystal boule after it. The growth is performed within a sealed quartz tube offering the possibility to control the atmosphere of the growth medium by constantly flowing gas in the tube.

4.1.4 Single crystal Laue Diffraction

To investigate the crystalline quality of the grown crystal boules and eventually extract single crystal samples, x-ray and neutron single crystal Laue diffraction

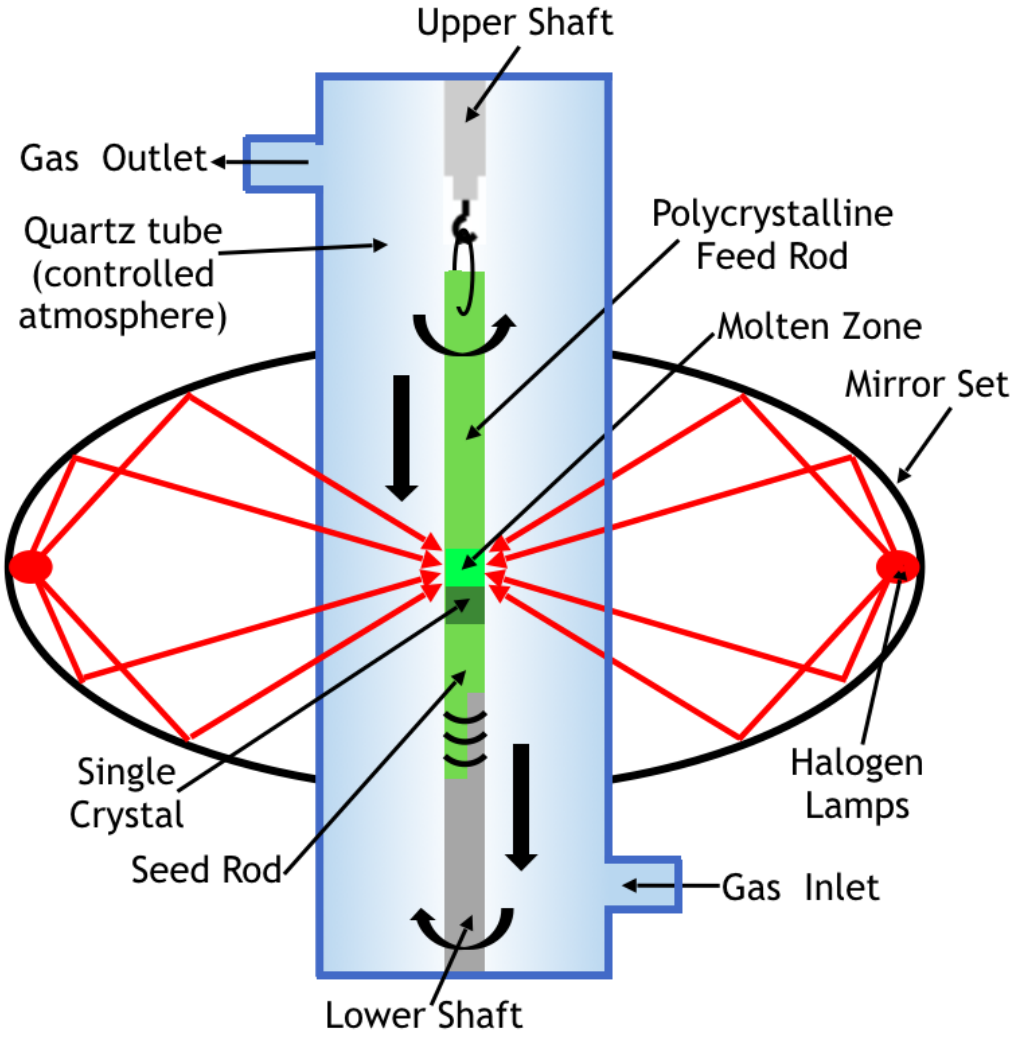

Figure 4.1: Schematic of the two mirrors image furnace employed for floating zone single crystal growth of $SrLn_2O_4$ samples. Both feed and seed rods are attached to the upper and lower shafts, respectively. A molten zone is created at the contact point between both rods by focusing the halogen lamps heating power at this particular point using two surrounding sets of mirrors. The homogeneity and stability of the molten zone is ensured by counter rotating both shafts. The crystal growth progression is achieved by slowly translating both shafts downwards. The quartz tube surrounding the shafts and rods is employed to control the growth atmosphere but also to protect the furnace from eventual chemical depositions of evaporated material.

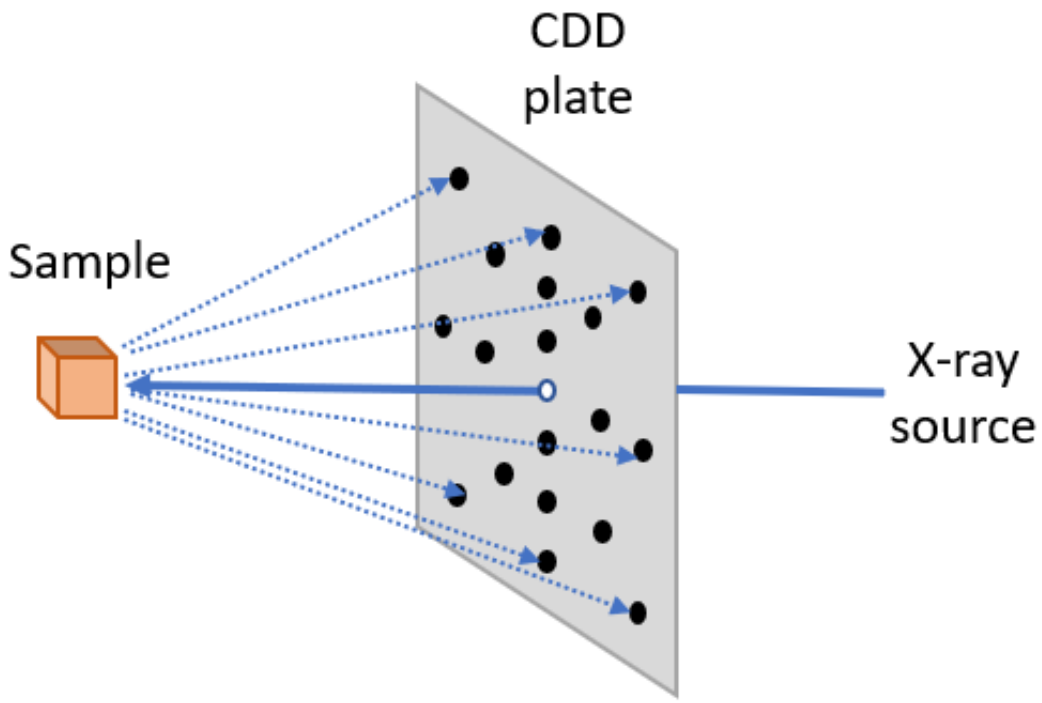

Figure 4.2: Schematic of an x-ray or neutron Laue camera employed to investigate the crystalline quality and to orientate single crystal samples. Diffraction in reflection mode is employed, the beam passes through a small hole in the center of the detector plate to reach the sample and be reflected back toward the detector plate. The techniques takes advantage of a polychromatic beam to illuminate every allowed reflection directed toward the CCD detector plate in a particular orientation of the crystal sample. A two dimensional reciprocal space image of the crystal face oriented toward the CCD detector is thus obtained.

techniques were employed. This technique uses a polychromatic beam that passes through a hole in the center of an image plate CCD detector before reaching the sample and being backscattered towards the detector, see Fig. 4.2. The beam being polychromatic, Bragg scattering condition will be satisfied for every set of lattice planes. A reciprocal space picture of the crystal face being oriented toward the detector will thus be obtained.

The Laue diffractograms created can be compared with simulations revealing the crystalline quality of the sample. Individual reflections of high crystalline quality samples can then be indexed disclosing the sample orientation in the lab reference frame. The sample can then be reoriented to place the principal crystallographic axes in the desired directions and be glued to a sample holder in provision for diffraction experiments.

The Laue diffraction investigation of the crystal samples used for measurements in this thesis were performed using the Warwick x-ray Laue camera as well as the ILL OrientExpress neutron Laue diffractometer see Fig. 4.3. The software CLIP [65] was employed to rapidly index the scattering patterns.

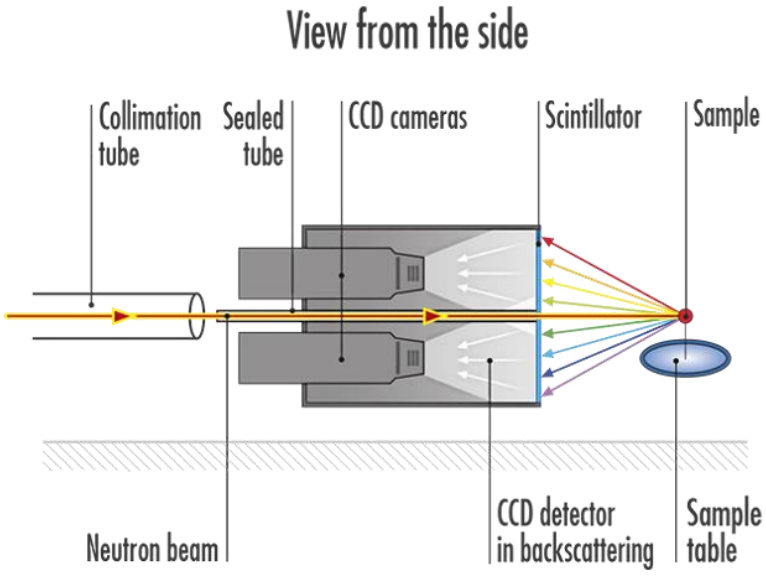

Figure 4.3: Schematic of the single crystal neutron Laue instrument OrientExpress. Laue diffraction techniques are exploited by this instrument employing a polychromatic beam of neutron in an objective to orientate and investigate the crystalline quality of single crystal samples. Figure reproduced from Ref. [66].

4.2 Bulk characterisation

4.2.1 Magnetic susceptibility and magnetisation measurements

Magnetic susceptibility $\chi(T)$ and low temperature magnetisation $M(H)$ measurements were made employing a Quantum Design Magnetic Property Measurement System (MPMS), see Fig. 4.4. This instrument takes advantage of Lenz's law by moving magnetised samples in the center of a coil resulting in the induction of a current within the coil. In the particular case of MPMS magnetometers, the sample is attached to a non magnetic sample stick and inserted into the center of a superconducting coil connected to a Superconducting Quantum Interference device (SQUID). A superconducting magnet provides a vertical static field onto the sample to magnetise it. The magnetised sample is then vertically translated in a series of

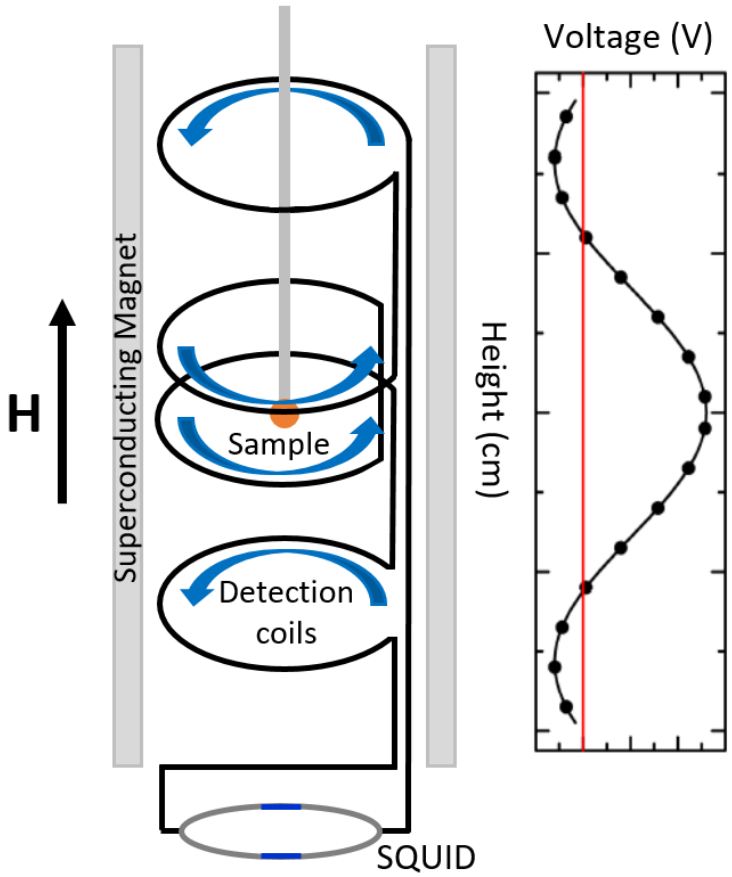

Figure 4.4: Schematic of a MPMS SQUID magnetometer. This instrument takes advantage of Lenz's law by magnetising a sample and translating it vertically in the center of superconducting coils to induce a current. The current is converted by the SQUID device into a voltage at discrete positions over the sample displacement. The resulting signal is fitted returning a measurement of the sample magnetisation.

discrete steps and measurements of the current induced in the coils are performed at every step, the SQUID converting the induced electric intensity into a voltage. The signal measured as a function of sample position can subsequently be fitted employing standard models, returning a measurement of the sample magnetisation in the field and temperature conditions considered. The measurement can then be repeated in different temperature and field conditions to investigate the $H - T$ magnetic phase diagram of the sample. The SQUID measurements presented in this thesis were made between 1.8 and 300 K, under applied field magnitudes ranging from 0 to 20.0 kOe.

Additional magnetisation measurements were performed on a Vibrating Sample Magnetometer (VSM), at temperatures ranging from 1.5 to 4.0 K and under field

magnitudes as high as 70 kOe, see Fig. 4.5. On this instrument, the sample is attached to a non magnetic stick and inserted into the center of a set of stationary pick up coils. An electromagnet applies a static magnetic field to the sample to induce its magnetisation. The sample is then vertically vibrated at 55 Hz with an amplitude of 1.5 mm, resulting in the induction an AC current in the pick up coils. The current is then converted into a voltage and the signal is fitted, returning a measurement of the sample magnetisation for the field and temperature conditions of the measurement. In this thesis I present VSM measurements made between 1.5 and 4.0 K under field magnitudes ranging from 0 to 70 kOe.

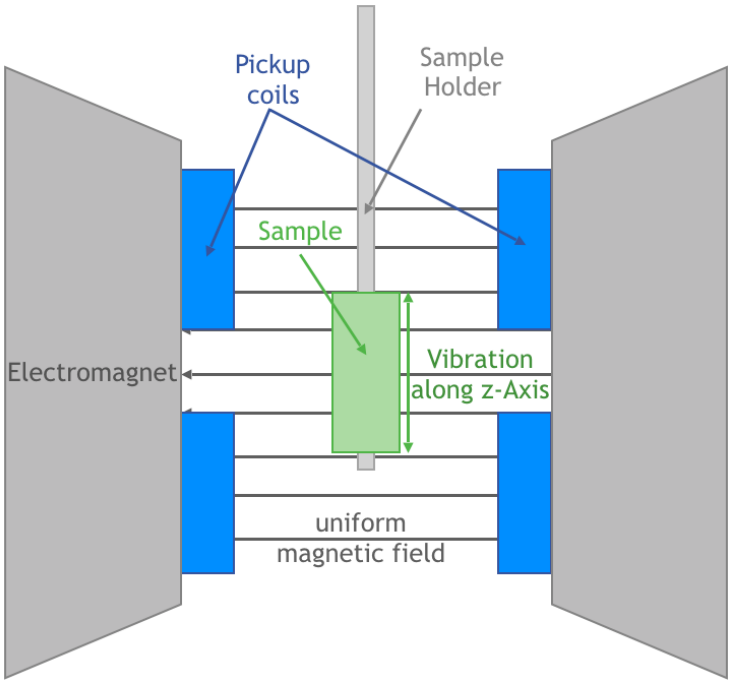

Figure 4.5: Schematic of a Vibrating Sample magnetometer (VSM). The sample magnetised by a stationary field is vertically vibrated at 55 Hz inducing currents in the pick up coils.

4.2.2 Specific heat measurement

The specific measurement of $SrLn_2O_4$ samples presented in the thesis were made with a Physical Property Measurement System (PPMS) heat capacity calorimeter using the relaxation method, see Fig. 4.6. On this instrument, the sample is placed on the surface of a little platform to which are attached a thermometer and a heater that are both connected to thermal baths via thin wires also used to support the platform itself. The measurement proceeds by first stabilising the sample temper-

ature, Apiezon grease is employed to improve the thermal contact between sample and platform. The heater is subsequently activated to progressively increase the sample temperature over a very limited temperature region (2 to 5% of the sample initial temperature). Once the sample temperature has reached the defined maximum value, the heater is switched off and the sample allowed to relax. Both temperature increasing and decreasing trends are monitored as a function of time and fitted using standard models, returning a measurement of the sample heat capacity in the experimental conditions of the measurement. Data collections can be performed in large range of temperature and field conditions for the investigation of the $H - T$ magnetic phase diagram of the sample.

I note that to employ this apparatus, samples should be solids such as crystal or solids made of pressed and preferably sintered polycrystalline materials. In the particular case of $SrNd_2O_4$ polycrystalline materials, the samples should weigh no more than a few milligrams to ensure for proper thermal behaviour using the relaxation method. Furthermore, to perform in field measurements it is necessary to pre-measure the device addenda, i.e. the field-induced specific heat variation of the sample platform and grease. The addenda measurement also implies measuring artefacts induced by the applied field onto the thermometer.

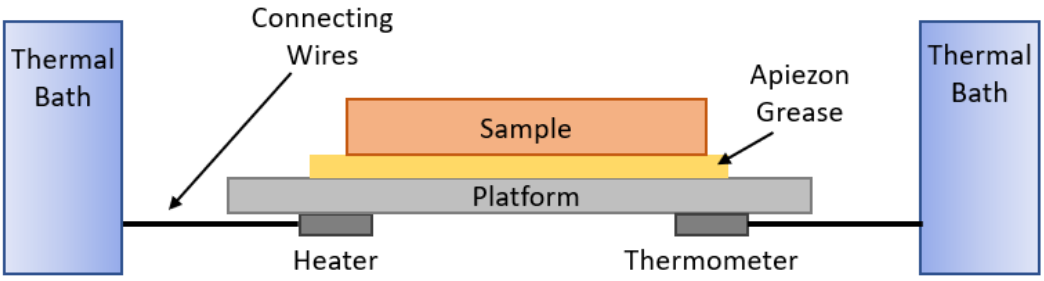

Figure 4.6: Schematic of a PPMS heat capacity calorimeter employed for specific heat measurements using the relaxation method. The sample lays on the surface of an Apiezon grease layer spread on top of the sample platform insuring optimal thermal conductivity. Heater and thermometer devices are attached to the platform and connected to thermal baths via thin wires. Figure adapted from the instrument users manual [67].

4.3 Neutron Powder Diffraction

Polycrystalline materials consist of very tiny crystallites randomly oriented one with respect to another. In the ideal case, i.e. if the powder grains are small (typically 1 to 10 microns) in comparison with the monochromatic beam diameter and if they

are oriented in a perfectly random way, the Bragg condition will be satisfied for every hkl set of lattice planes in the material. As a result, the diffracted beam consists of concentric circles known as the Debye-Scherrer rings, each ring corresponding to a particular hkl Bragg reflection of the material, see Fig. 4.7. A two dimensional detector is often used on powder diffractometer to measure a horizontal cut through the intensity rings. A two dimensional scattering intensity pattern is obtained as a function of the scattering angle that can be converted to units of the scattering vector **Q** employing eqn. 3.26. The diffraction pattern can then be indexed and refined using the Rietveld refinement analysis method previously discussed, see subsection 3.6.

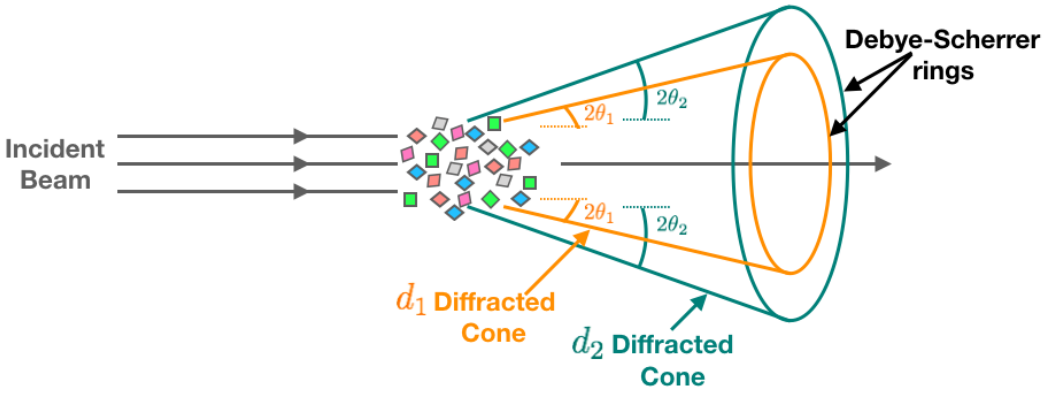

Figure 4.7: Schematic of the polycrystalline diffraction process. Figure adapted from Ref. [68].

4.3.1 D20 (ILL), High intensity neutron powder diffractometer

The D20 (ILL) instrument is a very high flux neutron powder diffractometer equipped with a large two dimensional detector bank enabling to measure scattering intensities up to large scattering angles on small and/or absorbing samples, see Fig. 4.8. This instrument is principally used to investigate both crystalline and magnetic structures of polycrystalline materials. It uses a very intense monochromatic neutron beam that scatters through the material in transmission mode, producing Debye-Scherrer intensity rings centered around the primary (incoming) beam axis. As seen on the instrument diagram, the detector bank measures a horizontal cut from the center of the scattering rings towards scattering angle values being near 180°. The ring's intensities are integrated along the vertical aperture of the detector bank and a scattering pattern displayed as a function of 2θ angle is returned to the user.

To modify the wavelength of the monochromatic beam, the take-off angle of the instrument can be changed by selecting a different monochromator orientation and simultaneously rotating the sample and detector bank around the monochromator axis. Different holes in the concrete protective wall allow to collect the beams at the different take-off angles. Increasing the take-off angle up to 120° increases the wavelength of the monochromatic beam and provides a better resolution to the measurement. Reducing the take-off angle on the other hand decreases the resolution, but is granting access to higher scattering **Q** values.

The instrument is equipped with a regular orange cryostat allowing for the cooling of samples down to 1.5 K in order to perform accurate structural analyses with reduced Debye-Waller effects, as well as to investigate low temperature magnetic orders. Dilution fridge cryostat and cryomagnets can also be implemented on the instrument for specific measurements.

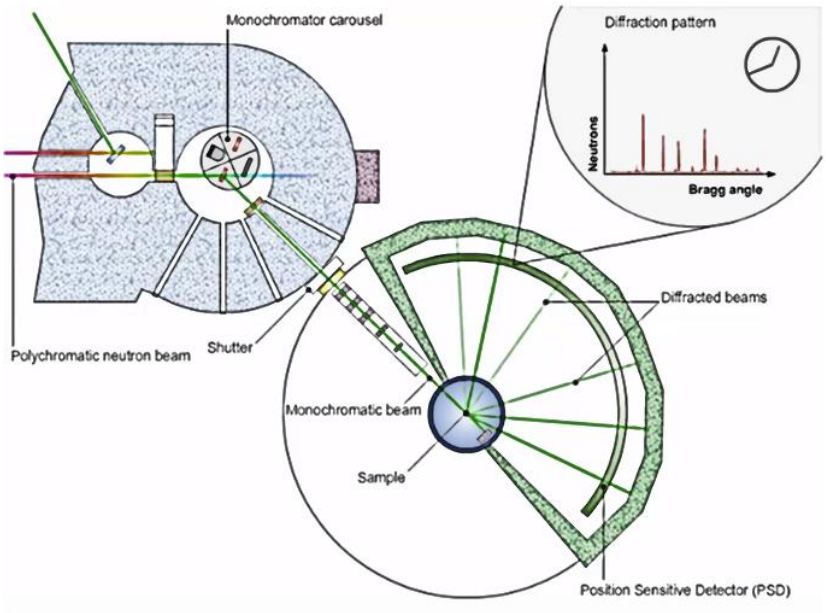

Figure 4.8: Schematic of the high intensity neutron powder diffractometer D20. The very high neutron flux used by the instrument allows to rapidly measure high intensity powder scattering patterns of high quality. To a certain extent, very small samples as well as materials containing absorbing elements can also be investigated with this instrument by taking advantage of the beam high intensity. Figure reproduced from Ref. [69].

4.3.2 D2B (ILL), High resolution neutron powder diffractometer

The D2B (ILL) instrument is a cold neutron powder diffractometer resembling and working similarly to the previously detailed D20 instrument, see Fig. 4.8. However, this instrument is set in high resolution mode and is used to collect data for high quality structural and magnetic Rietveld refinement analyses. This instrument is also equipped with a regular orange cryostat and both dilution fridge and cryomagnets can be implemented on request.

4.3.3 D7 (ILL), Polarised neutron diffractometer

The D7 (ILL) instrument is a cold polarised neutron powder diffractometer, used to study nuclear and magnetic short range ordered materials, see Fig. 4.9. The instrument uses a monochromatic beam that is first polarised along the z axis in the lab reference frame using a super mirror polarizer. A neutron spin mezei flipper is then used to flip the direction of the neutron spins pointing down. A guide field is also applied at the flipper position to preserve the beam polarisation along z. A set of xyz coils is subsequently use to set the polarisation of the beam along x, y or z axis directions defined within the lab reference frame. A large detector bank equipped with analysers allows for measurement of polycrystalline scattering intensities selecting the neutron polarisation. In practice, the scattered intensities corresponding to spin flipped and non spin flipped neutrons are individually measured for each of the three xyz directions of polarisation. These intensities are subsequently compared using eqns. 3.43, 3.44 or 3.45, separately returning both magnetic and nuclear components of the scattered signal, see section 3.7. This technique is particularly useful to individually observe diffuse magnetic intensities.

Polarised single crystal measurements are also possible on this instrument. The detector bank is able to rotate around the sample position offering the possibility to measure reciprocal space maps over almost 360°.

4.3.4 D4 (ILL), Hot neutron powder diffractometer

The D4 instrument is a hot neutron powder diffractometer designed to study partially disordered materials. This instrument essentially works like both D20 and D2B but is adapted to a short wavelength, high $\mathbf{Q}$ coverage and low resolution type of diffraction. Due to gaps between the detectors, a continuous scattering angle coverage is obtained by rotating the detector bank in discrete steps and by averaging the acquisitions performed at each step.

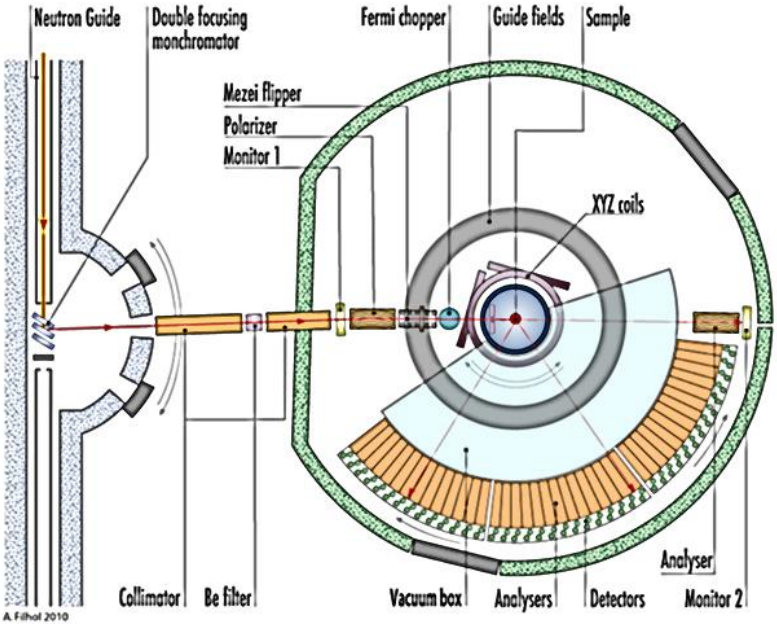

Figure 4.9: Schematic of the polarised neutron powder diffractometer D7. xyz polarisation analysis is implemented in this instrument, enabling accurate separations of the magnetic and nuclear components of the scattered intensities. Figure adapted from Ref. [70].

In this thesis project I have used D4 measurements to investigate the magnetic disorder in $SrLn_2O_4$ materials employing magnetic PDF (mPDF) analyses of the data. This data treatment technique is rather unexploited and is still under development considering the treatment of D4 data. The mPDF data analysis consists in Fourrier transforming the magnetic scattering signal collected over a large **Q** region and applies to the total magnetic scattering signal produced by both long and short types of magnetic orders. A real space profile picture of both long (static) and short range (dynamic) types of correlations acting in magnetic materials at a given temperature is returned from this data treatment. Of great interest, comparing the obtained profile with inter ionic distances can directly be associated to particular characteristics of the magnetic orders being stable in the experimental conditions of the measurement.

4.4 Single crystal neutron diffraction

Single crystal neutron diffraction measurements are performed employing two different techniques. The most commonly used technique employs a monochromatic

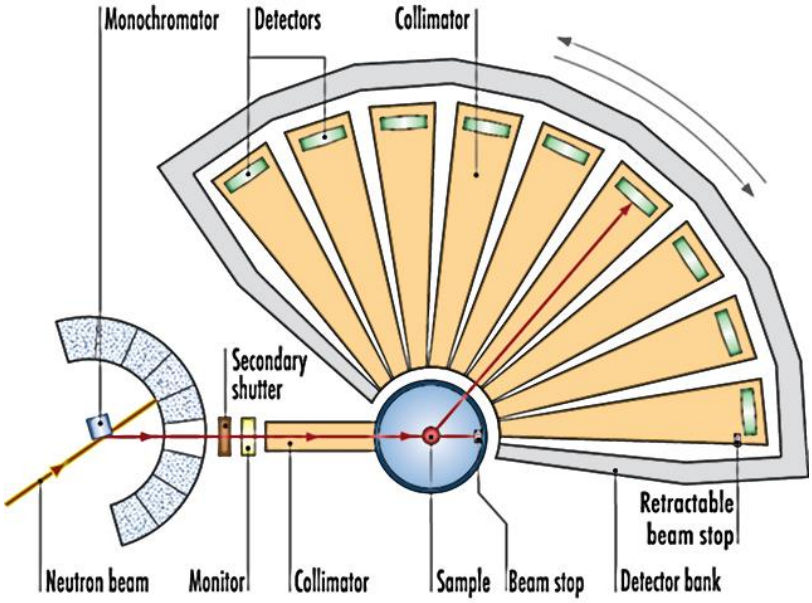

Figure 4.10: Schematic of the hot neutron powder diffractometer D4. The short wavelength of the neutron beam used by the instrument enables the measurement of powder scattering patters over large Q ranges. Such patterns being well suited for PDF and mPDF analyses. Figure adapted from Ref. [71].

beam that is able to activate a single (hkl) reflection at a time. Each reflection is individually measured using a small plate type of detector by successively orienting the sample (in respect to the beam direction of propagation) to satisfy each Bragg condition allowed by the material symmetry. The second technique uses a polychromatic beam of neutron that enables the activation of every symmetry allowed (hkl) reflections. Instruments exploiting this technique must be equipped with large detector banks covering large reciprocal space regions in order to measure simultaneously as many Bragg reflections as possible. This technique is known as Laue diffraction (see subsection 4.1.4) and is usually used to align crystal samples and verify their crystalline quality. However, it can be enhanced to a level enabling single crystal refinement analyses to be performed on the data. This enhancement consists in monitoring the travelling time (the time of flight (tof)) of each neutron from the target stations to the detector bank, disclosing their wavelengths. This knowledge enables to reconstruct the scattering pattern of the material and to differentiate between equivalent reflections. Time of flight diffraction is usually implemented at spallation sources with primary objective to maximise the instrument flux.

4.4.1 D9 (ILL), Single crystal hot neutron 4-circle diffractometer

The D9 (ILL) instrument is a four-circle hot neutron diffractometer employed for precise measurement of Bragg scattering intensities up to high **Q** values. D9 data are used for precise structural analyses of crystalline materials but can also be used to accurately refine magnetic structures. The 4-circle Eurelian cradle is a central part of this instrument offering a large reciprocal space coverage allowing for the collections of large sets of independent Bragg reflections.

To operate the Eurelian cradle, the two circles labelled as Φ and χ are employed to align the sample crystallographic directions according to the instrument axes. The third circle labelled as ω is subsequently used to orientate a particular set of lattice planes in diffraction conditions according to the beam direction. The area detector is finally set to the diffracted beam position by rotating around the 2-θ circle.

Both dilution fridge and cryomagnet devices can be implemented on the instrument. Employing the cryomagnet however prevents from using the Eurelian cradle, hence reducing the reciprocal space coverage of the instrument.

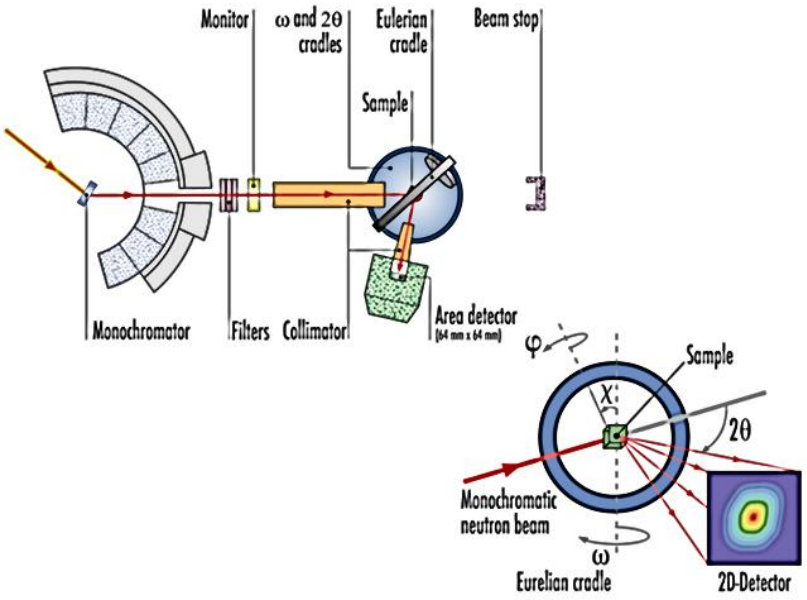

Figure 4.11: Schematic of the single crystal hot neutron 4-circle diffractometer D9. This instrument uses by a beam of hot neutron and is equipped with a Eurelian cradle enabling for accurate collections of large single crystal sets of Bragg reflections, up to high values of momentum transfers. Precise structural investigation of both magnetic and nuclear structures can thus be performed on this instrument. Figure adapted from Ref. [72].

4.4.2 D10 (ILL), Single crystal 4-circle neutron diffractometer

D10 is a high flux thermal neutron single crystal neutron diffractometer, see Fig. 4.12. This instrument works similarly to the previously described D9 instrument but the difference is that is uses a thermal neutron beam and is thus more adapted to accurately measure magnetic Bragg intensities located a low **Q** values. D10 is equipped with a Eurelian cradle and a unique 4-circle dilution fridge cryostat device can be implemented on the instrument. A cryomagnet can also be implemented on the instrument but requires the removal of the cradle.

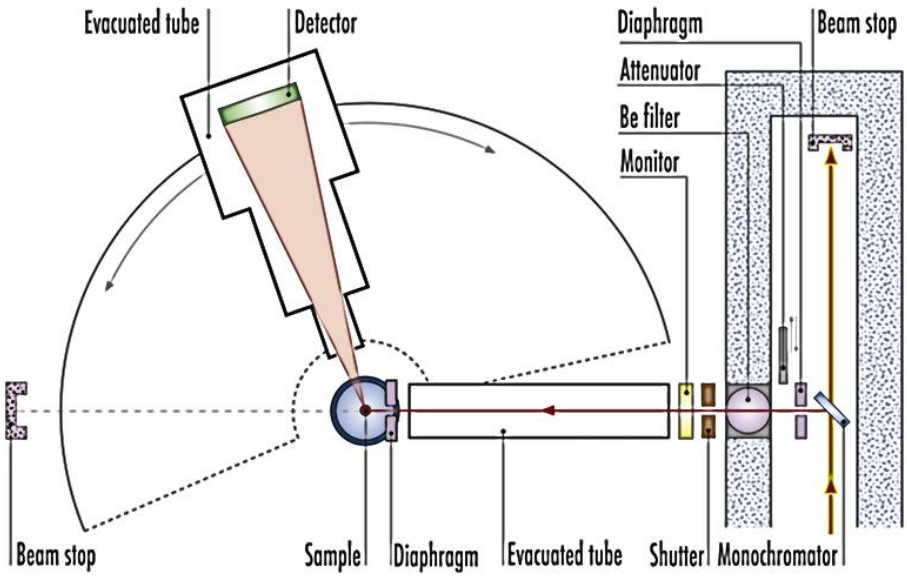

Figure 4.12: Schematic of the single crystal 4-circle neutron diffractometer D10. Using a beam of thermal neutron, this instrument is perfectly suited for the investigation of magnetic structures. Furthermore, the unique 4-circle dilution fridge device implemented on the instrument enables the collection of large sets of Bragg reflections at temperatures as low as 0.1 K. Figure adapted from Ref. [73].

4.4.3 WISH (ISIS), Time-of-flight neutron diffractometer

WISH is a time-of-flight (tof) neutron powder diffractometer implemented at the ISIS neutron spallation source. The two sets of large detector banks of the instrument provide an almost 360° coverage angle in the horizontal plane, but also present a substantial vertical coverage. Hence measurements of single crystal reciprocal space maps are also made possible on this instrument. A schematic of the instrument can be found in Ref. 4.4.3.

The WISH measurements presented in this thesis are all single crystal measurements. The time of flight technique is used on this diffractometer in order to maximise the diffracted signal by avoiding the monochromatiation of the beam. Of great interest, the tof analysis of the data allows to reconstruct the reciprocal space scattering maps of the crystal samples offering the possibility to observe individually equivalent reflections (e.g. Friedel pairs). WISH thus returns large and detailed pictures of the material reciprocal space. Single crystal scattering issues are however maximised by the use of a polychromatic neutron beam, adding difficulties in the data refinement analysis. For instance, single crystal absorption and extinction phenomena are strongly wavelength dependent and accurate corrections are difficult tasks to perform on polychromatic beams.

Chapter 5

Low temperature magnetic properties of $SrNd_2O_4$

5.1 Introduction

In this chapter, I present an investigation of the low temperature magnetic properties of the Nd variant of the $SrLn_2O_4$ family. Prior to the start of this research project, $SrNd_2O_4$ stood among the few last members of the family that had not yet been the subject of a magnetic investigation. The particular case of $SrNd_2O_4$ offers the possibility to study a variant of the family hosting a light rare earth element as the magnetic Ln^{3+} ions. In fact, Nd^{3+} considered as a free ion bears a magnetic moment being relatively smaller than those borne by a majority of the heavy rare earth ions. This particularity is expected to reduce the influence of the dipolar interactions, favouring the stabilisation of collinear orders aligned along c in the $SrLn_2O_4$ systems [37, 38]. Antiferromagnetic exchange interactions acting between near neighbours however, could be in a position to stabilise the magnetic moments entirely within the crystallographic ab-plane of the material [39, 40, 42].

5.2 Polycrystalline sample synthesis

The study of $SrNd_2O_4$ starts with the synthesis of this material as a polycrystalline sample. Several syntheses of this material, crystallising according to the orthorombic space group $Pnam(62)$ have been reported in the literature prior the start of this doctoral research work. The synthesis processes were however poorly detailed or not reported at all [74–76]. The high temperature chemical instability of $SrNd_2O_4$ is nevertheless clearly stated by the different sources, although neither the alteration

temperature nor the chemical nature of the resulting materials reported agree in between the different publications. The decomposition is reported to occur at 1370 [75] or at 2100°C [76], according to the sources considered. The first chemical products reported to result from the process are $Sr_3Nd_4O_9$ and $Sr_5Nd_8O_{17}$. In addition, the solid solutions $2(Nd_2O_3)$ x SrO, $4(Nd_2O_3)$ x 5SrO, $2(Nd_2O_3)$ x 3SrO [74], (Sr,Nd)O and $(Sr,Nd)_2O_3$ [75] are reported to stabilise at temperatures ranging from 1500 to 2350°C. This series of information revealing a rich, complex and largely unknown chemical phase diagram for the Nd_2O_3-$SrCO_3$ system.

The synthesis method previously employed for the synthesis of several members of the $SrLn_2O_4$ family, first reported by Karunadasa *et al.* is however well known [24]. The method takes advantage of the ionic solid diffusion process, occurring at high temperature in solid state polycrystalline materials. In practice, $SrLn_2O_4$ powders are obtained by finely mixing stoichiometric quantities of $SrCO_3$ and Ln_2O_3 powders in order to obtain a chemically homogeneous reacting medium. The mixture is then placed in a furnace for high temperature treatment, inducing the ionic diffusion to proceed between the powder grains of the two phases. The evaporation of residual elements also results from the high temperature heat treatment, allowing for the synthesis of chemically pure samples. Typically, the stoichiometric mixture of reactants is heated at 1500°C for a duration of 48 hours in air and under ambient pressure [24]. Intermediate grinding can be performed over the baking process in order to enhance the reaction yield, but as a drawback, will favour the depletion of Sr in the reacting mixture due to the high volatility of the latter. It was reported from the synthesis of several members of the family, that the Sr evaporation turns out to be responsible for the presence of a few remaining percents of Ln_2O_3 impurity polluting the reaction product. As a solution to this problem, the use of an off-stoichiometric ratio of the two starting components quantities considering a slight excess of $SrCO_3$ was suggested [63]. A reduction of the heat treatment temperature to 1350°C was also reported to reduce the Sr evaporation over the baking process, allowing for the synthesis of pure $SrLn_2O_4$ materials [63].

Considering this information, a first attempt to synthesis a polycrystalline sample of $SrNd_2O_4$ was experimented using a Sr excess corresponding to a $1 : 0.875$ off-stoichiometric ratio of the two reactants' relative molar quantities. The two powders where homogeneously mixed together in a mortar for approximately five minutes and subsequently introduced in an alumina crucible. The powder was also slightly pressed to increase its compacity and improve the ionic diffusion process between the different grains at high temperature. The mixture was heat treated at 1350°C over a 48 hours baking duration, in ambient atmosphere conditions. The

chemical nature of the synthesis product was then investigated using laboratory x-ray diffraction techniques. A Rietveld refinement analysis of the collected x-ray data was attempted, but no known chemical phases containing the Sr, O and Nd elements could be identified, revealing the partially reacted nature of the sample and the presence of several chemical phases. In order to eventually complete the reaction process, the heat treatment procedure was repeated and followed by an additional 1450°C baking treatment. X-ray data were collected in between these two baking treatments, successively returning unique patterns. These preliminary results reveal the clear chemical instability of the Nd_2O_3-$SrCO_3$ system in between 1350 and 1450°C, contradicting previously reported results. The use of a $SrCO_3$ excess in the preparation of the reacting mixture could also foster the synthesis of chemical phases containing large ratios of Sr over the Nd quantities, such as $Sr_3Nd_4O_9$ or $Sr_5Nd_8O_{17}$.

A series of new syntheses were attempted at lower temperature and in stoichiometric conditions, revealing the value of 1300°C as the optimal baking temperature for the synthesis of $SrNd_2O_4$ polycrystalline samples. The Rietveld refinement of the x-ray scattering pattern collected on the 1300°C baked sample confirmed the synthesis of the Nd variant of the $SrLn_2O_4$ family adopting the peculiar honeycomb structure described by Karunadasa *et al.* [24]. From this new series of synthesis, I also report that lower baking temperatures are not sufficient to induce solid state diffusion. Temperatures higher than 1300°C on the other hand, will alter the material. Shorter baking times were also experimented and revealed as inconclusive, due to clear reductions of the reaction progress achieved by the end of the baking duration. Despite the synthesis of good quality $SrNd_2O_4$ powder samples using this method, the impossibility to consider slight excesses of Sr in the composition of the reacting powder mixture, results in the synthesis of $SrNd_2O_4$ powder samples containing few percents of Nd_2O_3 as an impurity. The samples impurity concentration could however be significantly reduced by using rather large quantities of reacting materials. This method improves significantly the quality of the result by increasing the volume over surface ratio of the reacting medium. The ionic diffusion process being of lower efficiency on the surface of the reacting medium, increasing this ratio results in a dilution of the impurity phase within a larger amount of material. I report that approximately three grams of Nd_2O_3 and of the corresponding $SrCO_3$ quantities are optimal for the synthesis of rather pure samples of $SrNd_2O_4$. From the Rietveld refinement analysis of the x-ray pattern measured on my best result, I report the synthesis of a 94% pure $SrNd_2O_4$ powder sample. The remaining 6% corresponds to remaining Nd_2O_3 powder present in the sample under the $c2/m$ and

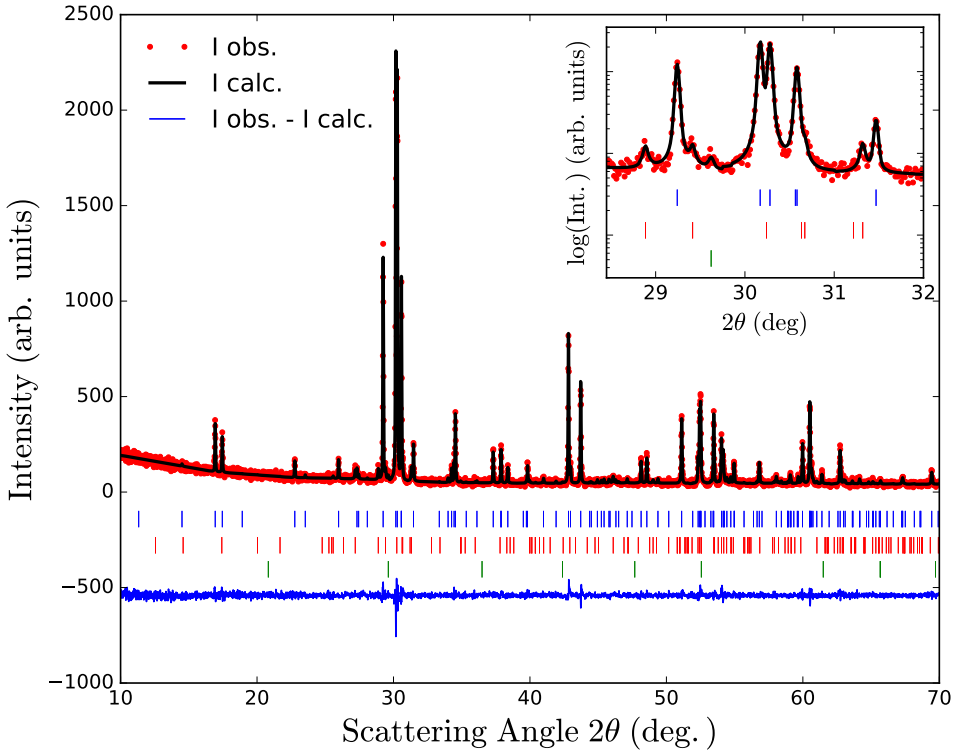

Figure 5.1: X-ray scattering pattern collected on a powder sample of $SrNd_2O_4$ containing a few percent of Nd_2O_3 present under two different allotropic forms. The data, fit and relative difference are respectively displayed in red, black and blue. Allowed reflections positions are presented as vertical lines beneath the data, in blue for the main $SrNd_2O_4$ phase and in red and green for the two Nd_2O_3 phases, respectively. The inset focuses on the scattering angle region hosting the Nd_2O_3 reflections, the logarithmic scale considered allowing for their proper visualisation.

$Pm\bar{3}m$ allotropic forms, with respective concentrations of 5.7 and 0.3%. The x-ray pattern measured on this polycrystalline sample is presented in Fig. 5.1, along with the fit obtained from the Rietveld refinement analysis. The Bragg reflection positions corresponding to the $SrNd_2O_4$ ($Pnam$) and Nd_2O_3 ($c2/m$) and ($Pm\bar{3}m$) phases are marked by blue, red and green vertical lines, respectively. The top left inset of the figure allows to properly visualise the presence of the weak Nd_2O_3 Bragg reflections by presenting the intensities on a logarithmic scale. A limited 2-θ angle coverage focusing on the region where impurity reflections are observed is also considered for clarity. Sitting above the red vertical line markers, three reflections identified as originating from the $c2/m$ phase are observed at 27.2, 28.86, 29.38 and 31.3 degrees, the first reflection being out of the scattering angle coverage. The presence of the second Nd_2O_3 phase on the other hand is less of a certainty, since it is attributed to a single peak visible at 29.62 degrees. It is evident that a proper Rietveld analysis must consider more than a single reflection. However the presence of this particular reflection does not correspond to the scattering pattern of any other known chemical phases containing the chemical elements used for the synthesis. Moreover, the scattering pattern of the $Pm\bar{3}m$ Nd_2O_3 phase displays a single strong peak at a position corresponding to the 29.62° observation. These arguments validate the probable presence of the $Pm\bar{3}m$, Nd_2O_3 phase in the sample, at a low but still significant concentration.

The study of the $SrNd_2O_4$ under polycrystalline form has also revealed the strong moisture sensitivity of the material. In fact a few hours of air exposure are sufficient for the material to absorb significant quantities of water. The neutron scattering data collected on the D7 instruments have revealed on average, the presence of 1.5 H nuclei per unit cell of the material (see subsection 5.18). The measurement however revealed the structural stability of the material, as well as a conservation of its magnetic properties despite the water molecule inclusions. Bulk characterisation techniques have on the other hand revealed that $SrNd_2O_4$ samples were suffering from the loss of Sr, resulting in growing Nd_2O_3 contents over time. It is not yet clear if this loss of Sr is induced by a contact with air containing moisture, or if it the result of a chemical instability of the material over time. In any case, in order to prevent for sample alterations, polycrystalline sample of the $SrNd_2O_4$ material must be stored in oxygen free atmospheres. The use of freshly baked samples is also recommended for accurate measurements.

	x-ray RT	
Ions	x	y
Sr	0.7440(8)	0.6485(6)
Nd1	0.4334(5)	0.1170(4)
Nd2	0.4062(4)	0.6090(4)
O1	0.227(4)	0.189(3)
O2	0.146(3)	0.493(4)
O3	0.494(4)	0.785(3)
O4	0.436(4)	0.418(3)

Table 5.1: Crystallographic parameters of the $SrNd_2O_4$ material crystallising according to the orthorombic *Pnam* space group with lattice parameters a = 10.1529(1), b = 12.2065(1) and c = 3.57097(3) Å. All ions are sitting at the 4*c* Wyckoff positions of general coordinates: x, y and 0.25 on the unit cell basis. The structural parameters and ionic positions were obtained from the Rietveld refinement analysis of powder x-ray scattering data collected on a polycrystalline sample at room temperature (RT).

5.3 Bulk characterisation

5.3.1 Structural investigation

The structural parameters of $SrNd_2O_4$ were first determined from the Rietveld refinement analysis of x-ray scattering data collected at room temperature (RT), on a polycrystalline sample of the material, see Fig. 5.1. In agreement with the structural characteristic of the $SrRE_2O_4$ family of materials, the scattering data confirms the crystallisation of $SrNd_2O_4$ under the form of calcium ferrite [36], by adopting the *Pnam*(62) orthorombic space group considering that all the different ions are sitting at the Wyckoff 4*c* positions. The refined structural parameters obtained from the x-ray scattering data are presented in table 5.1. Powder neutron diffraction (PND) techniques were also employed to complement the x-ray results, the result of these measurements being latter detailed, see subsection 5.4.1.

5.3.2 Magnetic susceptibility

I started the investigation of the magnetic properties of the $SrNd_2O_4$ compound, by measuring the temperature dependence of its magnetic susceptibility using a SQUID magnetometer. The measurement was performed on a 21.30 mg polycrystalline sample of high chemical quality. The sample was first cooled down to 10.0 K and centered in the instrument using a 500 Oe magnetic field. The field was subsequently ramped down to 0 Oe, before cooling the sample to 1.8 K, the lowest temperature that could be achieved by the cryostat implemented on the instrument. The temperature de-

pendence of the susceptibility was measured using a stable field of 500 Oe applied onto the sample, offering a good sensitivity to the sample magnetisation. It was also found that higher magnitudes of applied field were responsible for a polarisation of the sample grains according to the easy axis of the material, hence significantly influencing the reproducibility of the measurement. The data collection procedure includes a double measurement of each data point, the average of the two values being then considered, increasing the accuracy of the measurement. The first set of data was collected from 1.8 to 10 K, see Fig 5.2. The data reveals a clear cusp in the low temperature region of the diagram, indicating the presence of a temperature induced magnetic transition. The linear decrease trend measured above the transition temperature also reveals a weak irregularity of the system in between 4 and 5 K. This irregularity is however located at the He boiling point, and was observed as not fully reproducible from complementary measurements. This irregularity is thus very likely to be a simple measurement artefact. Additional data were collected when re-cooling the sample from 10 K down to 1.8 K, revealing a clear match between the field cooled (FC) and zero field cooled (ZFC) data.

The sample was subsequently warmed up to 5.0 K in order to neutralise potential field-induced frozen magnetic states, and directly cooled back down to 1.8 K in zero field conditions. Susceptibility data were again collected, but this time all the way to room temperature. Plotting the inverse of the measured susceptibility as a function of temperature reveals a linear behaviour of the data between 50 and 300 K, as well as the clear Curie-Weiss dependence of the material, see Fig. 5.3. By fitting the linear region of the data above the ordering temperature, I have extracted both the Weiss temperature and the Nd^{3+} effective magnetic moment values, θ_{CW} = -30.3(5) K and μ_{eff} = 3.54(1) μ_B, respectively. The large difference obtained between the calculated Weiss and observed transition temperature T_{N} = ~2.3 K, reveals the high frustration index of the material. In addition, the calculated value of the effective magnetic moment, borne by each Nd^{3+} ions corresponds to the tabulated free ion value of 3.3 - 3.7 μ_B [1], revealing the paramagnetic nature of the system at high temperature.

To further investigate the low temperature magnetic characteristics of the $SrNd_2O_4$ system, I have extended the magnetic susceptibility investigation by repeating the initial low temperature measurement under various magnitudes of applied field. In order to avoid significant measurement perturbations induced by the field polarisation of the sample grains, a sintered square shaped pellet of the material, glued on a solid sample holder was used for these measurements. Data were collected from 1.5 to 10.0 K under field magnitudes of 0.5, 1.0, 5.0, 10.0 and

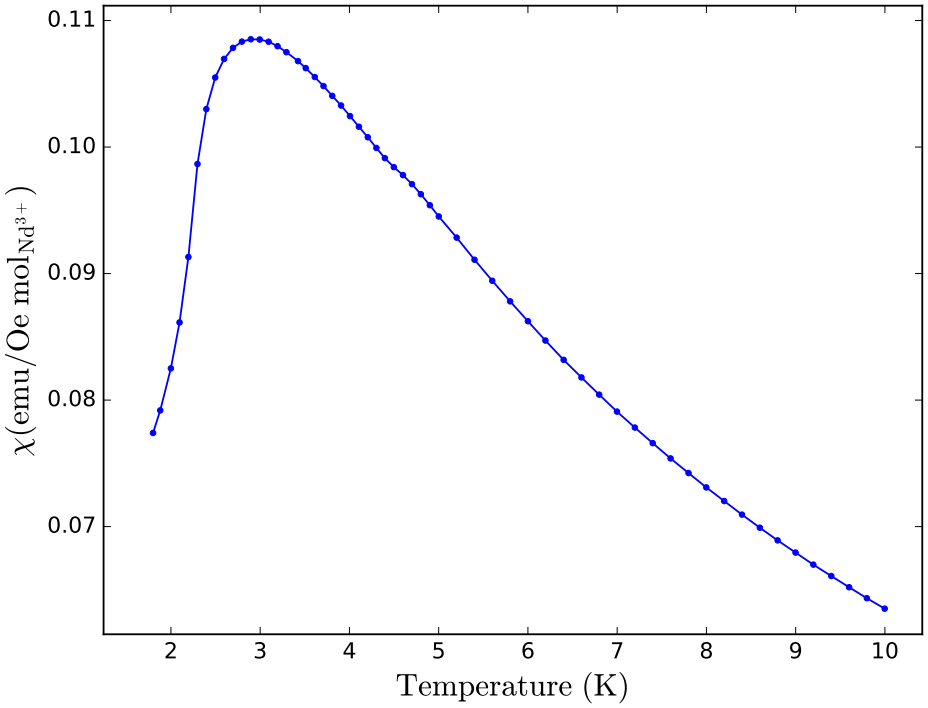

Figure 5.2: Low temperature magnetic susceptibility measurement performed on a polycrystalline sample of $SrNd_2O_4$ in zero field cooled conditions. The measurement was carried out using a SQUID magnetometer equipped with its regular cryostat and by applying a stable field of 500 Oe onto the sample. A clear magnetic transition is observed as a cusp observing a maximum at $\sim$2.8 K.

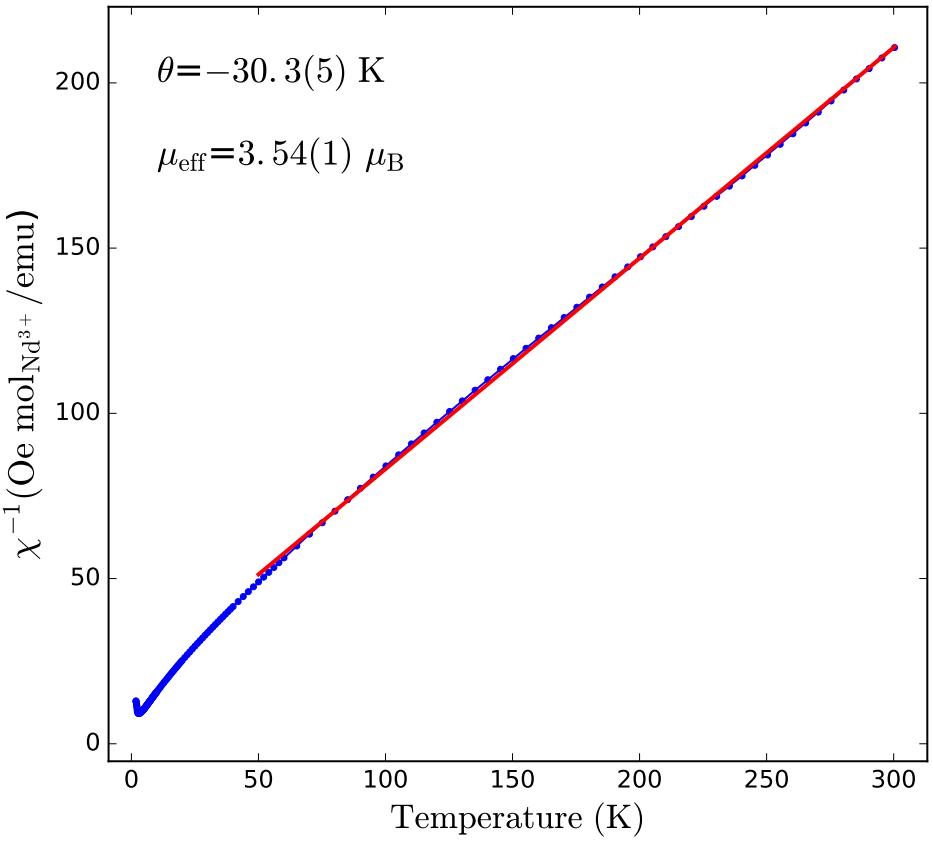

Figure 5.3: Inverse magnetic susceptibility data measured on a polycrystalline sample of $SrNd_2O_4$ from 1.8 to 300 K. The data are displayed as a blue dotted line. The magnetic transition is visible as a small inverted cusp located at about 2.8 K. The continuous red line represents the fit of the linear trend observed above 50 K, revealing the clear Curie-Weiss character of the system. The calculated Curie Weiss temperature and effective magnetic moment values obtained from the fit are respectively equal to -30.3(5) K and 3.54(1) μ_B.

20.0 kOe, see Fig. 5.4. From the data, I report the incapacity of the applied field magnitudes employed to totally suppress the low temperature magnetic transition. The transition temperature remaining rather stable up to 10.0 kOe, before significantly decreasing to ∼2.6 K for H = 20.0 kOe. When increasing the magnitude of the applied field from 10 to 20 kOe, the cusp indicative of the transition also becomes significantly broader with a significantly less pronounced decrease of the signal recorded when cooling the material under T_N.

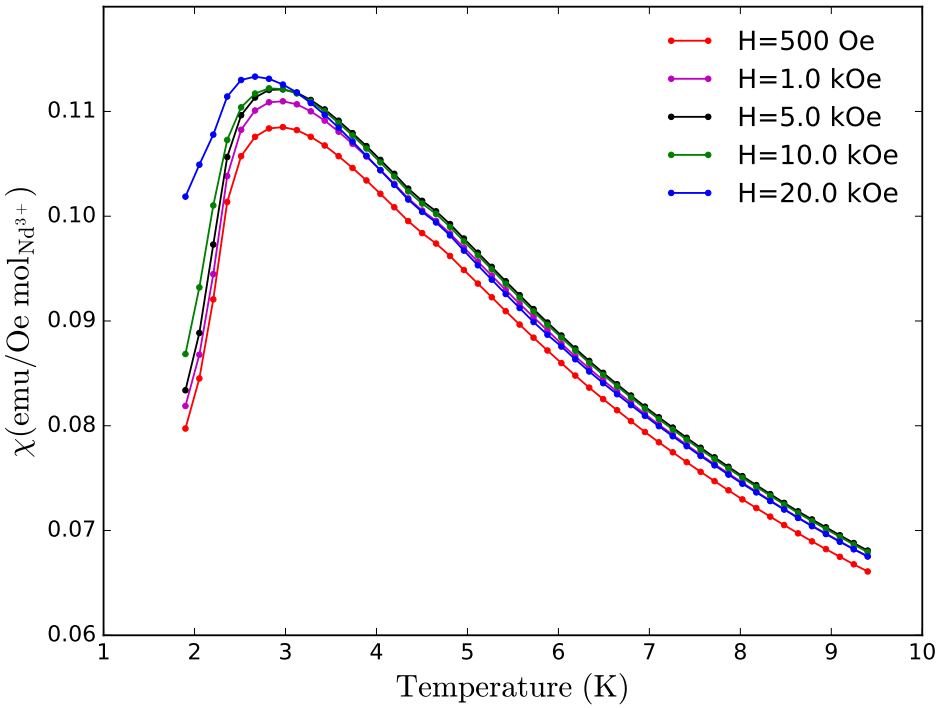

Figure 5.4: Low temperature susceptibility measured on a polycrystalline sample of $SrNd_2O_4$ under various magnitudes of applied field. Both FC and ZFC data being indistinguishable, only the later are presented on this diagram. The data reveals a reduction of the transition temperature as a function of increasing field magnitude as the tip of the cusp migrates towards lower temperature.

5.3.3 Specific heat

The specific heat of the $SrNd_2O_4$ material was measured on a polycrystalline sample using a PPMS calorimeter. The instrument was equipped with a He^3 insert, allowing it to reach 0.45 K as a minimal temperature. The sample consists of a 1.2 mg, solid, square shaped pellet of pressed polycrystalline material. A measurement of the

instrument addenda (i.e. sample platform + grease + thermometer) was carried out prior the start of the experiment for several values of applied field. In zero field conditions, data were collected from 10.5 to 0.45 K at regular temperature intervals, and subsequently remeasured while increasing the temperature back to 10.5 K. For both measurements, each data point was measured twice and an average of the two points was taken into account, increasing the measurement accuracy. Due to the clear match between both increasing and decreasing temperature trends, the two data sets have been combined and averaged, see Fig. 5.5. From the data, I report the presence of a clear lambda transition located at $T_N = 2.24$ K and corresponding to the magnetic transition previously observed in the low temperature magnetic susceptibility data, see sub-section 5.3.2. No secondary transitions are observed in the temperature region covered by these measurements. Following an interpolation of the data in the low temperature side of the diagram made possible by the addition of an artificial 0 K point, I have proceeded to the integration of the area located beneath the data points as a function of temperature. This integration returns the temperature evolution of the system's magnetic entropy, see Fig 5.5, inset. The entropy exhibits a clear asymptotic behaviour, but remains however significantly lower than the RLn2 value expected from a spin-1/2 system by 10 K. This difference reveals the retention of a significant quantity of magnetic disorder by the system down to the lowest measured temperature. The presence of remaining magnetic disorder below T_N is an effect of strong magnetic frustration, and will latter be confirmed by low temperature neutron scattering measurements. I should also note the remaining slight positive trend of the entropy at 10 K. This trend originates from the lattice vibrations becoming significant at approximately 8 K in $SrLn_2O_4$ lattices, thus contributing to the total entropy of the material above this temperature [37].

In parallel to the low temperature susceptibility measurements performed under applied field (see subsection 5.3.2), I have extended the low temperature heat capacity study by a series of infield measurements. Data were collected from 1.45 to 5.0 K under field values of 10.0, 20.0, 30.0 and 40.0 kOe, and up to 10.5 K for H = 0.0 and 60.0 kOe, see Fig. 5.6. Unlike the zero field data first presented in Fig. 5.5, the infield data were collected considering positive temperature increases only. The sample was also warmed above T_N and directly re-cooled in zero field conditions prior to each measurement, suppressing field-induced frozen states. From the data I report a clear reduction of the magnetic ordering temperature as a function of increasing field magnitudes. Furthermore, the lambda anomaly indicative of the transition becomes broader as an effect of field increase and is almost totally suppressed for H = 60.0 kOe, the highest field magnitude applied for this measurement.

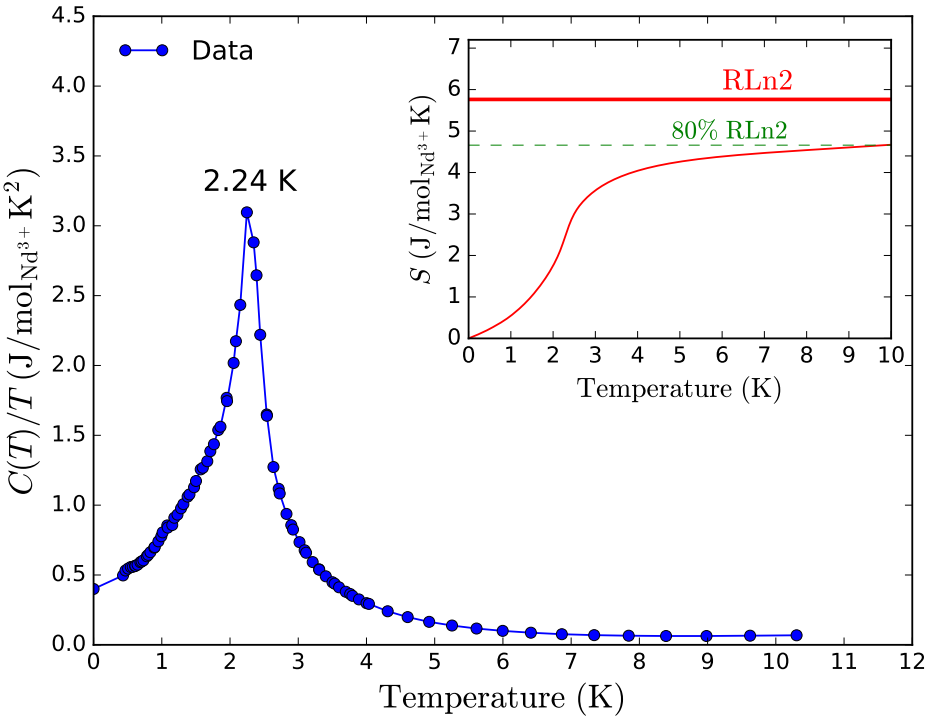

Figure 5.5: Low temperature $C(T)/T$ data collected on a polycrystalline sample of the $SrNd_2O_4$ material. The data reveal a sharp lambda transition of magnetic origin centered at $T_N = 2.24$ K. The temperature evolution of the magnetic entropy was computed by integrating over the area located beneath the $C(T)/T$ curve as a function of temperature, see figure inset. For this purpose the data were interpolated on the low temperature side by the addition of an artificial 0 K data point. The temperature evolution of the magnetic entropy reveals a clear asymptotic behaviour. The asymptote nevertheless reaches only 80% of the RLn(2) value expected for the full entropy recovery of a spin-1/2 system by 10 K. This clear difference reveals the retention of a significant quantity of magnetic disorder by the system down to the lowest measured temperatures.

The data also become significantly noisier in the transition temperature regions, revealing the magnetic instability of the system under such conditions of applied fields and temperatures. These measurements confirm the low temperature field-induced behaviour of the magnetic system previously observed from the susceptibility measurements series. The field and low temperature capacity of the PPMS calorimeter have on the other hand allowed to significantly extend the exploration of the low temperature $H - T$ magnetic phase diagram of the $SrNd_2O_4$.

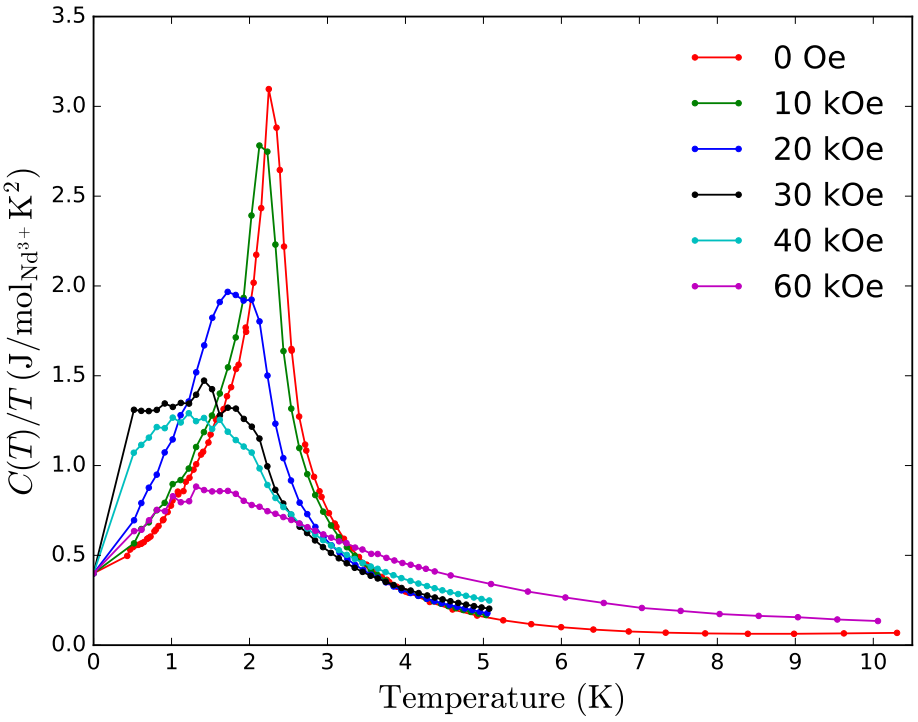

Figure 5.6: Low temperature $C(T)/T$ data measured on a polycrystalline sample of the $SrNd_2O_4$ material under different values of applied magnetic field. The data reveals a clear temperature reduction of the lambda anomaly position as well as its broadening seen as an effect of increasing field magnitudes. The transition being almost completely suppressed for H = 60.0 kOe.

The magnetic entropy recovery as a function of temperature was also computed from the data collected under different applied field values using interpolation of the data down to 0 K, see Fig. 5.7. The data reveal a clear reduction of the total entropy recoveries as a function of increasing applied field strength. Also, the "S" shaped trend of the zero field entropy recovery is progressively replaced by featureless dependencies. I have calculated that a 12% reduction of the 10 K entropy

recovery was induced by the application of a 60 kOe field onto the sample. This comparison reveals the growing proportion of remaining low temperature disorder in the material, as a function of increasing applied field magnitudes.

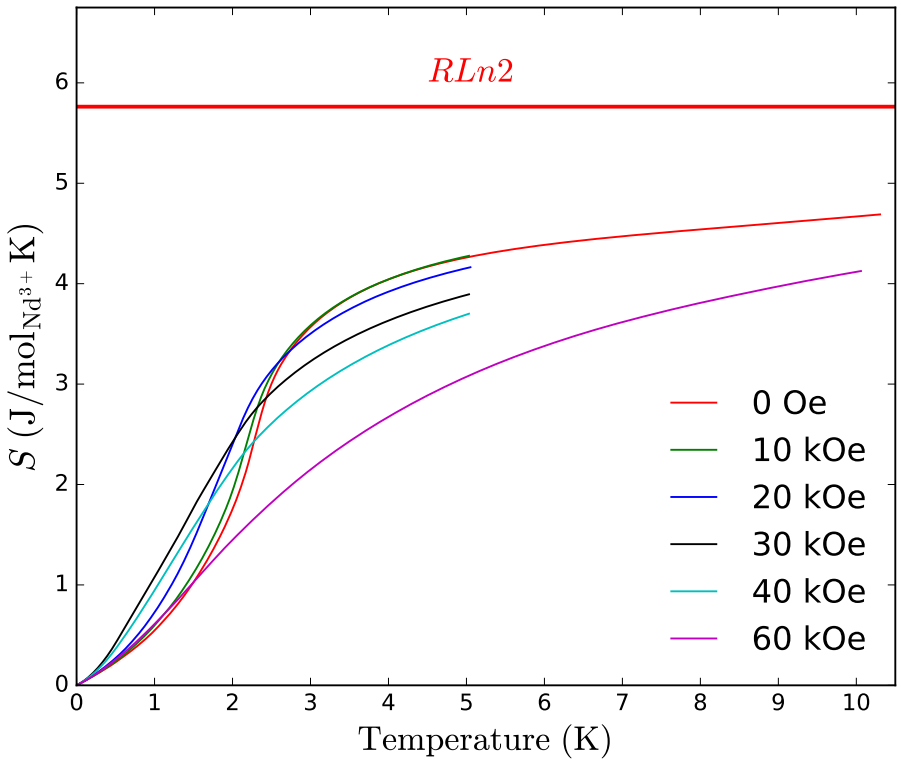

Figure 5.7: Magnetic entropy recovery of the $SrNd_2O_4$ system plotted as a function of temperature for different magnitudes of applied magnetic field. The data were obtained by integrating over the heat capacity data presented in Fig. 5.6 as a function of temperature. Interpolation of the data were performed on the low temperature side by artificially including 0 K data points. A progressive reduction of the magnetic entropy recovery is observed as a function of increasing field, revealing growing degrees of disorder in the system.

5.3.4 Magnetisation

In order to further investigate the low temperature field-induced magnetic behaviour of the $SrNd_2O_4$ material, previously sparkled by the results obtained from the heat capacity and susceptibility measurements (see subsections 5.3.2 and 5.3.3), the magnetisation properties of the material have been investigated at low temperatures. Measurements were first performed on a Vibrating Sample Magnetometer (VSM)

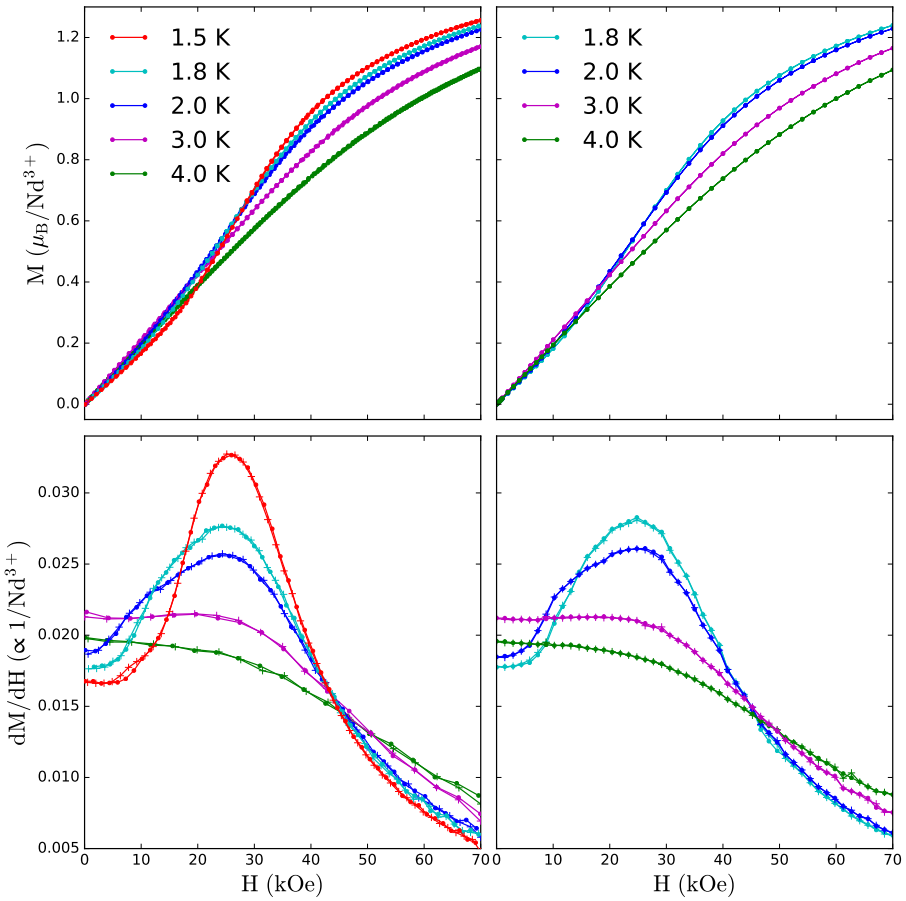

Figure 5.8: Top panels: Low temperature magnetisation measurements performed on a polycrystalline sample of the $SrNd_2O_4$ material. Data were collected under several temperature conditions in the vicinity of $T_N = 2.24$ K. The data presented on the left and right panels were collected on VSM and SQUID magnetometers, respectively. Bottom panels: Field derivative of the magnetisation data corresponding to the upper panels. The derivative of the data collected in field increasing and decreasing conditions, are respectively displayed as dots and crosses but are mostly superimposed in the investigated field range.

and subsequently repeated on a SQUID magnetometer. The SQUID device offering a significantly better accuracy than the VSM device, an appropriate scaling was applied to the VSM data for them to match with the SQUID observations.

Using the VSM device, data were collected on a 26.076 mg square shaped pellet of sintered polycrystalline material. Similarly to the susceptibility measurements performed under applied field, the use of a solid sintered sample is essential to avoid for a field-induced polarisation of the powder grains over the measurements. The sample was also properly secured with teflon tape on the measurement stick, suppressing potential field driven displacements. The SQUID measurement was performed in the same conditions as the previously described in-field susceptibility measurement (see subsection 5.3.2).

On both instruments, each data set corresponding to a particular temperature was first measured in zero field cooled conditions starting from the lowest field values, and subsequently remeasured over the field decrease, all the way back to the zero field point. Data were collected in between 0 and 70.0 kOe at 1.5, 1.8, 2.0, 3.0 and 4.0 K on the VSM device, see Fig 5.8 (top left), and at 1.8, 2.0, 3.0 and 4.0 K on the SQUID device, see Fig 5.8 (top right). Due to the high density of points measured by the VSM instrument, a ten points average was applied to the data, offering a smoothing of the observed features. At comparable temperatures, a very good agreement is returned from the data collected on the two instruments, hence allowing for the scaling of the VSM data to the data collected on the SQUID device.

As a first observation, I report a continuous increase of the high field magnetisation curve as an effect of temperature reduction. It is also clear that a full saturation of the system is not yet achieved by a field magnitude of 70.0 kOe, for any of the temperatures considered in these measurements. Although the high field asymptotic behaviour becomes more pronounced at the lowest temperatures. The magnetisation data sets collected at 3.0 and 4.0 K reveal rather featureless field dependencies. On the other hand the data sets collected at temperatures lower than 3.0 K reveal a clear "S" shaped dependence getting more pronounced as an effect of temperature reduction.

The derivatives of the magnetisation data collected on the VSM and SQUID devices are presented in the bottom, right and left panels of Fig. 5.8, respectively. The derivatives of the data collected in field increasing and subsequently in field decreasing conditions are successively represented by dots and crosses symbols. These features reveal the presence of a field driven magnetic transition observed at approximately 25 kOe for temperatures comprised between 3.0 and 1.5 K. The transition is visible as broad maxima in the field dependence of the derivatives, becoming sharper

as an effect of temperature reduction. Additionally, the derivatives corresponding to the 1.8 and 2.0 K measurements reveal the presence of a shoulder in the low field region of the transition. The shoulder position seems to be driven to higher field value as a effect of temperature reduction, before merging with the main transition maximum at 1.8 K.

5.3.5 $H-T$ phase diagram of the $SrNd_2O_4$

By determining the maxima of both specific heat and magnetisation derivative curves, I could start to recreate the $H-T$ phase diagram of the $SrNd_2O_4$ material considered in its polycrystalline form, see Fig. 5.9. By first considering the specific heat measurements performed under various field magnitudes (see Fig. 5.6), I could determine the transition temperatures corresponding to each value of applied field considered. Each of these temperatures were reported at the corresponding field positions and displayed as blue dots in the $H-T$ phase diagram. The rather linear trend obtained delimits a region of magnetic order on its low temperature side. By subsequently reporting as red dots the positions of the curve maxima revealed by the derivatives of the magnetisation measurements (see Fig. 5.8), a second transition line was brought to light. Moreover, the positions of the shoulders revealed on the low field side on the transitions by the derivative of the magnetisation measurements performed at 1.8 and 2.0 K, are displayed as green dots. The trend defined by these two points overwrites the previously described blue transition line obtained from the specific heat measurements, and reveals a net agreement between the two measurements. Hence two clear transition lines are present on the phase diagram, individually delimiting separate zones of stability for the different magnetic phases hosted by the system.

5.4 Neutron scattering investigation

The low temperature characterisation measurements performed on the $SrNd_2O_4$ material have revealed the temperature driven stabilisation of a magnetically ordered phase at 2.24 K, see section 5.3. In order to further progress in the understanding of the $SrNd_2O_4$ system and more generally of the $SrRE_2O_4$ family as a whole, it is essential to determine the nature of this magnetically ordered phase. For this purpose, powder neutron scattering techniques were employed and measurements have been performed on the two powder diffractometers D20 and D2B (ILL). The high resolution D2B diffractometer equipped with a regular orange cryostat was employed to collect high quality structural data and precisely refine the nuclear

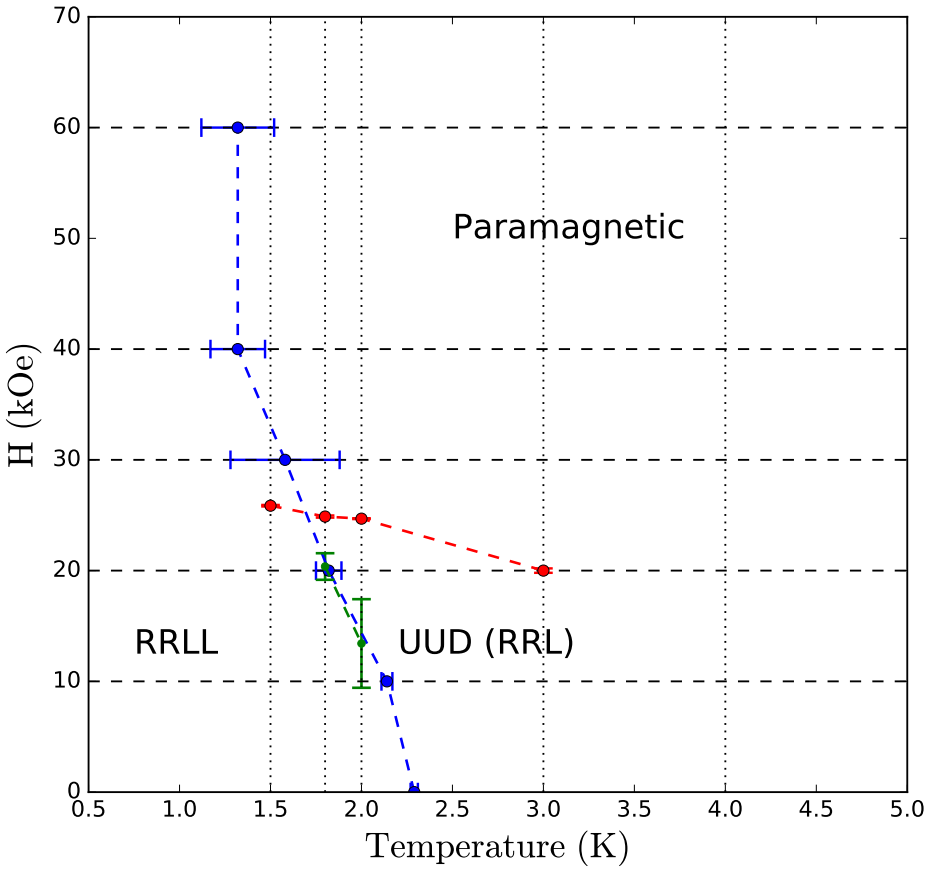

Figure 5.9: $H - T$ magnetic phase diagram of the $SrNd_2O_4$ in polycrystalline form. This diagram was constructed by combining the results obtained from both specific heat and magnetisation measurements (see Fig. 5.6 and 5.8). The associated values of temperatures and field magnitudes corresponding to transitions conditions revealed either by specific heat or magnetisation measurements are displayed as blue and red dots, respectively. Additional transition points corresponding to the shoulders revealed by the derivatives of the magnetisation curves collected at 1.8 and 2.0 K, are displayed as green dots. I suppose that the different zones defined approximately by the transitions lines could correspond with double Néel, UUD and paramagnetic phases, as labelled on the diagram. The dashed and dotted black lines represents the directions successively followed by both specific heat and magnetisation measurements, respectively.

structure of the material. The high intensity D20 diffractometer, was used to collect low temperature magnetic data in order to refine the magnetic structures stabilised below T_N. The instrument was first equipped with a regular orange cryostat and used to collect data at temperature ranging from RT to 1.6 K. The instrument was subsequently equipped with a dilution fridge cryostat enabling to reach temperatures as low as 70 mK, offering the possibility to track eventual secondary magnetic transitions. A neutron scattering investigation of the magnetic disorder present in the system and its temperature evolution across T_N was also performed. For this purpose, absolute measurements of the magnetic intensities were carried out on the D7(ILL) powder diffractometer by taking advantage of the spin polarisation analysis technique available on the instrument. Finally, a PDF analysis of the magnetic scattering signal was performed from data collected at various temperatures on the D4(ILL) powder diffractometer. Both D7 and D4 instruments were equipped with regular orange cryostats, enabling for measurements down to temperatures as low as 1.5 K.

5.4.1 Structural investigation, D20

As the starting point of a neutron scattering investigation, it is essential to verify the good chemical purity and thermal stability of the investigated sample. In addition, the high performance of the technique allows to precisely determine the structural parameters of the material. The high resolution D2B powder diffractometer was employed for this purpose. The sample was loaded in a single wall vanadium can, offering the possibility to measure diffraction patterns free of parasitic reflections. The instrument wavelength was set to 1.59 Å, granting access to an ideal reciprocal space coverage for nuclear scattering measurements. Scattering patterns were collected at room temperature and at 3.5 K using the high resolution mode of the instrument, see Fig. 5.10. From the Rietveld refinement analysis of the two data sets, I confirm the high chemical purity ($\approx 94\%$) of the sample corresponding to the $SrNd_2O_4$ material crystallising according to the *Pnam* space group. The nuclear crystallographic parameters of the $SrNd_2O_4$ material, obtained from the two refinement analyses are reported in table 5.2, along with a set of parameters obtained from data collected below T_N on the D20 instrument. Despite a slight shrinkage of the lattice parameters, the Rietveld analyses confirm the structural stability of the material over temperature reductions, and in particular over the magnetic ordering transition.

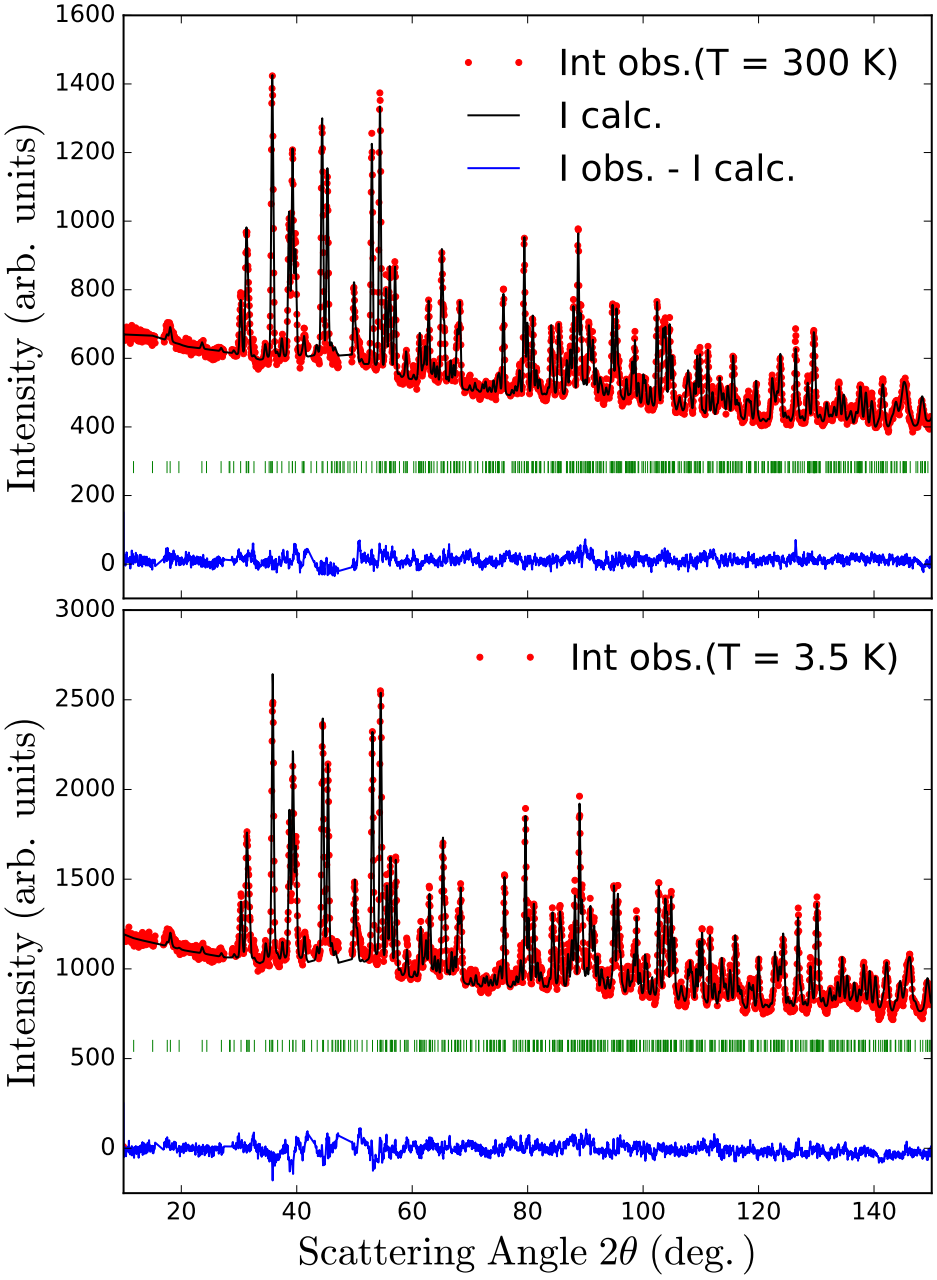

Figure 5.10: $SrNd_2O_4$ refined PND patterns collected at RT (top panel) and at 3.5 K (bottom panel), on the D2B instrument operated in high resolution mode with a wavelength of 1.59 Å. Measured intensities, fitted profile and their relative difference are displayed in red, black and blue, respectively. All space group allowed reflection positions are displayed as green vertical lines.

	D2B RT		D2B 3.5 K		D20 1.6 K	
Ions	x	y	x	y	x	y
Sr	0.7449(3)	0.6469(2)	0.7470(3)	0.6472(3)	0.7478(6)	0.6467(5)
Nd1	0.4335(3)	0.1175(2)	0.4332(3)	0.1164(2)	0.4312(5)	0.1164(4)
Nd2	0.4063(2)	0.6088(2)	0.4074(3)	0.6098(2)	0.4083(5)	0.6106(4)
O1	0.2235(3)	0.1892(3)	0.2221(4)	0.1889(3)	0.2186(7)	0.1911(5)
O2	0.1391(3)	0.4900(3)	0.1386(4)	0.4874(3)	0.1411(6)	0.4894(6)
O3	0.4980(4)	0.7844(3)	0.4943(4)	0.7847(3)	0.4940(6)	0.7884(5)
O4	0.4346(5)	0.4173(3)	0.4316(5)	0.4168(3)	0.4289(7)	0.4196(4)
a	10.1516(2)		10.1287(2)		10.1001(5)	
b	12.2051(2)		12.1781(5)		12.1445(5)	
c	3.5707(1)		3.5641(1)		3.5540(2)	

Table 5.2: Crystallographic parameters of the $SrNd_2O_4$ material crystallising according to the orthorombic *Pnam* space group. All ions are sitting at the 4*c* Wyckoff positions of general coordinates: x, y and 0.25 on the unit cell basis. The structural parameters and ionic positions were obtained from the Rietveld refinement analysis of neutron powder diffraction data collected on a the D2D and D20 diffractometers at RT, 3.5 K and 1.6 K.

5.4.2 Low temperature magnetic scattering, D20

A complete temperature evolution study of the magnetic scattering properties of the $SrNd_2O_4$ material was performed by measuring a series of scattering patterns at various temperatures, in the vicinity of T_N. These measurements were carried out on the D20 diffractometer equipped with a regular orange cryostat. The polycrystalline sample was loaded in a vanadium single wall can, allowing for the collection of diffraction patterns free of parasitic reflections. The instrument wavelength was set to 2.41 Å, offering a proper access of the magnetic Bragg peaks located in the low-Q region of the reciprocal space. Under these conditions, scattering patterns have been collected at 10.0, 5.0, 2.5, 1.9 and 1.6 K, in addition to high temperature patterns collected at 20.0 and 50.0 K. The 50.0 K nuclear pattern was subtracted from the low temperatures data sets, allowing for a direct isolation of the magnetic scattering intensities from the raw signal. The superimposition of the magnetic intensities collected between 10.0 and 1.6 K reveals the stabilisation of sharp magnetic Bragg reflections below 2.5 K, disclosing the stabilisation of a long range type of magnetic order in the system, see Fig. 5.11. Although, the first signs of weakly correlated short range types of magnetic orders appeared at approximately 10 K in the system, visible as very broad feature of low intensity centered at $\sim 25°$. By 5 K, the broad diffuse scattering feature is only slightly more intense than the 10 K observations. At 2.5 K

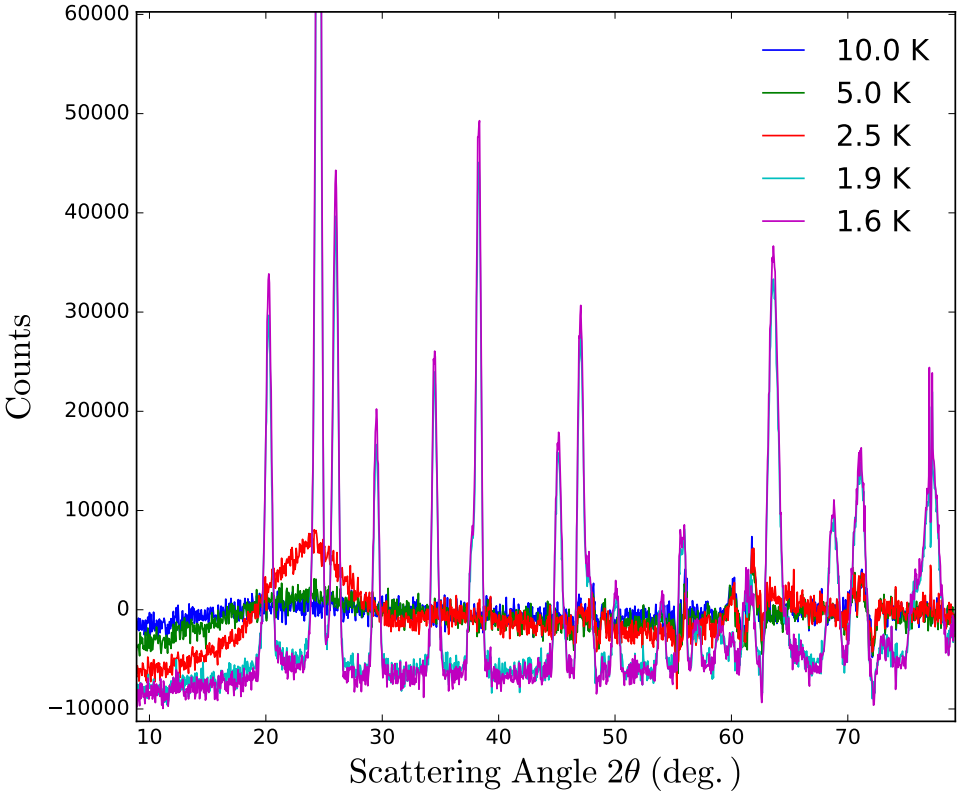

Figure 5.11: Temperature evolution of the magnetic scattering signal collected on a polycrystalline sample of the $SrNd_2O_4$ material. The data were collected on the D20 powder diffractometer (ILL) equipped with a regular cryostat and with a neutron wavelength of 2.41 Å. The magnetic signal was isolated from the raw data by subtraction of a 50 K nuclear background. The negative counts being displayed in the low scattering angle region result from the presence of diffuse magnetic scattering signal in the nuclear background data set inducing a slight over subtraction. The data reveal the successive stabilisation of short and long-range ordered magnetic phases. Diffuse magnetic signal remains visible in the low scattering angle region of the patterns collected below $T_N = 2.24$ K.

however, in the vicinity of the Néel temperature, an intense diffuse scattering signal is measured revealing a significant increase of the magnetic correlations inducing a higher degree of order in the system. From the data collected below T_{N}, at 1.9 and 1.6 K, I report the replacement of the large diffuse scattering feature observed at 2.5 K by sharp magnetic Bragg peaks, announcing the establishment of a long-range type of magnetic order in the system. Nevertheless, a small but significant quantity of diffuse signal remains present in the data below T_{N}, disclosing the retention of a significant quantity of magnetic disorder by the system. This remaining signal is mainly visible in the low scattering angle region of the scattering patterns, and slightly diminishes between the data collected at 1.9 and 1.6 K. Despite these tiny changes observed between the patterns collected below T_N, I confirm the stability of the long-rang magnetic order as well as the absence of further magnetic transitions down to 1.6 K.

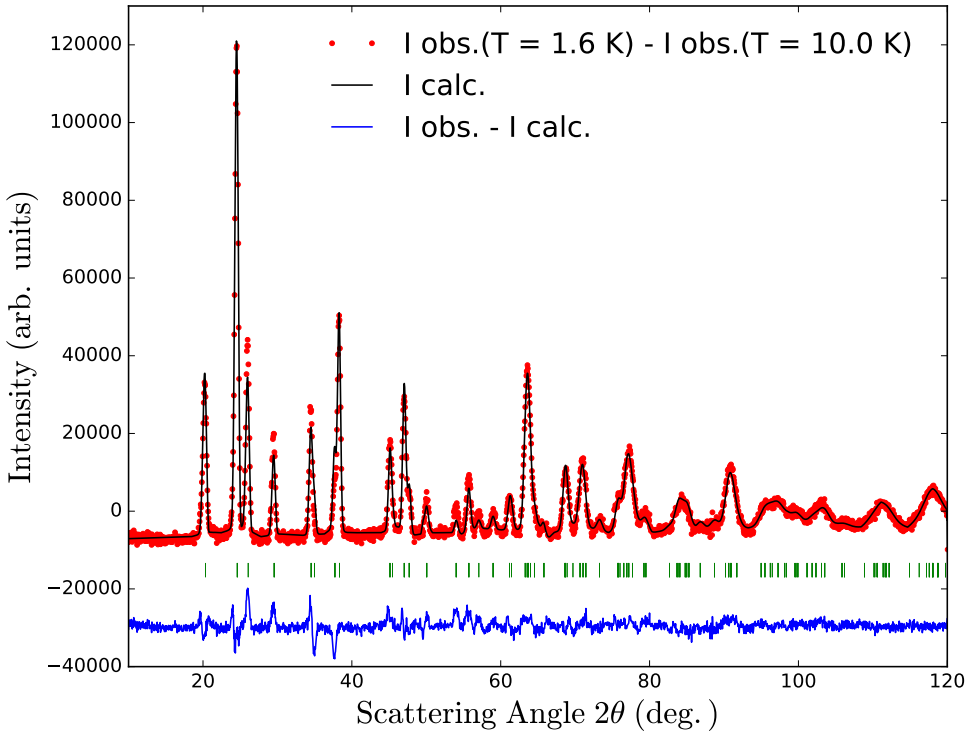

Figure 5.12: $SrNd_2O_4$ magnetic signal collected at 1.6 K on the D20 diffractometer and isolated from the row data by direct subtraction of a 10 K background. Data, fit and their relative difference are displayed in red, black and blue, respectively. The $\mathbf{k}$ = (0, 0.5, 0.5) symmetry allowed magnetic reflections positions are marked by vertical green lines.

In order to determine the nature of the long-range magnetic order stabilised below T_N, a Rietveld refinement analysis of the magnetic signal collected at 1.6 K was carried out after subtraction of a 10 K background. A 50.0 K background subtraction would not allow for a proper refinement analysis of the magnetic data. In fact, both the shape and height of the magnetic reflections are influenced by tiny intensity subtraction issues, induced by the slight shrinkage of the nuclear unit cell as an effect of temperature reduction. It is however absolutely fine to consider the 10.0 K data set as the nuclear background for this analysis despite the weak magnetic diffuse signal contained in the data. In fact, the Rietveld refinement analysis performed on the resulting magnetic signal only considers the Bragg peaks absolute intensities and shapes, thus any over-subtraction of diffuse features will be accommodated by the data treatment when specifying the background profile of the pattern.

As a first step in the process, the magnetic phase propagation vector $\mathbf{k} = (0, 0.5, 0.5)$, was determined from the relative position of both magnetic and nuclear reflections. This task was fulfilled with the help of the k-search program [55]. From the knowledge of the parent space group symmetry and of the propagation vector, an irreducible representation analysis of the magnetic symmetry (see section 3.6) was carried out using the program BasIreps [55], see Appendix A.2.2. The analysis returns two possibilities referred as Γ_1 and Γ_2, each of them considering six basis vectors, see Table 5.3. By consecutively employing the two Γ models to refine the magnetic data, I report in both cases the same excellent agreement obtained between data and fits (R Bragg factors equal to 10.62 and 10.73, respectively for Γ_1 and Γ_2). Identical structures are returned from the two refinements, revealing a double Néel (rrll) order solely established on a single type of Nd site and constrained within the crystallographic *ab*-plane of the material, see Fig. 5.13. The choice of the Gamma model however, selectively attributes the long range order to a particular Nd site. Hence, the magnetic order will be individually attributed to site Nd1 and site Nd2, by respectively employing Γ_1 and Γ_2 models. Furthermore, the long-rang order being only established on a single type of Nd sites reveals that half the number of magnetic moments are in a largely disordered state. Hence confirming the presence of magnetic disorder persisting in the system below T_N, as previously suggested from the specific heat data (see subsection 5.3.3).

The structural specificity of the long range magnetic order stabilised by the $SrNd_2O_4$ material below T_N, also reveals clear antiferromagnetic inter-ladders correlations. This characteristic is easily appreciated across the hexagons off-diagonal directions of the magnetic sub-lattice, or by viewing the structure along the *a* di-

Symmetry operations		BsV(1)	BsV(2)	BsV(3)	BsV(4)	BsV(5)	BsV(6)
x,y,z	Re	100	010	001	000	000	000
	Im	000	000	000	-100	0-10	001
-x,-y,z+1/2	Re	000	000	000	-100	0-10	00-1
	Im	100	010	00-1	000	000	000
-x+1/2,y+1/2,z+1/2	Re	100	0-10	00-1	000	000	000
	Im	000	000	000	-100	010	00-1
x+1/2,-y+1/2,z	Re	000	000	000	-100	010	001
	Im	100	0-10	001	000	000	000

Table 5.3: Symmetry operations and basis vectors of the Γ1 irreducible representations. This representation corresponds to the symmetry of the k=(0,0.5,0.5) modulated magnetic phase stabilised below $T_N = 2.24$ K on the $SrNd_2O_4$ crystalline structure. The Γ2 counterpart is simply obtained by using opposite signs for the basis vector coefficients corresponding to the third and forth symmetry operations (the two bottom rows), see Appendix A.2.2.

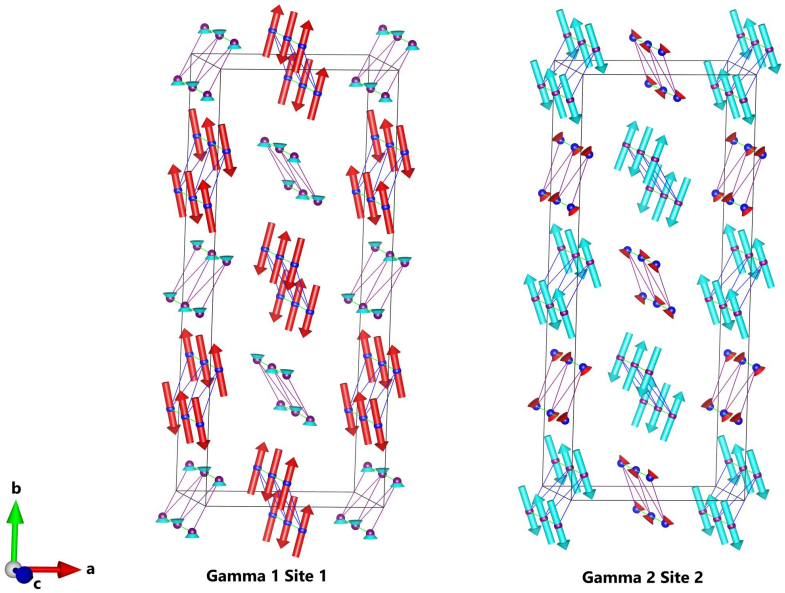

Figure 5.13: 3D geometrical representations of the magnetic structures stabilised by the $SrNd_2O_4$ material below T_N. The two structures represented were obtained by subsequently considering the Γ1 and Γ2 representations, individually attributing the long range order to a site Nd1 and site Nd2, respectively. The two magnetic structures are superimposable implying appropriate translations and rotations.

rection, see Fig. 5.14. This symmetry specificity could suggest the presence of an antiferromagnetic inter-ladder exchange interaction acting over the system, as already suggested from the study of $SrEr_2O_4$ [33], and of $SrDy_2O_4$ [27, 28]. Moreover, the influence of dipolar interactions over the inter-ladder ordering was ruled out from the computation of a model involving the NN, NNN and the shortest inter-ladder distances. The calculated dipolar energy reduction of 0.024 K induced by the inter-ladder antiferromagnetic ordering stands negligible in front of the ordering temperature of the material supporting the action of an exchange interaction.

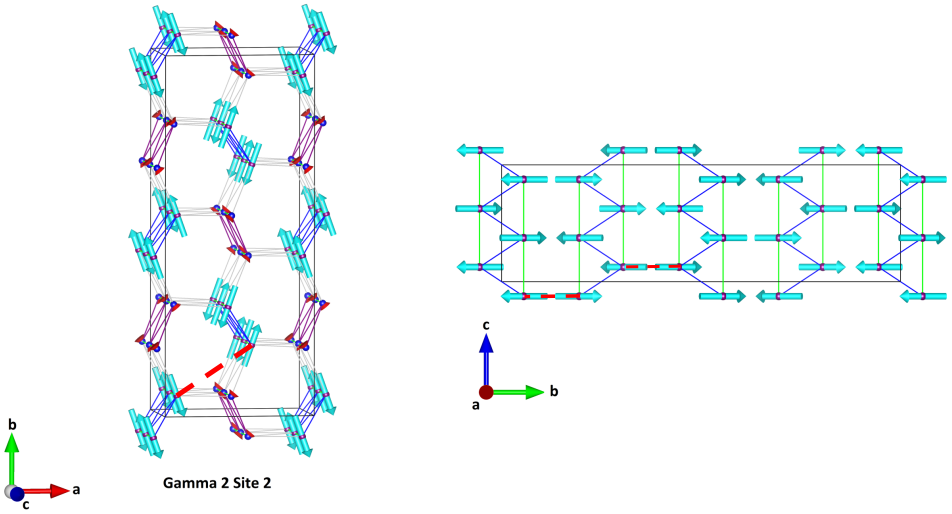

Figure 5.14: Representation of the magnetic structure stabilised by the $SrNd_2O_4$ material when viewed along the c (left) and a (right) axes. These representations allow for a clear visualisation of the inter-ladder antiferromagnetic ordering stabilised by the long range ordered phase. The inter-ladder exchange interactions suspected to induce this ordering are displayed as red dashed lines.

The results of the Rietveld refinement analysis carried out using subsequently the two irreducible representations, returned in both cases a magnitude of about 2 μ_B for the magnetic moments sitting on long range ordered site. Slightly less than 0.5 ordered Bohr magnetons are returned on the other site, remaining mainly disordered below T_N, see Table 5.4. This rather small ordered component established on the principally disordered site has been clearly evidenced by the Rietveld refinement analysis and hence should not be neglected. In fact, considering refinements of the data in the Γ_1-site Nd1 or Γ_2-site Nd2 configurations when fixing the value of the tiny ordered moment to zero respectively on site 2 and site 1, will increase

	m(a)		m(b)		Mtot	
	1.6 K	0.07 K	1.6 K	0.07 K	1.6 K	0.07 K
Nd1	0.44(2)	0.80(6)	1.900(5)	1.86(2)	1.95(2)	2.02(6)
Nd2	0.01(2)	0.34(7)	0.28(1)	0.32(4)	0.28(2)	0.47(8)

Table 5.4: Refined magnetic moments components of the magnetic structure stabilised below 2.24 K on the $SrNd_2O_4$ material. The magnitudes of the parameters are given in Bohr magnetons. The magnetic phase consists of a long range double Néel order constraining the magnetic moment within the *ab*-plane of material. The long range ordered phase was in the present case, arbitrarily attributed to the first Nd site, and can be swapped to the second site with equal probability. The parameters were obtained from Rietveld refinement analyses of data collected at both 1.6 (left columns) and 0.07 K (right columns).

the R Bragg to a value of about 13. Furthermore, a refinement analysis considering simultaneously the two Γ_1 and Γ_2 models, respectively established on site 1 and 2, including that the moments components are forced to be the same on both sites, also returns a R Bragg value of 13. These two geometrical configurations returning the same statistical weight, one cannot be preferred to the other. This argument legitimises the configuration including the presence of a small ordered component established on the principally disordered site returning the best goodness of fit.

Due to the large amount of magnetic disorder remaining in the system below T_N, in addition to the presence of a partially ordered phase established on one of the two magnetic sites, additional ordering transitions are possible in the yet unexplored milli-Kelvin region of the magnetic phase diagram. Up to this point, the lowest temperature investigation of the material was performed on the PPMS calorimeter, revealing the absence of specific heat anomalies in between T_N and 0.5 K (see subsection 5.3.3). In order to track any eventual magnetic transitions between T_N = 2.24 K and the lowest temperatures, I have collected additional scattering patterns at 1.0, 0.3 and 0.07 K on the D20 instrument. To cool the sample down to these temperatures, the instrument was equipped with a dilution fridge cryostat, and the sample loaded in a Cu sample can ensuring proper thermal conductivity and sample thermalisation. The scattering pattern collected at 0.07 K (the lowest measured temperature) has been superimposed to the patterns collected at 1.6 and 50 K, i.e. at a higher temperature below T_N, and at a temperature highly above T_N, see Fig. 5.15. Since, the 1.6 and 50 K data were collected in the same instrumental conditions they could directly be compared. However, an appropriate scaling had to be considered for a comparison with the 0.07 K data. The difference between on one hand the data collected below T_N, and on the other hand the 50 K pattern,

reveals the magnetic scattering intensities produced by the long range ordered phase. Despite a clear background mismatch appearing at $2\theta = 30°$ induced by the different instrumental conditions employed for the measurements, I report a clear agreement between the two magnetic patterns. This agreement reveals the stability of the magnetic system in between T_N and 0.07 K, and thus the absence of additional ordering transitions taking place in the system below T_N.

In order to appreciate the temperature evolution of the magnetic moments below T_N, a Rietveld refinement analysis was performed on the raw data collected at 0.07 K. This analysis was executed considering the simultaneous refinement of both nuclear and magnetic phases, in addition to the Cu phase (sample container) responsible for the presence of intense Bragg reflections seen on the diffraction pattern. An excellent agreement has here also been obtained between data and fit by considering both Γ_1 on site Nd1 or Γ_2 on site Nd2 configurations, confirming the temperature stability of the magnetic phase down to 0.07 K, see Tables 5.4. The comparison of the refinements results obtained at 1.6 and at 0.07 K suggests a tiny increase of the refined magnetic moments magnitude, and by consequent of the degree of magnetic order as an effect of temperature reduction. Although higher uncertainties have been returned from the 0.07 K refinement.

Considering the symmetry of the magnetic phase, the presence of magnetic domains is also expected to partition the sample grains. In fact, the equivalence between the propagation vectors **k** and -**k**, allows for the formation of two magnetic domains in equal proportions [39]. The magnetic configurations corresponding to the two domains are obtained one from another by flipping the horizontal orientations of the spins attached to a single leg of each triangular ladder, resulting into two energy equivalent magnetic configurations. The nuclear structure of the $SrLn_2O_4$ material is invariant when seen along a or $-a$ directions, and the two domains structures can be observed by successively orienting the structure according to these two directions, see Fig. 5.17. The stabilisation of two equally represented magnetic domains in the sample, can however not be confirmed due to mutual indistinguishably to Rietveld refinement analysis.

5.4.3 Low temperature polarised neutron scattering, D7

The temperature evolution of the magnetic scattering signal was also investigated using the neutron spin polarisation technique on the D7 diffractometer(ILL). The spin polarisation analysis of neutron scattering data also known as the 'xyz'-polarisation analysis, allows for an absolute separation of the different components of the scattering signal by selecting the scattered neutrons according to their spin directions [62].

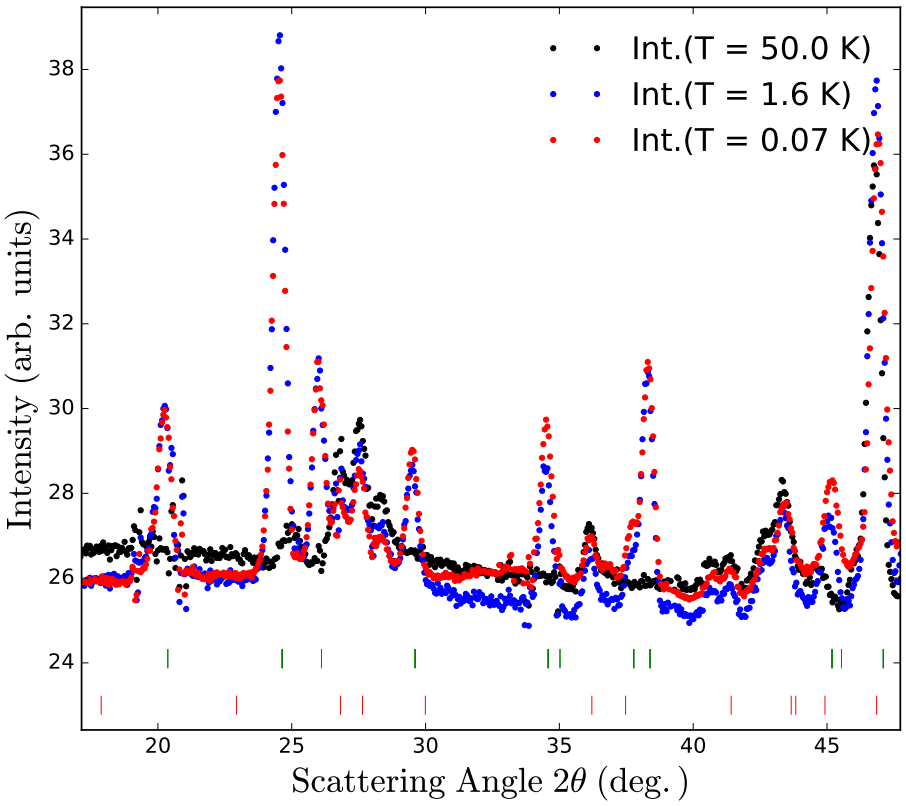

Figure 5.15: Neutron powder scattering patterns collected on a polycrystalline sample of the $SrNd_2O_4$ material at 50 (black), 1.6 (blue) and 0.07 K (red). The 50 K patterns represents the nuclear scattering contributions to the signal in the displayed 2θ region. The vertical green and red lines symbols mark the magnetic and the nuclear allowed Bragg peak positions, respectively. Despite a significant background mismatch induced by the special instrumental conditions employed for the lower temperature measurement, a very good agreement is returned between the magnetic intensities of the 1.6 and 0.07 K patterns. Such an agreement reveals the stability of the magnetic order down to the lowest temperatures, as well as the absence of second ordering transitions occurring below $T_N = 2.24$ K.

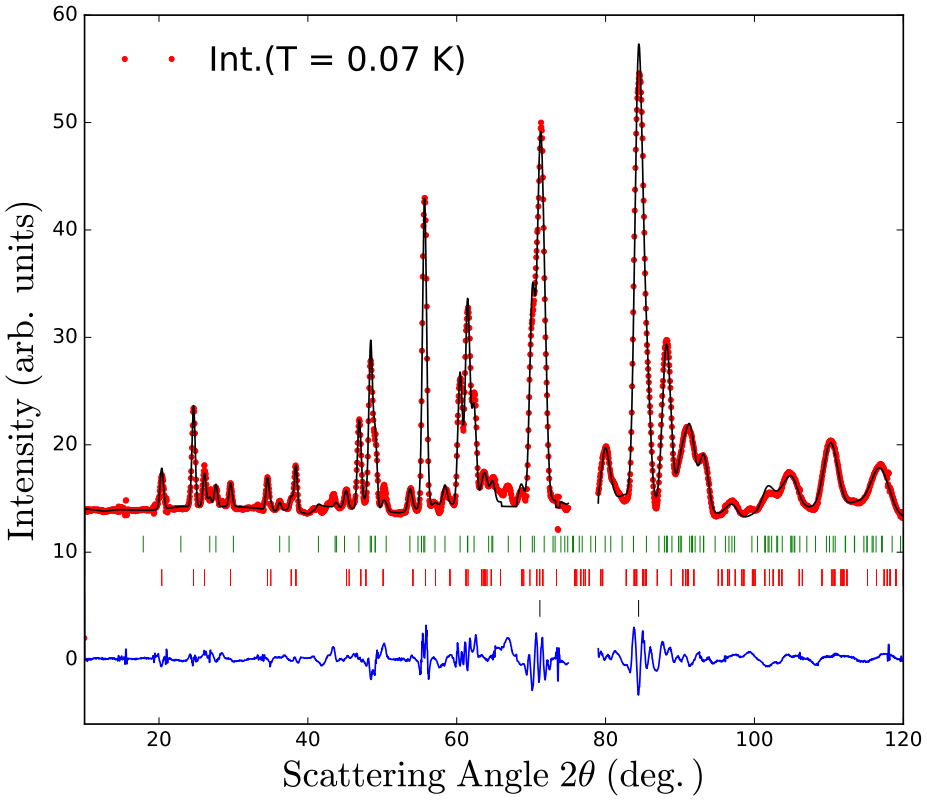

Figure 5.16: $SrNd_2O_4$ neutron scattering pattern collected at 0.07 K on the D20 diffractometer equipped with a dilution fridge cryostat and using a 2.41 Å monochromatic beam. Both nuclear and magnetic intensities are present in the data. The observed most intense reflections are produced by the Cu made sample container used for the measurement. Data, fit and their relative difference are displayed in red, black and blue, respectively. The symmetry allowed magnetic, nuclear and Cu nuclear reflections positions are respectively marked by vertical green, red and black lines.

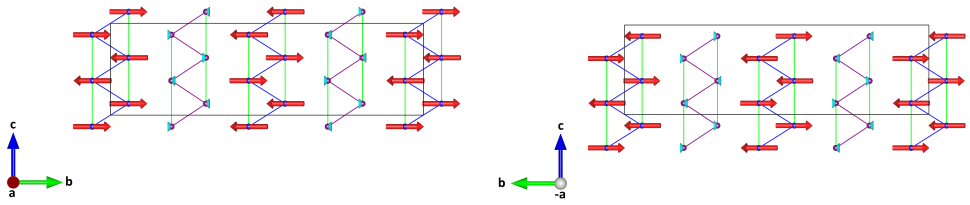

Figure 5.17: Structural representation of the two magnetic domains corresponding to the magnetic phase stabilised by the $SrNd_2O_4$ material. On the two representations, the magnetic order established on the right legs of each individual ladders stay unchanged, the left leg spin arrangement is however inverted.

An accurate visualisation of the magnetic diffuse features of low intensities is made possible by this technique, offering the possibility to investigate the magnetic disorder evolution while cooling the material across T_N with high precision. In comparison, the high temperature background subtraction technique used to extract the magnetic intensities from the D20 scattering patterns, induces an over-subtraction of the low intensity diffuse signal by neglecting the paramagnetic background present in the high temperature data set. This background over-subtraction is in particular revealed by the negative intensities obtained in the low-Q region of the magnetic patterns, see Fig. 5.11.

The instrument wavelength was set to 3.14 Å, enabling access to the reciprocal space low-Q region were the magnetic signal is intense. Scattering patterns were collected at 20, 3.0 and 1.5 K, the corresponding magnetic intensities were extracted from the raw data via spin polarisation analysis, see Fig. 5.18. I report the presence of clear diffuse features measured at the three different temperatures.

The rather flat Q dependence of the 20 K signal is interpreted as a combination between, on one hand the magnetic cross-section of the material in a paramagnetic state [49], and on the other hand a broad low intensity diffuse feature, see Fig. 5.19. The magnetic cross-section follows the cosine decrease trend of the magnetic form factor (see eqns. 3.37 and 3.38), with a calculated $Q(0)$ amplitude of 0.77 Barns/(Ste.f.u.). In order to compensate for the Q dependence of the magnetic cross-section, the low-Q values of the diffuse scattering feature must be of very low intensity and progressively increase as a function of Q, resulting in the flat dependence observed. This result reveals the presence of active magnetic correlation acting over the system already at 20 K.

By 3.0 K, a large diffuse feature is stabilised in the low-Q region of the pattern. The diffuse feature being very weak at the lowest Q values, it undergoes a

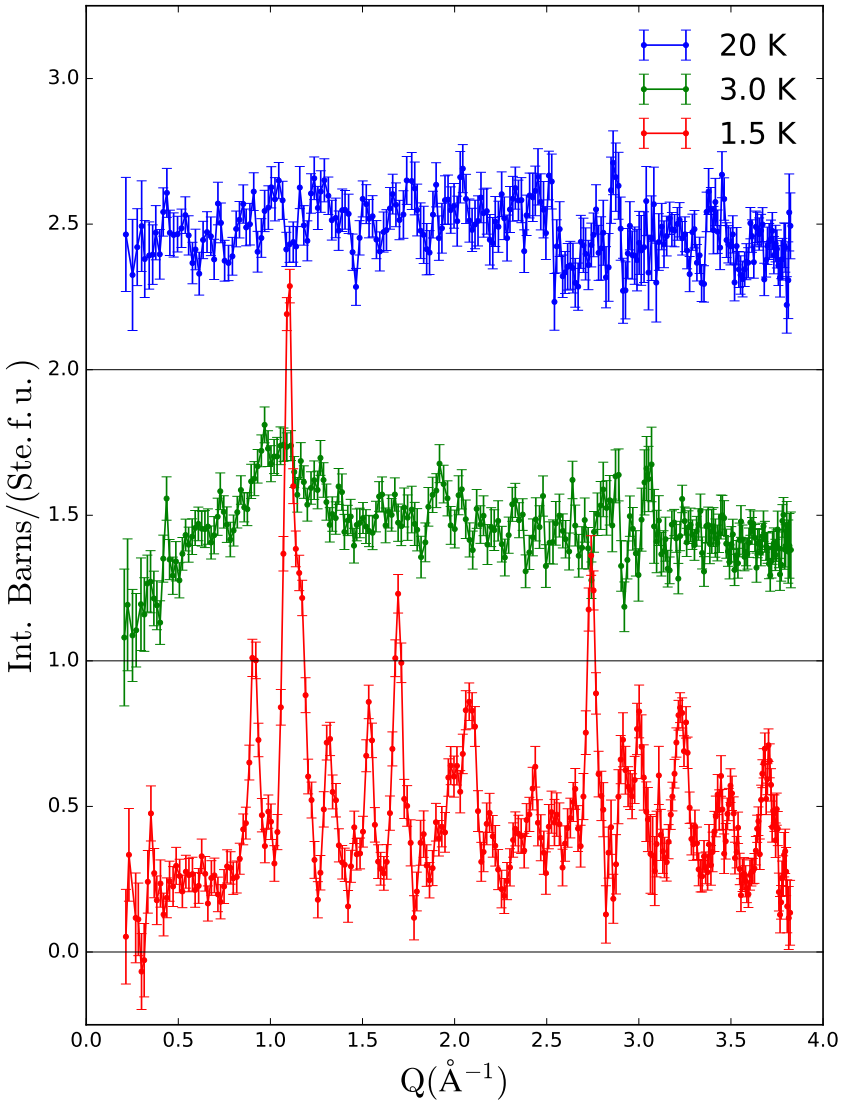

Figure 5.18: Temperature evolution of the magnetic scattering signal of the $SrNd_2O_4$ collected on the D7(ILL) instrument at 20 (blue), 3.0 (green) and 1.5 K (red). Spin polarisation analysis was employed to isolate the magnetic scattering patterns from the raw data and the displayed intensities (Int.) are normalised per steradian and per formula unit (Ste.f.u.). For clarity, intensity shifts were considered between the different data sets. The zero of each pattern being presented by a continuous black line. Diffuse signal is observed in the three displayed data sets, revealing both the presence of active correlations at 20 K and the retention of magnetic disorder below $T_N = 2.24$ K.

strong increase as a function of Q and forms a broad peak centered at $Q = 1$ Å^{-1}. This localised diffuse feature reveals the action of strong magnetic correlations competing in the system for the stabilisation of different magnetic phases.

The lowest temperature measurement was performed at 1.5 K, i.e. below the magnetic ordering transition. Despite the appearance of intense Bragg peaks produced by the long range magnetic order, I report a clear reduction of the diffuse scattering signal located in the low-Q region of the scattering pattern. Nevertheless, a clear diffuse component of the signal remains visible on the scattering pattern.

Integrating over the measured intensity as a function of Q reveals that 66% of the diffuse signal measured at 20 K, remains present in the data at 1.5 K, see Fig 5.20. This result confirms the retention of a large amount of magnetic disorder by the system, coexisting with the long-range ordered phase below $T_{\mathrm{N}} = 2.24$ K.

5.4.4 Magnetic PDF analysis, D4

To conclude the neutron scattering investigation of the $SrNd_2O_4$ material, I would like to present results obtained via magnetic Pair Distribution Function (mPDF) analysis of the magnetic scattering signal collected on the D4(ILL) neutron powder diffractometer. This rather unexploited data analysis technique is employed in the context of this thesis project for one of the first times. The mPDF signal, also known as the real-space correlation function is obtained by Fourier transformation of the magnetic scattering signal. The technique applies to the total magnetic scattering signal, i.e. principally to both sharp and diffuse features produced by the long and short range ordered magnetic phases, respectively. The quasi-instantaneous nature of the mPDF profile obtained by this technique offers a real-space picture of both long (static) and short range (dynamic) types of magnetic correlations, displayed as a function of relative ionic distances. Certain short range correlations can directly be associated with particular features of the magnetic phase being stable in the system in the conditions of the experiment [77].

The D4 powder diffractometer instrument is specially optimised to collect scattering intensities over large Q ranges. For this purpose, the instrument receives a short-wavelength neutron beam produced by the hot source of the ILL reactor. In addition, the large detector bank of the instrument is able to rotate around the sample in the horizontal scattering plane, maximising the detection angle coverage. The D4 diffractometer is thus perfectly suited to measure large magnetic scattering patterns being ideal for mPDF analyses.

For the measurements, the instrument wavelength was set to 0.5 Å and the sample loaded in a single wall vanadium can. Scattering patterns were collected

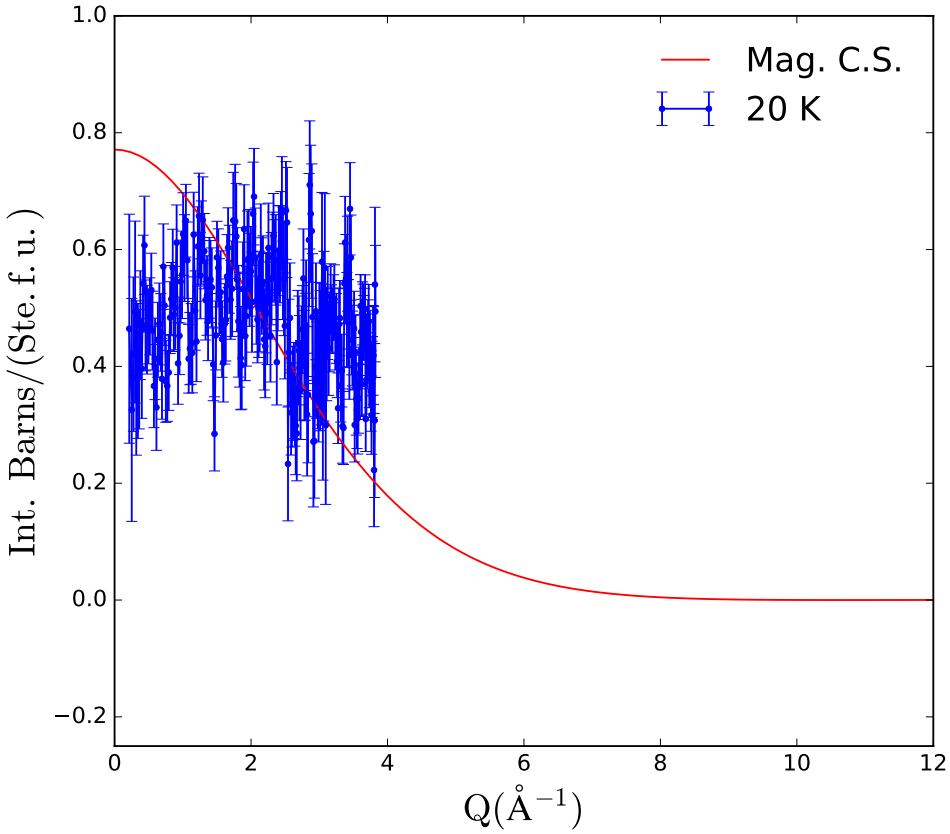

Figure 5.19: Q dependence of the magnetic cross-section corresponding to a formula unit of the $SrNd_2O_4$ material in a paramagnetic state (red), see eqns. 3.37 and 3.38. Magnetic scattering signal collected at 20 K on the D7 neutron diffractometer (blue). The measured signal is interpreted as a combination between the paramagnetic cross-section and a low intensity diffuse feature.

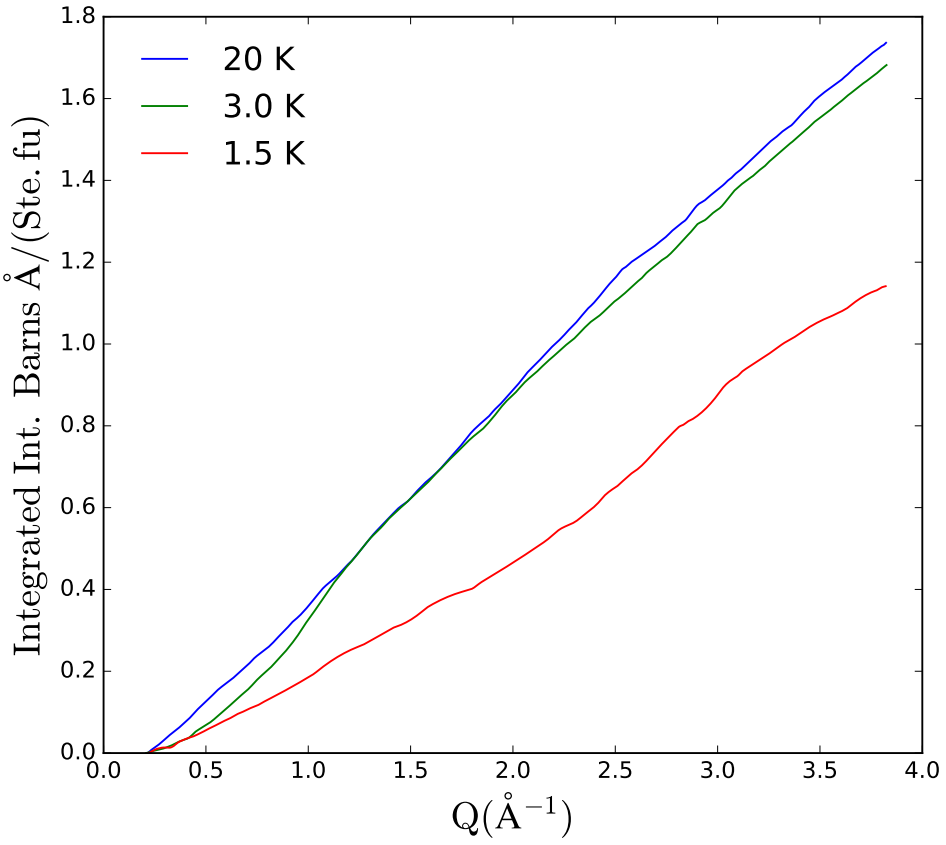

Figure 5.20: Integration of the $SrNd_2O_4$ diffuse magnetic patterns as a function of Q (magnetic Bragg peaks were not considered for the integration below T_N). The integrated patterns were collected on the D7 neutron diffractometer and correspond to the features presented in Fig. 5.18. The result reveals a 34% reduction of the integrated diffuse signal induced by the magnetic transition, confirming the presence of a large amount of magnetic disorder remaining in the system below $T_N = 2.24$ K.

at 20, 10, 4.1 and 2.2 K, in addition to a 50 K nuclear background, see Fig. 5.21. The magnetic patterns were isolated from the raw data using the high temperature nuclear background subtraction method, also previously employed on the D20 scattering data (see subsection 5.4.2). Despite the rather low-Q resolution of the instrument, the temperature evolution of the signal clearly reveals the stabilisation of broad diffuse features above T_N, progressively gaining intensity and sharpness over the magnetic long range ordering transition.

The mPDF functions corresponding to the magnetic patterns collected at 20, 10, 4.1 and 2.2 K were computed via Fourrier transformation, see Fig. 5.22. Their superposition on a single diagram reveals the significant evolution of the system as it is cooled through T_N. The particularly contrasting mPDF profiles obtained at 20, 10, and 4.1 K, expose the competitions of different sets of magnetic interactions successively influencing the system over the cooling procedure. Also, a significant increase of the features magnitudes is seen when cooling the sample through T_N, as a consequence of long range order establishment in the system. Due to the presence of both long and short range type of order coexisting under T_N, dynamic and static types of correlations populate the 2.2 K profile, being respectively visible as strong and weaker peaks. Relatively strong correlations however, start to stand out already in the 4.1 K profile. These dynamic correlations being induced by the small amount of short range order starting to correlate the system at temperatures preceding the transition. In particular, a strong negative peak is visible at $\sim$3.55 Å, and corresponds to the antiferromagnetic ordering of the spins propagating along the chains directions. The dominance of this peak over the 4.1 and 2.2 K profiles, reveals the leading character of first neighbours antiferromagnetic interactions acting along the chains in the $SrNd_2O_4$ system. As expected a second major peak stands at $\sim$7.1 Å, i.e. at twice the previous distance. This peaks thus corresponds to the ferromagnetic configuration of second neighbours along the chains directions. The difference of magnitude observed between these two major peaks reveals a net reduction of the correlations as an effect of increasing spin distances in the system. Moreover, I believe an additional negative peak located at $\sim$6.2 Å to correspond with the principally antiferromagnetic inter-ladder ordering stabilised by the long range ordered phase across the off-diagonal directions of the hexagons, as previously described (see subsection 5.4.2 and Fig. 5.14). Beyond these interesting observations, it is difficult to attribute other correlations to particular components of the long range ordered magnetic structure, mainly as a consequence of the growing numbers of Nd-Nd distances corresponding with these correlations distances.

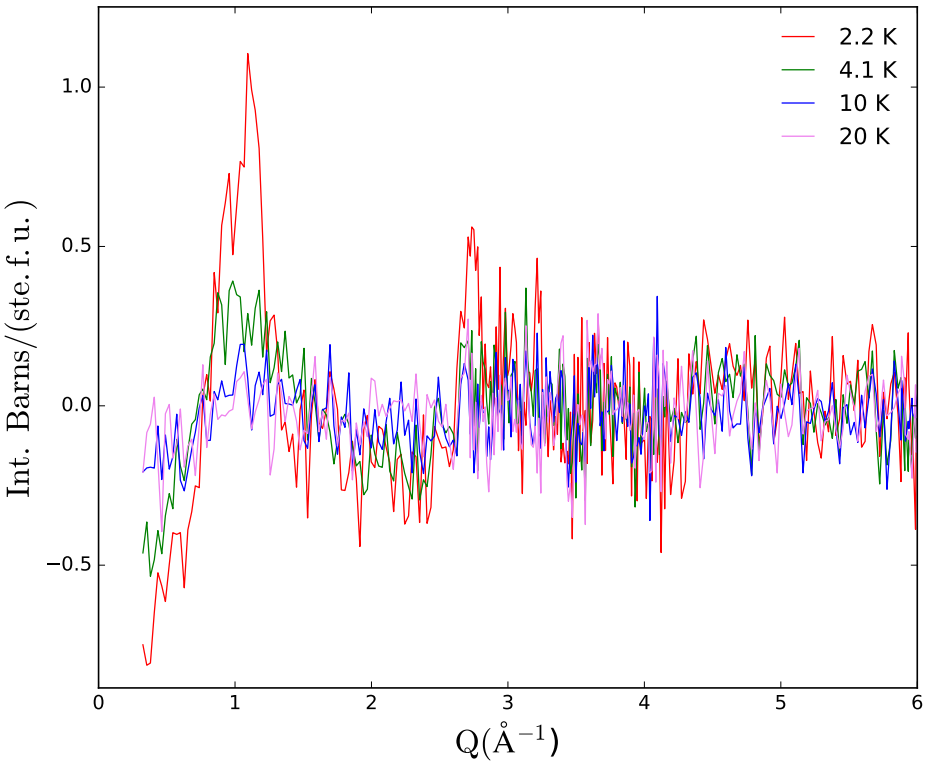

Figure 5.21: Magnetic scattering signal of the $SrNd_2O_4$ material collected on the D4 powder neutron diffractometer at 2.2 (red), 4.1 (green), 10 (blue) and 20 K (pink). The magnetic component of the signal was isolated by the subtraction of a 50 K nuclear background. The data reveals the stabilisation of broad diffuse features located in the low-Q region of the pattern, progressively gaining intensity as an effect of temperature reduction. The features become much more localised and intense below T_N.

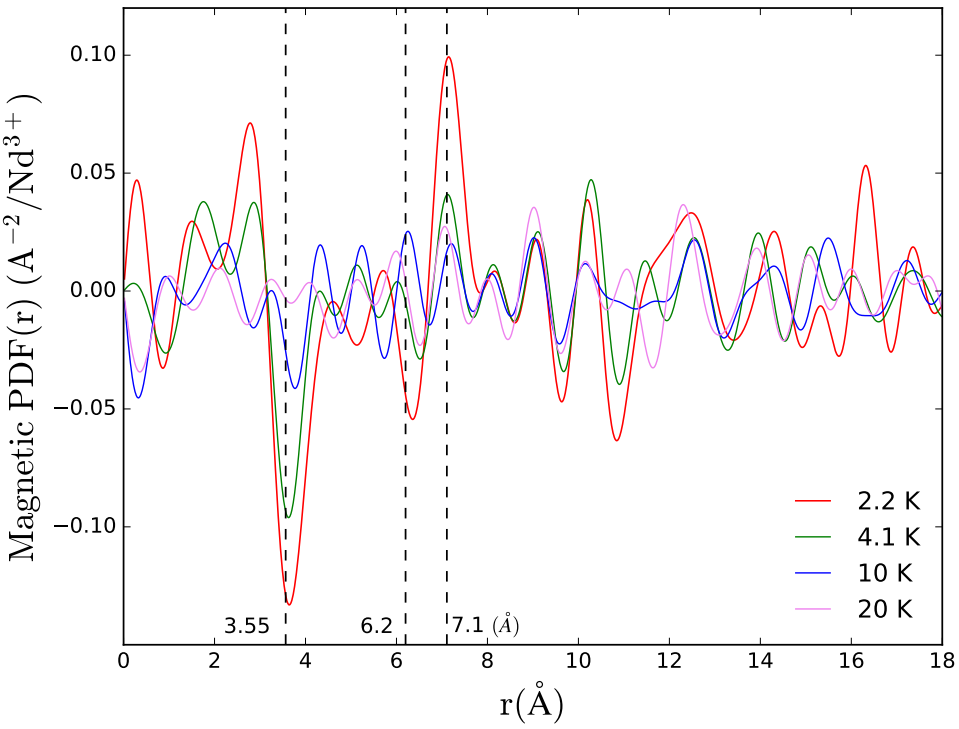

Figure 5.22: mPDF profile of the $SrNd_2O_4$ material obtained via Fourrier transformations of the magnetic scattering patterns collected on the D4 instrument at 2.2 (red), 4.1 (green), 10 (blue) and 20 K (pink), see Fig. 5.21. The features are presented as a function of relative inter-ionic distances considered in Å. While only dynamic correlations are contained in the profiles corresponding to temperatures higher than $T_N = 2.23$ K, correlations with both static and dynamic characters are present in the 2.2 K profile. Significant differences are also noticed between the profiles, revealing the strong influence of the temperature upon the actions of different sets of interactions competing in the system in the vicinity of T_N. The highlighted peaks located at ∼3.55 and ∼7.1 Å are believed to correspond with first and second neighbours correlations acting along the chains of the long range ordered phase, while the peak located at ∼6.2 Å corresponds with the inter-ladder antiferromagnetic correlations.

5.5 Summary and discussions

To summarise, this chapter presents a detailed experimental investigation of the low temperature magnetic properties of the $SrNd_2O_4$ material. This investigation was carried out using powder neutron scattering techniques as well as susceptibility and specific heat measurements. The low temperatures field-induced properties of the $SrNd_2O_4$ magnetic system, were also investigated with bulk characterisation techniques on polycrystalline samples. Due to single crystal sample unavailability, neutron scattering techniques were not employed to confirm and complement the results obtained from the in-field bulk measurements. In the following, I summarise the main results obtained at the different stages of the magnetic properties investigation of the $SrNd_2O_4$ system.

As the main results of the low temperature polycrystalline bulk investigation, I report the occurrence of a single magnetic transition taking place in the system at $T_N = 2.24$ K. The transition was observed as a sharp lambda anomaly in the specific heat data and as a clear cusp in the temperature dependence of the susceptibility. Above T_N, a clear Curie-Weiss behaviour was captured by the temperature dependence of the susceptibility indicating the dominance of antiferromagnetic correlations in the system. Finally, the retention of a large amount of magnetic disorder by the system down to the lowest temperatures was revealed by the limited values of entropy recovery calculated from the specific heat data at 10 K.

From the neutron scattering investigation, the magnetic order stabilised below T_N was identified as a long-range antiferromagnetic structure of double Néel type. The magnetic order propagates along the crystalline structure according to the vector $\mathbf{k}$=(0, 0.5, 0.5), the moments being confined within the crystallographic *ab* plane. Sizeable magnitudes are attributed to only half the number of Nd^{3+} ions, the remaining ions being involved in a short range type of magnetic order down to the lowest temperatures. The two magnetic phases are individually established on the two different types of Nd sites. However, it is not possible to individually determine a site allocation for the two magnetic phases from Rietveld refinement analyses of neutron scattering data. I have also extensively investigated the temperature evolution of both long and short range ordered magnetic phases employing different neutron powder scattering techniques. This investigation has confirmed the preservation of the short range ordered phase involving solely one of the two magnetic sites, down to temperatures significantly lower than T_N. Finally, a magnetic PDF analysis of the data has brought to light the temperature evolution of the different magnetic correlations acting over the system. These results have revealed

the strong temperature sensitivity of the system, and suggests a rather sequential mode of action for the different interactions being successively stabilised at different temperatures. This series of information disclosing the high complexity of the interaction scheme ruling the system at low temperatures.

The in-field bulk investigation of the material has revealed the preservation of the low temperature ordered magnetic phase, under applied field magnitudes as high as 60 kOe. A net reduction of the ordering temperature is however visible as an effect of field increase in the magnetic susceptibility and specific heat data. The degree of magnetic order in the system is also expected to significantly reduce as a function of increasing applied field strength, as suggested from the reduction of the magnetic entropy recoveries calculated from the specific heat data. Moreover I have observed the stabilisation of an intermediate field driven magnetic phase, induced by a $\sim$26 kOe external magnetic field in the low temperature region of the H-T phase diagram. Applied field magnitudes larger than 26 kOe will probably drive the system toward an entirely polarised state. This transition appearing between 4.0 and 3.0 K becomes more pronounced as an effect of temperature reduction, hence a significant increase of the quantity of magnetic order involved in this intermediate phase is expected as an effect of temperature reduction. By combining the results obtained from both specific heat and magnetisation measurements, I could define transition lines on a $H - T$ magnetic phase diagram of the material considered under its polycrystalline form. It is however yet difficult to propose a clear $H - T$ magnetic phase diagram for the $SrNd_2O_4$ system, and a complete single crystal bulk investigation of the system will be necessary to properly define the stability regions of the different phases. Neutron scattering investigations would conjointly be necessary to determine the nature of the field-induced magnetic phase, bearing in mind that different field-induced phases may emerge from the choice of applied field direction, relative to the crystallographic axes of the material.

Among the $SrLn_2O_4$ variants of the family, $SrNd_2O_4$ and $SrYb_2O_4$ are so far the only two members known to stabilise long range magnetic orders strictly confining the moments within the *ab*-plane of the materials. As an explanation I would like to point out that both Nd^{3+} and Yb^{3+} are considered as free ions, and bear magnetic moments being relatively smaller than those borne by the already considerably investigated group of ions classified between Gd^{3+} and Tm^{3+} on the periodic table. As a consequence, $SrNd_2O_4$ is expected to be significantly less influenced by the dipolar interactions favouring the stabilisation of Ising orders aligned along *c*, as in the case of $SrHo_2O_4$, $SrEr_2O_4$ [29, 37] and $SrGd_2O_4$, see subsection 6.4.2. Thus, I believe that with a rather weak dipolar contribution the magnetic Hamiltonian

of the $SrNd_2O_4$ system is left with the isotropic exchange interaction and single ion anysotropy, as the two most probable leading terms. In these conditions, the stabilisation of a long range double Néel (rrll) order on a triangular ladder structure can be theoretically explained by the frustrated J_1-J_2 model, in the strong antiferromagnetic J_1 limit [34, 39, 42]. J_1 and J_2 respectively corresponding to the antiferromagnetic NN interactions acting along the ladders legs and to the NNN interactions acting along the ladders rungs. This model hence implies the leading behaviour of the first neighbours antiferromagnetic exchange interactions (i.e. interactions acting along the legs) over the stabilisation of the long range ordered phase in the $SrNd_2O_4$. However, this model does not account for the antiferromagnetic inter-ladder ordering observed. The inclusion of an extra antiferromagnetic inter-ladder exchange interaction to the original J_1-J_2 model could however explain this aspect of the structure, the influence of dipolar interactions being ruled out of this case due to the large distances considered. The addition of an inter-ladder antiferromagnetic interaction to the J_1-J_2 model, was actually already considered to simulate the magnetic scattering produced by the short range ordered magnetic phase of the $SrEr_2O_4$ via Monte Carlo simulations [33]. An inelastic neutron scattering investigation of the material nevertheless remains necessary to confirm this model.

Finally, in order to further progress in the understanding of the system, the synthesis of single crystal samples of the material is crucial. I was not able to obtain this result due to the non congruent fusion properties of the $SrNd_2O_4$ material. Significant work would thus be necessary to determine the proper synthesis procedure for making single crystals samples of the material. These samples would allow to determine the anisotropy of the magnetic properties of the system, and to investigate the nature of eventual field-induced long range ordered phases using single crystal neutron scattering techniques. A single crystal investigation of the spin wave dispersion employing inelastic neutron scattering techniques would also help the understanding of the magnetic interactions scheme of the system.

Chapter 6

Low temperature magnetic properties of $SrGd_2O_4$

6.1 Introduction

This chapter is dedicated to the low temperature magnetic properties investigation of the $SrGd_2O_4$ material. This variant of the $SrLn_2O_4$ crystalline family differs from its counterparts by the spin only nature of the magnetic moments borne by the Gd^{3+} ions (considered in the ground state, i.e. L = 0). This intrinsic property of the Gd^{3+} ions results in a rather isotropic behaviour to the moments. Consequently strong anisotropic behaviours such as these reported from the investigation of the $SrHo_2O_4$ and $SrEr_2O_4$ family members, are not expected to be matched by the $SrGd_2O_4$ system [30, 33, 37]. In addition, the spin only nature of the Gd^{3+} magnetic moments minimises the crystal field effects being strong in $SrLn_2O_4$ materials. This particular variant of the family is thus expected to provide magnetic moments of classical Heisenberg type. The magnetic properties of the moments sitting on the two different Gd sites are also expected to be relatively similar. Moreover, the large magnetic moments borne by the Gd^{3+} ions are likely to induce significant dipolar interactions in the $SrGd_2O_4$ system, despite the rather large inter-ionic distances separating close Gd^{3+} neighbours. These different considerations render the magnetic property investigation of the $SrGd_2O_4$, an essential step in the elaboration of a systematic theoretical description of the $SrLn_2O_4$ family.

I present in this chapter the results obtained from neutron scattering investigations of the low temperature magnetic phases stabilised by the $SrGd_2O_4$ material. $SrGd_2O_4$ isotopically enriched polycrystalline and single crystal samples, containing 98% of the non-absorbing ^{160}Gd isotope were employed for these measurements.

$SrGd_2O_4$ happens to be the only member of the family reported to undergo two consecutive magnetic ordering transitions at low temperatures [63, 64]. Thus, the neutron scattering investigation of this material promises rich and interesting measurements.

6.2 Previously published results

The research work presented in this chapter focuses on an investigation of the low temperature magnetic properties of the $SrGd_2O_4$ material, and corresponds to a continuation of the extensive research already published on the subject [24, 38, 63, 64]. The interest dedicated to this particular material was first sparkled more than a decade ago by the group of Karunadasa *et al.* [24], who have reported the first synthesis of the material under polycrystalline form. Single crystal synthesis was then reported, along with a complete characterisation of the low temperature and low temperature field-induced magnetic properties of the material by O. Young [29, 64]. Of particular interest, $SrGd_2O_4$ has been reported to undergo two consecutive magnetic ordering transitions at $T_{N1} = 2.72$ and $T_{N2} = 0.47$ K see Fig. 6.1, making the material a unique case in the family. A strong Curie-Weiss dependence of the system is also reported from the susceptibility measurements, revealing the dominance of antiferromagnetic interactions over the system. A low temperature investigation of the field-induced properties of the magnetic system was also carried out, revealing the induction of successive transitions when applying the field along the crystallographic c axis. Applying a field along other crystallographic directions is reported to return uneventful magnetisation processes, disclosing the strong anisotropy of the system. The structural determination of the different magnetic orders stabilised by the material at low temperatures, however remained an unaccomplished task. In fact a neutron scattering investigation of the material is rather difficult due to the enormous thermal neutron absorption cross-section of natural gadolinium nuclei (49700 Barns). This parameter could nevertheless be significantly reduced by employing a beam of hot neutrons. In such conditions however, several magnetic peaks located in the low Q region of the reciprocal space will not be necessarily accessible and measurements will be of rather low resolution. The chances to successfully determine the nature of the stabilised magnetic orders are significantly reduced under such experimental conditions.

In an recent attempt to progress in the investigation of the $SrGd_2O_4$ system, bypassing the lack of neutron scattering data, Hasan *et al.* [38] have proposed a Monte Carlo investigation of the magnetic phases involved in the low temperature

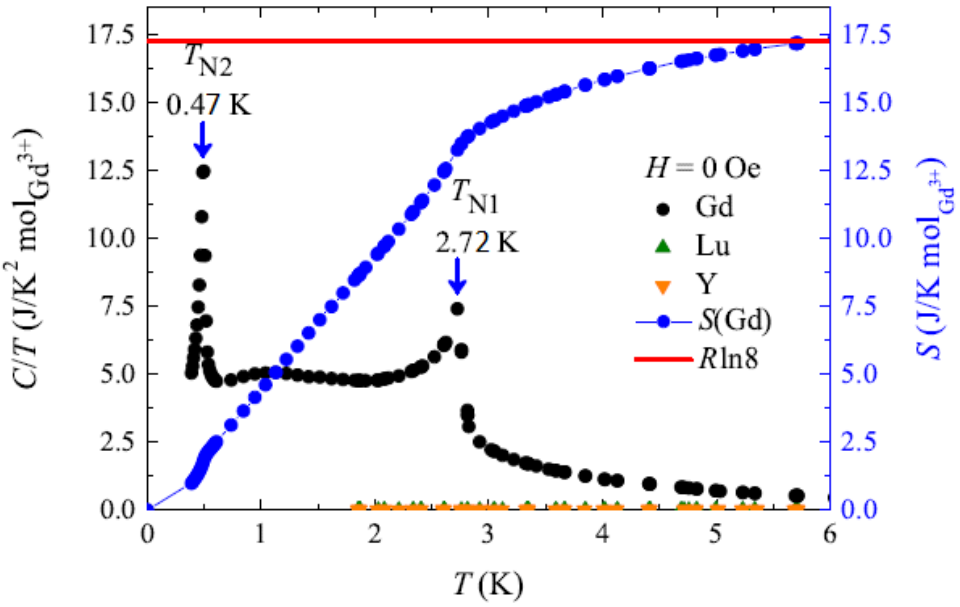

Figure 6.1: Low temperature $C(T)/T$ data collected on a polycrystalline sample of the $SrGd_2O_4$ material (non-isotopically enriched sample) by O. Young. The data reveal two sharp lambda transitions of magnetic origin centered at $T_{N1} = 2.72$ K and $T_{N2} = 0.47$ K. The temperature evolution of the magnetic entropy was computed by integrating over the area located beneath the $C(T)/T$ curve as a function of temperature and plotted according to the scale given on the righthand side. By the temperature of 6 K, the full magnetic entropy recovery expected for a mole of Gd^{3+} ions with $J = S = 7/2$, i.e. $R\ln(8)$ has been recovered by the system. Additional $C(T)/T$ data sets collected on the non-magnetic Lu and Y variants of $SrLn_2O_4$ family are included to the diagram. These data confirm the magnetic origin of the $SrGd_2O_4$ transitions as well as a negligible phonon contribution to the $SrGd_2O_4$ measurement below 6 K. Figure reproduced from Ref. [63].

$H(//c)$-T phase diagram of the material. The magnetic moments were treated as Heisenberg spins and implemented in different Hamiltonian models involving successively, unique dipolar interactions, unique Heisenberg exchange interactions, or a combination of the two. An additional Zeeman term was later added to the different Hamiltonian configurations in an attempt to model the field-induced behaviour of the system.

Of particular interest, the magnetic structures returned from the simulations involving the different Hamiltonians models in zero-field conditions are presented in the publication [38]. In the purely dipolar Hamiltonian case, a structure of Néel type consisting of ferromagnetic ordering along the chains with two adjacent chains paired antiferromagnetically is stabilised on both Gd sites. Furthermore, inter-ladder interactions in between the two Gd sites are made antiferromagnetic by the dipolar interactions. The pure exchange interactions Hamiltonian has returned two magnetic transitions at low temperatures. More complex structures are however proposed in this case. By combining both dipolar and exchange interaction terms, two ordering transitions taking place at temperatures agreeing qualitatively with the bulk experimental results are returned from the simulation. The magnetic orders stabilised below the two consecutive transitions are identical, the structures only differ considering the magnetic moments magnitudes. Similarly to the magnetic phase returned in the purely dipolar case, a Néel order is established on the two types of Gd sites. The structure however differs considering a more complex inter-ladder ordering. In fact ferromagnetic inter-ladder coupling along the a direction and antiferromagnetic inter-ladder coupling along the b direction are returned from this combined interactions configuration.

The qualitative agreement reached in zero field conditions between the experimental observations and the simulation results, hence suggests the implication of both dipolar and exchange interactions in the $SrGd_2O_4$ system. The importance of considering the dipolar interactions as a leading term in the $SrGd_2O_4$ system was on the other hand previously disregarded by previous authors [64]. It will later become very interesting to compare both theoretically and experimentally determined magnetic structures in order to further understand the interactions scheme of the $SrGd_2O_4$ system.

6.3 Sample synthesis

In order to investigate the $SrGd_2O_4$ material using neutron scattering techniques, high quality polycrystalline and single crystal samples containing the non-absorbing

^{160}Gd isotope must be prepared. For this purpose, a powder sample of Gd_2O_3 enriched at 98% in ^{160}Gd has been purchased from Trace Sciences International (Lot. 121-2). Due to the prohibitive cost of this material, I could only prepare about four grams of polycrystalline $SrGd_2O_4$ powder. The powder sample was subsequently re-employed to prepare isotopically enriched single crystal samples.

6.3.1 Polycrystalline sample synthesis and characterisation

A synthesis method to obtain $SrGd_2O_4$ polycrystalline samples using the solid state diffusion method, was already detailed by Karunadasa *et al.* [24]. This method was previously employed for the syntheses of polycrystalline samples of the Tb, Dy, Ho, Er, Tm and Yb variants of the $SrLn_2O_4$ family [25, 29, 35, 37, 78, 79]. The method first consists in homogeneously mixing stoichiometric quantities of $SrCO_3$ and Ln_2O_4 powders. The mixture is subsequently baked at 1500°C for a total of 48 hours, with several intermediate grindings.

The method was later improved by O. Young for the purpose of enhancing the chemical quality of the samples. In fact O. Young has determined that employing a slight excess of $SrCO_3$ in the reacting powder mixture, allows to compensate for the Sr evaporation over the synthesis process. The right amount of extra $SrCO_3$ to be considered was precisely determined and corresponds to the off-stoichiometric ratio 1 : 0.875. She also suggested a reduction of the baking temperature to 1350°C, to reduce the Sr evaporation over the baking procedure. In such conditions the syntheses of pure $SrGd_2O_4$ polycrystalline samples was reported.

The results presented by O. Young were verified through a series of test syntheses, prior proceeding to the synthesis involving the isotopically enriched Gd_2O_3 powder. From the results, I found that it is difficult to claim the synthesis of chemically pure sample of $SrGd_2O_4$. In fact, even by employing the reactants according to the suggested off-stoichiometric ratio, I could find traces of Gd_2O_3 in the resulting sample. The presence of small impurity percentages being measurable employing high quality powder x-ray scattering data. Moreover, similarly to the synthesis of the $SrNd_2O_4$ material, I have found a correlation between the chemical quality of the resulting sample and the amount of reactants involved in the synthesis. As expected, the larger reactants quantities involved the better is the chemical quality of the synthesised polycrystalline sample. I report an initial Gd_2O_3 quantity of at least three grams to be used for optimal results.

Precautions were taken for the synthesis involving the ^{160}Gd isotope due to the prohibitive cost of this material. Thus the synthesis was performed in two steps, each time employing half the available quantity of Gd_2O_3. A furnace failure could

	x-ray RT	
Ions	x	y
Sr	0.7499(4)	0.6497(3)
Gd1	0.4268(3)	0.1124(2)
Gd2	0.4172(3)	0.6118(2)
O1	0.224(2)	0.176(1)
O2	0.131(2)	0.480(2)
O3	0.506(2)	0.788(2)
O4	0.431(3)	0.415(1)

Table 6.1: Crystallographic parameters of the material crystallising according to the orthorhombic *Pnam* space group with the lattice parameters a = 10.1348(1), b = 12.0639(1) and c = 3.47607(2) Å. All ions are sitting at the 4*c* Wyckoff positions of general coordinates: x, y and 0.25 on the unit cell basis. The structural parameters and ionic positions were obtained from the Rietveld refinement analysis of powder x-ray scattering data collected on a polycrystalline sample at room temperature.

compromised the proper synthesis of the material, hence the precious Gd_2O_3 powder might have been lost in a one step process. Using the two steps option on the other hand, implies that a few percentages of unreacted Gd_2O_3 are expected to remain in the final product. This detail was thought not to be problematic at the time since, from susceptibility measurements the Gd_2O_3 was reported to remain paramagnetic down to at least 1.75 K [64].

The reaction products obtained from the two batches were investigated using x-ray scattering techniques, confirming the synthesis of polycrystalline samples of the $SrGd_2O_4$ material. The refined crystalline parameters of the material are reported in table 6.1. From the Rietveld refinement analysis of the data, I also report the very good chemical quality of the products. Traces of Gd_2O_3 in the samples were however revealed by the presence of tiny Bragg reflections slightly emerging from the background of the scattering patterns, see Fig. 6.2. The Rietveld refinement analysis returning sample purities of 97.7 and 98.7% for the first and second batches, respectively. The two powder batches were later homogeneously mixed up, thus the overall purity of the sample is estimated at 98.2%.

Despite the rather high purity of the synthesised samples, an additional issue comes from the absorption of water by the $SrGd_2O_4$ material. This phenomenon was already evidenced by O. Young and later confirmed by the neutron scattering measurements. Moreover, I suspect a chemical decomposition of the material induced by the water absorption over time, as for the $SrNd_2O_4$ material. The chemical decomposition is expected to release the Sr from the material, and thus to increase

the quantity of Gd_2O_3 in the material over time. Both polycrystalline and single crystal samples should consequently be stored under pure Ar atmosphere or under vacuum.

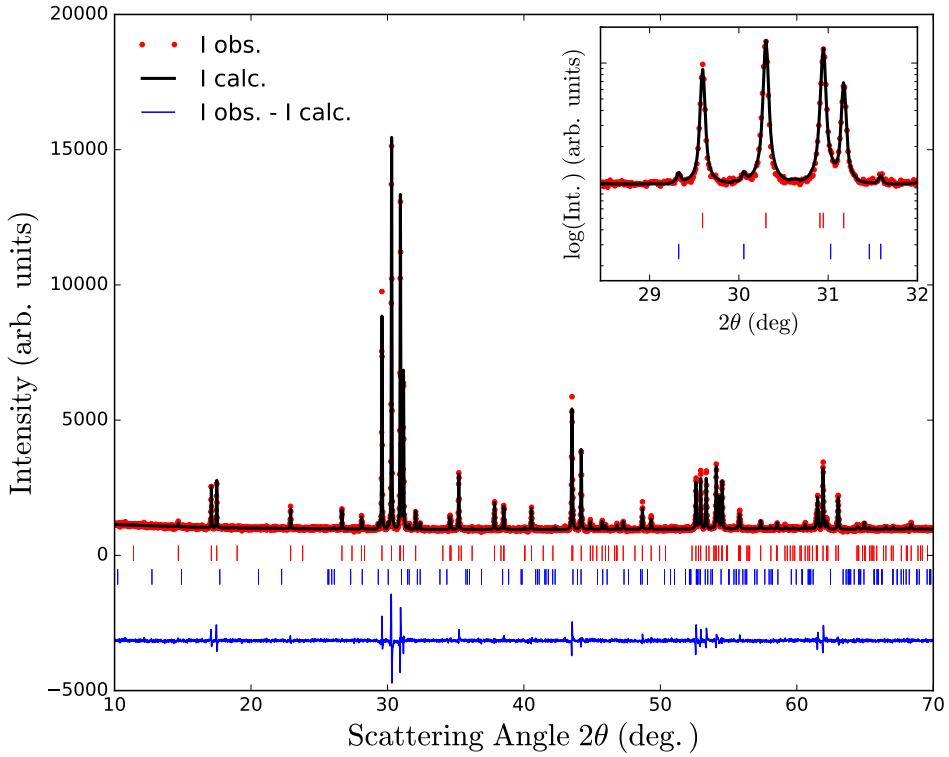

Figure 6.2: X-ray scattering pattern collected on a powder sample of $SrGd_2O_4$ containing a few percents of Gd_2O_3. The data, fit and relative difference are respectively displayed in red, black and blue. Allowed reflection positions are presented as vertical lines beneath the data, in red for the main $SrNd_2O_4$ phase and in blue for the Gd_2O_3 phase. The figure inset focuses on the scattering angle region hosting the Gd_2O_3 reflections, the logarithm scale employed allowing for their proper visualisation.

It is also important to mention that the Gd_2O_3 found in the reaction products of the syntheses is present under a monoclinic form, crystallising according to the $C2/m$ space group. In contradiction with the results obtained by O. Young, I have later clearly evidenced a magnetic transition taking place in the Gd_2O_3 material at about 3.9 K. In fact the transition was evidenced as a clean cusp in the temperature dependence of the susceptibility measured on a SQUID magnetometer, see Fig. 6.3. In addition, powder neutron scattering patterns were collected on the

D4 instrument, at several temperatures in the vicinity of the ordering transitions. A powder sample containing natural Gd was employed for these measurements and the instrument wavelength was set to 0.5 Å in order to significantly reduce the sample absorption. The data discloses the stabilisation of a short range type of order at about 4 K. In addition, I report the observation of intense magnetic Bragg reflections measured at 1.6 K, suggesting the progressive establishment of a long range ordered magnetic phase in the material below ∼4 K. This magnetic transition was actually evidenced long ago by Miller *et al.* [80], who reported the transition from susceptibility measurements performed between 1 and 6 K. Additional susceptibility measurement results performed on the cubic phase of the material are presented in Miller's paper. The temperature dependence of the data corresponds to the results presented by O. Young, suggesting that her measurement was performed on a sample containing the cubic phase of the material. Despite a paramagnetic behaviour observed down to 1.75 K, the cubic phase eventually undergoes a magnetic transition below 1.6 K previously evidenced from specific heat and neutron scattering measurements [81–83]. The ordering transitions of both cubic and monoclinic Gd_2O_3 phases occurring in between the two $SrGd_2O_4$ transition temperatures, it is thus clear that a few percent of Gd_2O_3 present in the $SrGd_2O_4$ samples can significantly perturb both neutron scattering and bulk investigations. Implying that $SrGd_2O_4$ probably slowly decomposes chemically by contact with air containing moisture, the concentration of Gd_2O_3 is expected to increase over time in the sample. One must thus be very cautious with the interpretation of the low temperature data measured on the isotopically enriched $SrGd_2O_4$ sample.

The low temperature magnetic properties of the isotopically enriched $SrGd_2O_4$ samples were investigated and compared with corresponding published results collected on samples containing natural Gd. This investigation involves solely susceptibility measurements performed on a SQUID magnetometer since it was the unique non destructive method available, see Fig. 6.4. From the low temperature data collected on the isotopically enriched sample, I report a magnetic transition seen as a cusp at about 2.7 K confirming the previously published results. The clear Weiss dependence of the data seen above the first ordering transition temperature is also confirmed. This dependence being well appreciated by plotting the inverse of the data as a function of temperature, see Fig. 6.5. By fitting the dependence of the data collected above 50 K with a linear profile, I have extracted both Curie-Weiss temperature and effective moment magnitude values, respectively equal to -8.4(2) K and 8.12(1) μ_B. These values are rather close to the corresponding values of -9.8(3) K and 7.68(1) μ_B previously published [63]. I suspect the small disagree-

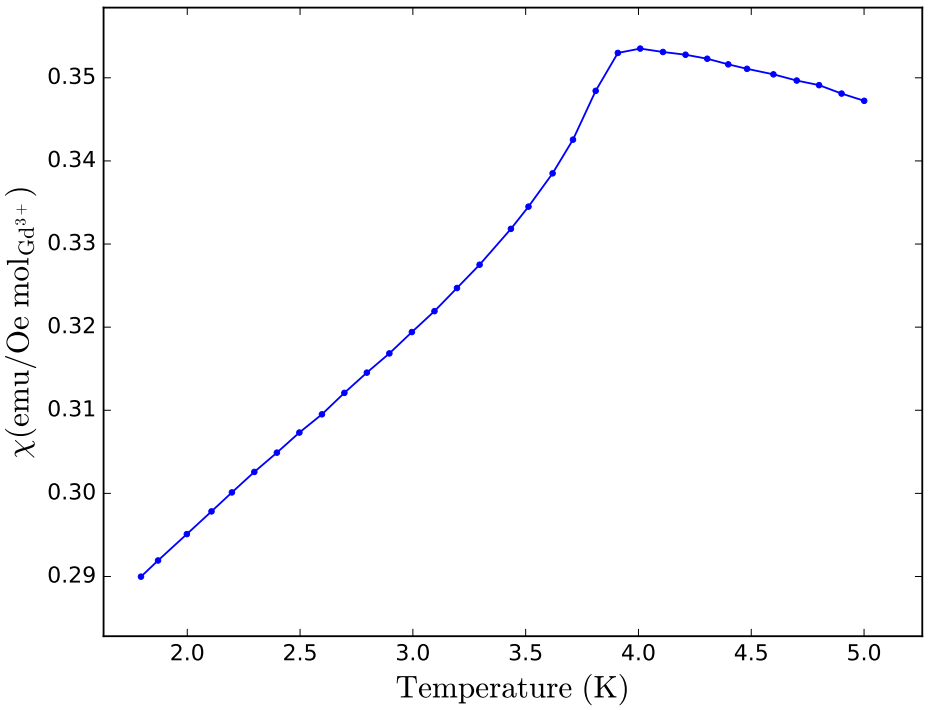

Figure 6.3: Low temperature susceptibility measurement performed on a polycrystalline sample of the monoclinic Gd_2O_3 material. The temperature evolution of the magnetic susceptibility was measured in zero field cooled conditions, between 1.8 and 5.0 K. An applied field of 500 Oe was employed for the measurement. A clear cusp is visible by 3.9 K, highlighting the occurrence of a magnetic transition taking place in the material at this temperature.

ments obtained between the two sets of results to originate from the presence of a few percent of Gd_2O_3 in the isotopically enriched sample, perturbing both the measurement and the data normalisation. Despite this impurity issue, the magnetic properties of the isotopically enriched sample match the previously published magnetic characteristics of the $SrGd_2O_4$ system with good agreements.

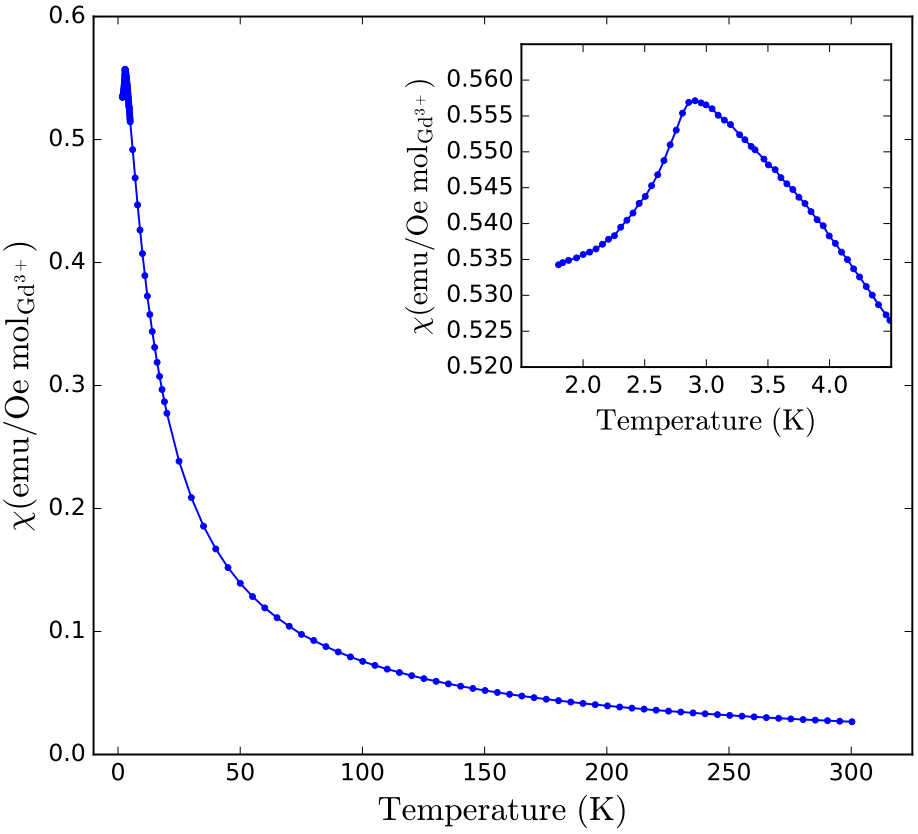

Figure 6.4: Susceptibility measurement performed on the $SrGd_2O_4$ sample enriched at 98% in the ^{160}Gd isotope. A field of 1000 Oe was applied onto the sample and the data measured in zero-field cooled conditions, starting from the lowest temperatures. The figure inset focuses on the low temperature part of the diagram, revealing a clear cusp indicative of a magnetic phase transition taking place at about 2.7 K. A clear Weiss behaviour is also seen above the ordering transition. These observations correspond with the previously published results obtained from measurements performed on samples containing natural Gd [63, 64].

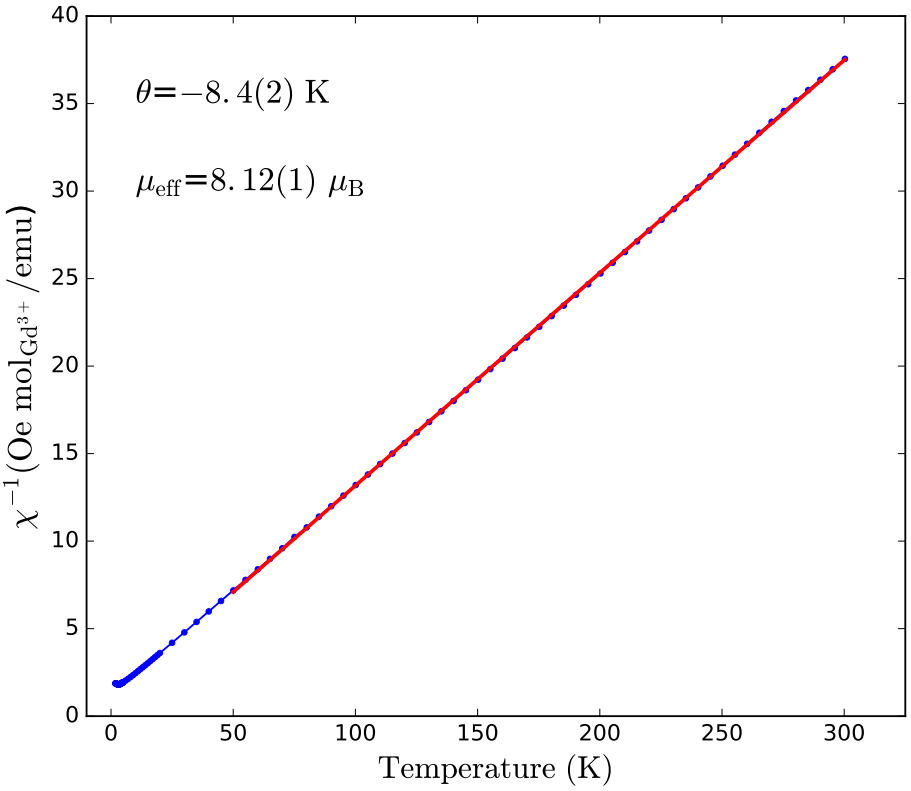

Figure 6.5: Inverse magnetic susceptibility measured on the isotopically enriched $SrGd_2O_4$ polycrystalline sample. The data corresponds to the susceptibility data presented in Figure 6.4. A clear Weiss behaviour is seen above $T_{\text{N1}} = 2.72$ K. From a fit of the linear trend performed above 50 K (red), I have extracted the Curie-Weiss temperature and the effective magnetic moment magnitude. These values are respectively equal to -8.4(2) K and 8.12(1) μ_B.

6.3.2 Preparation and characterisation of single crystal samples

The availability of single crystal samples represents the possibility to employ single crystal neutron scattering techniques for the investigation of $SrLn_2O_4$ materials. Single crystal diffraction techniques offer precise nuclear and magnetic structural information and allow to investigate the directionality of the magnetic properties. In addition, single crystal inelastic scattering techniques offer to investigate the magnetic interaction scheme acting within the systems [25, 28, 30, 31, 33–35]. Investigating the $SrGd_2O_4$ material under the form of a single crystal has other particularly important advantages. In fact, the floating zone method employed for the crystal growth allows to segregate the impurity phases out of the main phase when crystallising the material. It is thus particularly interesting to prepare single crystal samples from the isotopically enriched polycrystalline sample, in order to eliminate the few percentages of monoclinic Gd_2O_3 from the material. The low temperature single crystal neutron scattering investigation of the $SrGd_2O_4$ material, should thus not be perturbed by the presence of a magnetic impurity in the sample.

The synthesis of single crystal samples of the $SrGd_2O_4$ material was realised under the supervision of Prof. Balakrishnan and M. Ciomaga Hatnean. A single crystal growth method for the synthesise of high quality single crystals samples of $SrLn_2O_4$ materials utilising the floating zone technique, was already published by Balakrishnan *et al.* [84]. The synthesis of high quality single crystal samples of the Gd variant of the family employing the floating zone method was however quite an exercise. In fact, only tiny single crystals samples have previously been obtained from highly cracked boules by O. Young [64]. Hence, the method had to be improved in order to synthesise bigger crystals appreciated for neutron scattering investigations. The prohibitive cost of the isotopically enriched material also requires a well established and reproducible method: a failure would strongly penalise the research project. Several test attempts were consequently carried out, on samples containing natural Gd in order to improve the growth process.

My single crystal synthesis protocol of $SrGd_2O_4$ single crystal samples starts with the preparation of polycrystalline feed rods of pressed polycrystalline material. The rods were subsequently sintered for 24 hours at 1100°C for toughness improvement, see Fig. 6.6. Due to the rather small amount of isotopically enriched powder available, ∼5 mm in diameter and ∼3 to 5 cm in length rods were prepared for the tests. Feed rods of about ∼7 mm in diameter containing natural Gd were previously employed by O. Young [64]. Beyond material quantity considerations, I also expect to reduce the boules inner tensions inducing the significant cracking of the material by reducing the feed rods diameters. The use of a single crystal seed as a growth

support, also significantly improves the chances of crystallising large single crystals samples. However, due to the unavailability of such seeds, a feed rod was employed for the first test growth and subsequently reused over the different attempts.

The single crystal growth attempts performed by O. Young were carried out using a four mirrors xenon lamp image furnace. The best results were obtained in air under ambient pressure conditions, for a growth speed of 3 mm/hr [64]. I have subsequently intended to reduce the boule cracking occurring over the cooling due to the high temperature gradient applied onto the system, by reducing the growth speed to 1.5 mm/hr. After a few failed attempts I have decided to employ a two mirrors halogen furnace (Canon Machinery SC1-MDH 11020), presenting a slightly less localised hot spot. My best test-result was obtained under a 2 bar argon atmosphere, at a growth speed of 3 mm/hr. Both the seed and the feed rod were in addition counter rotated at a speed of 15 rpm. A crack free translucent single crystal boule of approximately $\sim$35 mm^3 was obtained, significantly surpassing the previously obtained results, see Fig. 6.7.

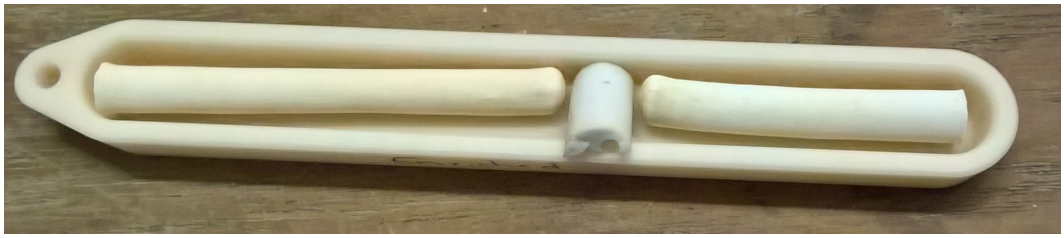

Figure 6.6: Feed rods of pressed polycrystalline $SrGd_2O_4$ material, prepared for floating zone single crystal growth. The left rod consists of isotopically enriched material, the right rod consists of natural $SrGd_2O_4$ material prepared as a test. The rods were subsequently sintered for toughness improvements.

Isotopically enriched $SrGd_2O_4$ single crystal samples were later grown by reapplying the process determined from my test growths. A feed rod of $\sim$2.8 mm in length and $\sim$0.5 mm in diameter was prepared employing the entire quantity of the material available. In order to avoid an isotopic contamination of the material by contact with the seed containing natural Gd, a 1 mm thick pellet was first cut off from the rod and melted on the seed surface to act as a spacer. The growth was then carried on and the crystallisation of a translucent crystal boule finally appeared after a little more than 1 cm of growth progression, see Fig. 6.8.

Seven small crystal fragments of various shape and size were extracted from the translucent part of the boule. The respective mass of each fragment is equal to 0.1813, 0.0818, 0.0504, 0.0374, 0.0127, 0.0161 and 0.01349 g (total mass 0.39339 g). The crystals will now be referred according to this order. The fragments were

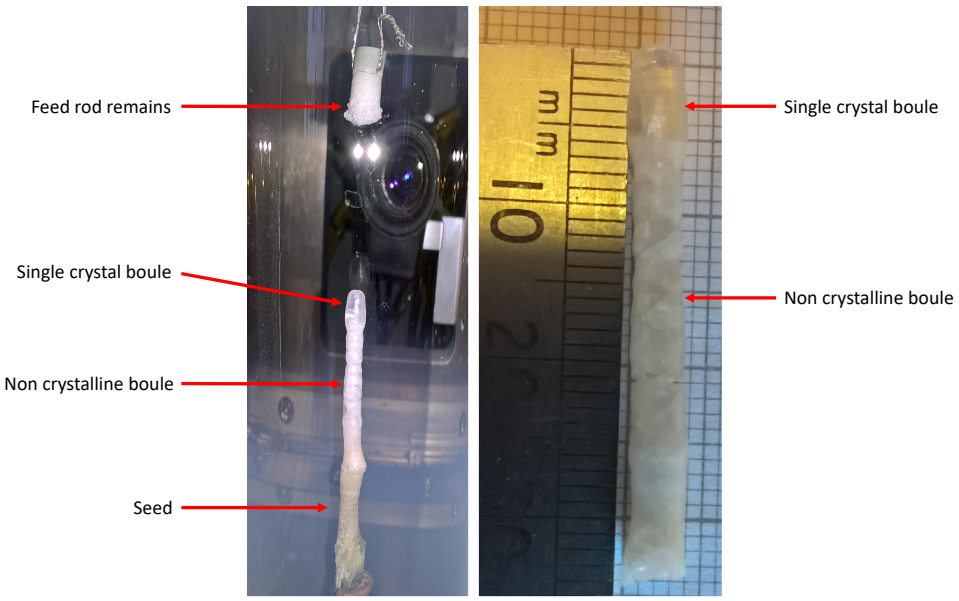

Figure 6.7: Largest crystal boule obtained from my $SrGd_2O_4$ single crystal test growth series. Left panel: Inside view of the halogen lamp image furnace where the crystal boule, the remaining part of the feed rod and the seed are visible. Right panel: Resulting boule. The translucent part was grown under argon atmosphere while the rest of the boule was grown in air.

individually checked for good crystallinity using x-ray and neutron Laue diffraction techniques. Several samples were in fact disregarded from this investigation due to poor crystalline qualities. The high crystalline quality of samples N°1 and 5 was however revealed from the Laue pictures, see Fig. 6.9. The magnetic properties of the samples were also verified from susceptibility measurements performed on a SQUID magnetometer down to 1.8 K. Due to the rather irregular shapes of the crystal fragments preventing from easy gluing on sample platforms, they were not oriented for the susceptibility measurements. Consequently, due to the strong anisotropy of the system [63] it was only possible to verify the temperature value of the first ordering transition (T_{N1}) as well as the high temperature dependence of the susceptibility. From the susceptibility data collected on samples N°1 and 5, I report the observation of single magnetic transitions occurring at approximately 2.7 K. Clear Curie-Weiss dependencies of the data were also observed in the data collected above T_{N1}. From the results of both Laue and magnetic susceptibility investigations performed on samples N°1 and 5, I report the synthesis of two high quality single crystal samples of the isotopically enriched $SrGd_2O_4$ material. These two samples were later employed for single crystal neutron scattering experiments

Figure 6.8: Picture of the crystal boule obtained from the single crystal growth of the isotopically enriched $SrGd_2O_4$ material. A small translucent boule containing several single crystal fragments was obtained (left). A principally polycrystalline rod of $SrGd_2O_4$ material containing natural Gd was employed as seed and support for the growth (right). A small pellet of isotopically enriched material was previously melted on top of the seed to act as a spacer preventing for the isotopic contamination of the enriched material.

on the D10(ILL) and 4F2(LLB) instruments, respectively.

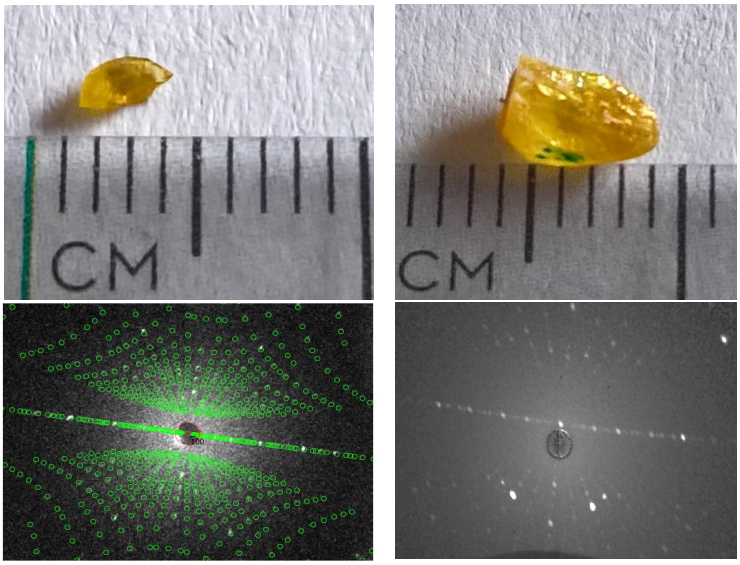

Figure 6.9: Left: Photograph and indexed neutron Laue scattering pictures of single crystal N°5. The indexation was made using the CLIP software [65]. Right: Photograph and x-ray Laue picture of single crystal N°1.

I will finally conclude the description of the isotopically enriched bulk characterisation results by discussing the surprising colour difference obtained between enriched (green) and non-enriched (colourless) grown single crystal samples, see Fig. 6.7 and 6.8. The colour difference between the two samples was actually already notified when the materials where still in the form of Gd_2O_3 powders. The isotopically enriched samples was yellowish while the natural material was white as it is reported by several suppliers. The then synthesised powder samples of $SrGd_2O_4$ kept this colour difference, as it can be seen on Fig. 6.6 the right rod is whiter as it corresponds to the natural material. In fact, the colour properties of rare earth oxide materials are known to result from f-f electronic transitions that are influenced by the oxidation degree of the Ln ion [85]. I thus suspect the presence of oxygen vacancies to influence the colour of the isotopically enriched material. This property of the isotopically enriched sample is not expected to influence the magnetic properties of the material since no noticeable difference of magnetic properties could be determined from the bulk investigation of the two different samples. Furthermore, the neutron scattering investigation of the enriched sample described in the following sections will reveal a precise agreement between the ordering temperature of enriched and natural samples.

6.4 Neutron scattering investigation

The recent low temperature characterisations of the $SrGd_2O_4$ material have revealed of a rich low temperature $H(//c)$-T magnetic phase diagram, and of particular interest the presence of two temperature driven magnetic ordering transitions occurring successively at 2.72 and 0.47 K, see section 6.2. Neutron scattering techniques offer a unique possibility to investigate the low temperature magnetic phase diagram of the $SrGd_2O_4$ material, and to improve my restricted understanding of this particular system. In addition, due to the particular characteristic of the magnetic Gd^{3+} ions, the information gained from the neutron scattering investigation are expected to be crucial in the general understanding of the $SrLn_2O_4$ systems. Employing thermal neutrons to investigate the material is however impossible due to the huge absorption cross-section of Gd nuclei. Hot neutrons experiments are on the other hand significantly less affected by absorption issues and could be employed to investigate the low temperature magnetic properties of the material. Although, this option remains complex since the intense low-Q magnetic Bragg reflections would not necessary be accessible under such conditions. In fact, an attempt to determine the nature of the magnetic orders stabilised by the two consecutive low temperature transitions has already been unsuccessful [86]. The availability of $SrGd_2O_4$ material isotopically enriched with the non-absorbing ^{160}Gd element, has since then lifted the neutron absorption issues, offering a completely different perspective in the neutron scattering investigation of the material.

In this section, I report a detailed neutron scattering investigation of the low temperature properties of the $SrGd_2O_4$ material. As a first step, the nature of the magnetic long range ordered phases successively stabilised below 2.72 and 0.47 K was investigated. For this purpose, both powder and single crystal neutron scattering techniques have been employed and measurements respectively performed on the D20 and D10 diffractometers at the ILL. Similarly to the investigation of the $SrNd_2O_4$ polycrystalline material, the D20 instrument was first equipped with a regular orange cryostat in order to collect high quality magnetic and nuclear data at temperatures ranging from RT to 1.5 K. The instrument was subsequently equipped with a dilution fridge insert offering the possibility to reach temperatures as low as 70 mK. A detailed study of the temperature evolution of the magnetic scattering was carried out from the D20 data. In addition, the nature of the magnetic order stabilised below T_{N1} was solved. However, due to the presence of a significant amount of monoclinic Gd_2O_3 powder polluting the sample, I was not able to refine the nature of the magnetic order stabilised below the T_{N2} transition. In order

to overcome this issue, the study was complemented by measurements performed on the D10 single crystal diffractometer, the Gd_2O_3 impurity being absent in the crystal sample. For this purpose, I took advantage of the 4-circle dilution fridge set up available on the D10 instrument and collected large data sets below the two ordering transitions temperatures. The nature of the magnetic order successively stabilised under T_{N1} and T_{N2} were solved from the D10 data. The same result was obtained from both D20 and D10 data concerning the nature of the magnetic order stabilised at T_{N1}. A magnetic PDF analysis of the diffuse signal collected at low temperature on the D4 powder diffractometer was finally carried out. The instrument was equipped with a regular orange cryostat enabling to reach 1.5 K as a minimum temperature. Data could thus not be measured below T_{N2} on this instrument. On the other hand, the hot neutron beam employed on the instrument offered the possibility to run the measurement on a $SrGd_2O_4$ sample containing natural Gd. The chemical quality of this particular sample was significantly higher than the quality of the isotopically enriched sample, resulting in the collection of high quality data sets.

6.4.1 Structural investigation, D2B, D20 and D10

Similarly to the neutron scattering investigation of the $SrNd_2O_4$ system (see section 5.4), I have preceded the investigation of the low temperature characteristics of the enriched $SrGd_2O_4$ material by verifying both chemical and crystalline qualities of the samples. The crystalline stability of the material over the experimental temperature range was also verified.

Structural data have been collected on the polycrystalline sample employing both D2B and D20 powder diffractometers. The structural information returned from the data collected on the two instruments being in excellent agreement, I have decided to present solely the D2B results. The quality of the data collected on the D2B instrument set in high resolution mode slightly surpasses the quality of the D20 measurements, hence justifying this choice. For the measurement, the sample was loaded in a single wall vanadium can, offering the possibility to measure diffraction patterns free of parasitic reflections. The instrument wavelength was set to 1.59 Å, granting access to an ideal reciprocal space coverage for nuclear scattering measurements. A scattering pattern was collected at RT, a temperature at which no magnetic order is present in the material. From the Rietveld refinement analysis of the data, I report an excellent agreement obtained between data and fit, confirming the $SrGd_2O_4$ nature of the sample crystallising according to the *Pnam* space group as first described by Karunadasa *et al.* [24], see Fig. 6.10. The structural parameters

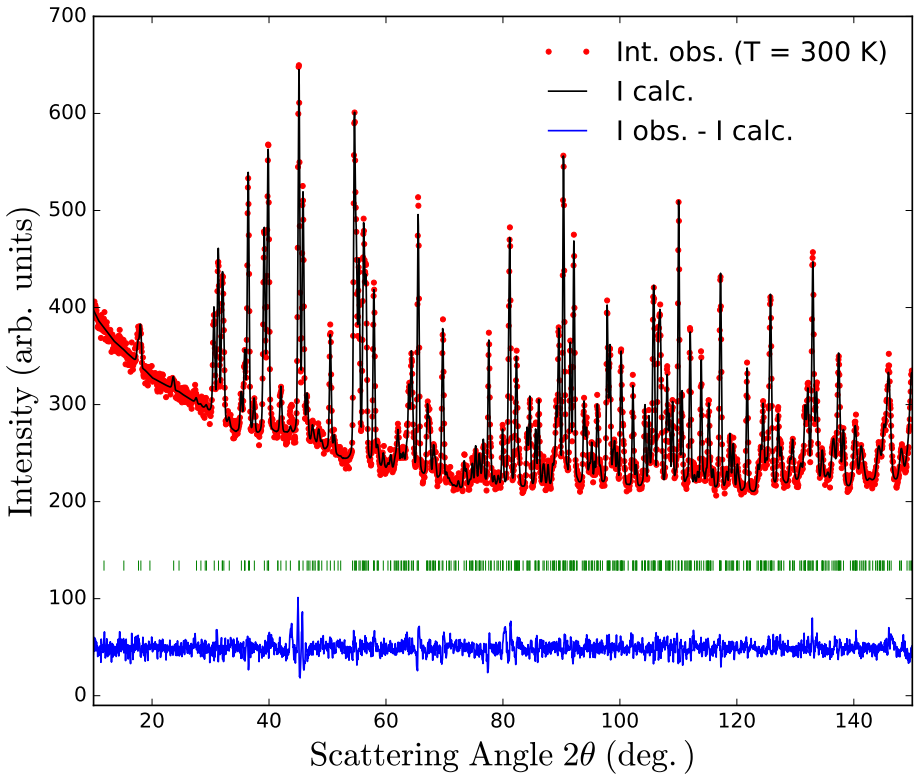

Figure 6.10: Room temperature PND scattering pattern collected on the isotopically enriched $SrGd_2O_4$ polycrystalline sample. The measurement was performed on the D2B instrument in the high resolution mode and using a neutron wavelength of 1.59 Å. Data, fit and their relative difference are respectively displayed in red, black and blue. All symmetry allowed reflections corresponding to the material space group *Pnam* are marked by vertical green lines.

	D2B RT		D10 10 K		D10 100 mK	
Ions	x	y	x	y	x	y
Sr	0.7503(2)	0.6492(2)	0.746(5)	0.654(4)	0.749(5)	0.650(7)
Gd1	0.4259(2)	0.1132(2)	0.422(6)	0.118(5)	0.435(3)	0.113(3)
Gd2	0.4171(2)	0.6113(2)	0.413(4)	0.618(3)	0.419(2)	0.614(3)
O1	0.2159(3)	0.1814(3)	0.212(5)	0.182(4)	0.230(6)	0.187(6)
O2	0.1309(3)	0.4813(3)	0.115(5)	0.480(6)	0.131(5)	0.487(6)
O3	0.5072(3)	0.7845(2)	0.510(6)	0.785(4)	0.508(5)	0.786(6)
O4	0.4259(3)	0.4205(2)	0.434(4)	0.415(4)	0.431(5)	0.417(5)
a (Å)	10.1464(2)		10.05(3)		10.05(2)	
b (Å)	12.0780(2)		11.97(4)		11.95(2)	
c (Å)	3.4802(1)		3.458(8)		3.461(4)	

Table 6.2: Crystallographic parameters of the isotopically enriched $SrGd_2O_4$ material, crystallising according to the orthorhombic *Pnam* space group. All ions are sitting at the 4*c* Wyckoff positions of general coordinates: x, y and 0.25 on the unit cell basis. The structural parameters and ionic positions were obtained from the Rietveld refinement analysis of PND data collected at RT on the D2D diffractometers, as well as from single crystal refinement analysis of data collected on the D10 single crystal diffractometer at 10 K and 100 mK. Despite a weak shrinkage of the unit cell dimensions, the results reveal the excellent thermal stability of the material.

obtained from the Rietveld refinement analysis are presented in Table 6.2. Moreover, the absence of clear impurity reflections in the collected pattern reveals the good chemical quality of the sample. The absence of large quantities of monoclinic Gd_2O_3 polluting the sample is thus verified.

In addition to the PND measurements, the crystalline structure of the isotopically enriched material was refined from single crystal data collected on the D10 instrument. Instrumental setting characteristics will be detailed in the following section 6.4.3. The chemical purity of sample N°5 employed for the measurement has permitted the collection of high quality data sets down to the lowest temperatures. The structural parameters obtained from the single crystal refinement analysis of data set collected at 10 K and 100 mK are also displayed in Table 6.2. Both nuclear and magnetic structural parameters were refined simultaneously when treating the 100 mK data set. At these two temperatures, I report excellent agreements obtained between both data and fits confirming the structural PND results. The structural stability of the material over temperature reductions, and in particular over the magnetic ordering transitions is thus confirmed.

The data collected on the D20 instrument have also permitted to refine the measurement of the sample ^{160}Gd isotopic purity by adjusting the neutron scattering

length of the sample over the structural refinement procedure. An isotopic purity of 99% was returned from this analysis.

6.4.2 Low temperature magnetic scattering, D20

The neutron scattering study of the $SrGd_2O_4$ low temperature magnetic properties starts with a detailed investigation of the magnetic signal evolution as a function of temperature. For this purpose, PND scattering patterns were collected on the D20 instruments at various temperatures. A particular attention was devoted to investigate the temperature evolution of the magnetic signal through both ordering transitions. For this series of measurements, the instrument was employed in high resolution mode and the wavelength set to 2.41 Å enabling a proper visualisation of the high intensity magnetic Bragg reflections located at low-Q values. A regular orange cryostat allowing to cool the sample down to a minimal temperature of 1.5 K was employed to investigate the evolution of the system through the first transition. A vanadium sample can was used, offering the possibility to measure a set of scattering patterns free of parasitic reflections. A dilution fridge cryostat was later implemented on the instrument in order to investigate the temperature evolution of the magnetic signal through the second transition. For this purpose, the sample was loaded in a Cu can enabling for proper thermalisation down to the lowest temperatures. Due to the rather small amount of sample available as well as to the still rather large neutron absorbing properties of the sample, double wall sample containers were used for these measurements.

I begin the results presentation by focusing on the evolution of the system through the first transition, T_{N1}. Scattering patterns have been collected from RT down to 2.0 K, smaller temperature steps were considered in the vicinity of T_{N1}. A scattering pattern collected at 50 K containing no signs of magnetic order was employed as nuclear background and subtracted from the lower temperature runs in order to isolate the magnetic signal. The magnetic intensities are presented as a function of the 2-θ scattering angle in Fig. 6.11. A tight selection was considered among the many available patterns in an objective to display a combination of the data, revealing in the clearest manner the successive steps experienced by the system over the passage through T_{N1}. While progressively cooling the sample below 50 K, I report the first observation of a broad low intensity diffuse magnetic feature in the 20 K data. This principal diffuse feature centered at a scattering angle value of $\sim$27°, slowly and continuously gains intensity while cooling the sample down. The feature also becomes more localised to finally reach a maximal intensity at the temperature of 2.84 K. At 2.70 K, the intensity of the diffuse features has slightly

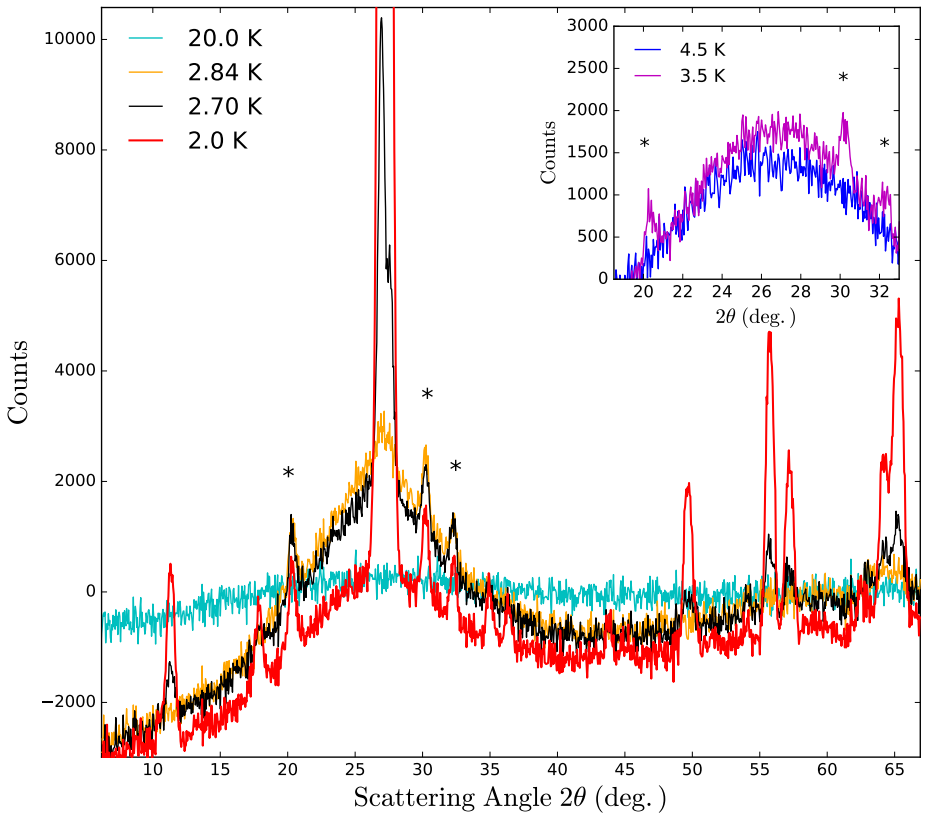

Figure 6.11: Temperature evolution of the magnetic scattering signal collected on the isotopically enriched polycrystalline sample of $SrGd_2O_4$ through $T_{N1} = 2.72$ K. The data were collected on the D20 (ILL) neutron powder diffractometer set in high resolution mode with $\lambda = 2.41$ Å, and equipped with a regular orange cryostat. The magnetic signal was isolated from the raw data by subtraction of a 50 K nuclear background. At about 20 K, the data reveals the stabilisation of a broad diffuse feature centered at a scattering angle value of ∼27°. The feature progressively increases and becomes more localised until a maximum is reached at 2.84 K. At 2.7 K, the intensity of the diffuse feature starts to decrease letting small magnetic Bragg reflections to emerge. Below T_{N1}, the 2.0 K pattern reveals a large increase of the Bragg intensities as well as a significant decrease of the diffuse feature remaining however intense and quite localised. The Gd_2O_3 impurity reflections are labelled by star symbols. The impurity transition is revealed by the superimposition of the 4.5 and 3.5 K patterns displayed in the figure inset.

decreased in order to compensate for the stabilisation of the yet small magnetic Bragg peaks, revealing the induction of long range order starting to populate the system. By 2.0 K a significant increase of the magnetic Bragg peaks intensities as well as a significant decrease of the diffuse feature, indicate the full stabilisation of the long range ordered phase over the system. The diffuse feature remains however quite significant and localised at 2.0 K, revealing the retention of a large quantity of magnetic disorder by the system. It is thus clear that both long and short range type of magnetic orders coexist in the system between the two transition temperatures. I also report the presence of three relatively small magnetic Bragg peaks stabilised above 3.5 K and labelled by star symbols on the scattering patterns, see inset of Fig. 6.11. This set of three reflections originates from the magnetic ordering of the Gd_2O_3 impurity phase, it should by consequence be carefully disregarded. I am aware that a significant portion of the diffuse feature previously described might originate from short range order hosted by the impurity phase. However, I believe this portion to remain small since no significant decrease of the diffuse feature is induced by the impurity long range ordering.

I now consider the temperature evolution of the magnetic scattering through the second ordering transition, T_{N2}. A detailed measurement was performed by collecting a series of scattering patterns between 1.0 K and 100 mK with temperature steps of 100 mK, reduced to 25 mK in the vicinity of the transition temperature. In addition, a 10 K pattern was collected to be used as nuclear background for this series of measurements, higher temperature patterns were unfortunately not collected. The intensity of the diffuse scattering present in the 10 K data being relatively weak in comparison with the features present in the low temperatures data sets, a very small over-subtraction of the background will be induced without significantly affecting the magnetic observations. A restricted selection of magnetic patterns revealing the different temperature steps of the signal evolution over the transition is presented in Fig. 6.12. As a first observation, I report the rather smooth and progressive evolution of the magnetic features between 1.0 K and T_{N2}. Both diffuse and sharp features observed in this temperature region are not significantly modified as an effect of temperature reduction, and correspond to the previously detailed 2.0 K observations. At 475 mK, I report the emergence of a new set of sharp magnetic reflections revealing the stabilisation of a secondary long range ordered phase starting to propagate through the material, see peaks labelled as 1, 2 and 3. By 400 mK, the data simultaneously reveals a significant increase of the newly stabilised Bragg peaks, and a severe reduction of the diffuse feature intensity. The secondary phase reflections then continue to gain intensity before maxima are

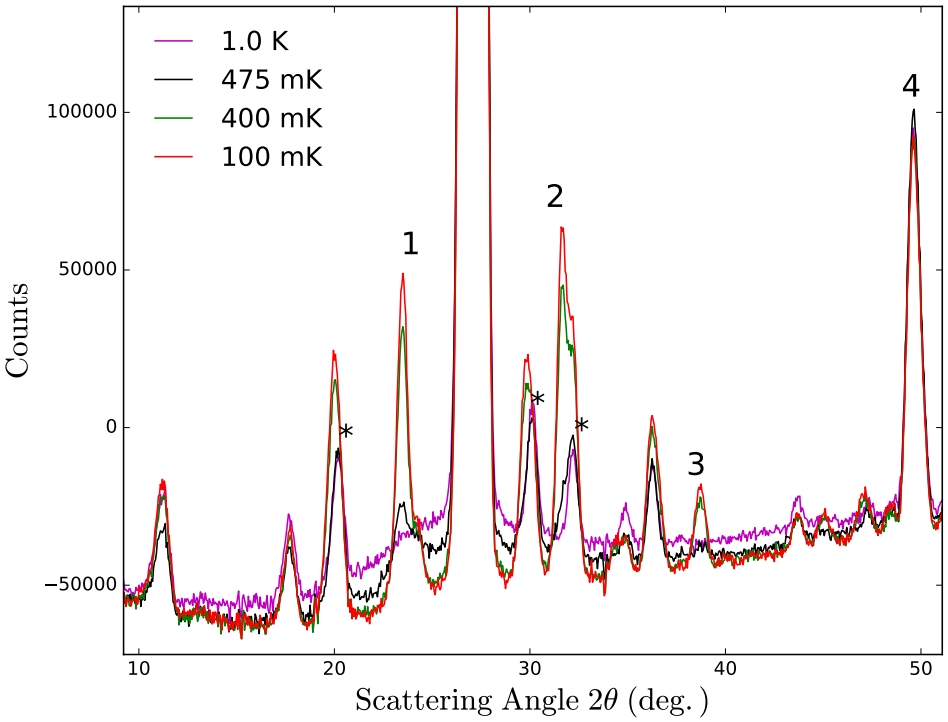

Figure 6.12: Temperature evolution of the magnetic scattering signal collected on the isotopically enriched polycrystalline sample of $SrGd_2O_4$ through $T_{N2} = 0.47$ K. The data were collected on the D20 (ILL) neutron powder diffractometer equipped with a dilution fridge cryostat and with a neutron wavelength of 2.41 Å. The magnetic signal was isolated from the raw data by subtraction of a 10 K nuclear background. The data reveals a clear reduction of the diffuse signal as an effect of temperature reduction. The stabilisation of a secondary long range ordered phase is also clearly evidenced from the appearance of additional sharp magnetic peaks in between 475 and 400 mK, see peaks labelled as 1, 2 and 3. Several peaks stabilised below T_{N1} are clearly unaffected by the second ordering transition, suggesting the preserving of the primary magnetic phase below T_{N2}, see peak 4. The impurity peaks labelled with star markers remain unaffected by the temperature reduction.

reached by 350 mK. The Bragg intensities then remain stable down to 100 mK, the lowest measured temperature. The background of the scattering patterns remains stable below 400 mK, suggesting the absence of significant diffuse features staying in the data below this temperature. A zoom on the scattering region hosting peak 1 is displayed in Fig. 6.13, offering a clear visualisation of its temperature evolution through the ordering transition.

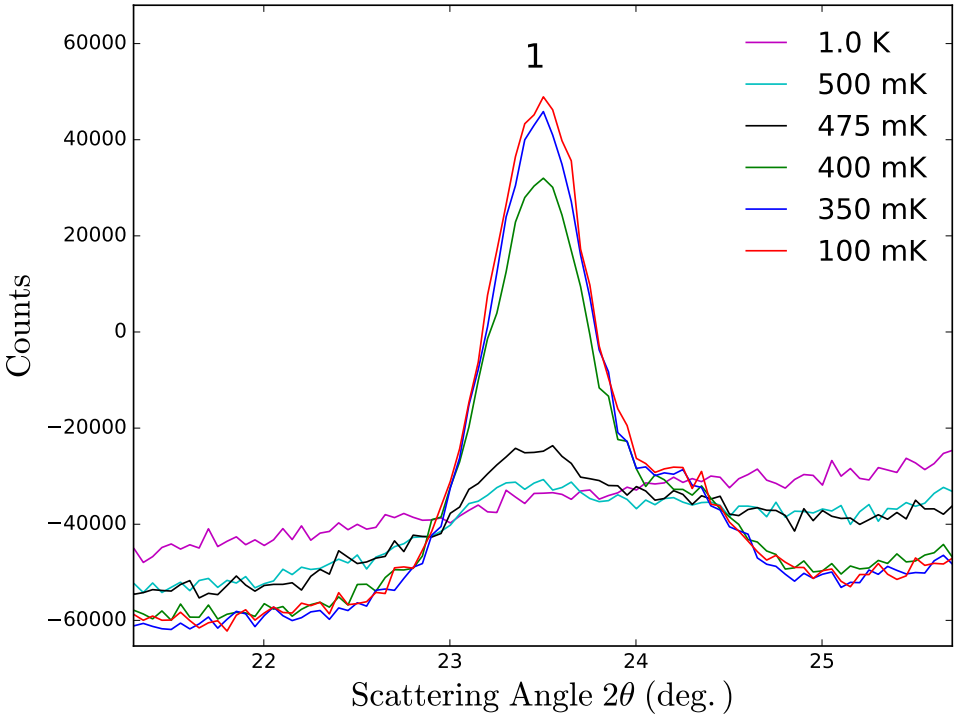

Figure 6.13: Temperature evolution of peak 1 through $T_{N2} = 0.47$ K. Despite a few additional temperatures displayed on this diagram, both the colour scheme and peaks labelling correspond with these employed on Fig. 6.12. Peak 1 is purely magnetic and belongs uniquely to the secondary magnetic phase. The data reveals the peak appearance between 500 and 475 mK, followed by a strong intensity increase down to 350 mK, the intensity then remains rather stable down to the lowest temperatures.

It is also important to mention that most Bragg reflections stabilised over the first transition remain rather stable over the second transition. In fact, two distinct reflections sets appear as superimposed on scattering patterns collected at temperatures lower than $T_{N2} = 0.47$ K. For instance the peak labelled as 4, stabilised over the first transition does not undergo noticeable intensity changes over the second

transition. It can consequently be deduced that the long range magnetic phase stabilised over the first transition is not significantly affected by the second ordering transition, the signal being mostly transferred from the diffuse feature to the Bragg peaks. The two long range ordered magnetic phases, thus coexist in the system at temperature lower than T_{N2}. At this stage of the data analysis the nature of the magnetic phases is still unknown, nevertheless possible scenarios start to appear. A first possibility would be to individually attribute each magnetic long range ordered phase to a particular Gd site. Another possible configuration would involve having both Gd sites contributing to each magnetic phases, the secondary phase should thus be considered as an additional component to the magnetic structure.

It would be interesting at this stage of the study to further investigate for the presence of low intensity diffuse scattering features remaining in the data under 400 mK. The eventual presence of such features would indicate a retention of magnetic disorder by the system under this temperature. Polarised neutron scattering techniques enabling for a precise extraction of the magnetic component of raw scattering patterns would be the tool of choice for this purpose.

To further progress in the understanding of the magnetic $SrGd_2O_4$ system, Rietveld refinement analysis techniques were employed to treat the D20 PND magnetic scattering patterns of the two long range ordered magnetic phases. From these analyses, I was able to refine the nature of the primary long range magnetic phase stable in the system from T_{N1} down to the lowest temperatures. The diffractogram regions hosting the Gd_2O_3 impurity reflections were excluded for the analysis, although no strong reflections belonging to the primary phase were present in the excluded zones, see Fig. 6.14. The nature of the secondary magnetic phase stabilised below T_{N2}, could however not be determined from the D20 PND data due to the superimposition of a few reflections and impurity peaks, see Fig 6.12. Nevertheless, by comparing the structural reflections 2-Θ positions with these of the reflections appearing below T_{N2} it is clear that a $\mathbf{k} \neq 0$ propagation vector will be required to describe the structure of the secondary magnetic phase.

In order to determine the nature of the primary long range ordered phase, two high quality data sets collected at 1.6 K and 100 mK over counting times of five hours were analysed via Rietveld refinement analyses. A 4 K nuclear background collected in the same experimental conditions was subtracted from the data, enabling the isolation of the low temperature magnetic Bragg intensities, see Fig. 6.14. By first comparing both the 1.6 K magnetic and the 4.0 K nuclear patterns, I report the clear commensurability of the primary magnetic phase to the nuclear structure. A propagation vector is consequently not needed to describe the symmetry of this mag-

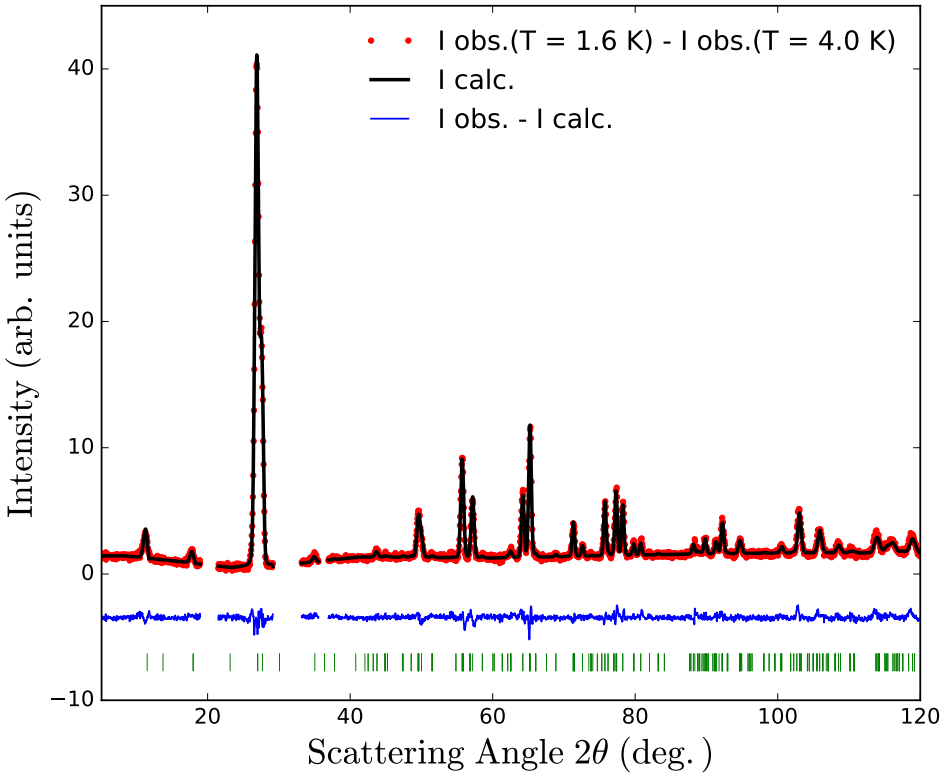

Figure 6.14: Magnetic signal of the $SrGd_2O_4$ collected at 1.6 K on the D20 diffractometer with a neutron wavelength of 2.41 Å. The magnetic component of the signal was isolated from the raw data by direct subtraction of a 4 K background. Data, fit and their relative difference are displayed in red, black and blue, respectively. All the symmetry allowed magnetic reflection positions are marked by vertical green lines. The strongest reflection is indexed as the superimposition of the (1,2,0) and (2,0,0) reflections. (2,0,0) corresponding to the right shoulder side of the peak.

Symmetry operations		BsV(1)
x,y,z	Re	001
	Im	000
-x,-y,z+1/2	Re	00-1
	Im	000
-x+1/2,y+1/2,z+1/2	Re	001
	Im	000
x+1/2,-y+1/2,z	Re	00-1
	Im	000

Table 6.3: Symmetry operations and basis vectors of the Γ7 irreducible representation, corresponding to the symmetry of the commensurate magnetic structure stabilised on the $SrGd_2O_4$ system below T_{N1}, see Appendix A.2.1.

netic order. Similarly to the Rietveld refinement analysis procedure employed for the investigation of the $SrNd_2O_4$ material (see section 5.4.2), an irreducible representation analysis of the system is carried out utilising the BasIreps software [55]. For this analysis, both the nuclear structure symmetry and the magnetic phase propagation vector ($\mathbf{k} = 0$) are used as input parameters. A set of eight Γ models considering either one or two basis vectors is returned from the analysis, see Appendix A.2.1. A trial and error approach, successively testing the different model's compatibility with the 1.6 K magnetic data is subsequently carried out. The Γ7 model, considering magnetic moments having a single component aligned along the crystallographic c axis, is determined as the unique solution compatible with the data. The symmetry characteristics of the Γ7 irreducible representation are described in table 6.3. According to this model, the strongest peak of the 1.6 K pattern centered at ∼27° is indexed as the (1,2,0) reflection. On the right side of the peak, a shoulder well visible at about 28° (in particular in the 2.70 K pattern, see Fig. 6.12) corresponds to the (2,0,0) reflection. Refinements of the 1.6 K and 100 mK magnetic patterns employing the Γ7 magnetic symmetry have returned excellent agreements between data and fits (R Bragg equal to 5.88 and 10.22, respectively), implying that only the commensurate reflections were considered at the lower temperature.

The refined structure consists of a long range collinear order involving the two Gd sites, the magnetic moments being ferromagnetically aligned along the Gd^{3+} one dimensional chains (i.e. along c), see Fig. 6.15. Of particular interest, each magnetic chain is paired antiferromagnetically with the three nearest chains making the spins alternate from up to down around the structural hexagons. For the two different magnetic sites, refined magnetic moment magnitudes of 6.24(1) and 4.37(1) μ_B were obtained at 1.6 K, increasing to 7.43(3) and 5.79(3) μ_B at 100 mK. The re-

fined moments magnitudes are respectively attributed to the two different types of magnetic sites, and displayed as red and cyan arrows on Fig. 6.15. Still, the insensitivity of Rietveld refinement analysis techniques to the different magnetic sites when investigating $SrLn_2O_4$ materials, an issue first discussed in the $SrNd_2O_4$ case (see section 5.4.2) does not allow one to attribute the magnetic moments to a particular Gd site and I have here arbitrarily decided to attribute the larger moment magnitudes to site Gd1. Furthermore, having determined the nature of the primary magnetic phase, it is now possible to rule out the magnetic structure scenario individually attributing each magnetic phase to a particular Gd site.

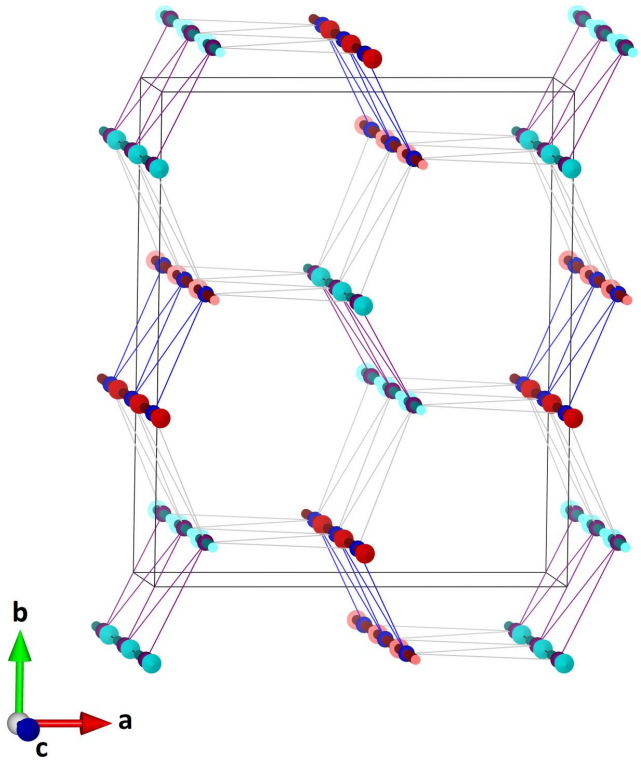

Figure 6.15: Representation of the primary magnetic structure stabilised by the $SrGd_2O_4$ material. This magnetic order remains stable in the system from T_{N1} down to the lowest temperatures. The two different magnetic moment magnitudes displayed as red and cyan arrows have been arbitrarily attributed to sites Gd1(blue) and Gd2(purple), respectively. The orthorhombic shaped box represents both the magnetic and nuclear unit cells of the materials.

6.4.3 Low temperature magnetic scattering, D10

With as principal objective to solve the nature of the secondary long range ordered phases stabilised on the $SrGd_2O_4$ material below T_{N2}, the use of single crystal neutron scattering techniques appeared as the experimental tool of choice. As previously detailed in D20 PND results section 6.4.2, the presence of a significant amount of monoclinic Gd_2O_3 impurity in the isotopically enriched $SrGd_2O_4$ polycrystalline sample prevented me from determining the nature of this phase. Growing single crystals from the polycrystalline material has permitted to segregate the impurity phase from the $SrGd_2O_4$ material, resulting in the synthesis of chemically pure crystal samples (see section 6.3.2). The perfect experimental conditions were thus reached in order to successfully determine the secondary phase nature employing single crystal diffraction techniques.

The 4-circle single crystal diffractometer D10 (ILL), offering a large reciprocal space coverage with high resolution was chosen for the experiment. The wavelength of the neutron beam was set to 2.36 Å, granting access to the reciprocal space region where the magnetic intensities are the strongest. The instrument was also equipped with a special 4-circle dilution fridge cryostat device, enabling to cool the sample down to a minimal temperature of 100 mK while keeping the 4-circle rotation potential.

The small crystal sample N°5 (see Fig. 6.9) with a mass of 0.0127 g was chosen for the experiment, implying that it had the best crystalline quality among the available samples. In order to ensure the proper thermalisation of the sample at the lowest temperatures, the crystal was glued to the tip of a Cu pin using a specific low temperature thermally conductive glue.

By considering the results returned by the D20 PND experiment, I expect to observe the addition of a secondary incommensurate component to the magnetic structure while cooling the sample over the second transition. The primary phase remaining stable below T_{N2}, consists of a magnetic order stabilised on both Gd sites and aligned along the c axis of the material. A secondary component to the structure is thus likely to be found in the ab plane of the material.

Due to the unavailability of single crystal magnetisation as well as infield heat capacity data collected according to the a and b axis at dilution fridge temperatures, it was not possible to predetermine the orientation of the secondary component within the ab plane. Consequently, it was decided to align either the a or b axes of the crystal parallel to the pin direction. In such a way by orienting the pin vertically, the measurement would be sensitive to eventual a or b components of the secondary structure with good resolution in the horizontal plane (in the lab reference

frame). These experimental conditions significantly simplify the measurement and offer the possibility to access a large number of inequivalent reflections. Due to the asymmetry of the sample shape as well as gluing convenience reasons, it was finally decided to align the crystal a axis along the pin direction. The Cu pin was then secured to the Eulerian cradle of the instrument, and the crystal orientation adjusted relatively to the diffractometers axes implying χ and φ rotations, see Fig 6.16.

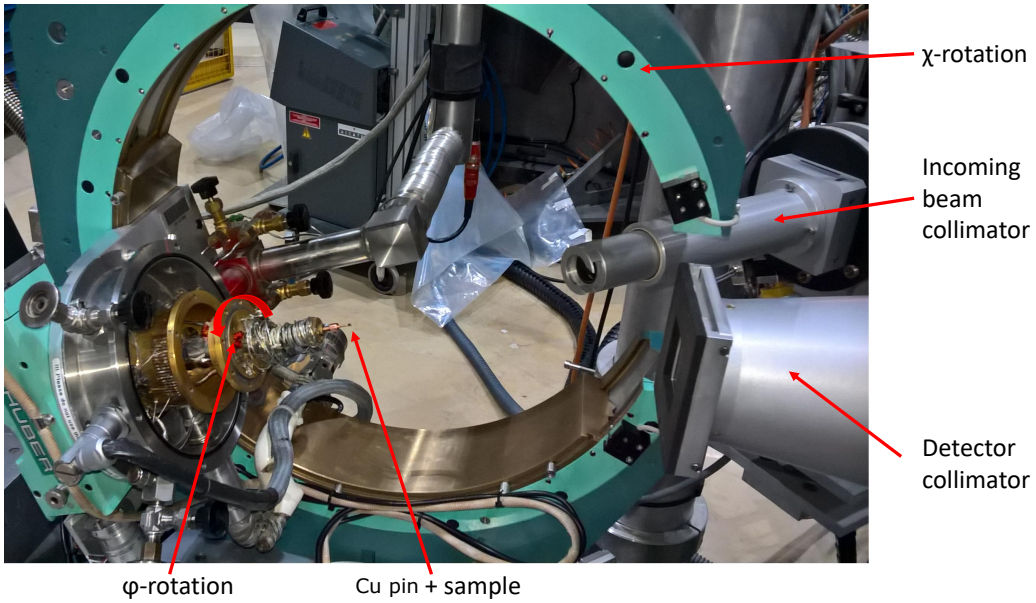

Figure 6.16: Photograph of the D10 Eulerian cradle. The mounted $SrGd_2O_4$ single crystal sample is visible in the centre of the picture, along with the Cu pin. Both incoming monochromatic beam and detector collimators are present on the right side of the image. The large ring corresponds to the χ circle. φ is less visible and highlighted by the curved red arrows.

As a first step in the progression of the experiment, a precise crystalline structure investigation of the isotopically enriched $SrGd_2O_4$ sample was carried out. For this purpose, a large set of nuclear reflections were collected at 10 K. The structure was refined using single crystal diffraction techniques applied to a set of 37 inequivalent reflections. From the structural refinement results, I report an excellent agreement reached between fit and data (R Bragg = 7.09), confirming the previously published results [24, 63]. The refined structural parameters obtained are presented in Table 6.2 along with the results previously determined from the D2B PND experiment, revealing a good agreement between the two sets of parameters. In addition to the structural parameters of the $SrGd_2O_4$ material, the extinction parameters of the crystal sample were refined from the 10 K data set. The pre-

cise determination of these parameters (see subsection 3.6), linked to the crystal mosaicity is essential in single crystal refinement analysis processes.

The second step of the experiment progression is dedicated to the structure refinement of the primary magnetic phase. The nature of this magnetic order being already known from the previous Rietveld analysis of the D20 data (see section 6.4.2), this task was performed to compare and confirm both instruments observations. Consequently, a large set of commensurate (h,k,l) reflections was collected at 700 mK and the measurement repeated at 100 mK. The two temperatures sets of data were treated via single crystal refinement analysis techniques, implying simultaneous refinement of both nuclear and magnetic structures. At both temperatures, an excellent agreement is obtained between the data and fit returning R Bragg factors equal to 13.96 at 700 mK and 9.68 at 100 mK. The magnetic structures obtained from the analyses confirm the nature of the magnetic order previously reported from the D20 data treatment (see Fig. 6.15), as well as its stability down to the lowest temperatures. At 700 mK, the refined magnetic moment magnitudes equal 6.4(8) and 5.2(8) μ_B, respectively on Gd1 and Gd2 sites. By comparison with the corresponding results obtained from the data collected at 1.6 K on the D20 instrument, a slight increase of the moment magnitudes is noticed as an effect of temperature reduction. At 100 mK, the refined moment magnitudes have reached 7.2(5) and 5.9(5)μ_B on the two different Gd sites, values closely agreeing with the D20 results obtained at the same temperature. By comparing the rather close refined magnitudes obtained at 1.6, 0.7 and 0.1 K, the temperature evolution of these values seems to proceed in a smooth manner over $T_{\mathrm{N2}} = 0.47$ K, see Fig 6.17. This result suggests that the secondary transition does not significantly affect the primary magnetic phase. This characteristic was previously suggested from the temperature stability of the commensurate reflections measured over the T_{N2} transition on the D20 instrument. Such an absence of correlation between the two magnetic phases seems to indicate the operation of two independent ordering mechanisms, as if two different sets of interactions were subsequently acting over the system.

The structural determination of the secondary magnetic phase corresponds to the third step of the experiment progression. In order to accomplish this task, I have first proceeded to Q scans along the reciprocal space vectors directions. The precise positions of a few satellite reflections were identified along the l axis, revealing a propagation vector $\mathbf{k}$ = (0,0,0.42). At low-Q values, the strong satellite reflections were observed in the (h,0,l) scattering plane, disclosing the probable orientation of the magnetic moments according to the b axis of the material. Having determined the magnetic phase propagation vector, an irreducible representation analysis could

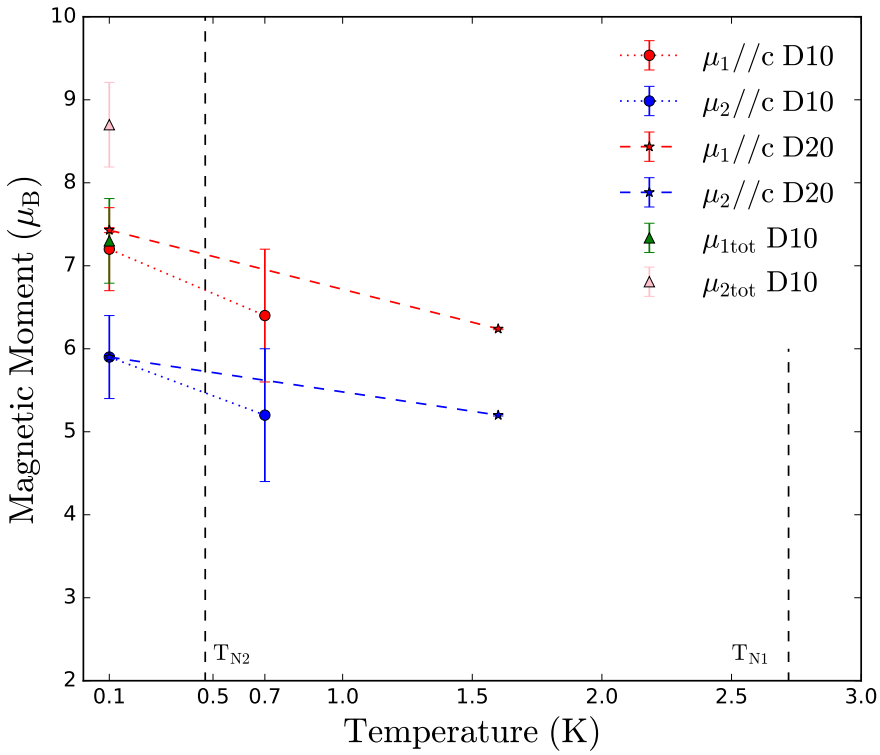

Figure 6.17: Temperature evolution of Gd1 and Gd2 ordered magnetic moments in the $SrGd_2O_4$ material. The evolution of Gd1 and Gd2 components involved in the primary ($\mathbf{k} = 0$) phase are displayed in red and blue, respectively. Circle and star markers correspond to the D10 and D20 results, respectively. In addition, below T_{N2} the combination of the magnetic moments components corresponding to both ordered phases attributed to Gd1 and Gd2 sites are in turn represented with green and pink triangle markers. I note the good agreement between both D10 and D20 refined magnitudes of the primary phase.

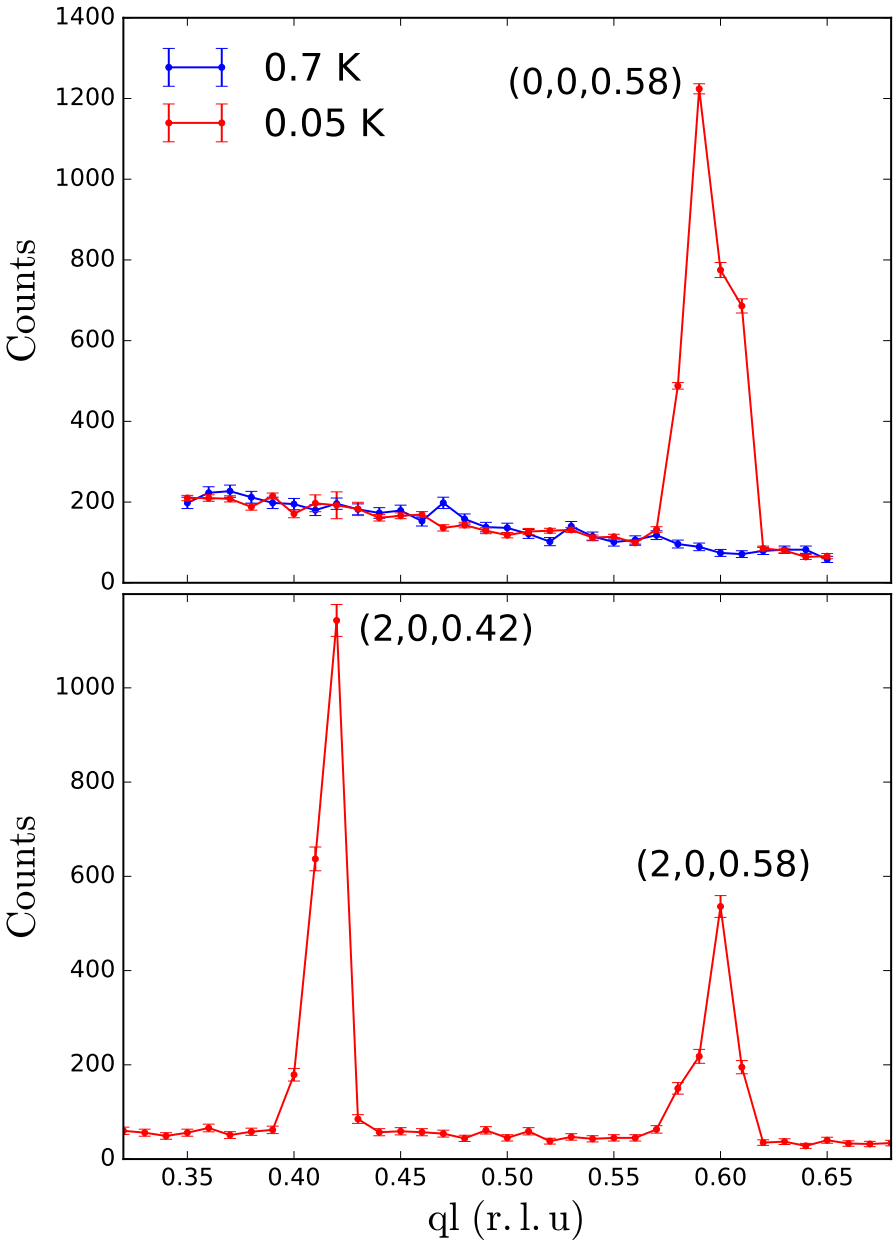

Figure 6.18: $SrGd_2O_4$ single crystal Q scan measurements, performed along the l reciprocal space direction (defined in reciprocal lattice units). The measurement was performed on the 4F2 diffractometer (LLB) used in elastic mode. The scans performed at 0.05(red) and 0.7 K(blue) reveal the stabilisation of magnetic satellites indexable considering a $\mathbf{k}$ = (0,0,0.42) propagation vector. Crystal sample N°1 was employed for the measurement.

be conducted returning a set of four Γ models, see Appendix A.2.4. The symmetry of each model is described by a set of three basis vectors possessing both real and imaginary components, see table 6.4. This particularity reveals the modulated nature of the magnetic order. In order to precisely refine the nature of this magnetic phase, a substantial number of independent satellites were collected in a large reciprocal space area. From the result of the refinement, I report the stabilisation of a $\mathbf{k} = (0,0,0.42)$ antiferromagnetic modulation in which the moments are aligned along the b directions, see Fig. 6.19. The symmetry of this magnetic order corresponds to the Γ1 irreducible representation model described in table 6.4. Moreover, the outcome of the refinement analysis clearly discloses the involvement of both Gd type of sites within the modulation. The refined amplitudes of the modulations being equal to 1.2(1) and 6.5(1) μ_B are attributed to sites Gd1 and Gd2, respectively. I note that since Gd1 sites were attributed the largest moments in the primary magnetic phase, it is necessary to assign the largest refined moment values of the second phase to Gd2 sites in order to keep the combined magnitudes in a range of values acceptable for Gd^{3+} ions. In that respect, the Gd2 magnetic moments sitting at the highest amplitude points of the modulations bear ordered moment magnitudes of ∼8.8(5) μ_B. Within the error bars, this value is slightly larger than the Gd^{3+} free ion value of ∼7.98 μ_B and suggests a significant uncertainty on the refinement scaling factor of the secondary phase, see Fig. 6.17. On Gd1 sites combining the ordered components of both magnetic phases result in moment magnitudes of ∼7.3(5) μ_B. Despite the refinement scaling uncertainty, these results suggest the full or nearly full involvement of the Gd1 and Gd2 moments within the long range order established on the material below T_{N2}. Nevertheless, the modulated character of the secondary phase implies that on average the magnetic moments do keep a significant disordered component down to the lowest temperatures.

A few secondary phase satellites were later remeasured on the 4F2 (LLB) triple axis diffractometer by proceeding to Q scans in elastic mode. The largest available isotopically enriched $SrGd_2O_4$ crystal sample (N°1) was employed for this measurement in order to maximise the reflection intensities. These set of data nicely reveal the satellites stabilisation when cooling the sample over T_{N2} were chosen to illustrate my result description, see Fig. 6.18.

I would now like to call attention on the interesting ferromagnetic arrangement separating each oscillations along the 1D chains at the lowest amplitude points of the modulations, see Fig. 6.19 bottom. Considering the magnetic order on the triangular ladder scale, this characteristic breaks the double Néel (uudd) ordering of the moments at regular points along the c direction. In the $SrLn_2O_4$ systems, the

Symmetry operations		BsV(1)	BsV(2)	BsV(3)
x,y,z	Re	4.0211 0 0	0 4.0211 0	0 0 4.0211
	Im	0 0 0	0 0 0	0 0 0
-x,-y,z+1/2	Re	-1 0 0	0 -1 0	0 0 1
	Im	3.8948 0 0	0 3.8948 0	0 0 -3.8948
-x+1/2,y+1/2,z+1/2	Re	1 0 0	0 -1 0	0 0 -1
	Im	-3.8948 0 0	0 3.8948 0	0 0 3.8948
x+1/2,-y+1/2,z	Re	-4.0211 0 0	0 4.0211 0	0 0 -4.0211
	Im	0 0 0	0 0 0	0 0 0

Table 6.4: Symmetry operations and basis vectors of the Γ1 irreducible representation, corresponding to the symmetry of the $\mathbf{k}$ = (0,0,0.42) incommensurate phase stabilised on the $SrGd_2O_4$ system below T_{N2}.

stabilisation of double Néel orders is thought to result from the dominance of nearest neighbour antiferromagnetic exchange interaction J_1, over next nearest neighbours antiferromagnetic exchange interaction J_2 [34, 39, 40, 42]. As previously defined, J_1 and J_2 are individually acting along the legs and the rungs directions of the ladders, respectively. In the particular $SrGd_2O_4$ case, it seems that a severe competition between both J_1 and J_2 types of interactions forces the system to alternately satisfy both interactions resulting in the observed modulations. In that respect, the $SrGd_2O_4$ system stands as a particular case within the family calling for theoretical description.

The combination of both refined magnetic phases corresponding to the magnetic structure stable in the system below T_{N2}, is presented in Fig. 6.20. This exotic order could be described as a modulated antiferromagnetic wave of spins propagating along the chains directions, the modulations being separated by spins having ferromagnetic b components. Another aspect of the refined structure reveals significantly different ordered spin magnitudes sitting on the two different Gd type of sites. Taking into account that both sites are stabilising the same type of magnetic orders, such a difference of ordered magnitude can only be attributed to the crystal field interactions. The spin only nature of the Gd^{3+} moments on the other hand is expected to significantly reduce the influence of the crystal field interactions over the $SrGd_2O_4$ system. This contradiction thus reveals the very strong influence of crystal field interactions over the magnetic properties of the $SrLn_2O_4$ materials.

As previously described, the stabilisation of the magnetic phase secondary component is thought to result from the competition of equivalent J_1 and J_2 interactions. On the other hand, the primary component of the structure corresponds to

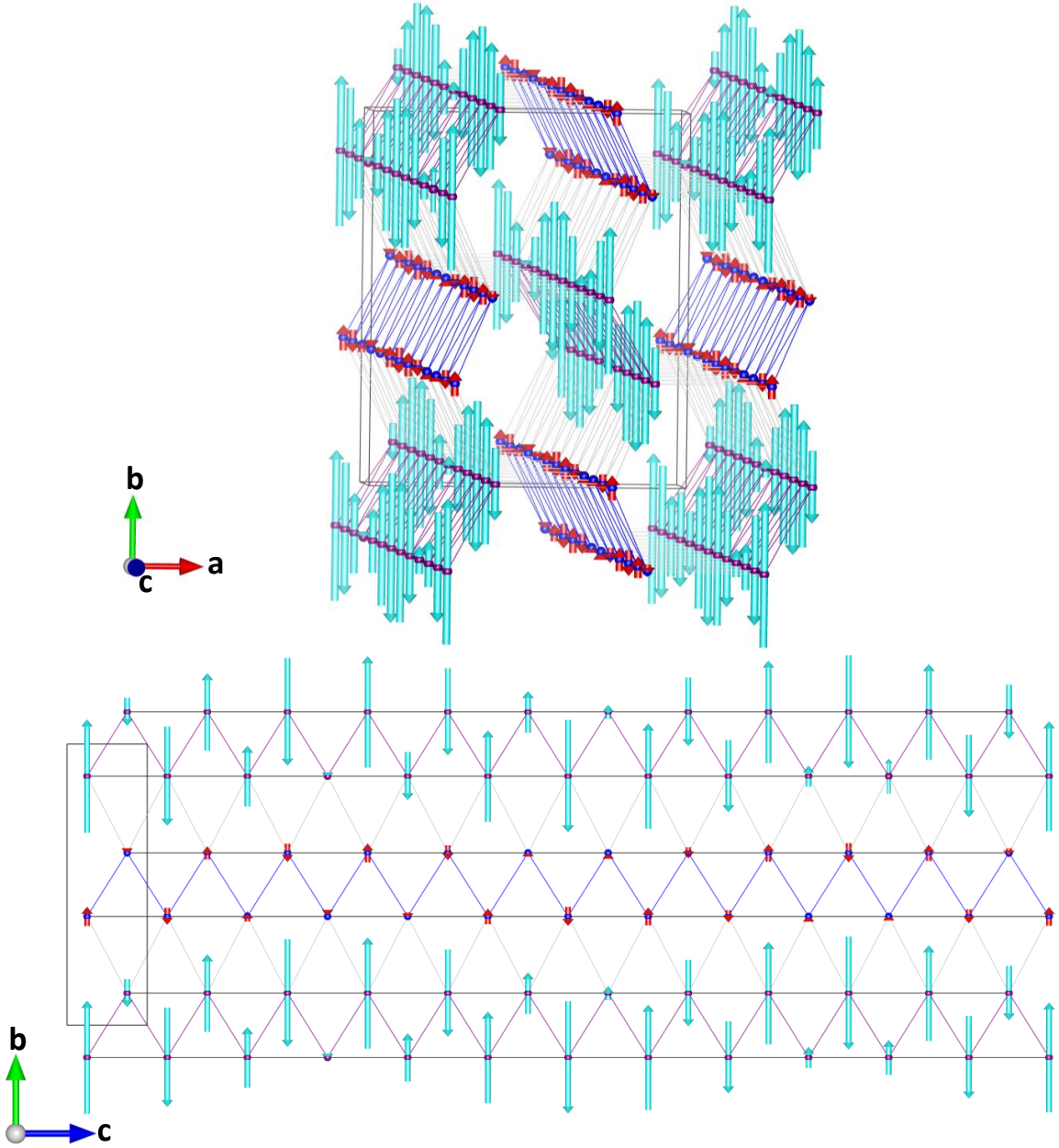

Figure 6.19: Representation of the $\mathbf{k}$ = (0,0,0.42) incommensurate magnetic structure stabilised on the $SrGd_2O_4$ system, under T_{N2}. Top: 3D representation of the structure considering two undulations along the c direction. The spin modulations of different amplitudes, displayed in red and cyan being arbitrarily attributed to site Gd1(blue) and Gd2(purple), respectively. Bottom: 2D representation of the magnetic modulations, as seen in the bc plane. The clear antiferromagnetism of the modulations, as well as the ferromagnetic order separating of each undulation are easily appreciated on this representation.

a Néel up-down-up-down (udud) type of order. This type of order, also established along the chains direction in the Ho and Er variants of the family is representative of the strong J_1 configuration. It is thus not possible to explain the simultaneous presence of the two separate components of the structure by solely implying a simple J_1 and J_2 model. This problem thus calls for the consideration of a additional type of interaction, being responsible for the ordering of one of the two components. It becomes interesting to mention at this point of the study that a model involving solely dipolar interactions between close neighbours (implying equal moment magnitudes on both sites), returns a Néel order with the moments aligned along c [37, 38]. The stabilisation of the primary component of the structure could thus be induced by the dipolar interactions while exchange interactions would stabilise the secondary component at a lower temperature.

6.4.4 Magnetic PDF analysis, D4

I would finally like to terminate the presentation of my low temperature investigation of the $SrGd_2O_4$ magnetic system, by detailing PND data collected from 30 to 2.2 K on the D4 diffractometer(ILL). This additional PND investigation of the material, complements the previously detailed temperature evolution study of the magnetic scattering signal collected on the D20 instrument over the first transition, see subsection 6.4.2. Of great interest, the short wavelength neutron beam available on the powder diffractometer D4, has offered the possibility to investigate the scattering of a non-isotopically enriched $SrGd_2O_4$ powder sample. In fact, the absorption cross-section of the strongly absorbing Gd isotopes are reduced to significantly lower figures employing a 0.5 Å neutron beam, granting the possibility to investigate the material utilising neutron scattering techniques. This measurement hence represents a unique possibility to compare sets of neutron scattering data collected on natural and isotopically enriched $SrGd_2O_4$ material. Moreover, the short wavelength neutron beam available on the D4 diffractometers offers a unique possibility to measure scattering patterns over a large Q region ranging from 0.5 to 6 $Å^{-1}$. The measurement resolution as a drawback effect, significantly reduces in such experimental conditions in comparison with the D20 measurements. The magnetic scattering patterns are on the other hand optimal for Fourier transformations of the signal into mPDF features, offering real space pictures of both static and dynamic correlations present in the system [77].

The measurement was performed employing a regular orange cryostat allowing to lower the sample temperature down to approximately 1.6 K. In virtue of the natural Gd_2O_3 material large availability, in comparison with its rare and

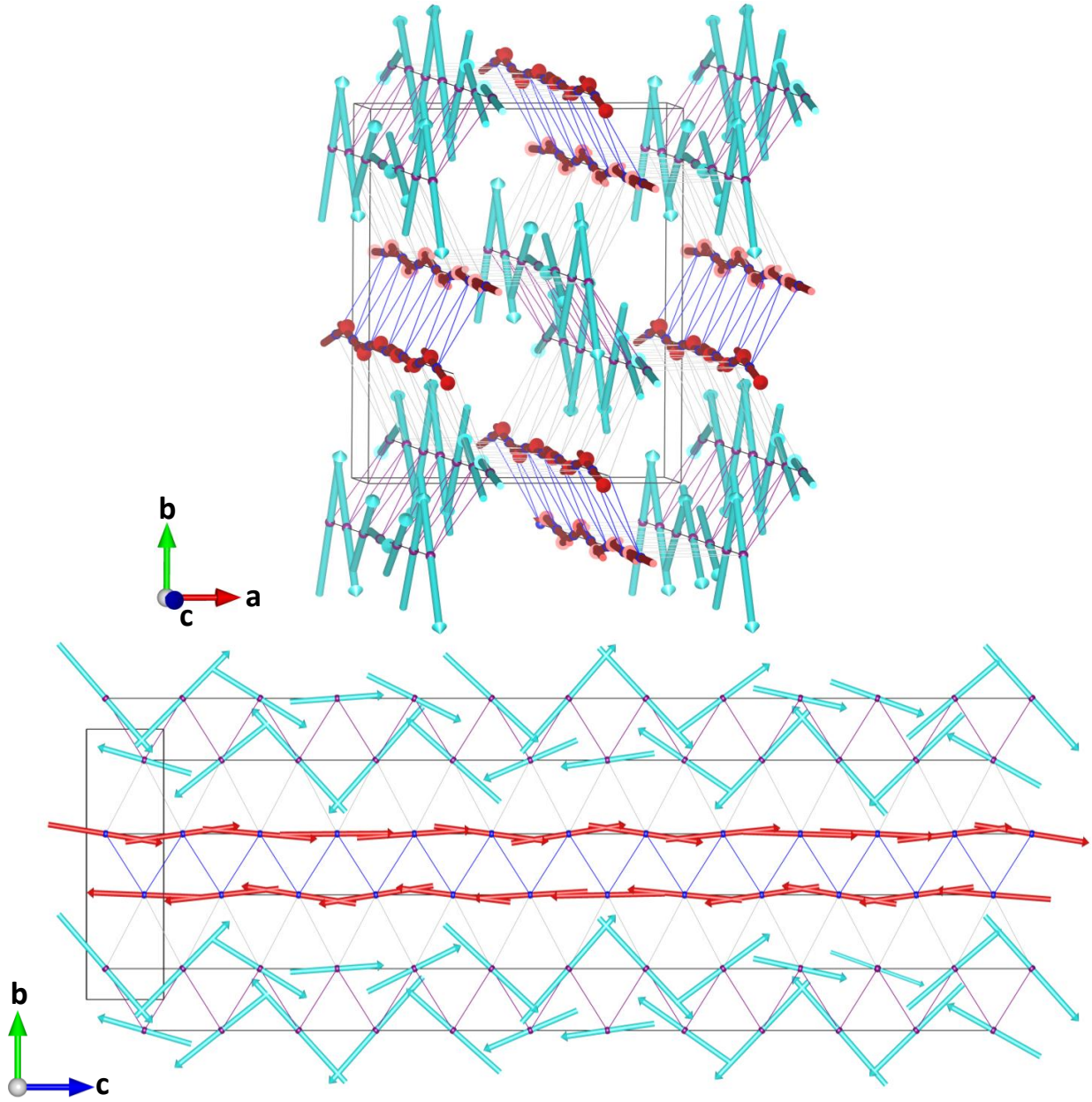

Figure 6.20: Geometrical representation of the magnetic structure obtained by combining both magnetic phases stable on the $SrGd_2O_4$ system below T_{N2}. The ordered components of the magnetic moments attributed to both Gd1 and Gd2 sites are displayed as red and cyan arrows, respectively. The black orthorhombic shaped box materialises the nuclear unit cell of the material. Top: 3D representation of the structure. For clarity purposes, only one spin modulation was considered along the c axis of the material. Bottom: 2D representation of the structure as seen within the bc plane when selecting a layer of the material containing a single ladder according to the a axis. Two modulations of the structure are here considered according to the c directions.

prohibitively expensive isotopically enriched version, a new sample could be baked shortly before the experiment. From an x-ray scattering characterisation of the material performed shortly prior the start of the PND experiment, I report the absence of a significant Gd_2O_3 content in the sample. The presence of additional magnetic features originating from the monoclinic Gd_2O_3 ordering, as previously observed in the D20 data should thus be reduced to insignificant values in this new measurement. Considering the range of temperatures available on the D4 instrument as well as the low absorbing properties of the sample in the instrumental conditions, the sample could be loaded in a single wall vanadium can. Optimal experimental conditions were thus offered to accurately measure the temperature evolution of the magnetic signal through T_{N1}, without being concerned by the addition of external features to the magnetic patterns.

Scattering patterns were collected at nine different temperatures in between 30 and 2.2 K. In addition, a 50 K nuclear background pattern containing no traces of magnetic order was collected and subtracted from the lower temperature patterns. The resulting nine magnetic patterns were superimposed and plotted as a function of Q, see Fig. 6.21. The data reveals the presence of short range order in the system already visible at 30 K and corresponding to a weak diffuse feature centered at about 1.2 $Å^{-1}$. This principal diffuse feature subsequently gains intensity and becomes more localised while reducing the temperature, until a maximum of intensity is monitored at 3.2 K. Below 3.2 K, the replacement of a significant proportion of the diffuse signal by intense and sharper reflections marks the system's first transition, from short to long range magnetic order. Furthermore, the magnetic patterns collected at 2.4 and 2.2 K reveal that a significant part of the diffuse feature remains well visible despite the stabilisation of intense Bragg reflections. Hence it is confirmed that both long and short range types of order coexist in the system in between the two ordering transitions, as previously reported from the D20 data.

Moreover, the D4 data does not reveal the stabilisation of sharp magnetic reflections in between 3.0 and 4.0 K, revealing the absence of a significant quantity of Gd_2O_3 impurity in the sample employed for the measurement. The magnetic features observed on the patterns are by consequence all attributed to the $SrGd_2O_4$ material, with no ambiguities. Considering the D20 data, some doubts remained regarding the diffuse feature proportions to be attributed to the Gd_2O_3 impurity. Nevertheless, by comparing the D20 and D4 measurements results, I confirm that by all points the temperature evolution of the magnetic scattering features attributed to both natural and isotopically enriched $SrGd_2O_4$ materials coincide in between the two data sets. The validity of the D20 observations as well as my interpretations of

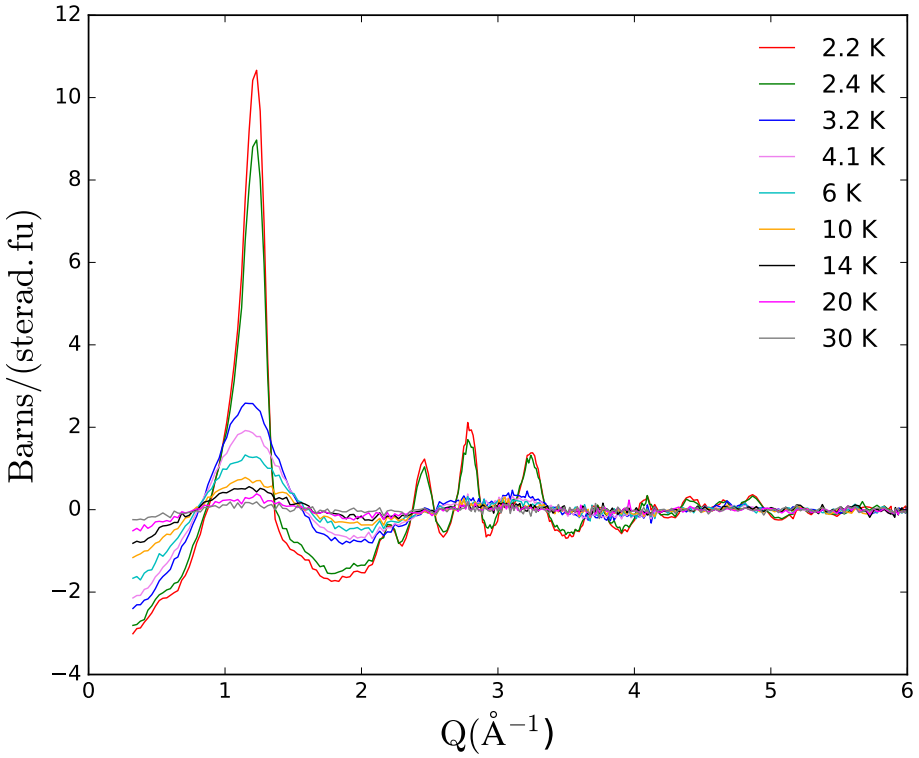

Figure 6.21: Magnetic scattering signal of the $SrGd_2O_4$ material collected on the D4 powder neutron diffractometer at temperatures ranging from 30 to 2.2 K. The magnetic signal component of each pattern was isolated by the subtraction of a 50 K nuclear background. The data reveals the stabilisation of broad diffuse features, progressively gaining intensity as an effect of temperature reduction. The features become much more localised and intense below the long range ordering transition temperature $T_{N1} = 2.72$ K.

the data proposed in the D20 result subsection 6.4.2, is consequently confirmed by the D4 observations.

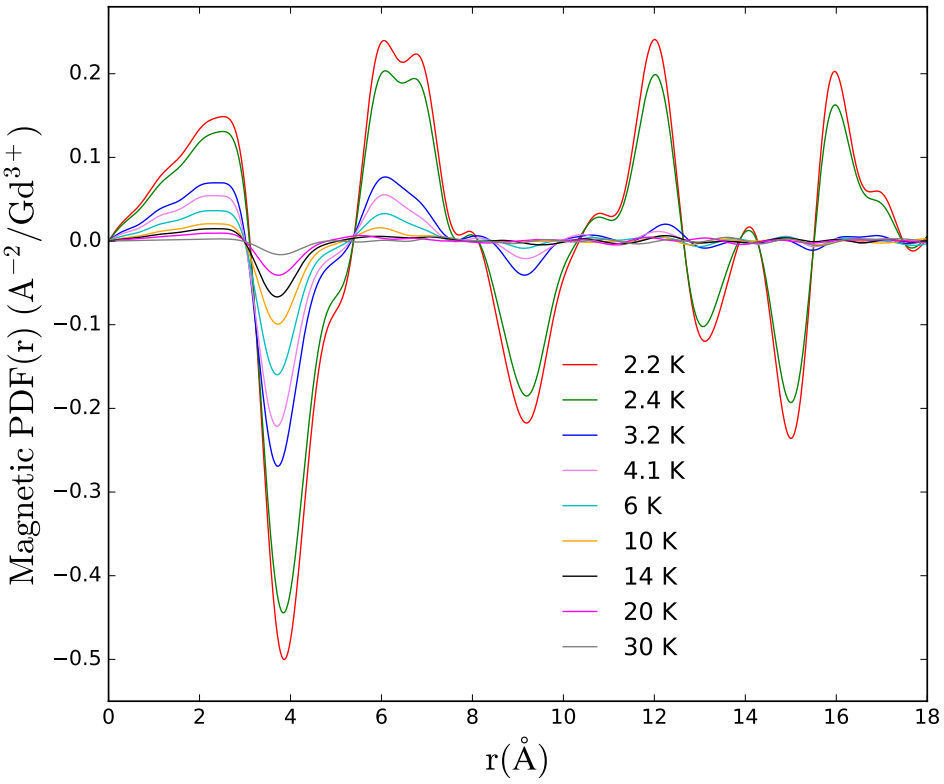

Figure 6.22: mPDF signal of the $SrGd_2O_4$ material obtained from Fourier transformations of the magnetic scattering patterns collected on the D4 instrument between 30 and 2.2 K previously displayed on Fig. 6.21. The data reveals the stabilisation of static correlations at temperatures lower than 3.2 K, corresponding to the system long range ordering induced by the transition at $T_{N1} = 2.72$ K. In addition, the features reveal the presence of dynamic correlations acting upon the system up to temperatures as high as 30 K.

The mPDF functions corresponding to the magnetic patterns collected between 30 and 2.2 K were computed via Fourier transformation and plotted as a function of inter ionic distances, see Fig. 6.22. From the data, I report the first stabilisation of features corresponding to dynamic correlations in the 30 K mPDF function. The magnitude and sharpness of the feature subsequently increases in a rather continuous manner as a effect of temperature reduction from 30 to 3.2 K. A sudden increase of the features' magnitudes and sharpness, corresponding to the primary long range ordering of the system is later observed in between 3.2 and

2.4 K. The large magnitude and rather localised character of the features displayed by the 2.2 and 2.4 K mPDF functions, are characteristic of static types of correlations induced by the long range ordered phase stabilised in the system at these temperatures. In comparison with the results previously obtained from the $SrNd_2O_4$ investigation (see subsection 5.4.4), the significantly larger peak widths obtained in the $SrGd_2O_4$ case is in perfect agreement with the participation of both Gd sites in the stabilisation of the long range ordered phase below T_{N1}. The positive slope present between 0 and ∼2.5 Å, reveals the stabilisation of ferromagnetic order propagating along the chains. The large magnitude of this feature indicates that magnetic moments involved in the ferromagnetic order point parallel to the chains directions of propagation [77]. The first negative peak centered at ∼3.8 Å at 2.2 K, on the other hand corresponds with the antiferromagnetic pairing of adjacent ferromagnetic chains, i.e. (Gd1-Gd1 = 3.612(5) Å, Gd2-Gd2 = 3.719(5) Å, Gd1-Gd2 = 3.884(4) and 4.112(4) Å). It is however difficult to determine an order of priority for the stabilisation of both ferro- and antiferromagnetic components of the magnetic phase. In fact, the stabilisation of both the ferromagnetic trend and the antiferromagnetic peak seem to proceed at rather close temperatures. Finally, due to the rather large width of the features located beyond this first negative peak, it is difficult at the current data treatment status to identify further correlations with the different features of the primary magnetic phase.

6.5 Summary and discussions

In this chapter, I have detailed a neutron scattering investigation of the different magnetic phases stabilised by the $SrGd_2O_4$ material at low temperatures. This neutron scattering investigation complements the bulk investigation work previously performed by Karunadasa *et al.* [24] and O. Young *et al.* [63, 64]. In order to localise the new progress among the previously published results, this chapter begins with a summary of the important results obtained by these two authors.

My neutron scattering investigation consists of diffraction measurements performed on both polycrystalline and single crystal samples of the $SrGd_2O_4$ material. $SrGd_2O_4$ material isotopically enriched at 99% in the non-absorbing ^{160}Gd isotope, or holding a natural content of the Gd element were employed for these measurements. A primary section in the chapter is hence dedicated to the preparation of both polycrystalline and single crystal samples of the $SrGd_2O_4$ material. The neutron scattering investigation is later detailed in different sections, progressively including the results obtained from different experiments. The overall order chosen

to present the different results considers a progressive description of the different mechanisms acting upon the system as an effect of temperature reduction. Additional results are later presented in order to both compare and confirm the different observations. In the following, I propose to the reader a summary of the principal results obtained through the series of neutron scattering experiments performed on the $SrGd_2O_4$ material.

The principal result of my neutrons scattering investigation consists in the successful structural determination of both long range magnetic phases consecutively stabilised by the two low temperature transitions undertaken by the material. The knowledge of the structural characteristics corresponding to the two magnetic orders, represents an essential information in the progression of the understanding of the $SrGd_2O_4$ magnetic system, and more generally of the $SrLn_2O_4$ family. An accurate determination of these characteristics was thus necessary, hence measurements have been performed employing different scattering techniques. The first magnetic transition occurring at $\sim$2.72 K, was found to stabilise a commensurate up-down-up-down (udud) Néel order aligning the moments along the c direction on both Gd type of sites. Different ordered moment magnitudes are however obtained for the two different types of sites. Though, it was impossible to establish a parallel between on one hand the type of Gd site, and on the other hand the obtained refined ordered moment magnitudes. This primary magnetic order is not significantly affected by the system second ordering transition occurring at $\sim$0.47 K, and remains stable down the lowest temperatures. Progressive increases of the ordered moment magnitudes are however observed, as an effect of temperature reduction below T_{N1}. The secondary magnetic phase stabilised below $\sim$0.47 K corresponds with a modulated (rrll) double Néel type of order, aligned along b and generated by a $\mathbf{k} = (0,0,0.42)$ propagation vector. The modulation periodically breaks the (rrll) order, being replaced by local points of right-left-right-left (rlrl) Néel order. Similarly to the primary phase, the two types of Gd sites are involved within the secondary ordered phase and are being attributed to different ordered moment magnitudes. In the material the two magnetic phases are superimposed as two separately ordered components, resulting in a composite magnetic structure stable from T_{N2} down to the lowest temperatures.

A detailed study of the magnetic scattering temperature evolution across the two ordering transitions is also proposed, revealing the action of two different ordering mechanisms successively acting over the system. In fact, I have first reported the stabilisation of an intense diffuse scattering feature preceding the primary long range ordering transition. The primary magnetic transition subsequently induces

a strong intensity reduction of this diffuse feature, replaced by intense magnetic Bragg peaks. The diffuse feature nevertheless, remains largely visible in the data down to the second transition temperature. The secondary transition afterwards results in the almost complete destruction of the remaining diffuse feature, benefiting to the emergence of a new incommensurate set of Bragg peaks. The stability of the primary phase reflections through the secondary transition, as well as the sudden consumption of different portions of the diffuse scattering feature reveal the action of two separate ordering mechanisms acting successively over the system. The temperature evolution of the scattering features through the primary transition was in addition investigated on a sample containing natural Gd by taking advantage of a short wavelength neutron beam. This particular set of data confirmed the previously detailed results.

Regarding the structural characteristics of the two subsequently stabilised long range ordered phases, it is understood that in both cases the magnetic orders can be explained employing the J_1-J_2 model. As previously detailed, this model implies two types of antiferromagnetic exchange interactions acting between first and second neighbours on the magnetic ladders. J_1 and J_2 are respectively interacting along the legs and rungs directions of the magnetic ladders. The primary magnetic phase of Néel (udud) type, corresponds to the strong J_2 limit. The secondary magnetic order on the other hand is believed to result from equivalent J_1 and J_2 interactions, resulting in a modulated combination of (rrll) and (rlrl) types of orders. Considering that both magnetic phases coexist in the system below T_{N2}, as well as the fact that both Gd sites are involved by each magnetic phases, it is impossible to employ two different J_1-J_2 models to simultaneously explain the two types of ordering. This problem in addition to the previously detailed low temperature binary dynamics of the system, calls for the involvement of an additional sets of magnetic interactions to the J_1-J_2 model. Of great interest, a model implying solely magnetic dipolar interactions between close neighbours bearing equal moment magnitudes, results in the stabilisation of a Néel order aligned along c. The up-down alternation of the magnetic spins around the structural hexagons reveals the absence of frustration in the dipolar model when applied to the $SrLn_2O_4$ systems. The dipolar interactions being anisotropic, it is natural to consider the spin directions aligned parallel to c since the first neighbours are found in this direction. The dipolar model thus fits surprisingly well the nature of the primary order. This purely dipolar model combined with the J_1-J_2 model attributed to the secondary phase, stands as a first coarse description of the $SrGd_2O_4$ magnetic system calling for further investigations. Interestingly, such a combination of dipolar and exchange

interactions was already proposed by Hasan and Southern in order to theoretically describe the $SrGd_2O_4$ system [38]. The two authors having aimed to simulate the bulk magnetic properties of the system via Monte Carlo simulations. It should also be mentioned that the $SrEr_2O_4$ system has already been reported to stabilise a long range Néel order aligning the Er1 moments along c, in addition to a short range (rrll) order involving the Er2 moments. These two types of orders were claimed to be respectively induced by dipolar and strong antiferromagnetic exchange interactions [31], supporting my understanding of the Gd system.

Within the frame of a global understanding of the $SrLn_2O_4$ systems, the implication of the results obtained from the investigation of the $SrGd_2O_4$ material in parallel with the previously published $SrEr_2O_4$ theoretical results are quite significant. In fact, it has now become clear that the stabilisation of (udud) Néel orders aligned along c are most probably induced by strong close neighbour dipolar interactions. This type of collinear order being uniquely observed in the case of Ln^{3+} ions having relatively large free ion magnitudes, e.g. $SrGd_2O_4$, $SrHo_2O_4$ and $SrEr_2O_4$. I believe that members of the family containing Ln^{3+} ions having smaller moment magnitudes are significantly less influenced by the dipolar interactions, and thus would not be in a position to stabilise the Néel order aligned along c. The strong J_1 and J_2 antiferromagnetic interactions, however can stabilise magnetic orders within the ab-plane of these materials, e.g. in the $SrNd_2O_4$ and $SrYb_2O_4$ cases. Both configurations can also be combined in a bipartite structure as in the particular $SrGd_2O_4$ case, or be separately established in the two different magnetic sites of the system such as in the $SrEr_2O_4$ case [31, 33]. This understanding of the physics of the $SrLn_2O_4$ systems can thus be considered as an essential progression in the study of these materials.

In order to verify my understanding of the $SrGd_2O_4$ magnetic system, it would be interesting to investigate the spin wave dispersion of the material employing inelastic neutron scattering techniques. Such an neutron scattering experiment was actually already attempted within the frame of this thesis. However, due to the rather small size of the isotopically enriched single crystal samples available, I were not able to collect enough signal to observe the inelastic excitations. This experiment was performed on the 4F2 triple axis diffractometer using a beam of thermal neutrons located at the LLB reactor source (Saclay). The flux available on this instrument is actually significantly lower than fluxes available on similar triple axis instruments alimented by other neutron sources. Thus, despite the small size of the crystal sample available there is still the chance to observe the spin dispersions of the system at low temperature. It could also be a possibility to regrind the sin-

gle crystal samples and attempt powder inelastic scattering experiments in order to maximise the signal. There is thus still hope to successfully elucidate the magnetic interaction scheme of the $SrGd_2O_4$ material.

Finally, investigating the field-induced properties of the material at low temperature taking advantage of neutron scattering techniques, remains among the future investigation perspectives of the $SrGd_2O_4$ system. In fact as reported by O. Young *et al.* [63, 64], long range ordered magnetic phases are expected to be stabilised when applying the field along the crystallographic c axis of the material. From the nature of the magnetic order stabilised bellow T_{N2}, interesting properties are also expected to be revealed by applying the field along the b axis. Determining the nature of the different field-induced magnetic phases should provide additional information for the development of my understanding of the system.

Chapter 7

Field-induced magnetic properties of $SrEr_2O_4$

7.1 Introduction

This chapter is dedicated to a neutron scattering investigation of the low temperature magnetic properties of the $SrEr_2O_4$ material. This particular variant of the $SrLn_2O_4$ family has already been the object of extensive investigations over the last decade from several authors. The work of the Warwick University Superconductivity and Magnetism (S&M) group and collaborators represents the major part of the already published work on the subject. The results presented in this chapter thus correspond with a project continuation, offering additional information to an already rather advanced understanding of the system.

It was in fact already established that $SrEr_2O_4$ stabilises a long range ordered magnetic phase below 0.71 K [37]. This magnetic order involving solely the magnetic moments sitting on Er1 sites consists of ferromagnetic ordering propagating along the chain directions, with two nearest neighbour chains being paired antiferromagnetically. This Ising type of order is induced by a ferromagnetic dipolar interaction acting along the chains' direction [31]. The magnetic moments borne by the Er2 site on the other hand are involved in a short range ordered phase of double Néel type, being mostly aligned along a [33]. This phase principally results from the strong competition of antiferromagnetic exchange interactions acting between first and second neighbours along the ladders legs and rungs directions, respectively [31, 33]. The absence of significant correlation acting between the two separate subsystems at low temperature was also clearly evidenced [33]. Of great interest, very different site dependant single ion anisotropies were also revealed in

the ground state, with easy axis of magnetisation parallel to the c and a axes for the first and second Er sites, respectively. This particularity of the system results in the observation of two separately evolving magnetic subsystems when subjected to an external magnetic field [31, 32].

I propose in this chapter to investigate the influence of such strong site-dependent anisotropy characteristics, over the magnetisation properties of the system at dilution fridge temperatures. Single crystal neutron diffraction techniques were employed for this purpose, and a series of experiments was conducted considering magnetic fields successively applied along the two easy axis directions of magnetisation.

7.2 Previously published results

Within the frame of the already advanced investigation of the $SrEr_2O_4$ material, this late participation to the project consists in the study of specific characteristics of the system, fully relying on the previously published results. It is thus necessary to begin this chapter by giving an accurate summary of the previously published results and to detail the implications of my results within this context. In the following, I detail the previously published results in a comprehensive order by synthesising the successively published papers in separate paragraphs.

The interest concerning the study of the low temperature magnetic properties of the $SrEr_2O_4$ material was sparked by Karunadasa *et al.* [24], who reported the first polycrystalline synthesis of the material. A low temperature characterisation of the material, consisting of magnetic susceptibility measurements was also reported revealing the paramagnetic nature of the system down to 2.0 K, the lowest temperature measured. The clear Weiss behaviour of the inverse susceptibility plotted as a function of temperature indicates the presence of strong antiferromagnetic interactions acting between the Er^{3+} ions. The presence of short range magnetic order is also reported to develop below 20 K, resulting in the observation of a broad intensity feature in NPD scattering patterns.

Beyond this point, further progress in the $SrEr_2O_4$ investigation are the fruits of research projects accomplished by O.A. Petrenko and collaborators. The first step in the investigation of the $SrEr_2O_4$ proposed by this author consists in extending the characterisation and neutron scattering measurements of the material down to dilution fridge temperatures [37]. From a specific heat measurement a sharp magnetic transition taking place at $T_N = 0.71$ K indicative of a long range ordering transition is evidenced, see Fig. 7.1 a). In addition, a broad maximum centered at

$\sim$1.5 K is observed preceding the sharp transition and identified as originating from the stabilisation of a short range ordered magnetic phase. A significant participation of low lying crystal field effects in the stabilisation of the broad maximum is also attested. A low temperature NPD investigation is later proposed confirming the stabilisation of both successively stabilised short and long range ordered phases. From a Rietveld refinement analysis of a magnetic pattern collected below T_{N}, the nature of the long range order was determined as consisting of ferromagnetic order established along the chains directions. Two adjacent chains are paired antiferromagnetically, resulting in a magnetic structure of Néel type. This magnetic phase being however solely established on a single type of Er site, the second site remaining largely disordered down to the lowest temperatures. A respective site attribution for the two types of magnetic orders hosted by the system below T_{N} being beyond the potential of Rietveld refinement analysis, long and short range orders were arbitrarily attributed to Er1 and Er2 sites, see Fig. 7.1 b). The refined magnitudes of the ordered magnetic moments associated to the long range order equals 4.5 μ_B, while less than 0.5 μ_B are attributed to the principally disordered phase. Such a difference of ordered magnitudes suggests the strong influence of crystal field effects over the system, as previously suggested from the interpretation of the specific heat data. The strong single ion anisotropy of the system was furthermore evidenced from single crystal magnetisation measurements performed above T_{N}. For this purpose, the crystal growth protocol for the synthesis of high quality single crystal samples of the $SrNd_2O_4$ material, was elaborated by Prof. Balakrishnan [84]. The floating zone techniques available at Warwick University were employed for the growth, resulting in the production of large single crystal boules of high crystalline quality.

The availability of large single crystal samples of the $SrEr_2O_4$ had in addition permitted to consider single crystal neutron scattering techniques to further investigate the low temperature magnetic phases stabilised by the material [33]. Large intensity maps of the neutron magnetic scattering signal could be collected below T_{N} in the (h,k,0) scattering plane of the material, confirming the stabilisation of a long range order of Néel types aligned along c, see equivalent measurement on Fig. 7.6 a). Concerning the short range ordered phase, undulated diffuse features propagating along k were measured in the (0,k,l) plane, see equivalent measurement on Fig. 7.11 a). These features were already observed at 0.8 K and are reported to gain intensity upon cooling down to dilution fridge temperatures. Interestingly, the diffuse features are present at $l = \pm 1/2, \pm 3/2$ and equivalent positions revealing a $\mathbf{k}$ = (0,0,0.5) propagation vector. The modulations propagating along k imply for the magnetic moments of the short range ordered phase, to be only weakly corre-

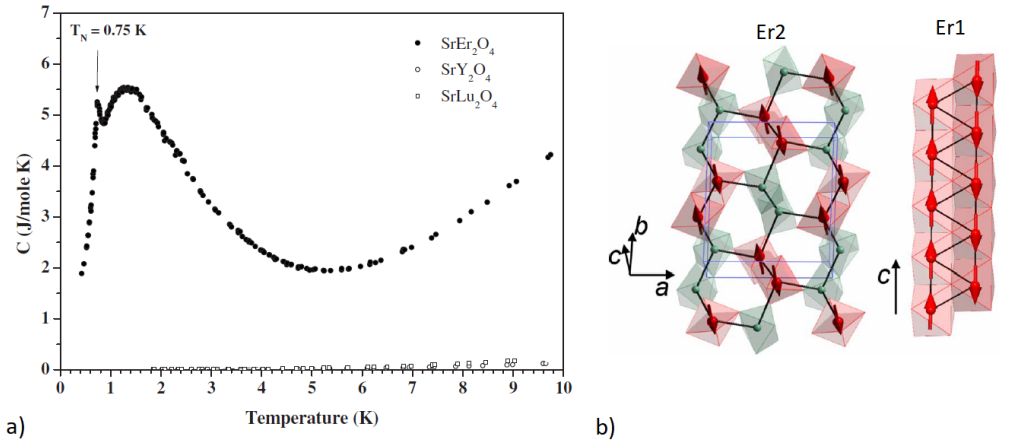

Figure 7.1: $SrEr_2O_4$ previously published results by ref. [37]. a) Temperature evolution of the $SrEr_2O_4$ specific heat measured on a single crystal sample of the material. A sharp transition of magnetic origin is evidenced at $T_N = 0.71$ K. Additional measurements performed on the Y and Lu non-magnetic members of the $SrLn_2O_4$ family are included on the diagram, revealing the small phonon contribution of the crystalline structure to the measurement below 10 K. b) Magnetic structure stabilised by the $SrEr_2O_4$ material below T_N and determined from NPD measurements. A long range order of Néel type (udud) is solely stabilised on the Er1 site, the second site remaining largely disordered below T_N. Figure reproduced from Ref. [37].

lated along the b axis. It was not clearly identified at the time if the diffuse features were one dimensional in nature or if the signal was significantly expending along the h direction. Thus, it was not possible to determine if the magnetic correlations are confined within the $a-c$ plane or uniquely acting along c. By analysing the low temperature intensity pattern of the diffuse features collected in the $(0,h,l)$ scattering plane, it was determined that magnetic moments belonging to the short range ordered phase point principally toward the a axis direction. Hence, two different crystallographic axes are respectively chosen as pointing directions by the magnetic moments involved in the two separate phases revealing a very Ising-like character for the system. Moreover, upon cooling the system through T_{N}, the absence of correlations between the ordering of the long range phase and the intensity evolution of the diffuse features, indicates a clear lack of coupling between the two coexisting phases. Such an independence between the two phases reveals the presence of two separate magnetic sub-lattices in the system, confirming the stabilisation of each phases on a single type of Er site. These results suggest the crystal field environments surrounding both magnetic sites to be radically different. However it has been suggested from the result of the specific heat measurement, that the difference in crystal field environments can not be considered as the unique reason for the stabilisation of two different magnetic phases on the material. The presence of different sets of interactions respectively acting between the magnetic moments sitting on the two different types of sites was thus suggested. Implying these arguments, Monte Carlo simulations of the short range ordered phase were carried out employing a model consisting of strong antiferromagnetic exchange interactions acting in between first neighbours on the magnetic ladder frame. The J_1-J_2 model was first considered, J_1 and J_2 respectively acting between first neighbours along the legs and the rungs directions. Magnetic patterns were calculated from the simulations results, exposing a net agreement with the experimental observations employing a $J_1/J_2 = 5$ ratio. If the antiferromagnetic exchange interaction J_1 does prevail in this configuration, this result also suggests the strong competition between both J_1 and J_2 as a probable explanation for the short range ordering to prevail down to the lowest temperatures.

The following step in the low temperature investigation of the $SrEr_2O_4$ system consisted in investigating the directionality of the system anisotropy employing both single crystal susceptibility and magnetisation measurement techniques [32], see Fig. 7.2 a) and b), respectively. Susceptibility curves were measured from 0.5 to 400 K, by successively applying a weak magnetic field along the three crystallographic directions of the material. A comparison of the high temperature trends adopted by the different curves revealing the system anisotropy as being of easy axis

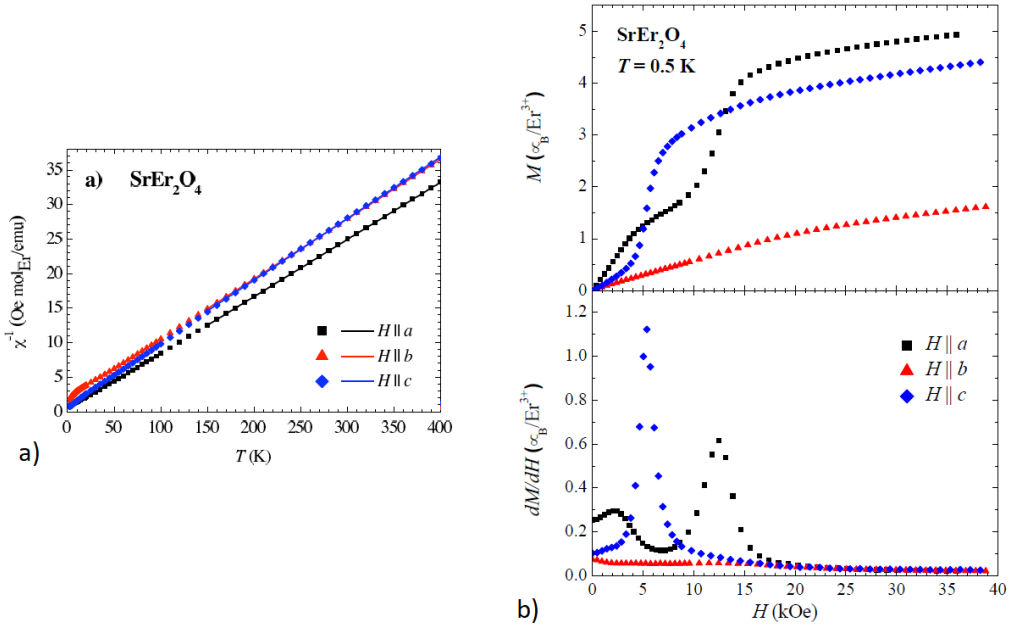

Figure 7.2: $SrEr_2O_4$ previously published results by ref. [32]. a) $SrEr_2O_4$ single crystal inverse magnetic susceptibility measurements obtained by applying a magnetic field of 1 kOe along the different crystallographic axes of the sample over the temperature range of 2-400 K. b) single crystal magnetisation measurements performed at 0.5 K for H alternately applied along a, b and c. Figure adapted from Ref. [32].

type. The crystallographic a direction being the easy axis of anisotropy. A series of magnetisation measurements subsequently performed at 0.5 K along the three crystallographic direction of the material revealed the low temperature easy plane nature of the magnetisation. The crystallographic b axis being the hard direction of magnetisation at 0.5 K. Still increasing asymptotic trends are adopted by the three curves at high field values, disclosing that a full polarisation of the system has not yet been achieved for a field magnitude of about 40 kOe applied in any of the three crystallographic directions. The magnetisation curves collected in H // a and H // c configurations display several crossing points as the magnitude of H is increased from 0 to ∼20 kOe. The field derivatives of the magnetisation curves were computed, bringing to light two successive field-induced transitions occurring in the H // a configuration. The first transition is seen as a broad feature of rather low magnitude, presenting a maximum at ∼2 kOe. On further increase of the field, a local minimum is encountered at ∼7 kOe, and followed by a strong re-increase of the trend creating a second localised maximum at ∼12.5 kOe. The maximum indicative of the second transition culminating significantly above the low field maximum, I expect the second transition to stabilise long range ordered magnetic phases in the system. It is also important to mention that the magnetisation value measured at ∼7 kOe corresponds to about a third of the maximum value collected at 40 kOe. This ratio suggesting the stabilisation of a two up one down (uud) type of spin arrangement propagating along the magnetic ladders, the spin being aligned along the field direction. This particular phase being only stable in the intermediate field range defined by the two ordering transitions. An additional transition is subsequently disclosed by the derivative of the H // c magnetisation curve, displaying a single maximum located at ∼6 kOe. This third maximum culminating significantly above the H // a maximum, a long range ordered magnetic phase is here also expected to be stabilised. A recent repetition of the H // a magnetisation measurement was conducted by a collaborator at the Néel institut (Grenoble). Magnetisation data were collected at various temperatures ranging from 2.0 to 0.09 K. The data reveal significantly more acute transitions as the lowest temperatures are approached, as well as a significant drift toward lower field values for the second transition. Very different field-induced behaviours are thus observed according to the crystallographic axes of the material revealing the stabilisation of three distinct magnetic phases. These observations suggest that different physics separately associated to the two different Er sites are separately contributing to the system magnetisation in the different field configurations.

Considering these intriguing magnetic properties of anisotropy as well as the

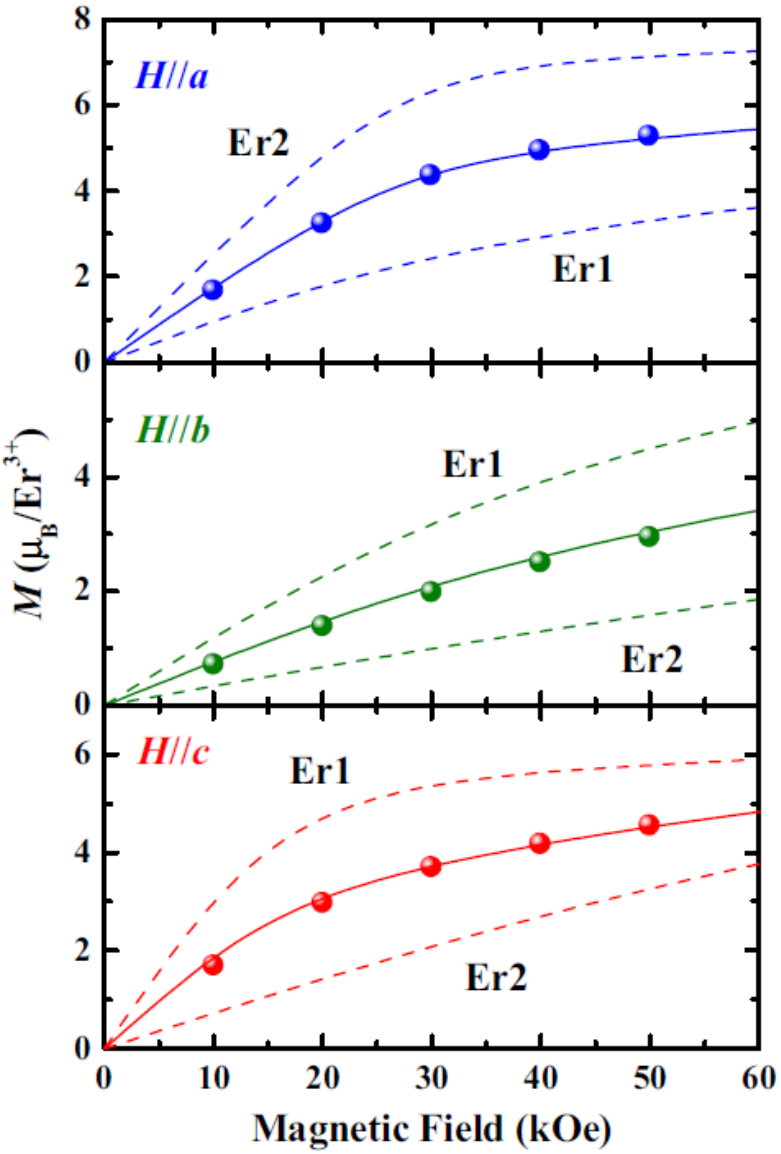

Figure 7.3: Measured (symbols) and calculated (solid lines) $SrEr_2O_4$ single crystal magnetisation curves for H applied according to the three crystallographic axes of the material at $T = 5$ K. The individual field evolution of sites Er1 and Er2 magnetic moments are displayed as dashed lines. Figure reproduced from Ref. [31].

very different low temperature magnetic phases individually stabilised on both Er sites, it was decided to investigate the single ion properties of the material by determining the sets of crystal fields parameters corresponding to both Er sites [31]. The characteristics of the magnetic interactions acting between neighbouring Er sites were also explored in order to propose a ground state magnetic Hamiltonian for the system. The crystal field environment surrounding the magnetic ions sitting at the two crystallographically inequivalent Er1 and Er2 sites were thus determined by combining results obtained using inelastic neutron scattering, site selective optical and electron paramagnetic resonance techniques. The inelastic neutron scattering measurements were performed using a polycrystalline sample of the $SrEr_2O_4$ material, while for the site selective optical and electron paramagnetic resonance measurements, a slightly Er doped single crystal of the non magnetic yttrium variant of the $SrLn_2O_4$ family was employed. The result of this analysis returning two sets of crystal field parameters being related to the crystallographic axis of the material. The low temperature magnetisation curves of the system were subsequently simulated considering for both sites, a calculated set of close neighbours magnetic interactions corresponding to the stabilisation of the low temperature phases, see Fig.7.3. The experimentally determined site specific sets of crystal field parameters were in addition included to the Hamiltonian of the model. The simulated magnetisation curves, particularly well matching the experimental observations confirm the proper understanding of the magnetic interactions schemes corresponding to both Er sites. The accuracy of the experimentally determined sets of crystal field parameters is also confirmed. Of particular interest, the specificity of the Hamiltonian model employed for the simulations considers the allocation of the long range ordered phase to the Er1 site. Moreover in this particular phase, the ferromagnetic chains propagating along c were considered as being stabilised by dipolar interactions. The second site hosting the short range ordered phase on the other hand results from the strong competition of close neighbour antiferromagnetic exchange interactions, as previously suggested by Ref. [33].

From these results, it is clear that both single ion effects and collective interactions should be considered for a proper understanding of the complex low temperature properties of the $SrEr_2O_4$ material. The magnetic ground state and field-induced properties of the two different Er sites in the system were also understood as being governed by completely different physics revealing strongly Ising-like behaviours. This particularity of the $SrEr_2O_4$ system being quite unusual and intriguing has ignited my interest to determine the nature of the different field-induced magnetic phases stabilised by the system at dilution fridge temperatures. The struc-

tural characteristics of these phases are expected to provide precious information in order to confirm and improve the peculiarities of the system Hamiltonian.

7.3 Neutron scattering investigation

With an objective to determine the nature of the field-induced magnetic phases stabilised in both H // a and H // c configurations, as well as to further understand the transitions mechanisms experienced by the spins, single crystal neutron scattering techniques were utilised through a series of experiments. In the following, I start the presentation of my results obtained from experiments performed on the D9 (ILL) and WISH (ISIS) neutron diffractometers when applying the magnetic field along the c axis of the material structure. The measurements results obtained in the H // a configuration corresponding to experiments performed on both WISH and D10 (ILL) diffractometers are subsequently detailed.

The single crystal diffractometer D9 equipped with a cryomagnet, was first employed in an objective to determine the nature of the field-induced order stabilised in the H // c configuration. The regular cryostat available at the time on the instrument would only provide a base temperature of 1.5 K, i.e. a temperature significantly higher than T_{N}. However, single crystal magnetisation measurements previously performed at 1.6 and 2.0 K with H // c, clearly evidenced the occurrence of the field-induced magnetic transition taking place in between 10 and 15 kOe [31, 37]. Thus for the neutron scattering measurement, a field magnitude of 20 kOe was applied along the c axis of the crystal sample, ensuring the stabilisation of the field-induced magnetic phase in the system. In these conditions, a large collection of sharp magnetic reflections could be measured and exploited to determine the nature of the field-induced magnetic order. Furthermore, in order to guarantee a very high precision on the measurement, a rather small single crystal sample was chosen, reducing absorption, multiple scattering and extinction measuring issues.

Then considering the WISH experiments, large reciprocal space maps of intensity were collected taking advantage of the substantial detector banks coverage available on the instrument. The collection of these scattering maps offering precious information regarding the evolution of the different scattering features as a function of applied field magnitudes and temperatures. The instrument was equipped with a dilution fridge cryostat and a cryomagnet, enabling for measurements at temperatures as low as 60 mK under various magnitudes of applied field. A rather large $SrEr_2O_4$ single crystal sample was employed for the measurement in the H // c configuration, in an objective to maximise the scattering intensities and reveal low

intensity details. Furthermore, the measurement in the H // a configuration was performed prior to the addition of the second detector bank to the instrument. The reciprocal space coverage presented on the scattering maps is consequently halved in this configuration.

To accurately determine the nature of the different field-induced phases stabilised at low temperatures in the H // a configuration, data were collected on the D10 single crystal diffractometer. For this purpose, the instrument was equipped with a dilution fridge cryostat and a cryomagnet. Large collections of magnetic reflections were measured at ∼60 mK under various field values and subsequently treated via single crystal refinement analysis techniques. The successive magnetic structures obtained returning a progressive visualisation of the magnetic orders evolution as a function of applied field magnitudes. The field evolution of several magnetic reflections characteristic of the different orders hosted by the systems were also investigated at the lowest temperatures. The temperature evolution of these reflections was in addition investigated under several values of applied field. A small single crystal was here also employed for the experiment to maximise the measuring accuracy.

I would like to clearly mention at this point, that the single crystal samples used in the frame of these neutron scattering investigation were grown prior to the start of this PhD project by Prof. G. Balakrishnan and T.J. Hayes. These samples were however unlabelled and unprepared for neutron scattering experiments, hence crystallinity inspections, orientation and adequate surface cuts were considered in the frame of this late investigation of the $SrEr_2O_4$ system. In addition, the experiment conducted on the WISH diffractometer in the H // a configuration was also performed prior to the start of this project. The results of this experiment were however left unexploited and a retrieval of both data and experimental measurement conditions had to be considered. The treatment of the data and the production of accurate maps of scattering intensity could then be achieved. Information about the single crystal sample employed for these particular measurement on the other hand could not be retrieved.

7.3.1 H // c, WISH, D9

By applying a field along the c axis of the material at a temperature lower than T_N, I expect to perturb in priority the long range Néel order established on Er1 sites. The magnetic chains of this phase are ferromagnetically aligned along c but two adjacent chains are paired antiferromagnetically. Thus when applying the field, half the number of spins involved in this particular magnetic phase will find themselves in

an unstable equilibrium state favouring spin-flip transitions. Because of the sudden jump experienced at low field by the 0.5 K magnetisation curve measured along c (see Fig. 7.2 b)), I expect the system to undergo a metamagnetic transition resulting in the alignment of all Er1 ferromagnetic chains along the field direction, i.e. along c. On further increase of the field, a progressive destruction of the short range ordered magnetic phases hosted by Er2 sites is also expected to proceed, resulting in the system full polarisation along c.

To verify these assumptions, I first investigated the nature of the low temperature field-induced magnetic order stabilised by the $SrEr_2O_4$ material using single crystal neutron diffraction techniques on the D9 diffractometer. The wavelength of the instrument was set to 0.5 Å, the instrument receiving neutrons from the reactor's hot source. A small single crystal of high crystalline quality with dimensions respectively equal to ∼1.1, 3.8 and 2.9 mm along a, b and c was chosen for the experiment, see Fig. 7.4. Glued to the tip of an aluminium pin, it was inserted within the cryomagnet and oriented with the c axis set vertically, i.e. along the direction of the applied field. It was subsequently cooled down to 1.5 K, the base temperature of the cryostat. Once this temperature was reached and stabilised, the external magnetic field was turned on and progressively increased until a magnitude of 20.0 kOe was reached, stabilising the field-induced order in the system. In these conditions, a set of ∼540 commensurate reflections was collected, returning 130 inequivalent reflections after data reduction. The sharp nature of the measured reflections confirming the field-induced stabilisation of a long range magnetic order in the system. An additional set of intensities was later collected at 20 K in zero field conditions, and subsequently subtracted from the low temperature data to isolate the magnetic component of the signal. A correction for absorption was in addition applied to the data, employing the Datap [58, 59] software. A linear absorption coefficient $\mu = 0.9270$ cm^{-1} was computed employing the neutron cross sections parameters tabulated in [87], and a precise modelisation of the sample shape were used for this calculation. The magnetic intensities were then considered in a single crystal refinement analysis utilising the FullProf software suite [55]. As expected, the best fit was returned employing a ferromagnetic irreducible representation considering the spins aligned along c (see Appendix A.2.1, IRrep or Γ4). Refined moments magnitudes of 5.41(8) and 1.92(8) μ_B, being individually allocated to the two different Er sites were obtained. Averaging these two values returns a very good agreement with the previously published magnetisation data collected at 2.0 K [31], confirming the accuracy of both measurement and data refinement procedures. As previously discussed, it is not possible from refinement analyses of scattering data to determine

the site allocation of different magnetic phases simultaneously hosted by $SrLn_2O_4$ materials. However, from the previously published knowledge of the $SrEr_2O_4$ system (see section 7.2), it is evident that Er1 sites are hosting the largest ordered moment magnitude aligned along c.

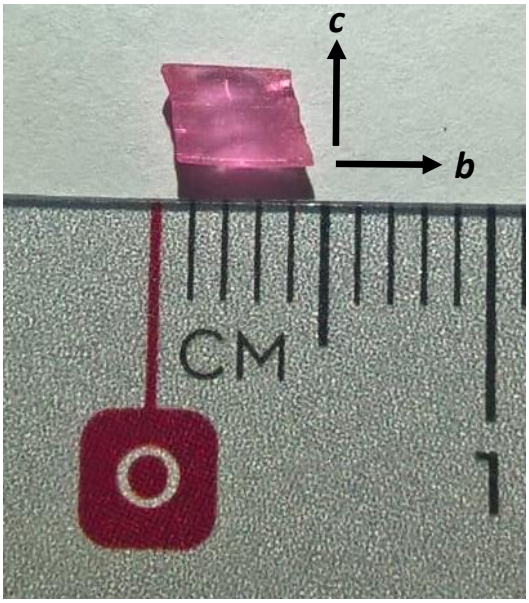

Figure 7.4: Single crystal sample of $SrEr_2O_4$ employed for the D9 experiment in the H // c configuration. For the experiment, the sample was glue to the tip of an Al pine, aligning the crystallographic c direction parallel with the pin axis. The largest face of the sample (facing up on the picture) was cut perpendicularly to the a direction within the bc plane.

Two dimensional reciprocal space intensity maps of the material were subsequently produced utilising the WISH diffractometer. These maps offering global visualisations of the magnetic scattering features evolution, as a function of applied field magnitudes and of temperatures. In order to visualise the strongest effect of the field-induced transition, I focused on measuring the magnetic intensities located in the (h,k,0) scattering plane. Thus similarly to the D9 measurement, the c axis of the sample was aligned vertically in the centre of the cryomagnet, i.e. along the applied field direction. In this experimental configuration, the (h,k,0) scattering plane is aligned horizontally within the lab reference frame. (h,k,0) scattering patterns can then be recreated on the detector banks using the time-of-flight technique implemented on the instrument. The sample, a rather large single crystal of dimension respectively equal to approximately (4 x 6 x 10 mm) according to the crystallographic axis a, b and c (implying only the thickest parts of the sample) was

attached to a copper oxide free sample holder, ensuring for proper thermalisation at the lowest temperatures, see Fig. 7.5. The measurement procedure consisted in collecting scattering patterns at regular intervals of applied field magnitude ranging from 0 to 50 kOe, while keeping the temperature constant. The procedure was repeated at several values of temperature ranging between 60 mK (cryostat base temperature) and 0.8 K. The sample was warmed up to 5 K in between every temperature interval considered, ensuring for the destruction of field-induced frozen states. A large coverage of the $H//c$ - T magnetic phase diagram of the material was thus investigated over this experiment. Nuclear patterns were in addition collected at 14.5 K, and subtracted from the low temperature data in order to isolate the magnetic component of the signal.

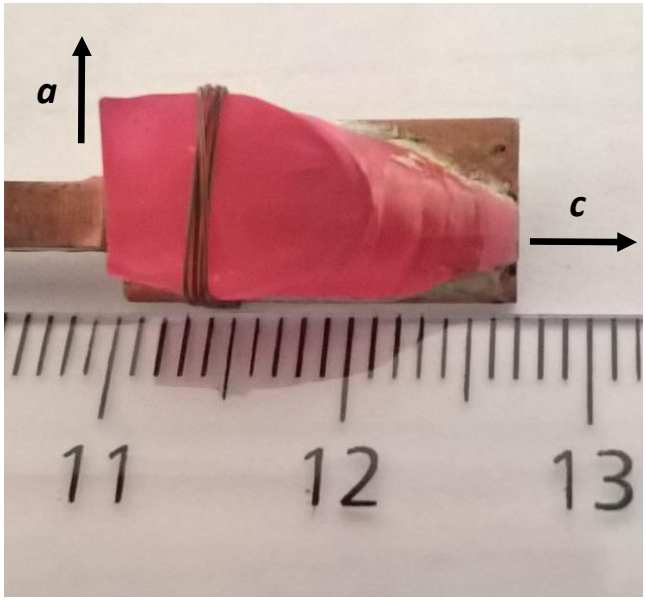

Figure 7.5: Single crystal sample of $SrEr_2O_4$ employed for the WISH experiment in the H // c configuration. The crystallographic c direction of the sample is aligned along the Cu pin direction, i.e. parallel to the ruler direction, see black arrow. The largest face of the crystal, glued to the sample holder plate area is cut perpendicular to the b axis and thus defines the ac plane of the crystal.

Figure 7.6 presents a combination of (h,k,0) magnetic scattering patterns collected at ∼60.0 mK, under the applied field magnitudes of 0.0, 3.0, 6.0 and 50.0 kOe. This successive evolution of the scattering features captures most of the physics involved in the field-induced transition process. In zero field conditions, the measured scattering patterns corresponds with the previously published $\mathbf{k} = 0$ long range Néel order established on Er1 sites [33, 37]. The observed pattern of well

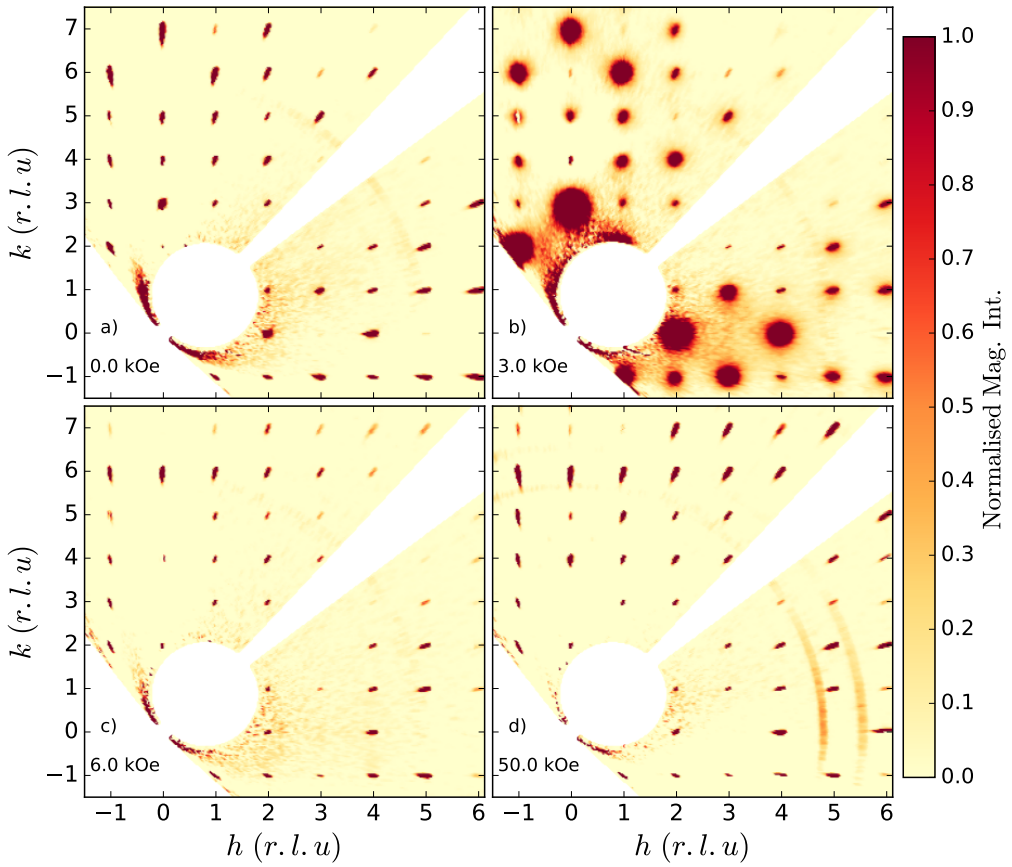

Figure 7.6: Single crystal scattering maps of the $SrEr_2O_4$ system measured at 60 mK, under field magnitudes of 0.0, 3.0, 6.0 and 50.0 kOe, applied along the c axis of the crystallographic structure. The measurements were performed on the WISH (ISIS) instrument and the data were collected in the (h,k,0) scattering plane of the material. The data are plotted as a function of h and k expressed in reciprocal lattice units ($r.l.u$). The two quadrants visible on the panels correspond to the two detector banks implemented on the instrument. Only the magnetic components of the data is considered on these diagrams for clarity. The evolution of the scattering patterns successively reveals the destruction of the zero field long range Néel order, followed by the stabilisation of a long range ordered ferromagnetic phase for $H = 6.0$ kOe, and by a progressive increase of the field-induced ferromagnetic component for $6.0 \leq H \leq 50.0$ kOe. The circles visible on the 50 kOe panel are both Cu and Al scattering powder lines. Their intensity increase seen under high applied field magnitude is induced by a slight field-induced motion of the sample holder. A correction for absorption as well as a vanadium normalisation of the scattering intensities were considered for the preparation of these maps.

defined magnetic Bragg peaks, in particular includes several strong antiferromagnetic reflections such as the (0,k=odd,0) or ($\pm$1,k=even,0) series, see Fig. 7.6, a). By 3.0 kOe, the data reveals a replacement of the sharp and localised reflections by broad diffuse features, the strong antiferromagnetic reflections being particularly affected, see Fig. 7.6, b). On further increase of the field magnitude, I have observed a progressive disappearance of the diffuse features, replaced anew by sharp and well defined Bragg reflections for $H = 6.0$ kOe, see Fig. 7.6, c). This $\mathbf{k} = 0$ magnetic pattern displaying strong ferromagnetic reflections such as the (0,k=even,0) or ($\pm$1,k=odd,0) series, confirms the stabilisation of a long range ferromagnetic order aligned along c, as previously observed with the D9 instrument. I note that the rather low field magnitude being sufficient to drive the system from antiferromagnetism to ferromagnetism is consistent with the metamagnetic nature of the transition. By subsequently increasing the field in a progressive manner all the way from 6.0 to 50 kOe, no sudden intensity variations were monitored confirming the absence of additional field-induced transitions in agreement with the magnetisation results. A general increase of the Bragg intensities is however monitored, evidencing a development of the ferromagnetic ordered component of the system as a function of increasing applied field magnitudes, see Fig. 7.6, d).

Due to the large crystal sample employed in an objective to maximise the measured intensities of the measurements, a single crystal refinement analysis of the magnetic data could not be accomplished. In fact I have intended to correct the data for absorption but the polychromatic beam of neutron exploited by the WISH instrument, as well as the large size of the sample rendered this task uncertain. In addition, multiple scattering and extinction artefacts are expected to significantly affect the observations by either adding intensities to particular weak and forbidden reflections or reducing the intensities of normally strong reflections. Moreover, the 14.5 K nuclear background subtracted is not particularly adequate for the preparation of a magnetic reflection set dedicated to refinement analyses. As previously mentioned while detailing the refinement procedures employed for the $SrNd_2O_4$ (see subsection 5.4.2), the slight shrinkage experienced by the nuclear unit cell as a function of temperature reduction significantly reduces the accuracy of the background subtraction procedure.

It is however interesting to individually compare these scattering maps with simulations in order to capture the principal characteristics of the magnetic phases involved in the transition. Simulated scattering maps corresponding to different magnetic structures were produced with the help of the software Mag2Pol [57], see Fig. 7.7. To enhance the diagrams clarity in addition to the colour gradient, the

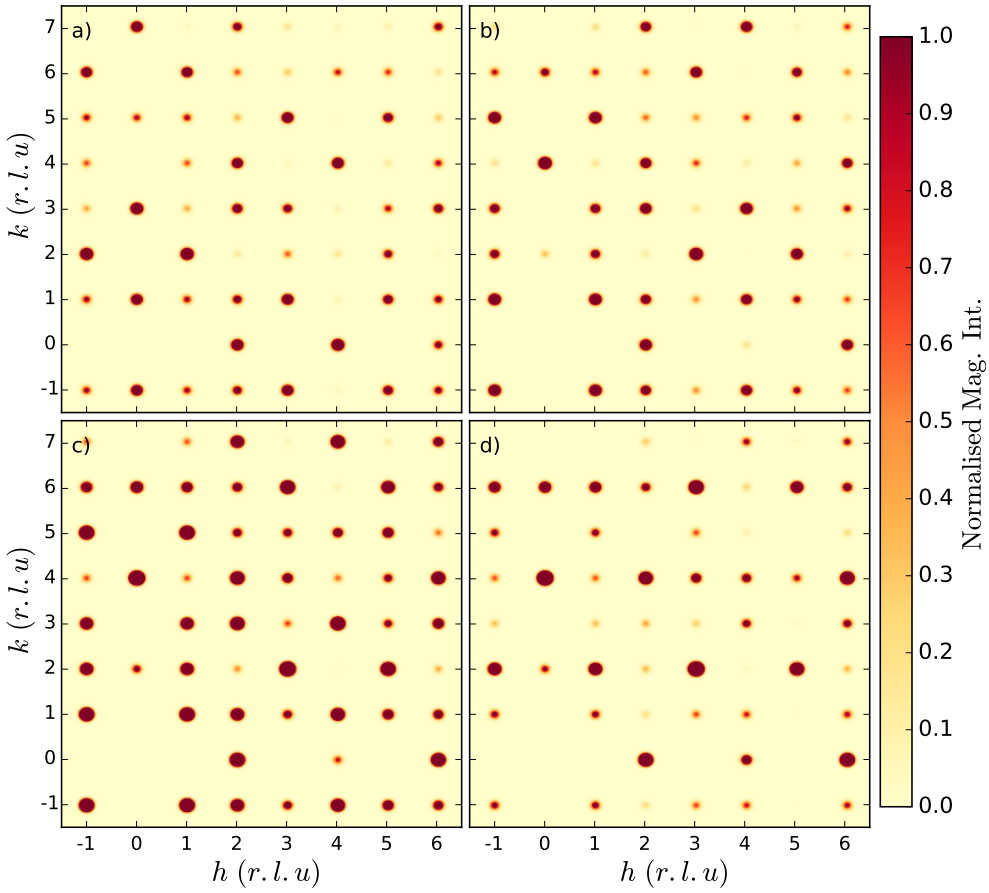

Figure 7.7: Simulated (h,k,0) single crystal neutron scattering maps of magnetic intensities corresponding to different magnetic orders stabilised on the $SrEr_2O_4$ system. The intensities were simulated with the Mag2Pol software using a 2.0 Å monochromatic neutron beam. Also, to facilitate the comparisons, the (h,k,0) coverage presented corresponds with the experimental coverage of the scattering maps presented in Fig. 7.6. a) considers a Néel order aligned along c, employing 4.5 μ_B on Er1 sites. b) considers a ferromagnetic order aligned along c, employing 5.0 μ_B on Er1 sites. c) considers a ferromagnetic order aligned along c, employing 9.5 and 0.5 μ_B on Er1 and Er2 sites, respectively. d) considers a ferromagnetic order aligned along c, employing 6.0 and 4.0 μ_B on Er1 and Er2 sites, respectively.

reflection diameters are proportional to the intensities. I start by comparing the zero field data, with simulated intensities obtained considering a Néel order involving magnetic moments of 4.5 μ_B aligned along c on the Er1 sites, in agreement with the previously published powder results [37]. The simulated scattering map is displayed in the top left panel of Fig. 7.7. A rather good agreement is obtained with the experimental scattering pattern, confirming the previously published NPD results. However, the addition or absence of particular reflections in the experimental pattern such as (4,±1,0), (0,4,0) and (6,0,0) reveals the non quantitative nature of the WISH data, making single crystal refinement analyses impossible to proceed with. I have then intended to simulate the scattering pattern corresponding to the applied field magnitude of 6.0 kOe, see Fig. 7.7, b). From the previously published magnetisation measurements, I expect an average of ∼2.25 μ_B per Er^{3+} aligned along the c axis under these field and temperature conditions [31, 32]. However, I have monitored the diffuse scattering features generated by the Er2 magnetic moments remaining rather stable in the (h,k,-1/2) plane, up to applied field magnitudes higher than 10 kOe, see Fig. 7.8. It is thus clear that only Er1 magnetic sites significantly contribute to the field-induced long range order under a field value of 6.0 kOe. I have consequently considered 5.0 μ_B ferromagnetically aligned along c on Er1 sites uniquely for the simulation. This value being consistent with the 4.5 μ_B borne by the Er1 sites in the zero field conditions. Despite a few clear differences, the simulation result shows a net agreement with the experimental scattering pattern. In particular the peculiar lozenge shaped features centered around the (0,3,0) and (0,5,0) positions are well reproduced. With a field magnitude of 50.0 kOe, ∼5 μ_B per Er^{3+} are expected to be ferromagnetically aligned along the field direction in order to match the magnetisation measurement results [31, 32]. Under this rather high value of applied field, the diffuse scattering features previously observed in the (h,k,-1/2) scattering plane have completely disappeared, I thus expect the magnetic moments sitting on both sites to contribute in the field-induced ferromagnetic order. In order to verify this argument, two simulations were performed, the first one considering 9.5 and 0.5 μ_B (see Fig. 7.7, c)) and the second one 6.0 and 4.0 μ_B (see Fig. 7.7, d)), respectively aligned along c on Er1 and Er2 sites. Comparing both simulated intensity maps with the experimental results confirms the stabilisation of a field-induced ferromagnetic order principally hosted by Er1 sites. In fact, the significant discrepancies observed between the data and simulated scattering maps d), confirms that ferromagnetic orders individually established on the two Er sites cannot involve magnetic moments of equivalent magnitudes.

This last result is in disagreement with the refinement analysis of the D9 data,

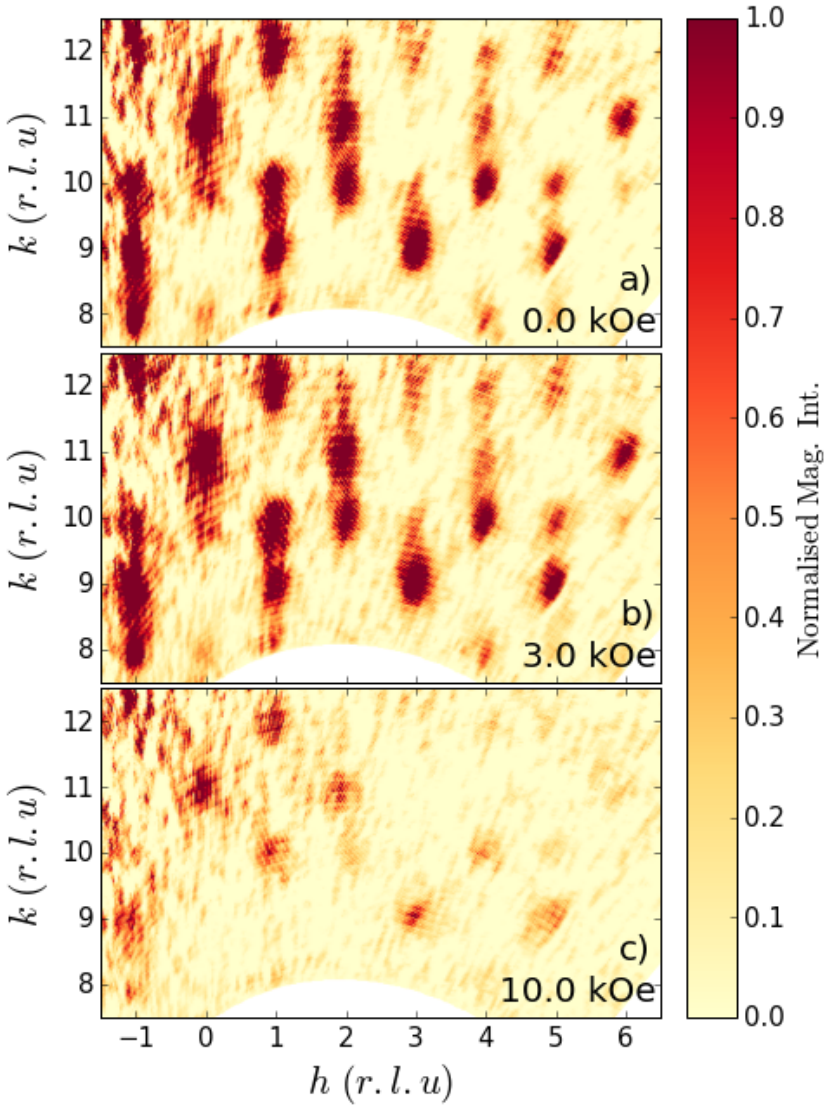

Figure 7.8: Magnetic diffuse scattering features of the $SrEr_2O_4$ system measured at 60 mK on the WISH diffractometer. These features were observed in the (h,k,-1/2) scattering plane and are produced by the short range ordered phases hosted by Er2 sites. These successive intensity maps were collected in the $H//c$ configuration under applied field magnitudes of 0.0, 3.0 and 10.0 kOe. The limited vertical aperture of the cryomagnet is responsible for the high k region considered on the maps.

returning sizeable ferromagnetic components for the magnetic moments established on both Er sites in the field-induced phase. Such a difference of behaviour could be explained by the distant measuring temperatures considered for the WISH and D9 measurements. The stability of the zero-field short range ordered phase hosted by Er2 sites is thus significantly enhanced at 60 mK in comparison with the 1.5 K observations. This result discloses the strong temperature strengthening of this magnetic phase as the temperature is lowered to dilution fridge temperatures.

A more accurate visualisation of the scattering features was in addition considered, through the production of one dimensional intensity profiles corresponding to cuts performed in the previously detailed scattering maps. This representation offers the possibility to superimpose in a clear manner, the scattering features measured at a particular reciprocal space position under various magnitudes of applied field. The field evolution of the four (1,6,0), (0,3,0), (4,0,0) and (0,6,0) reflections, exhibiting characteristic behaviours through the field-induced transition are considered in a combined diagram, see Fig. 7.9. These reflections were also chosen due to their large magnitudes, reducing the influence of scattering artefacts and imperfect nuclear background subtraction issues on the measurement. The two reflections (1,6,0) and (4,0,0) are both undergoing a strong intensity decreases between 0.0 and 3.0 kOe, resulting in the stabilisation of broad diffuse features surrounding weak Bragg peaks. By 6 kOe, these two reflections have become much more localised and the diffuse scattering components previously observed have disappeared. A significant increase of the sharp features stabilised at 6.0 kOe is then observed when raising the field magnitude to 50 kOe. The (0,3,0) reflection also displays quite an interesting behaviour, by having completely disappeared when the field magnitude of $\sim$6.0 kOe is reached. A large amount of diffuse scattering was also previously monitored as a broad feature surrounding a weak peak for $H = 3.0$ kOe. Reflection (0,6,0) behaves in opposition with the (0,3,0), in a sense that the first significant intensities are monitored once the applied field magnitude of 6.0 kOe is reached. A strong increase of the peak intensity in then monitored between 6.0 and 50.0 kOe.

The fits displayed as continuous lines on top of the data points were obtained from the combination of a back-to-back exponential [56] with a double Sigmoidal function [88], respectively fitting the sharp and diffuse components of the reflections, see Fig. 7.9. Both functions presenting a significant asymmetry, accounting for the peculiar peak shape of time-of-flight type of reflections. The intensities of both sharp and diffuse components of the peaks being directly obtained from the fitting procedure, the field evolution of these quantities could be separately reported in an additional combined diagram, see Fig. 7.10. Such combination of information

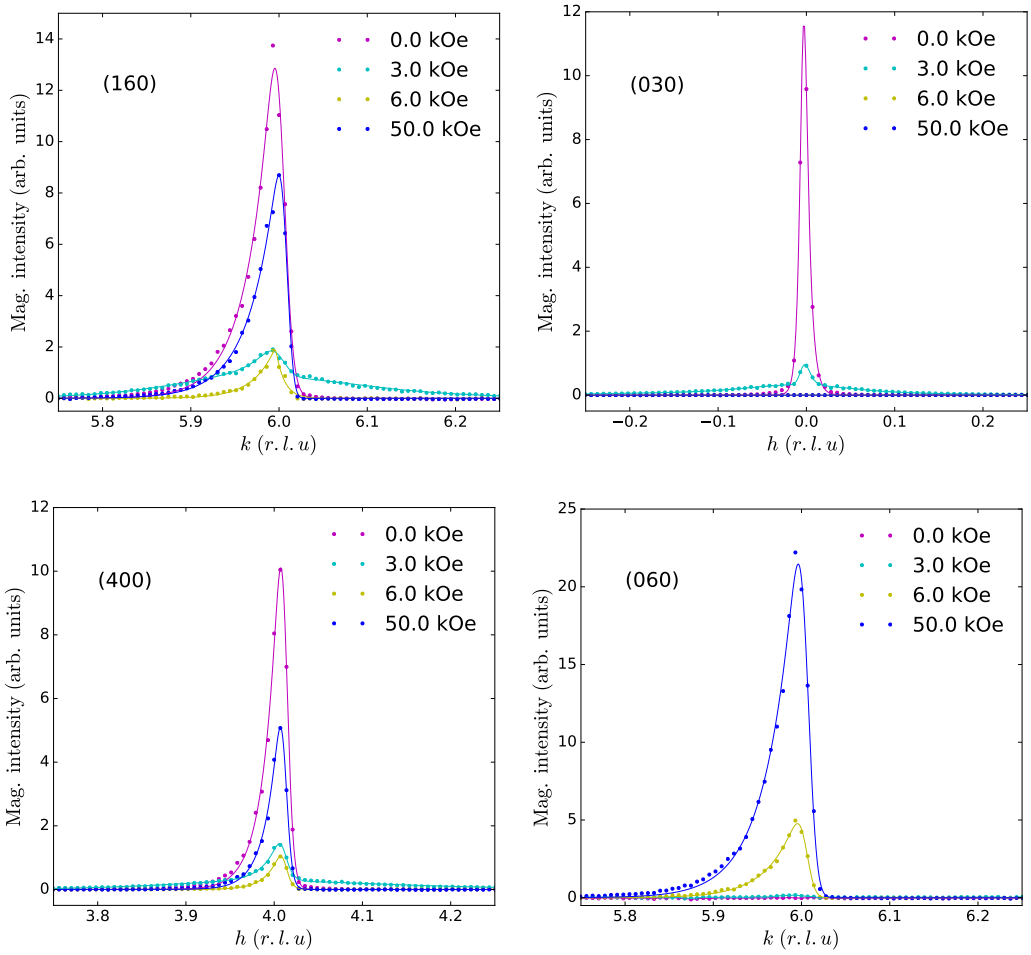

Figure 7.9: One dimensional intensity profiles of the magnetic reflections (1,6,0), (0,3,0), (4,0,0) and (0,6,0), collected on a single crystal of the $SrEr_2O_4$ system as a function of field applied along c. The profiles were obtained by proceeding to cuts along the principal scattering directions of the intensity maps presented in Fig. 7.6. While the intensities are shown in arbitrary units, the same data treatment procedure was executed for each reflection, making the intensities directly comparable. The data collected at 0.0, 3.0, 6.0 and 50.0 kOe are successively represented in magenta, cyan, yellow and blue, respectively. Data and fits being individually represented by dots and continuous lines. The fitting procedure considers the combination of a back-to-back exponential and of a double Sigmoidal, respectively accounting for the sharp and diffuse component of the reflections.

offers the possibility to display a detailed evolution of the field-induced behaviour of individual reflections, as well as to superimpose the observations measured at 0.06, 0.5 and 0.8 K. For clarity, the field evolution of the reflections' diffuse components if existing, are displayed in the lower insets of the panels. Also, in order to accurately evidence the magnetic transition, field steps of 1.0 kOe are observed from 0.0 to 10.0 kOe in between the data points.

I begin to detail the data solely considering the lowest temperature measurements. A strong decay of the sharp antiferromagnetic components of reflections (1,6,0), (0,3,0), (4,0,0) is first monitored, starting at an applied field magnitude comprised between 1 and 2 kOe. Between 4 and 5 kOe, the Bragg components of these reflections have already reached minimal values, indicating the complete destruction of the initial long range magnetic order established on Er1 sites. Simultaneously, these reflections have stabilised strong diffuse components for $1 \leq H \leq 2$ kOe, revealing the induction of large magnetic disorder quantities in the system. A decrease of intensity starting at $\sim$2.0 kOe is later undergone by the diffuse features, indicating a progressive reduction of the magnetic disorder previously induced. A complete annihilation of the diffuse features is subsequently achieved between 5 and 6 kOe. Moreover, between 4 and 5 kOe the Bragg intensity minima evidenced by reflections (1,6,0), (0,3,0), (4,0,0) is directly followed by a re-increase of the (1,6,0) and (4,0,0) Bragg intensities. The emergence of the purely ferromagnetic (0,6,0) Bragg reflection is in addition simultaneously monitored. The purely antiferromagnetic reflection (0,3,0), has on the other hand completely disappeared beyond $\sim$5 kOe. By then increasing the field magnitude up to 50.0 kOe, no additional transition is observed in the evolution of the scattering intensities. Combining all this information reveals precious details regarding the mechanisms of the transition. In fact, I understand that a destruction of the zero field long range order established on Er1 sites starts between 1 and 2 kOe, resulting in the induction of magnetic disorder in the system. Between 2 and 3 kOe, while the long range order destruction continues, the quantity of magnetic disorder starts to diminish indicating the stabilisation of a new field-induced short range magnetic order in the system. Between 5 and 6 kOe, the long range order originating from the zero field phase is entirely destroyed. This destruction is directly succeeded by the long range order stabilisation of the field-induced phase, having annihilated the magnetic disorder established.

The mechanism of this transition is consistent with the case of a field-induced transition evolving from a long range ordered dipolar Ising antiferromagnetic state to a long range ordered ferromagnetic state on the frame of a lattice of magnetic ladders. The spins and the magnetic field are aligned along the ladders legs. On the

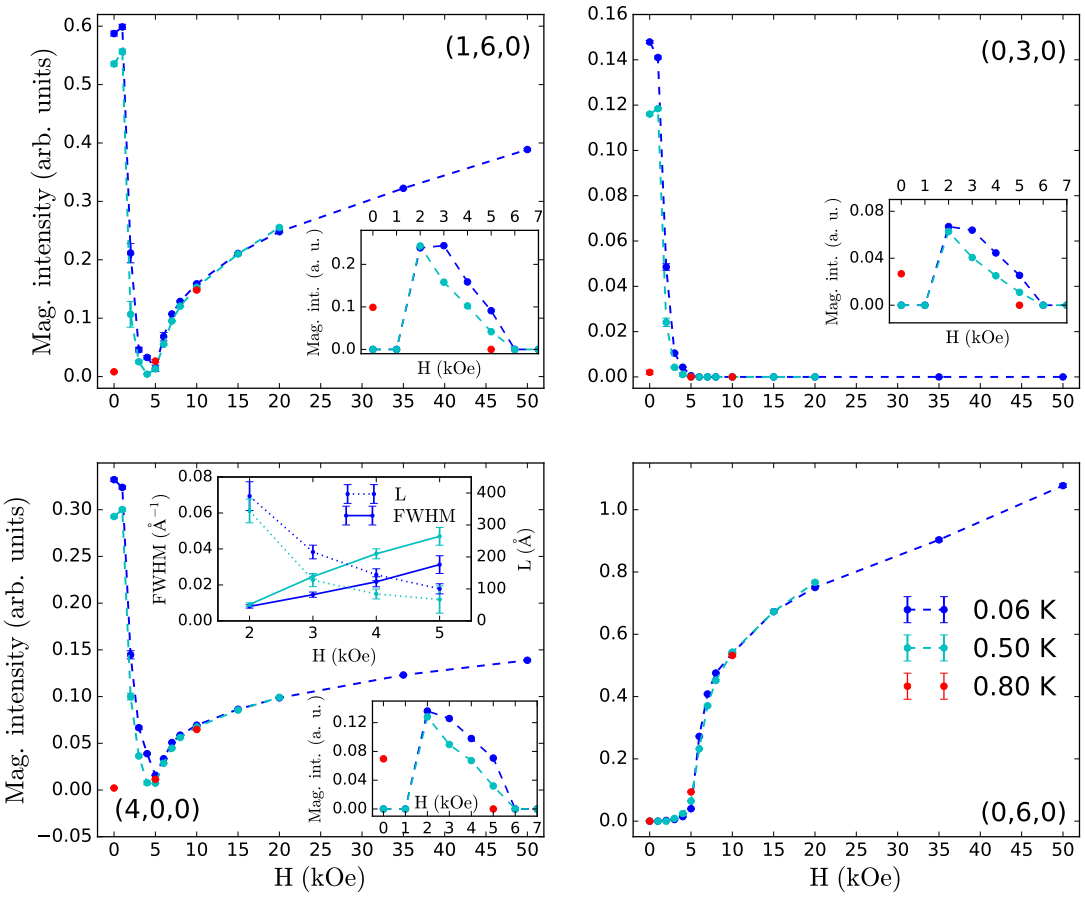

Figure 7.10: Field evolution of both sharp Bragg and diffuse components of $SrEr_2O_4$ single crystal magnetic reflections, collected on the WISH diffractometer. The intensity evolutions of the diffuse features are displayed in the lower insets of the panels. The field evolutions of the diffuse features FWHM are in addition presented along with the related correlation lengths in the upper insets. Data displayed in blue, cyan and red corresponds to the features measured at 0.06, 0.5 and 0.8 K, respectively. Sharp and diffuse components of the reflections were obtained by fitting the reflections profiles employing a back-to-back exponential and a double Sigmoidal function, respectively. For each of the four reflections considered in the diagram, the 2-dimensional profiles employed for the intensity integrations were obtained repeating the procedure employed for the preparation of the reflection profiles presented in Fig. 7.9.

M(H) phase diagram of such systems, the antiferromagnetic state remains stable under field magnitudes smaller than a lower boundary. The ferromagnetic phase on the other hand is stabilised by a field magnitude higher than an upper boundary. The intermediate region corresponds to a metastable mixed phase state consisting of ferromagnetic domains in an antiferromagnetic matrix [47]. This result is consistent with the previously published results stating the dipolar nature of the magnetic interactions stabilising the long range magnetic phase on Er1 sites [31].

I can now focus on the effect of the temperature over the transition. Comparing the field evolution of both Bragg and diffuse components of intensities collected between 0.0 and 10.0 kOe at 0.06, 0.50 K, reveals very similar behaviours. The field-induced transition visible in the evolution of the Bragg components of reflections (1,6,0) and (4,0,0) is only slightly more localised and sharp at the lowest temperature. The diffuse components of reflections (1,6,0), (0,3,0) and (4,0,0) are seen to appear and disappear at the same field values at the two different temperatures, with only a slight decrease of intensity monitored at 0.50 K. At 0.80 K on the other hand, the low field situation is significantly different. In fact, no Bragg intensities are monitored for $H < 5$ kOe. Similarly to the lower temperature measurements, the Bragg intensities of the field-induced phase appear between 4 and 5 kOe. The field-induced behaviour of the Bragg components monitored between 5 and 10 kOe also matches the lower temperature observations. These observations reveal a clear insensitivity for the field-induced magnetic phase stabilisation to temperature variations comprised between 0.06 and 0.80 K. The exclusive participation of Er1 magnetic moments in the transition process at least up to 0.80 K is consequently disclosed.

It would have however been interesting to monitor and confirm the larger participation Er2 magnetic moments in the high field magnetisation process of the system as an effect of temperature increases. The field evolutions of the scattering features collected at 0.50 and 0.80 K, however do not exceed applied field magnitudes of 20.0 and 10.0 kOe, respectively. It is thus not possible to verify these assumptions and confirm the D9 results. Tiny Bragg component increases of reflections (1,6,0) and (0,6,0) are nevertheless monitored under field magnitudes of 20.0 kOe, while increasing the temperature from 0.06 to 0.50 K.

The field evolution of the diffuse component FWHM of the (4,0,0) reflection measured along the h direction, as well as the related correlation length L(Å) = $2\pi(\text{FWHM})^{-1}$ [30, 89] of Er1 spins according to the a axis, are furthermore presented in the additional upper inset of the (4,0,0) panel (see Fig. 7.10). Prior to the appearance of diffuse magnetic scattering for $1 \leq H \leq 2$ kOe the correlation lengths of the long range ordered phase are considered as infinite on the scale of magnetic

domains. The appearance of diffuse scattering on the other hand, reveals the significant decrease of these values. Hence for $H = 2.0$ kOe at 60.0 mK, I have calculated that the spins are correlated at ∼390 Å according to the crystallographic a direction. This value progressively decreases as a function of field increase until a minimum of ∼100 Å is reached for $H = 5.0$ kOe, the diffuse scattering having completely disappeared for $H = 6.0$ kOe. At 0.5 K, the field-induced decrease trend is accentuated returning maximum and minimum values of ∼343 and ∼65 Å for the applied field magnitudes of 2.0 and 5.0 kOe, respectively. The correlation lengths obtained at 0.80 K were not considered on the diagram due to excessively large fitting uncertainties induced by the broad and rather asymmetric shape of the corresponding diffuse scattering features. These last results confirming the progressive destruction of the antiferromagnetic Ising state in the metastable region of the system M(H) phase diagram.

7.3.2 H // a, WISH, D10

I now focus on investigating the low temperature field-induced behaviour of the $SrEr_2O_4$ magnetic system in the H // a configuration. As previously detailed, single crystal magnetisation measurements performed at 0.5 K have revealed the occurrence of two successive magnetic transitions taking place at ∼2 and ∼12.5 kOe [32] (see section 7.2). In the intermediate field region defined by the transitions, the magnetisation data reveals a plateau having a central value equal to about a third of the subsequently stabilised high field asymptotic trend. This peculiar magnetisation feature suggests the stabilisation of a two up one down (uud) type of magnetic order involving magnetic spins aligned parallel and anti-parallel to the field direction. Increasing the field beyond ∼12.5 kOe results in the plateau destruction marked by the second transition. The asymptotic trend subsequently measured indicates the full polarisation of Er2 moments along the field direction. From the determination of the crystal field parameters as well as the elaboration of a close neighbours interaction scheme model for both Er sites, the magnetisation of the system was predicted to be principally induced by the Er2 magnetic moments in the particular H // a configuration [31]. Consequently I expect to observe subsequent re-orderings of the Er2 magnetic phase evolving from short range antiferromagnetic to long range ferromagnetic order via the stabilisation of an intermediate (uud) state. The Er1 magnetic sublattice is only expected to take part in the system magnetisation in the high field asymptotic region of the magnetisation data.

To verify these assumption and obtain a clear understanding of the reordering mechanisms adopted by the system in the H // a applied field configuration,

single crystal neutron scattering maps were collected in the $(0,k,l)$ scattering plane employing the WISH diffractometer. A series of scattering maps was consecutively collected under regular intervals of applied field considering a progressive magnitude increase between 0 and 30.0 kOe. Despite weak variations, the sample temperature was kept stable between 140 and 200 mK over the series of measurements. An additional scattering map was latter collected in zero field condition at the temperature of 15.5 K to be used as a nuclear background. The low temperature magnetic intensities were thus obtained after subtraction of the nuclear signal resulting in the production of purely magnetic scattering maps. A combination of the magnetic patterns revealing each principal step of the system field evolution is presented in Fig. 7.11.

The scattering map collected in zero-field conditions includes a combination of commensurate antiferromagnetic Bragg intensities with diffuse incommensurate scattering rods produced by the long range ordered Er1 and by the short range ordered Er2 magnetic sublattices, respectively, see Fig. 7.11 a). For precision, the commensurate reflections located at $(0,k,0)$ positions do also appear on the previously detailed zero field $(h,k,0)$ scattering maps, see Fig 7.6. The diffuse intensity rods are located at $(0,k,\pm 1/2)$ and at other l equal half integer positions, in agreement with the previously published results [33]. Furthermore, from previous investigation of the diffuse scattering rods utilising neutron scattering techniques, the question of the diffuse features dimensionality remained unanswered. It was in fact not determined if the diffuse scattering was essentially propagating as one dimensional features along the k direction, or if the features were significantly expanding in the $(h,k,0)$ scattering plane. The answer to this question is actually found in the previously displayed scattering maps collected in the $(h,k,-1/2)$ scattering plane in zero-field condition, see Fig 7.8 a). This representation clearly reveals the one dimensional nature of the diffuse intensity rods located at integer h positions. Consequently implying the presence of significant correlations between Er2 magnetic moments according to both a and c directions while they are only weakly correlated according to b.

By subsequently switching on the magnetic field and progressively increasing the magnitude, I report the destruction of the one dimensional intensity rods replaced by more localised diffuse features progressively migrating in the $(0,k,l)$ plane to reach $l = \pm 1/3$, $\pm 2/3$ and other corresponding positions for $2 \leq H \leq 4$ kOe. On further increase of the field, the diffuse scattering features remain stable at these positions up to a maximal value of $\sim$12.0 kOe where significant intensity reductions are monitored, see Fig. 7.11 b), c) and d). In agreement with the previously pub-

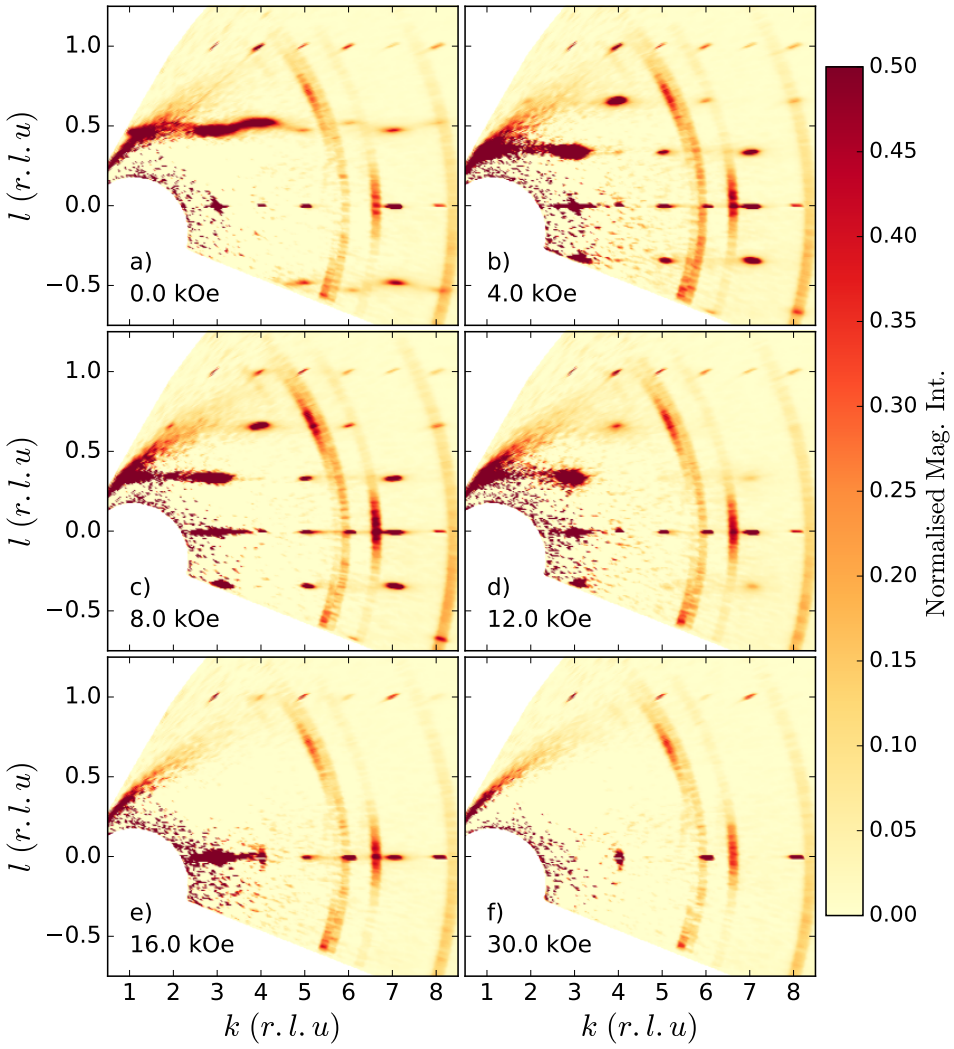

Figure 7.11: Single crystal (0,k,l) neutron scattering intensity maps of the $SrEr_2O_4$ magnetic system, measured as a function of applied field magnitude in the H // a configuration between 140 and 200 mK. A 15.5 K nuclear background was subtracted from the data, hence solely the magnetic intensities are here displayed. For applied field magnitudes lower than ∼12 kOe, commensurate and incommensurate scattering features are produced by the magnetic phases hosted by Er1 and Er2 sublattices, respectively. Under higher field magnitudes, a commensurate order is fully stabilised in the system. The measurement was performed on the WISH diffractometer, equipped at the time with a single detector bank, hence the scattering maps size reduction in comparison with these presented in Fig. 7.6. The circles of scattering intensities superimposed to the crystalline reflections are Cu and Al powder lines, their intensity variations are due to slight field-induced motions of the sample holder.

lished magnetisation data, these results confirm the stabilisation of an intermediate field-induced magnetic phase for $2 \leq H \leq 12$ kOe. Furthermore, the incommensurability of this order defined by a $\mathbf{k} = (0,0,1/3)$ propagation vector is consistent with the stabilisation of a two up one down (uud) modulation propagating along the chain directions. It should however be borne in mind that, although the incommensurate scattering features become quite localised and sharper, once established at the $l = \pm 1/3, \pm 2/3$ positions their diffuse character does not disappear. The field-induced magnetic phase thus remains in a short range ordered configuration in its entire domain of field stability. The strong antiferromagnetic reflections produced by the Néel order established on Er1 sites, on the other hand remain mostly unaffected in this intermediate region of applied field magnitude, confirming the unique participation of Er2 magnetic moments in the stabilisation of the field-induced phase.

Thereafter increasing the field magnitude to 16.0 kOe, induces a complete disappearance of the incommensurate diffuse scattering features announcing the full destruction of the intermediate field-induced order. The strong antiferromagnetic reflections produced by the Er1 zero-field phase do still remain stable in these conditions, despite the net appearance of diffuse scattering intensities surrounding the Bragg component of the reflections, see Fig. 7.11 e). These reflections only vanish from the scattering maps for $18 \leq H \leq 20$ kOe, leaving a purely ferromagnetic pattern of sharp $\mathbf{k} = (0,0,0)$ Bragg reflections indicating the full field polarisation of the system, as suggested from the magnetisation results, see Fig 7.11 f).

It is also interesting to note the early appearance of ferromagnetic Bragg reflections in the transition process. In fact, the intense ferromagnetic reflection (0,6,0) being absent from the scattering pattern in zero-field conditions, is first monitored without ambiguities between 2 and 4 kOe. The sharp nature of this commensurate reflection indicates the long range ordered nature of the ferromagnetic phase stabilised. Nevertheless, it is yet impossible to determine if this additional component to the magnetic structure of the system is to be attributed to a particular Er site, or if it involves both of them. I however suspect the Er2 magnetic sublattice to be principally responsible for this observation. In fact, due to the strong involvement of Er2 magnetic moments in the low field region of the $H \,//\, a$ configuration, it would not be surprising to observe the induction of a ferromagnetic component aligned along a in addition to the (uud) modulation. I also suspect this ferromagnetic component to grow in magnitude in a progressive manner as the field is increased, and to be responsible for the destruction of the intermediate (uud) modulation through the second field-induced transition. The addition of a small ferromagnetic component to the Er1 magnetic moments is also expected to be induced via spin canting under

significantly high field magnitudes.

As previously discussed in the H //c section (7.3.1), the non quantitative nature of the scattering data collected on the WISH instrument does not allow to proceed with accurate single crystal refinement analyses. Consequently, in order to determine the nature of the intermediate magnetic order stabilised by the Er2 magnetic moments as well as to follow the field-induced evolution of the $\mathbf{k} = (0,0,0)$ phases, an additional neutron scattering experiment was carried out on the D10 single crystal diffractometer.

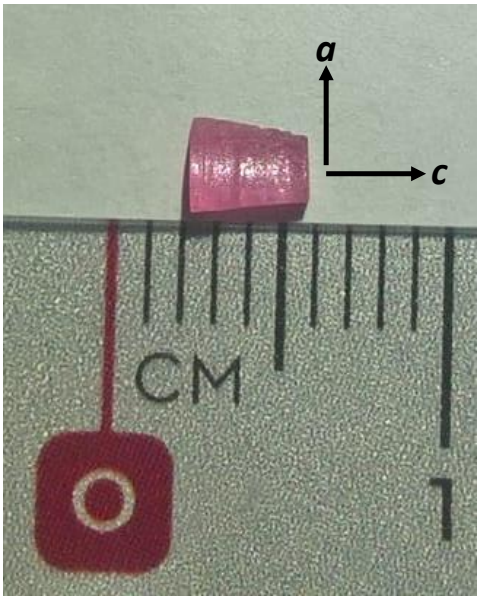

Figure 7.12: Single crystal sample of $SrEr_2O_4$ employed for the D10 neutron scattering investigation of the material field-induced behaviour in H // a configuration. The crystal was glue to the tip of a Cu pin, with the crystallographic direction a aligned parallel to the pin axis.

To reproduce the experimental condition of the WISH measurement, the D10 instrument was equipped with a dilution fridge cryostat and a cryomagnet. A rather small cuboid shaped single crystal sample of dimension equal to ∼2.5, 1 and 3 mm according to a, b and c was employed for the measurement, see Fig. 7.12. Such a small sample was chosen with an objective to reduce measuring issues such as multiple scattering, extinction and absorption. For the measurement, the sample was glued to the tip of a Cu pin with the crystallographic a direction aligned parallel with the pin axis. Cu was chosen as sample holder material to ensure an optimal low temperature thermalisation of the sample. The sample was then introduced and secured in the cryostat with the a axis set vertically, i.e. along the direction of the

applied field. In these conditions, the sample was cooled down to 50 mK, the base temperature of the cryostat. The instrument wavelength was set to 1.26 Å to ensure for high resolution measurements of the magnetic reflections.

At this low temperature with the field direction set along a, I have decided to monitor the intensities of several purely magnetic reflections as a function of increasing applied field magnitudes. I expect from these measurements to monitor accurate intensity variations and to determine important aspects of the transition mechanisms adopted by the system, as it is subjected to the presence of an external field. The purely ferromagnetic (0,6,0), the purely antiferromagnetic (0,±3,0) and the incommensurate satellites (0,0,±1/3) reflections are here considered offering direct insights into the field evolution of the different magnetic phases populating the system, see Fig. 7.13. The field derivatives of the (0,6,0) and (0,±3,0) intensities trend were in addition computed and displayed on the diagrams, precisely materialising the transitions. In the following, I detail these results considering a logical progression revealing the evolution of the different magnetic phases present in the system as a function of increasing applied field magnitudes.

In agreement with the previous results, the ferromagnetic reflection (0,6,0) is completely extinct in the absence of a field while strong intensities are monitored at the (0,±3,0) positions, see Fig. 7.13 top and middle panel. The commensurate magnetic phases hosted by the Er1 magnetic sublattices being antiferromagnetic in nature, only strong antiferromagnetic intensities are monitored at $\mathbf{k}$ = (0,0,0) positions [31, 33, 37]. Slightly increasing the field up to 2 kOe is however enough to induce significant Bragg intensities at the (0,6,0) position, indicating the field stabilisation of long range ferromagnetic order in the system, see Fig. 7.13 top panel. A kink in the field dependence of this reflection is then monitored between 2 and 3 kOe and followed by a significant increase of the trend. Such an abrupt change of intensity coincides with the stabilisation of the Er2 intermediate field-induced phase, and occurs simultaneously with the positioning of the satellites reflections at the $\mathbf{k}$ = (0,0,1/3) positions, see Fig. 7.13 lower panel. The field evolution of the Er1 antiferromagnetic reflections (0,±3,0) on the other hand, only shows smooth decreases of intensity under these low magnitudes of applied field. Consequently, I understand that the field-induced ferromagnetic component is to be attributed in priority to the Er2 magnetic sublattice in addition to the incommensurate (uud) modulation. The Er1 magnetic sublattice seems to simply witness the transition while being only weakly affected by the presence of the field. Such a difference of field-induced behaviour revealed by the two magnetic sublattices indicates a clear lack of correlation between Er1 and Er2 magnetic moments in low field conditions.

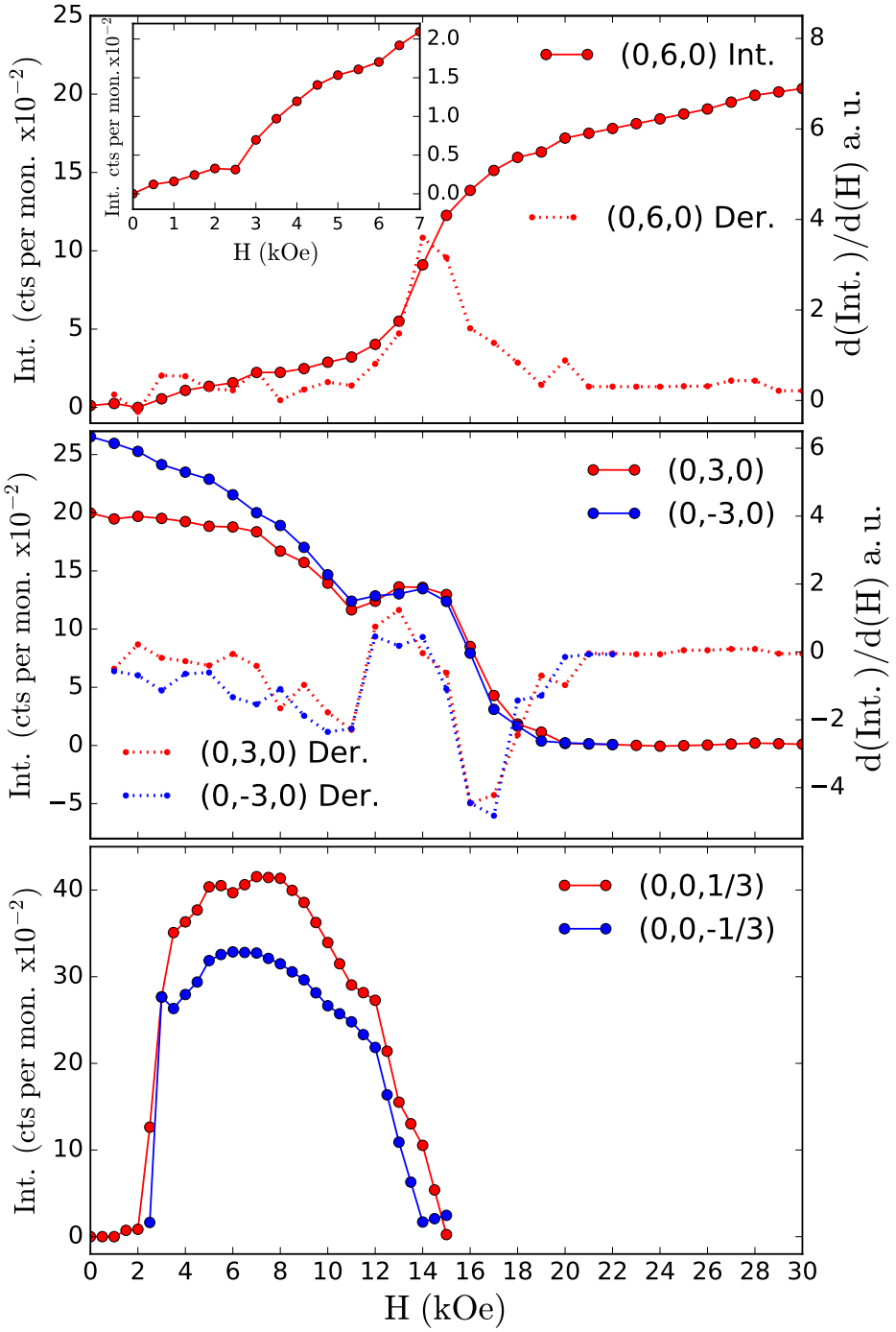

Figure 7.13: $SrEr_2O_4$ field-induced evolution of integrated neutron scattering intensities collected at the (0,6,0), (0,±3,0) and (0,0,±1/3) positions in the H // a configuration, see continuous lines. These purely magnetic reflections were collected on the D10 single crystal neutron diffractometer at 50 mK with λ=1.26 Å. The dotted lines correspond to the field-induced derivatives of the intensity trends. The inset of the upper panel focuses on the low field region of the diagram, evidencing a weak field-induced transition. The displayed intensities are scaled to the instrument monitor counting.

On further increase of the field, the (0,0,±1/3) satellites continue to gain intensity until maxima are reached between 6 and 8 kOe. Smooth decreases of the trends are subsequently monitored up to ∼12 kOe when a sudden drop of intensity is undertaken by the equivalent two reflections. By ∼14 kOe the intensities of the incommensurate satellites have completely vanished, indicating the full destruction of the intermediate phase. This transition coincides with a strong increase of the (0,6,0) intensities revealing a clear ferromagnetic transition occurring in the system, as materialised by the field derivative of the intensity trend. The antiferromagnetic (0,±3,0) Bragg intensities remaining largely visible under these field magnitudes, it is thus logical to attribute this ferromagnetic reordering of the system to Er2 magnetic moments. I thus believe the destruction of the intermediate (uud) modulation to result in the full polarisation of Er2 magnetic moments along the field direction for $12 \leq H \leq 14$ kOe.

In this intermediate field region, the induced behaviour of the Er1 antiferromagnetic Néel order is somehow significantly more complicated. In fact, two successive transitions are monitored as materialised by the two successive extrema of the derivative functions. Of particular interest, the first transition occurring at about 11 kOe just precedes the Er2 ferromagnetic reordering transition, while the second transition occurring between 14 and 16 kOe just follows it. These results suggest the presence of correlations between the two magnetic sublattices as if the smooth field destruction of the Néel order was suddenly stopped and inverted by the Er2 ferromagnetic reordering. A strong decrease of intensity subsequently follows the second transition to result in a complete destruction of the antiferromagnetic signal for $H = 20$ kOe. Considering the slowly increasing asymptotic behaviour of the (0,6,0) reflection in the high field region of the diagram, I understand that a full polarisation of the system has progressively been achieved.

The field evolution of the ferromagnetic reflection (0,6,0) revealing two successive transitions is very consistent with the magnetisation measurements performed below T_N [32]. An additional transition has here been evidenced in the field evolution of the Er1 antiferromagnetic order through the intensity variation of the (0,±3,0) reflections. This additional magnetisation feature suggests the adoption of a complex reordering mechanism by the Er1 magnetic moments while the Néel order is destroyed. In order to further progress in the understanding of this physics, I propose in the following to determine the nature of the different magnetic phases hosted by the system in every field region of interest.

For this purpose, I have successively collected sets of 151 commensurate and independent reflections, under field magnitudes of 0.0, 6.0, 11.0 and 14.0 kOe

at a temperature of 50 mK. A reduced set of 113 ferromagnetic reflections was in addition collected in the high field state for $H = 30.0$ kOe. Concerning the intermediate phase stabilised by the Er2 sublattice, a set of 227 independent reflections was collected under a field magnitude of 6.0 kOe at positions defined by the $\mathbf{k} = (0,0,1/3)$ propagation vector. This measurement was performed at a temperature of 350 mK. As previously mentioned, these reflections do not have a real Bragg character, as conventionally requested for single crystal refinement analyses. Nevertheless for $H = 6.0$ kOe, i.e. in the phase's most stable field region, the shape of the satellite reflections was revealed by the WISH measurement to have become quite localised see Fig. 7.11. Furthermore, the D10 Omega scans of the reflections have returned rather well defined features of high intensity, see Fig. 7.14. In such conditions, I assume the feasibility of a single crystal refinement analysis employing the set of $\mathbf{k} = (0,0,1/3)$ satellites reflections in an objective to determine the nature of the incommensurate field-induced magnetic phase.

I start detailing the refinement results only considering the evolution of the commensurate phases in the system. The determination of the incommensurate field-induced order will be subsequently detailed. The single crystal refinement analysis procedures were executed employing the FullProf software suite [55].

Regarding the refinement analyses of the commensurate magnetic phases, the procedure employed considers a simultaneous refinement of both magnetic and nuclear orders for the data collected under the field magnitudes of 0.0, 6.0 and 30.0 kOe. In fact, no high temperature nuclear background subtraction could be applied to these data sets due to a slight field-induced motion of the sample holder that occurred prior to measuring the 5.0 K nuclear set of data. The $H = 11.0$ and 14.0 kOe data sets, on the other hand were collected afterwards, along with the nuclear data set and could thus be accurately background subtracted. Hence, uniquely the magnetic phases were considered in the refinement analyses of these particular data sets, resulting in more accurate results. I note that in order to improve the quality of the fits, a correction for absorption was applied to each data sets employing the Datap software [58, 59]. The refined commensurate magnetic structures obtained for the different magnitudes of applied field are represented in a combined diagram revealing the progressive field polarisation of the system, see Fig. 7.15. In zero-field conditions, the refinement analysis confirms the previously published NPD results by revealing an excellent agreement between data and fit. Only the magnetic moments sitting on Er1 sites were considered for this particular refinement analysis. For $H = 6$ kOe, the magnetic moments sitting on both sites were considered. The refinement results revealed a slight canting of the Néel

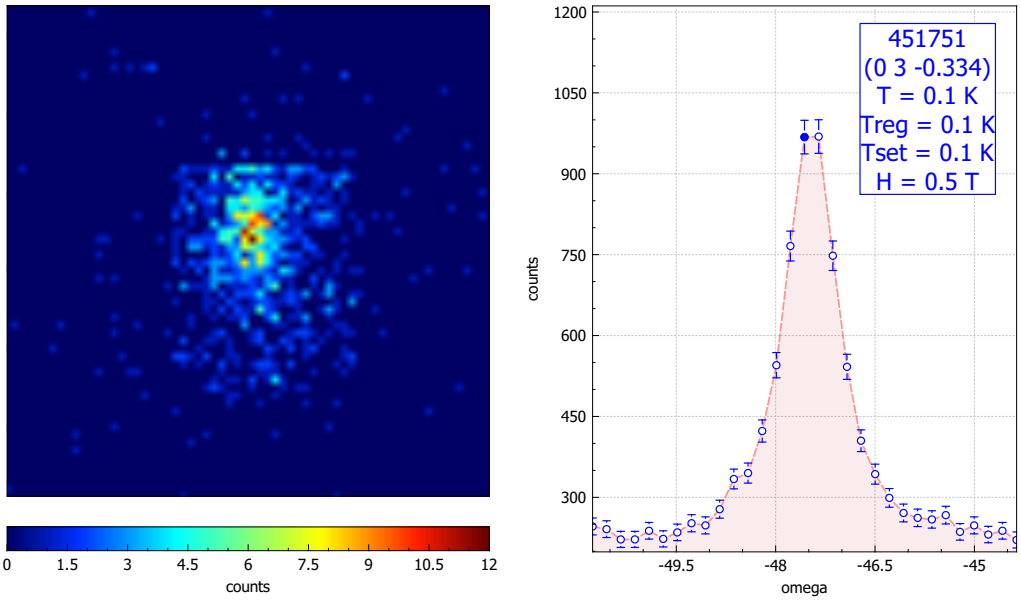

Figure 7.14: $SrEr_2O_4$ single crystal neutron scattering measurement of the (0,3,-0.334) satellite reflection. This measurement was performed on the D10 instrument at 350 mK, under a field magnitude of 6.0 kOe applied along the crystallographic a axis of the material. Left: Two dimensional intensity mapping of the reflection performed in the Omega center of the peak. Right: Omega profile of the peak obtained by integrating the scattering intensities present on the 2D maps over a discrete range of Omega positions. The full marker point located at the top of the peak corresponds to the intensity integrated at the particular Omega position represented on the left intensity map. These two diagrams were produced employing the Rplot data visualisation software [90].

	m(a)		m(c)	
H(kOe)	Er1	Er2	Er1	Er2
0.0	0.0	0.0	3.9(3)	0.0
6.0	0.6(4)	0.8(4)	3.5(1)	0.0
11.0	1.4(1)	2.4(1)	3.4(1)	0.0
14.0	1.9(2)	3.2(2)	3.8(2)	0.0
30.0	3.3(2)	7.3(5)	0.0	0.0

Table 7.1: Field evolution of the a and c components of the long range commensurate magnetic phases hosted by the $SrEr_2O_4$ system in H // a configuration. The magnitudes of the parameters are given in Bohr magnetons. The parameters corresponding to H =0.0, 6.0 and 30.0 kOe were obtained via simultaneous refinements of both magnetic and nuclear phases. For H = 11.0 and 14.0 kOe on the other hand, the magnetic phase was refined alone, returning lower uncertainties.

order along the field direction, in addition to the stabilisation of a ferromagnetic phase hosted by the Er2 sublattice. These two separate field-induced ferromagnetic components being long range ordered in nature. On further increase of the field, I report a progressive increase of these two ferromagnetic components, until a fully polarised state is reached for H = 30.0 kOe. The refined magnetic moments parameters corresponding to the different magnitudes of applied field experimentally considered are reported in Table 7.1. I would like to clarify that I am not entirely sure about the occurrence of the Néel order canting reported at 6.0 kOe. In fact including this component to the refinement model does significantly improves the result of the fit but on the other hand, the refinement calculation is visibly less stable. The significant uncertainties of the resulting refined parameters highlight this instability. However, since I was in a position to refine the data collected under H = 11.0 and 14.0 kOe after nuclear background subtraction, the refinement results obtained in such conditions are significantly more accurate than those obtained for H = 6.0 kOe. These higher field results confirming the necessity to include a ferromagnetic component to the Er1 magnetic sublattice in the refinement procedure, it is thus legitimate to consider this component to be already present for H = 6.0 kOe and to progressively increase as the field magnitude is raised. I would also like to point out the small regain of stability experienced by the Er1 Néel order between 11.0 and 14.0 kOe, in agreement with the previously detailed field behaviour of the (0,±3,0) reflections.

I now consider the refinement analysis of the incommensurate phase employing the set of $\mathbf{k}$ = (0,0,1/3) satellite reflections collected at 350 mK under a field

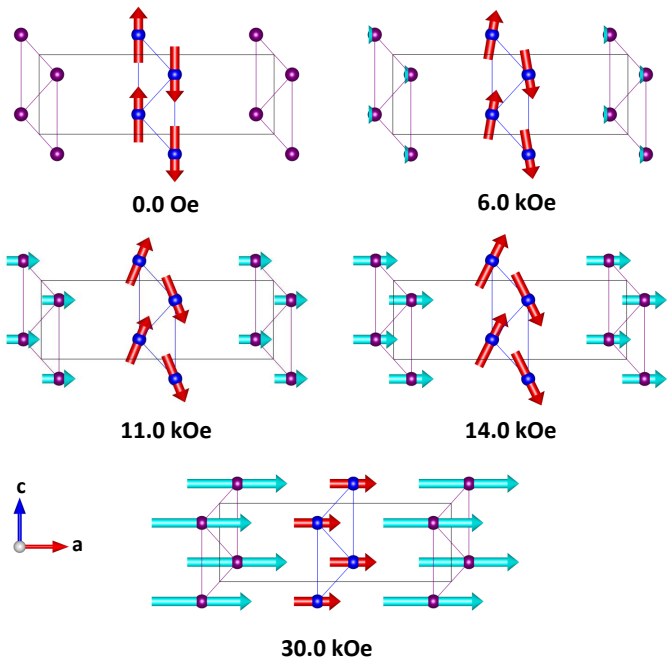

Figure 7.15: Commensurate long range ordered component of the magnetic phase hosted by the $SrEr_2O_4$ material, represented as a function of applied field magnitude in the H // a configuration. A depiction of the ac plane of the material unit cell is here employed for the visualisation of the magnetic structure evolution, a single layer of magnetic ladders is considered along the b direction for clarity. Er1 (blue spheres) and Er2 (purple spheres) magnetic moments are represented as red and cyan arrows, respectively.

Symmetry operations		BsV(1)	BsV(2)	BsV(3)
x, y, z	Re	2 0 0	0 2 0	0 0 2
	Im	0 0 0	0 0 0	0 0 0
-x, -y, z+1/2	Re	-1 0 0	0 -1 0	0 0 1
	Im	1.73 0 0	0 1.73 0	0 0 -1.73
x+1/2, -y+1/2, -z+1/2	Re	-1 0 0	0 1 0	0 0 1
	Im	1.73 0 0	0 -1.73 0	0 0 -1.73
-x+1/2, y+1/2, -z	Re	2 0 0	0 -2 0	0 0 2
	Im	0 0 0	0 0 0	0 0 0

Table 7.2: Symmetry operation and basis vectors of the Γ2 irreducible representation, corresponding to the symmetry of the field-induced incommensurate (uud) modulation stabilised by the $SrEr_2O_4$ system, see Appendix A.2.3.

magnitude of 6.0 kOe. To first determine the symmetry of this magnetic order, an irreducible representation analysis was executed considering the symmetry of the nuclear phase and the $\mathbf{k}$ = (0,0,1/3) propagation vector employing the BasIreps software [55], see Appendix A.2.3. The result of this analysis returned four different Γ models involving three basis vectors. By successively testing the different Γ models, a clear agreement between the data and the fit was obtained employing the Γ2 model uniquely, see Table 7.2. As expected, the resulting magnetic phase consists of a two up one down (uud) modulation progressing along the chains, the magnetic moments pointing along the field direction (i.e. along a). The refined magnitude of the modulation is equal to 1.22(2) μ_B, hence the order consists in a succession of two 1.22(2) μ_B up spins followed by a single 2.44(4) μ_B down spin, see Fig. 7.16. Subsequently adding the Er2 ferromagnetic component aligned along the field direction, as previously determined from the refinement of the commensurate structure results in an almost perfect (uud) order, see Fig. 7.16. The large up moments having a magnitude of 2.0(2) μ_B and the small down moment of 1.6(2) μ_B, this resulting (uud) spin phase is in perfect agreement with the observation of the 1/3 magnetisation plateau [32]. Furthermore, considering the field-induced ferromagnetic component stabilised on the Er1 sublattice, an average ferromagnetic magnitude of ∼0.7(3) μ_B is obtained per Er^{3+} ion for H = 6.0 kOe. This result is consistent with the recent magnetisation measurement performed at 0.09 K. It thus confirms the reliability of my data analyses and of my understanding of the different magnetic phases successively hosted by the material as the field magnitude is increased [43, 44].

By combining the refinement results with the field evolution of the magnetic reflections (0,6,0), (0,±3,0) and (0,0,±1/3) displayed in Fig. 7.13, I am now in a

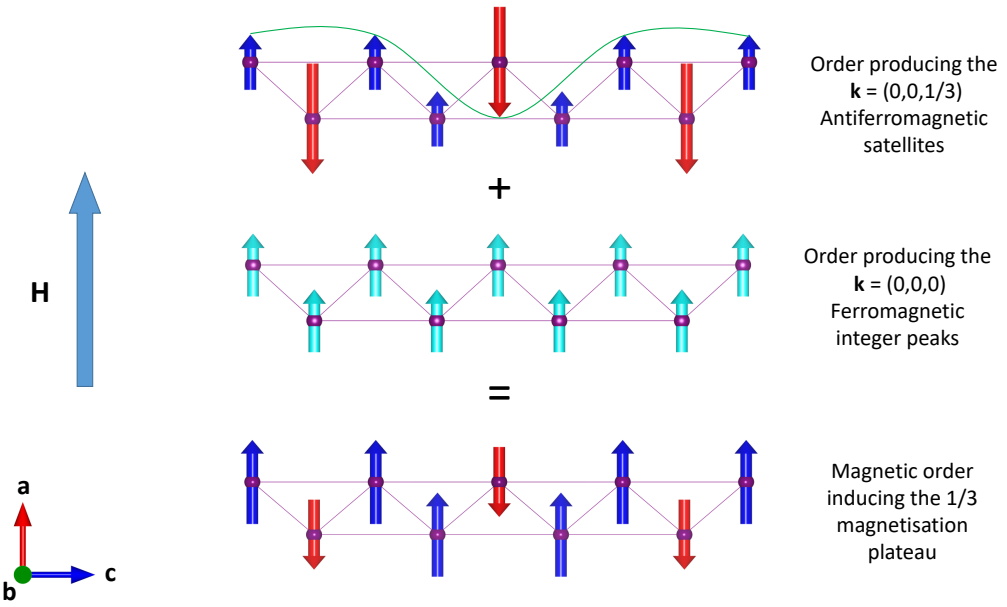

Figure 7.16: $SrEr_2O_4$ combination of the different magnetic phases hosted by the Er2 magnetic sublattice under a field magnitude of 6.0 kOe applied along the crystallographic a axis. A single magnetic Er2 ladder is repetitively employed for the depiction of the different phases. Top: $\mathbf{k} = (0,0,1/3)$ (uud) antiferromagnetic modulation. Middle: Commensurate ferromagnetic component. Bottom: (uud) magnetic order resulting from the combination of the two previous phases. Magnitudes of 2.0(2) (blue) and 1.6(2) μ_B (red) are alternating in a blue, blue, red order progressing along the chains directions. The resulting magnetic phase in addition to the Er1 ferromagnetic component being responsible for the observation of the 1/3 magnetisation plateau [32].

position to propose an accurate scenario for the reordering mechanisms adopted by the system as a function of field magnitudes. The first reaction of the system to the application of low field magnitudes is the stabilisation of small long range ordered ferromagnetic components superimposed to the zero-field magnetic phases of both Er sublattices. While these ferromagnetic components progressively gain in magnitude as the field is increased, the Er2 sublattices undergoes a reordering transition and stabilises the (uud) modulation between 2 and 3 kOe. The combination of the (uud) modulation with the Er2 ferromagnetic component surviving the transition equalises the magnitudes of the up and down spins, producing a perfect (uud) order in the phase most stable field region (i.e. in the center of the magnetisation plateau). As the ferromagnetic component of the system continues to grow while increasing the field magnitude, the (uud) modulation eventually becomes unstable resulting in an additional transition toward a purely Er2 field polarised state occurring between 12 and 14 kOe. The zero-field Er1 Néel order on the other hand suffers a rather progressive ferromagnetic polarisation as the field is increased from the lowest values. The total field polarisation of the Er1 moments only occurs at $\sim$20 kOe, i.e. under a significantly stronger field magnitude than the one requested for the polarisation of Er2 moments. The whole system is consequently ferromagnetically polarised in these conditions. The overall very different field-induced behaviour of the two different Er sublattices seems to indicate a clear absence of correlations between the two different types of magnetic moments. However, the refinements results have in addition confirmed the return of stability experienced by the Er1 Néel order corresponding to the first antiferromagnetic transition revealed by the field evolution of reflections (0,$\pm$3,0). This particular transition occurring under a field magnitude of 11 kOe, just precedes the (uud) modulation destruction, as if the modulation instability was re-stabilising the Néel order. This observation could indicate the presence of magnetic correlations between Er1 and Er2 magnetic moments under such conditions of applied field.

7.4 Summary and discussions

This chapter presents a neutron scattering investigation of the different magnetic phases subsequently stabilised by the $SrEr_2O_4$ system, in both H // a and c configurations. This research study is part of the already well advanced low temperature investigation of the material magnetic properties, corresponding to a series of papers previously published by various authors [24, 31–33, 37]. In fact, the nature of the low temperature magnetic phases and of the corresponding sets of magnetic interactions

responsible for their stabilisation was already known for both Er sites, prior to the start of this PhD project [31, 33, 37]. The strong anisotropy of the system had also been characterised due to the observation of very different field-induced behaviours when alternately applying the field along the principal crystallographic directions of the material [32]. From the determination of both Er sites sets of crystal fields and close neighbours interactions, the field-induced behaviour of the system was predicted to be principally due to Er2 and Er1 magnetic moments in the H // a and c configurations, respectively. To verify these assumptions, a series of neutron scattering experiments was carried out on the WISH, D9 and D10 diffractometers. The WISH instrument was employed in order to produce reciprocal space maps of scattering intensities offering global qualitative pictures of the system scattering features as a function of field magnitudes in both H // a and c configurations. Both D9 and D10 single crystal diffractometers were in addition employed in order to achieve precise measurements of the magnetic system scattering intensities as a function of field magnitude, in an objective to refine the nature of the successive magnetic phases hosted by the system.

The principal result of these neutrons scattering investigations concerns the very different reordering spin mechanisms individually adopted by the two Er sublattices as fields are applied along the a and b crystallographic axes of the $SrEr_2O_4$ material. In the H // c configuration, the Er1 magnetic sublattice undergoes a metamagnetic transition aligning the magnetic spins along the chains directions (i.e. parallel to c) already under a field magnitude as low as 6 kOe. The Er2 short range ordered antiferromagnetic phase however, remains stable up to field magnitudes larger than 10 kOe, before being also ferromagnetically polarised by the field. In the H // a configuration, the situation is dramatically different for the $SrEr_2O_4$ system. In fact, the Er2 magnetic moments are principally affected by the presence of the field in this configuration. The Er2 zero-field magnetic phase responds to the application of the field by undergoing a transition towards a (uud) order between 2 and 3 kOe. The up and down spins being aligned parallel and anti-parallel to the field direction, respectively. This particular magnetic state enables the system to reduce its instability while it is targeted by the field. The (uud) order remains stable in the system up to field magnitudes comprised between 12 and 14 kOe, and is successively replaced by a ferromagnetically polarised state. The Er1 zero-field Néel order on the other hand, remains present in the system up to $\sim$20 kOe. A rather continuous ferromagnetic field polarisation of this phase progressively annihilate the Néel order resulting in the overall polarisation of the system.

To conclude, the unusual successive observation of a metamagnetic transi-

tion and of a (uud) order for H respectively applied along c and a, reflects the highly anisotropic Ising-like character of the $SrEr_2O_4$ system. The different reordering mechanisms separately adopted by the two different magnetic sublattices in the different applied field configurations are consistent with the previously published simulated predictions, supporting the characteristics of the proposed magnetic Hamiltonian for the system [31, 43, 44, 47].

Chapter 8

Conclusion

This thesis project is dedicated to the investigation of the low temperature magnetic properties of $SrNd_2O_4$, $SrGd_2O_4$ and $SrEr_2O_4$ members of the $SrLn_2O_4$ crystalline family. The interest for the study of these frustrated magnets was sparkled about 15 years ago by the work of Karunadasa *et al.*, who synthesised and characterised several members of the family [24]. Since this initial publication, extensive experimental investigations of various members of the family were carried out, largely employing neutron scattering techniques. This substantial work having given rise to several publications from various authors and research groups. Lately, the involvement of theorists in the project has permitted to start gaining advanced understandings of the magnetic properties of a few members of the family [31, 38]. The number of experimentally investigated $SrLn_2O_4$ variants being however too little to characterise recurrent properties within the family, this thesis project principally aimed at extending these investigations towards additional $SrLn_2O_4$ materials. Consequently, it was decided to proceed with the low temperature investigations of both $SrNd_2O_4$ and $SrGd_2O_4$ materials. At this time neither of these two variants of the family had been subjected to successful neutron scattering investigations, thus their low temperature magnetic properties were largely unknown. Furthermore, with an objective to complement both already well advanced experimental and theoretical studies of the Er variant of the family, I focused on investigating the low temperature field-induced properties of this material employing single crystal neutron diffraction techniques. This particular aspect of the investigation aimed to confirm and complement published predictions based on the theoretical understanding of this material.

The core of this thesis considers three results chapters, individually dedicated to my investigations of the $SrNd_2O_4$, $SrGd_2O_4$ and $SrEr_2O_4$ materials. In

the following I propose a resume of the principal results obtained through these investigations, and detail my understanding of these systems. Finally, I propose a few prospects for a continuation of this research work.

The investigation of the $SrNd_2O_4$ material started with the synthesis of high quality polycrystalline samples. This material being chemically unstable at high temperature and suffering from non-congruent melting properties, the growth of single crystal samples could not be achieved. From the bulk characterisation of polycrystalline samples, a low temperature magnetic phase transition was identified taking place at 2.24 K. The nature of the stabilised phase was subsequently investigated employing neutron powder diffraction techniques, revealing a $\mathbf{k} = (0,1/2,1/2)$ long range double Néel order involving solely the magnetic moments sitting on a single type of Nd site. The magnetic moments being confined within the $a - b$ plane of the material, the magnetic order is seen as right-right-left-left (rrll) spin chains progressing along the legs of the triangular ladders. On the other hand, the magnetic moments sitting on the other type of Nd site only stabilise a short range ordered version of the double Néel order. These moments remain in a principally disordered state down to the lowest temperatures.

The work performed on the $SrGd_2O_4$ variant of the family consisted in investigating the nature of the magnetic phases stabilised by the material at low temperature. This investigation was carried out employing both powder and single crystal neutron diffraction techniques on samples containing the non-absorbing ^{160}Gd isotope. The determination of the synthesis protocol of both polycrystalline and single crystal samples of the material, along with the bulk characterisation of their low temperature magnetic properties had been already realised prior to the start of this PhD project. Of particular interest, the material was known to undergo two consecutive temperature driven magnetic transitions at 2.72 and 0.47 K [63]. The results of the neutron scattering investigations revealed the stabilisation below 2.27 K of a Néel order established on both Gd sites. This order corresponding with a ferromagnetic alignment of the moments along the chains directions of propagation, two adjacent chains being paired antiferromagnetically resulting in an up-down alternation of spins circulating around the structural hexagons of the nuclear structure. This long range order was also observed to remain stable in the system down to the lowest temperatures, the second transition simply consisting in the stabilisation of an additional ordered component to both types of Gd magnetic moments. This additional component was determined as a $\mathbf{k} = (0,0,0.42)$ spin modulation propagating along the c axis. The order involved in the modulation was found to consists in an alternation of double Néel (rrll) and simple Néel (rlrl) orders, the magnetic

moments pointing in the b direction.

The results obtained from the $SrGd_2O_4$ investigation are central regarding my understanding of the magnetic properties of the whole family. In fact, the two consecutive stabilisations of magnetic orders appearing as two independent phenomena, indicate the operation of two distinct sets of interactions separately acting over this system. Considered individually, the stabilisations of these two magnetic orders could nevertheless be explained by the theoretical J_1 and J_2 exchange interaction model [34, 39, 42]. J_1 and J_2 are the antiferromagnetic first and second neighbour interactions acting along the legs and rungs of the magnetic ladders, respectively. It is however impossible to consider the simultaneous actions of exchange interactions stabilising two different types of orders on the same magnetic ladder. It is thus evident that one of the two magnetic phases results from the action of a different types of magnetic interaction. As a matter of fact, the primary Néel order can also be understood as being stabilised by non-frustrated near neighbour dipolar interactions [38]. Ferromagnetic ordering prevails along the chains due to short distances, while antiferromagnetism couples two adjacent chains due to the larger distances involved. Furthermore, a similar Néel order is also known to be hosted by the Er1 magnetic sublattice of $SrEr_2O_4$ at low temperature. This magnetic phase was claimed by theorists to be stabilised by close neighbours dipolar interactions in agreement with my understanding of the $SrGd_2O_4$ system [31]. Moreover, the second Er sublattice stabilises a short range double Néel order principally aligned along a, and understood as resulting from the competitions of J_1 and J_2 antiferromagnetic interactions [33]. Due to these results, I have reached the conclusion that the stabilisation of Néel orders aligning the magnetic moments ferromagnetically along the chains directions are to be induced by strong dipolar interactions. Consistently, this type of order is found to be uniquely stabilised by the members of the family bearing the largest magnetic moments. On the other hand, I understand the stabilisation of magnetic orders lying within the $a-b$ plane of the materials as being induced by strong antiferromagnetic exchange interactions. The different variants of $a-b$ plane orders characterised through the family are well explained by the J_1-J_2 model. Finally, I believe the absence of long range ordering individually affecting particular magnetic sites of $SrEr_2O_4$ systems to result from the strong single ion anysotropy of these material. Interestingly in the particular $SrGd_2O_4$ case, the strong crystal field effects are significantly reduced by the spin only nature of the Gd^{3+} spins. Consequently, as rarely observed in the $SrLn_2O_4$ family the two Gd magnetic sites were able to stabilise the same magnetic orders at low temperatures.

The investigation of the $SrEr_2O_4$ material differs from the $SrNd_2O_4$ and

$SrGd_2O_4$ investigations by focusing on a particular aspect of an already well advanced study of the low temperature properties of this magnetic system. As previously mentioned, $SrEr_2O_4$ was reported to stabilise two different magnetic orders individually attributed to both Er sublattices at low temperature. The Er1 magnetic phase consists in a long range (udud) Néel order, while Er2 magnetic moments stabilise a short range (rrll) double Néel order. The Er1 and Er2 magnetic phases are theoretically described as resulting from strong dipolar and strong antiferromagnetic exchange interactions, respectively [31]. In addition, the responses of the system when being alternately subjected to magnetic fields applied along to the a and c directions were predicted to be principally due to reorderings of the Er2 and Er1 magnetic sublattices, respectively [31]. The in-field single crystal neutron scattering investigations of the system confirmed these predictions. First in H // c configuration, the Er1 sublattice was seen to undertake a metamagnetic transition flipping the direction of the spins pointing anti-parallel to the applied field direction. The H //a configuration however, the stabilisation of an intermediate (uud) order involving Er2 moments was observed in the direction of the field. Hence, two contrasting phenomena were observed for the two orthogonal directions of the applied field, reflecting the highly anisotropic Ising-like nature of the $SrEr_2O_4$ material and confirming the theoretical predictions [43, 44, 47].

To conclude, in order to confirm my understanding of the $SrLn_2O_4$ magnetic systems, it is essential to precisely characterise the nature and characteristics of the different magnetic interactions acting over the systems. For this purpose a series of low energy neutron spectroscopy measurements should be performed on the different variants of the family. In fact, the single crystal spin wave dispersions of the $SrEr_2O_4$ variant of the family were recently investigated at dilution fridge temperatures on the 4F triple axis spectrometer (LLB). The data treatment is in progress and the results should soon be published. It would also be very interesting to extend our investigation of the low temperature dynamics of these systems, in particular with AC-susceptibility measurements. In addition, completing the treatment of the D4 data is essential to the dynamic investigation. Reverse Montecarlo analyses [91] are currently employed to fit the patterns with the help of the Spinvert software [92] returning accurate pictures of the dynamic correlations acting over the systems. On an other aspect, investigating the low temperature field-induced properties of both $SrNd_2O_4$ and $SrGd_2O_4$ materials also promises interesting results subject to the availability of single crystals. In particular, it would be interesting to verify if the orders stabilised by dipolar and exchange interactions do independently and in a systematic way respond to fields applied parallel to the spin directions by

metamagnetic and up-up-down transitions, respectively.

Appendix A

A.1 .pcr files

A.1.1 x-ray .pcr file

This FullProff input .pcr file corresponds to the structural characteristic of the $SrNd_2O_4$ material and should be used to refine x-ray scattering intensities collected on a Panalytical X-Pert Pro MPD x-ray diffractometer.

```
COMM SrNd2O4_250117
! Current global Chi2 (Bragg contrib.) =      3.282
! Files => DAT-file: srnd2o4_march_19.xrdml,  PCR-file: srnd2o4_march19
!Job Npr Nph Nba Nex Nsc Nor Dum Iwg Ilo Ias Res Ste Nre Cry Uni Cor Opt Aut
  0   7   4  12   0   0   1   1   0   0   1   0   0   0   0   0   0   0   0
!
!Ipr Ppl Ioc Mat Pcr Ls1 Ls2 Ls3 NLI Prf Ins Rpa Sym Hkl Fou Sho Ana
  0   0   1   2   1   0   4   0   0  -3  13  -1   1   0   0   0   0
!
! Lambda1  Lambda2    Ratio    Bkpos    Wdt    Cthm     muR   AsyLim   Rpolarz  2nd-muR -> Patt# 1
 1.540598 1.540590  0.50000   30.000  8.0000  0.9000  0.0000   35.00    0.0000  0.0000
!
!NCY  Eps  R_at  R_an  R_pr  R_gl     Thmin       Step       Thmax    PSD    Sent0
 30  0.05  1.00  1.00  1.00  1.00     10.0036   0.013130    89.9932   0.000   0.000
!
!2Theta/TOF/E(Kev)   Background  for Pattern#  1
       10.8631       111.4227         0.00
       15.9226        69.2105         0.00
       24.7768        49.8633         0.00
       28.7202        39.3102         0.00
       32.0685        30.5159         0.00
       38.9137        32.2748         0.00
       44.7917        34.0336         0.00
       56.1012        26.9983         0.00
       65.9226        32.2748         0.00
       75.2232        32.2748         0.00
       81.6964        30.5159         0.00
       89.1369        30.5159         0.00
!
!
     8    !Number of refined parameters
!
!  Zero    Code    SyCos    Code   SySin    Code  Lambda     Code MORE ->Patt# 1
  0.04589    0.0  0.00000    0.0  0.00000    0.0 0.000000    0.00   0
!-------------------------------------------------------------------------------
!  Data for PHASE number:   1  ==> Current R_Bragg for Pattern#  1:    34.39
!-------------------------------------------------------------------------------
SrNd2O4
!
!Nat Dis Ang Pr1 Pr2 Pr3 Jbt Irf Isy Str Furth       ATZ    Nvk Npr More
  7   0   0 0.0 0.0 1.0   0   0   0   0   0       7041.561   0   5   0
!
!
P n a m                 <--Space group symbol
!Atom   Typ       X         Y         Z      Biso       Occ     In Fin N_t Spc /Codes
Nd1    Nd      0.43342  0.11702  0.25000  0.00000   1.00000   0   0   0    0
               0.00     0.00     0.00     0.00      0.00
Nd2    Nd      0.40620  0.60903  0.25000  0.00000   1.00000   0   0   0    0
               0.00     0.00     0.00     0.00      0.00
Sr     Sr      0.74400  0.64851  0.25000  0.00000   1.00000   0   0   0    0
               0.00     0.00     0.00     0.00      0.00
O1     O       0.22727  0.18910  0.25000  0.00000   1.00000   0   0   0    0
```

```
              0.00     0.00     0.00     0.00      0.00
O2     O      0.14588  0.49293  0.25000  0.00000   1.00000   0   0   0    0
              0.00     0.00     0.00     0.00      0.00
O3     O      0.49394  0.78470  0.25000  0.00000   1.00000   0   0   0    0
              0.00     0.00     0.00     0.00      0.00
O4     O      0.43580  0.41843  0.25000  0.00000   1.00000   0   0   0    0
              0.00     0.00     0.00     0.00      0.00
!-------> Profile Parameters for Pattern #  1
!  Scale        Shape1      Bov      Str1      Str2      Str3   Strain-Model
 0.87878E-06   0.62389   0.49765   0.00000   0.00000   0.00000       0
   11.00000     0.000     0.000     0.000     0.000     0.000
!      U         V         W         X         Y        GauSiz   LorSiz Size-Model
  0.017273  -0.007098   0.003497   0.000000   0.000000   0.000000   0.000000    0
    0.000     0.000     0.000     0.000     0.000     0.000     0.000
!     a         b         c        alpha      beta       gamma      #Cell Info
  10.152918  12.206456   3.570971  90.000000  90.000000  90.000000
   0.00000    0.00000    0.00000    0.00000    0.00000    0.00000
!  Pref1    Pref2      Asy1      Asy2      Asy3      Asy4
  1.00978  0.00000  0.00000  0.00000  0.00000  0.00000
    0.00     0.00     0.00     0.00     0.00     0.00
!------------------------------------------------------------------------------
!  Data for PHASE number:   2  ==> Current R_Bragg for Pattern#  1:    56.93
!------------------------------------------------------------------------------
Nd2O3
!
!Nat Dis Ang Pr1 Pr2 Pr3 Jbt Irf Isy Str Furth       ATZ    Nvk Npr More
  8   0   0 0.0 0.0 1.0   0   0   0   0   0       8203.472   0   5   0
!
!
C 2/m                 <--Space group symbol
!Atom   Typ       X         Y         Z      Biso       Occ     In Fin N_t Spc /Codes
Nd1    Nd      0.04116  0.00000  0.80898  0.00000   1.00000   0   0   0    0
              0.00     0.00     0.00     0.00      0.00
Nd2    Nd      0.14091  0.50000  0.53916  0.00000   1.00000   0   0   0    0
              0.00     0.00     0.00     0.00      0.00
Nd3    Nd      0.18896  0.50000  0.17303  0.00000   1.00000   0   0   0    0
              0.00     0.00     0.00     0.00      0.00
O1     O       0.02623  0.50000  0.65599  0.00000   1.00000   0   0   0    0
              0.00     0.00     0.00     0.00      0.00
O2     O       0.12918  0.00000  0.28565  0.00000   1.00000   0   0   0    0
              0.00     0.00     0.00     0.00      0.00
O3     O       0.17534  0.00000  0.97337  0.00000   1.00000   0   0   0    0
              0.00     0.00     0.00     0.00      0.00
O4     O       0.20188  0.00000  0.62689  0.00000   1.00000   0   0   0    0
              0.00     0.00     0.00     0.00      0.00
O5     O       0.00000  0.50000  0.00000  0.00000   1.00000   0   0   0    0
              0.00     0.00     0.00     0.00      0.00
!-------> Profile Parameters for Pattern #  1
!  Scale        Shape1      Bov      Str1      Str2      Str3   Strain-Model
 0.14055E-06   1.04722   0.49765   0.00000   0.00000   0.00000       0
   31.00000     0.000     0.000     0.000     0.000     0.000
!      U         V         W         X         Y        GauSiz   LorSiz Size-Model
```

```
  0.040326  -0.017137   0.006208   0.000000   0.000000   0.000000   0.000000    0
    0.000      0.000      0.000      0.000      0.000      0.000      0.000
!    a         b         c         alpha      beta       gamma      #Cell Info
 14.329334   3.714553   9.006899  90.000000 100.328094  90.000000
  51.00000   61.00000   71.00000    0.00000    0.00000    0.00000
!  Pref1    Pref2      Asy1      Asy2      Asy3      Asy4
 1.01031  0.00000  0.00000  0.00000  0.00000  0.00000
   0.00     0.00     0.00     0.00     0.00     0.00
!-------------------------------------------------------------------------------
!  Data for PHASE number:   3  ==> Current R_Bragg for Pattern#  1:    63.15
!-------------------------------------------------------------------------------
Nd2O3
!
!Nat Dis Ang Pr1 Pr2 Pr3 Jbt Irf Isy Str Furth       ATZ    Nvk Npr More
  3   0   0 0.0 0.0 1.0   0   0   0   0   0     701520.562   0   5   0
!
!
P m -3 m               <--Space group symbol
!Atom   Typ       X         Y         Z      Biso       Occ     In Fin N_t Spc /Codes
Nd1    Nd      0.00000  0.00000  0.00000  0.00000   1.00000   0   0   0    0
               0.00     0.00     0.00     0.00      0.00
Nd2    Nd      0.50000  0.50000  0.50000  0.00000   1.00000   0   0   0    0
               0.00     0.00     0.00     0.00      0.00
O1     O       0.00000  0.50000  0.50000  0.00000   1.00000   0   0   0    0
               0.00     0.00     0.00     0.00      0.00
!-------> Profile Parameters for Pattern #  1
!  Scale       Shape1      Bov      Str1      Str2      Str3   Strain-Model
 0.59979E-08   0.86645   0.49765   0.00000   0.00000   0.00000       0
   21.00000     0.000     0.000     0.000     0.000     0.000
!      U         V         W         X         Y       GauSiz   LorSiz Size-Model
  0.040326  -0.017137   0.006208   0.000000   0.000000   0.000000   0.000000    0
    0.000      0.000      0.000      0.000      0.000      0.000      0.000
!    a         b         c         alpha      beta       gamma      #Cell Info
  4.262635   4.262635   4.262635  90.000000  90.000000  90.000000
  41.00000   41.00000   41.00000    0.00000    0.00000    0.00000
!  Pref1    Pref2      Asy1      Asy2      Asy3      Asy4
 1.01031  0.00000  0.00000  0.00000  0.00000  0.00000
   0.00     0.00     0.00     0.00     0.00     0.00
!-------------------------------------------------------------------------------
!  Data for PHASE number:   4  ==> Current R_Bragg for Pattern#  1:     7.39
!-------------------------------------------------------------------------------
SrCO3
!
!Nat Dis Ang Pr1 Pr2 Pr3 Jbt Irf Isy Str Furth       ATZ    Nvk Npr More
  5   0   0 0.0 0.0 1.0   0   0   0   0   0       7015.994   0   5   0
!
!
C 2/m                  <--Space group symbol
!Atom   Typ       X         Y         Z      Biso       Occ     In Fin N_t Spc /Codes
Sr1    Sr      0.00000  0.50000  0.00000  0.00000   1.00000   0   0   0    0
               0.00     0.00     0.00     0.00      0.00
Sr2    Sr      0.00000  0.50000  0.50000  0.00000   1.00000   0   0   0    0
```

```
              0.00     0.00     0.00     0.00      0.00
C1     C       0.03440  0.00000  0.23242  0.00000   1.00000   0   0   0    0
              0.00     0.00     0.00     0.00      0.00
O1     O       0.11946  0.21669  0.30373  0.00000   1.00000   0   0   0    0
              0.00     0.00     0.00     0.00      0.00
O2     O       0.12596  0.00000  0.91032  0.00000   1.00000   0   0   0    0
              0.00     0.00     0.00     0.00      0.00
!-------> Profile Parameters for Pattern #  1
!  Scale        Shape1      Bov      Str1      Str2      Str3   Strain-Model
 0.10000E-09   0.86645   0.49765   0.00000   0.00000   0.00000       0
   80.50000     0.000     0.000     0.000     0.000     0.000
!      U          V          W          X          Y        GauSiz   LorSiz Size-Model
  0.040326  -0.017137   0.006208   0.000000   0.000000   0.000000   0.000000    0
    0.000      0.000      0.000      0.000      0.000      0.000      0.000
!     a          b          c        alpha       beta       gamma      #Cell Info
  7.032806   5.194408   8.370437  90.000000 112.895638  90.000000
  0.00000    0.00000    0.00000    0.00000    0.00000    0.00000
!  Pref1    Pref2      Asy1      Asy2      Asy3      Asy4
 1.01031  0.00000  0.00000  0.00000  0.00000  0.00000
   0.00     0.00     0.00     0.00     0.00     0.00
!  2Th1/TOF1    2Th2/TOF2  Pattern to plot
    10.010      51.164       1
```

A.1.2 Neutron nuclear structure .pcr file

Example of a .pcr file to be use for the refinement of neutron nuclear scattering data collected on our isotopically enriched (^{160}Gd) $SrGd_2O_4$ sample using the D2B (ILL) instrument.

```
COMMNAC d2b 09/10/2003
! Current global Chi2 (Bragg contrib.) =      2.031
! Files => DAT-file: SrGd2O4_RT_hr.dat,  PCR-file:
srgd2o4_rt_d2bhr_oleg_setting
!Job Npr Nph Nba Nex Nsc Nor Dum Iwg Ilo Ias Res Ste Nre Cry Uni Cor Opt
Aut
   1   5   1  32   2   1   0   1   0   0   1   0   0   0   0   0   0   0
0
!
!Ipr Ppl Ioc Mat Pcr Ls1 Ls2 Ls3 NLI Prf Ins Rpa Sym Hkl Fou Sho Ana
   0   0   1   0   1   0   4   0   0  -3  10   0   0   0   0   0   1
!
! Lambda1  Lambda2    Ratio    Bkpos    Wdt    Cthm     muR   AsyLim
Rpolarz  2nd-muR -> Patt# 1
 1.594002 1.594002  1.00000   40.000  5.5000  0.0000  0.9500   40.00
0.0000  0.0000
!
!NCY  Eps  R_at  R_an  R_pr  R_gl     Thmin       Step       Thmax    PSD
Sent0
 31  0.01  0.25  0.25  0.25  0.25      0.0000   0.050018   159.9500
0.000   0.000
!
!2Theta/TOF/E(Kev)   Background  for Pattern#  1
         4.1729       518.9830          0.00
         5.7519       464.6594          0.00
         7.9323       424.0728          0.00
        10.9398       386.6023          0.00
        13.4962       365.9874          0.00
        16.4662       349.2845          0.00
        20.1128       327.4670          0.00
        24.8496       312.1310          0.00
        29.3609       294.6827          0.00
        34.2105       271.7169          0.00
        38.3271       267.5298          0.00
        43.0263       271.0618          0.00
        53.1297       242.9632          0.00
        59.0508       235.1911          0.00
        66.3346       225.6191          0.00
        72.5000       213.4397          0.00
        79.3609       215.1724          0.00
        83.5432       213.4995          0.00
        88.1485       215.9407          0.00
        93.1767       217.5689          0.00
       101.4662       215.2840          0.00
       111.1936       214.6217          0.00
       117.8665       211.1647          0.00
       122.8947       209.1270          0.00
       128.6748       218.2612          0.00
       130.5075       221.2050          0.00
       135.8177       215.7440          0.00
       139.3233       213.3992          0.00
       143.6090       220.1901          0.00
       147.5564       218.8821          0.00
       152.2932       232.2659          0.00
       159.6992       241.0076          0.00
!
! Excluded regions (LowT  HighT) for Pattern#  1
      -30.30       10.00
      150.50      180.50
!
```

```
! Additional scattering factors for Pattern#  1
GD      0.90970   -0.02760   0
!
    28    !Number of refined parameters
!
!  Zero    Code    SyCos    Code   SySin    Code  Lambda     Code MORE -
>Patt# 1
  0.36710    0.0 -0.23968  191.0 -0.22295  201.0 0.000000    0.00   0
!-------------------------------------------------------------------------
-------
!  Data for PHASE number:   1  ==> Current R_Bragg for Pattern#  1:
4.30
!-------------------------------------------------------------------------
-------
NdPb
!
!Nat Dis Ang Pr1 Pr2 Pr3 Jbt Irf Isy Str Furth       ATZ    Nvk Npr More
   7   0   0 0.0 0.0 1.0   0   0   0   0   0       1865.341   0   5   1
!
!Jvi Jdi Hel Sol Mom Ter  Brind   RMua    RMub    RMuc   Jtyp  Nsp_Ref
Ph_Shift N_Domains
   0   3   0   0   0   0  1.0000  0.0000  0.0000  0.0000    1      0
0      0
!
! Max_dst(dist) (angles)  Bond-Valence Calc.
      4.5000      2.6000
!
P n a m                 <--Space group symbol
!Atom   Typ       X        Y        Z     Biso       Occ     In Fin N_t
Spc /Codes
SR     SR      0.75028  0.64925  0.25000  0.57118   0.50000   0   0   0
0
                11.00    21.00     0.00   261.00      0.00
GD1    GD      0.42591  0.11323  0.25000  0.30603   0.50525   0   0   0
0
                31.00    41.00     0.00   271.00    241.00
GD2    GD      0.41715  0.61131  0.25000  0.30603   0.49544   0   0   0
0
                51.00    61.00     0.00   271.00    251.00
O1     O       0.21589  0.18140  0.25000  0.51802   0.50000   0   0   0
0
                71.00    81.00     0.00   281.00      0.00
O2     O       0.13085  0.48129  0.25000  0.51802   0.50000   0   0   0
0
                91.00   101.00     0.00   281.00      0.00
O3     O       0.50722  0.78455  0.25000  0.51802   0.50000   0   0   0
0
               111.00   121.00     0.00   281.00      0.00
O4     O       0.42586  0.42053  0.25000  0.51802   0.50000   0   0   0
0
               131.00   141.00     0.00   281.00      0.00
!-------> Profile Parameters for Pattern #  1
!  Scale        Shape1      Bov      Str1      Str2      Str3   Strain-
Model
 0.31132       0.33831   0.00000   0.00000   0.00000   0.00000       0
   181.00000   211.000     0.000     0.000     0.000     0.000
!       U         V          W           X          Y        GauSiz
LorSiz Size-Model
   0.071080  -0.178783   0.192596   0.000000   0.000000   0.000000
0.000000    0
```

```
      0.000      0.000      0.000      0.000      0.000      0.000
0.000
!     a          b          c        alpha      beta       gamma
#Cell Info
  10.146380  12.077989   3.480190  90.000000  90.000000  90.000000
  151.00000  161.00000  171.00000    0.00000    0.00000    0.00000
!  Pref1    Pref2      Asy1     Asy2     Asy3     Asy4
  0.00000  0.00000  0.20035  0.03512  0.00000  0.00000
     0.00     0.00   221.00   231.00     0.00     0.00
!  2Th1/TOF1    2Th2/TOF2  Pattern to plot
      15.000     150.500       1
```

A.1.3 Neutron magnetic structure .pcr file

Example of a .pcr file to be use for the refinement of neutron magnetic scattering data collected on our isotopically enriched (^{160}Gd) $SrGd_2O_4$ sample using the D20 (ILL) instrument. This file was used to refine the incommensurate magnetic phase stabilised by the material below T_{N2}.

```
COMM Gd2 O4 Sr1 100mK
! Current global Chi2 (Bragg contrib.) =      20.62
! Files => DAT-file: 100mk_satellites_full_collection_2.int,  PCR-file: tn2_100mk_inc_oleg_setting_a_march
!Job Npr Nph Nba Nex Nsc Nor Dum Iwg Ilo Ias Res Ste Nre Cry Uni Cor Opt Aut
  1   0   1   0   0   0   0   0   1   0   0   0   0   0   1   0   0   0   1
!
!Ipr Ppl Ioc Mat Pcr Ls1 Ls2 Ls3 NLI Prf Ins Rpa Sym Hkl Fou Sho Ana
  0   0   1   0   1   0   4   0   0   1  10   0   1   0   0   1   0
!
!NCY  Eps  R_at  R_an  R_pr  R_gl     Thmin       Step       Thmax    PSD    Sent0
 20  0.05  1.00  1.00  1.00  1.00      0.0000   0.050016   159.9500   0.000   0.000
!
!
     3    !Number of refined parameters
!-------------------------------------------------------------------------------
!  Data for PHASE number:   1  ==> Current R_Bragg for Pattern#  1:    25.16
!-------------------------------------------------------------------------------
Gd2 O4 Sr1
!
!Nat Dis Mom Pr1 Pr2 Pr3 Jbt Irf Isy Str Furth       ATZ    Nvk Npr More
  2   0   0 0.0 0.0 1.0   1   4  -2   0   0       1338.080  -1   5   0
!
!
P -1                    <--Space group symbol for hkl generation
! Nsym   Cen  Laue Ireps N_Bas
    4     1     1    -1     3
! Real(0)-Imaginary(1) indicator for Ci
 0  0  0
!
SYMM x,y,z
BASR   4.0211  0.0000  0.0000   0.0000  4.0211  0.0000   0.0000  0.0000  4.0211
BASI   0  0  0   0  0  0   0  0  0
SYMM -x,-y,z+1/2
BASR  -1  0  0   0 -1  0   0  0  1
BASI   3.8948  0.0000  0.0000   0.0000  3.8948  0.0000   0.0000  0.0000 -3.8948
SYMM -x+1/2,y+1/2,z+1/2
BASR   1  0  0   0 -1  0   0  0 -1
BASI  -3.8948  0.0000  0.0000   0.0000  3.8948  0.0000   0.0000  0.0000  3.8948
SYMM x+1/2,-y+1/2,z
BASR  -4.0211  0.0000  0.0000   0.0000  4.0211  0.0000   0.0000  0.0000 -4.0211
BASI   0  0  0   0  0  0   0  0  0
!
!Atom   Typ  Mag Vek    X      Y      Z       Biso    Occ      C1      C2      C3
!    C4     C5     C6      C7      C8      C9      MagPh
Gd1    JGD3  1  0  0.43526 0.11290 0.25000 0.00000  1.00000   0.000   1.789   0.000  # ATOM GD1 COLOR 1
0 0 1
                0.00    0.00    0.00    0.00     0.00    0.00   11.00    0.00
    0.000   0.000   0.000   0.000   0.000   0.000  0.00000
     0.00    0.00    0.00    0.00    0.00    0.00     0.00
Gd2    JGD3  1  0  0.41871 0.61427 0.25000 0.00000  1.00000   0.000   0.347   0.000  # ATOM GD2 COLOR 0
0 1 1
                0.00    0.00    0.00    0.00     0.00    0.00   21.00    0.00
```

```
    0.000   0.000   0.000   0.000   0.000   0.000  0.00000
     0.00    0.00    0.00    0.00    0.00    0.00     0.00
!-------> Scale, Extinction and  Cell Parameters for Pattern #  1
!  Scale Factors
!   Sc1        Sc2         Sc3         Sc4         Sc5         Sc6
  32.28       0.000       0.000       0.000       0.000       0.000
       31.00        0.00        0.00        0.00        0.00        0.00
!  Extinction Parameters
! Ext1       Ext2       Ext3       Ext4       Ext5       Ext6       Ext7   Ext-Model
 0.1971E-01 0.1383E-01 0.2807E-01  0.000      0.000      0.000      0.000       4
      0.00       0.00       0.00       0.00       0.00       0.00       0.00
!    a         b         c        alpha      beta       gamma      #Cell Info
  10.018900  11.861199   3.389300  90.000000  90.000000  90.000000
   0.00000    0.00000    0.00000    0.00000    0.00000    0.00000
! x-Lambda/2  +          Not yet used parameters
    0.00000     0.00000     0.00000     0.00000     0.00000
      0.00        0.00        0.00        0.00        0.00
! Propagation vectors:
  0.0000000   0.0000000   0.4200000          Propagation Vector  1
   0.000000    0.000000    0.000000
!  2Th1/TOF1    2Th2/TOF2  Pattern to plot
      0.000     159.950       1
```

A.2 BasIreps files

The symmetry operations and basis vectors corresponding to particular Γ (IRrep) models can be directly pasted onto .pcr files.

A.2.1 BasIreps k = (0,0,0) file for $SrLn_2O_4$ materials

```
   ------------------------------
   Output of BasIREPS for FullProf
   ------------------------------
   The group of lines starting with the symbol of space groups and
   finishing with the last keyword BASI, may be pasted into the PCR file

                 X       Y       Z           for site:  1
 -> Gd1_1   :   0.4259  0.1132  0.2500  : (x,y,z)
 -> Gd1_2   :  -0.4259 -0.1132  0.7500  : (-x,-y,z+1/2)
 -> Gd1_3   :   0.9259  0.3868  0.2500  : (x+1/2,-y+1/2,-z+1/2)
 -> Gd1_4   :   0.0741  0.6132 -0.2500  : (-x+1/2,y+1/2,-z)

 => Basis functions of Representation IRrep( 1) of dimension  1 contained
2 times in GAMMA
    Representation number    :  1 for Site:  1
    Number of basis functions:  2

 ----- Block-of-lines for PCR start just below this line
P -1                          <--Space group symbol for hkl generation
! Nsym   Cen  Laue Ireps N_Bas
     4     1     1    -1     2
! Real(0)-Imaginary(1) indicator for Ci
  0  0
SYMM x,y,z
BASR   1  0  0   0  1  0
BASI   0  0  0   0  0  0
SYMM -x,-y,z+1/2
BASR  -1  0  0   0 -1  0
BASI   0  0  0   0  0  0
SYMM x+1/2,-y+1/2,-z+1/2
BASR   1  0  0   0 -1  0
BASI   0  0  0   0  0  0
SYMM -x+1/2,y+1/2,-z
BASR  -1  0  0   0  1  0
BASI   0  0  0   0  0  0
 ----- End-of-block of lines for PCR

 => Basis functions of Representation IRrep( 2) of dimension  1 contained
1 times in GAMMA
    Representation number    :  2 for Site:  1
    Number of basis functions:  1

 ----- Block-of-lines for PCR start just below this line
P -1                          <--Space group symbol for hkl generation
! Nsym   Cen  Laue Ireps N_Bas
     4     1     1    -1     1
! Real(0)-Imaginary(1) indicator for Ci
  0
SYMM x,y,z
BASR   0  0  1
BASI   0  0  0
SYMM -x,-y,z+1/2
BASR   0  0  1
BASI   0  0  0
SYMM x+1/2,-y+1/2,-z+1/2
BASR   0  0 -1
BASI   0  0  0
SYMM -x+1/2,y+1/2,-z
BASR   0  0 -1
BASI   0  0  0
```

```
 ----- End-of-block of lines for PCR

 => Basis functions of Representation IRrep( 3) of dimension  1 contained
2 times in GAMMA
    Representation number    :  3 for Site:  1
    Number of basis functions:  2

 ----- Block-of-lines for PCR start just below this line
P -1                          <--Space group symbol for hkl generation
! Nsym   Cen  Laue Ireps N_Bas
     4     1     1    -1     2
! Real(0)-Imaginary(1) indicator for Ci
  0  0
SYMM x,y,z
BASR   1  0  0   0  1  0
BASI   0  0  0   0  0  0
SYMM -x,-y,z+1/2
BASR  -1  0  0   0 -1  0
BASI   0  0  0   0  0  0
SYMM x+1/2,-y+1/2,-z+1/2
BASR  -1  0  0   0  1  0
BASI   0  0  0   0  0  0
SYMM -x+1/2,y+1/2,-z
BASR   1  0  0   0 -1  0
BASI   0  0  0   0  0  0
 ----- End-of-block of lines for PCR

 => Basis functions of Representation IRrep( 4) of dimension  1 contained
1 times in GAMMA
    Representation number    :  4 for Site:  1
    Number of basis functions:  1

 ----- Block-of-lines for PCR start just below this line
P -1                          <--Space group symbol for hkl generation
! Nsym   Cen  Laue Ireps N_Bas
     4     1     1    -1     1
! Real(0)-Imaginary(1) indicator for Ci
  0
SYMM x,y,z
BASR   0  0  1
BASI   0  0  0
SYMM -x,-y,z+1/2
BASR   0  0  1
BASI   0  0  0
SYMM x+1/2,-y+1/2,-z+1/2
BASR   0  0  1
BASI   0  0  0
SYMM -x+1/2,y+1/2,-z
BASR   0  0  1
BASI   0  0  0
 ----- End-of-block of lines for PCR

 => Basis functions of Representation IRrep( 5) of dimension  1 contained
1 times in GAMMA
    Representation number    :  5 for Site:  1
    Number of basis functions:  1

 ----- Block-of-lines for PCR start just below this line
P -1                          <--Space group symbol for hkl generation
! Nsym   Cen  Laue Ireps N_Bas
```

```
     4     1     1    -1     1
! Real(0)-Imaginary(1) indicator for Ci
  0
SYMM x,y,z
BASR   0  0  1
BASI   0  0  0
SYMM -x,-y,z+1/2
BASR   0  0 -1
BASI   0  0  0
SYMM x+1/2,-y+1/2,-z+1/2
BASR   0  0 -1
BASI   0  0  0
SYMM -x+1/2,y+1/2,-z
BASR   0  0  1
BASI   0  0  0
 ----- End-of-block of lines for PCR

 => Basis functions of Representation IRrep( 6) of dimension  1 contained
2 times in GAMMA
    Representation number    :  6 for Site:  1
    Number of basis functions:  2

 ----- Block-of-lines for PCR start just below this line
P -1                          <--Space group symbol for hkl generation
! Nsym   Cen  Laue Ireps N_Bas
     4     1     1    -1     2
! Real(0)-Imaginary(1) indicator for Ci
  0  0
SYMM x,y,z
BASR   1  0  0   0  1  0
BASI   0  0  0   0  0  0
SYMM -x,-y,z+1/2
BASR   1  0  0   0  1  0
BASI   0  0  0   0  0  0
SYMM x+1/2,-y+1/2,-z+1/2
BASR   1  0  0   0 -1  0
BASI   0  0  0   0  0  0
SYMM -x+1/2,y+1/2,-z
BASR   1  0  0   0 -1  0
BASI   0  0  0   0  0  0
 ----- End-of-block of lines for PCR

 => Basis functions of Representation IRrep( 7) of dimension  1 contained
1 times in GAMMA
    Representation number    :  7 for Site:  1
    Number of basis functions:  1

 ----- Block-of-lines for PCR start just below this line
P -1                          <--Space group symbol for hkl generation
! Nsym   Cen  Laue Ireps N_Bas
     4     1     1    -1     1
! Real(0)-Imaginary(1) indicator for Ci
  0
SYMM x,y,z
BASR   0  0  1
BASI   0  0  0
SYMM -x,-y,z+1/2
BASR   0  0 -1
BASI   0  0  0
SYMM x+1/2,-y+1/2,-z+1/2
```

```
BASR   0  0  1
BASI   0  0  0
SYMM -x+1/2,y+1/2,-z
BASR   0  0 -1
BASI   0  0  0
 ----- End-of-block of lines for PCR

 => Basis functions of Representation IRrep( 8) of dimension  1 contained
2 times in GAMMA
    Representation number    :  8 for Site:  1
    Number of basis functions:  2

 ----- Block-of-lines for PCR start just below this line
P -1                            <--Space group symbol for hkl generation
! Nsym   Cen  Laue Ireps N_Bas
     4     1     1    -1     2
! Real(0)-Imaginary(1) indicator for Ci
  0  0
SYMM x,y,z
BASR   1  0  0   0  1  0
BASI   0  0  0   0  0  0
SYMM -x,-y,z+1/2
BASR   1  0  0   0  1  0
BASI   0  0  0   0  0  0
SYMM x+1/2,-y+1/2,-z+1/2
BASR  -1  0  0   0  1  0
BASI   0  0  0   0  0  0
SYMM -x+1/2,y+1/2,-z
BASR  -1  0  0   0  1  0
BASI   0  0  0   0  0  0
 ----- End-of-block of lines for PCR
                X       Y       Z           for site:  2
 -> Gd2_1   :   0.4174  0.6113  0.2500  : (x,y,z)
 -> Gd2_2   :  -0.4174 -0.6113  0.7500  : (-x,-y,z+1/2)
 -> Gd2_3   :   0.9174 -0.1113  0.2500  : (x+1/2,-y+1/2,-z+1/2)
 -> Gd2_4   :   0.0826  1.1113 -0.2500  : (-x+1/2,y+1/2,-z)

 => Basis functions of Representation IRrep( 1) of dimension  1 contained
2 times in GAMMA
    Representation number    :  1 for Site:  2
    Number of basis functions:  2

 ----- Block-of-lines for PCR start just below this line
P -1                            <--Space group symbol for hkl generation
! Nsym   Cen  Laue Ireps N_Bas
     4     1     1    -1     2
! Real(0)-Imaginary(1) indicator for Ci
  0  0
SYMM x,y,z
BASR   1  0  0   0  1  0
BASI   0  0  0   0  0  0
SYMM -x,-y,z+1/2
BASR  -1  0  0   0 -1  0
BASI   0  0  0   0  0  0
SYMM x+1/2,-y+1/2,-z+1/2
BASR   1  0  0   0 -1  0
BASI   0  0  0   0  0  0
SYMM -x+1/2,y+1/2,-z
BASR  -1  0  0   0  1  0
BASI   0  0  0   0  0  0
```

```
 ----- End-of-block of lines for PCR

 => Basis functions of Representation IRrep( 2) of dimension  1 contained
1 times in GAMMA
    Representation number    :  2 for Site:  2
    Number of basis functions:  1

 ----- Block-of-lines for PCR start just below this line
P -1                          <--Space group symbol for hkl generation
! Nsym   Cen  Laue Ireps N_Bas
     4     1     1    -1     1
! Real(0)-Imaginary(1) indicator for Ci
  0
SYMM x,y,z
BASR   0  0  1
BASI   0  0  0
SYMM -x,-y,z+1/2
BASR   0  0  1
BASI   0  0  0
SYMM x+1/2,-y+1/2,-z+1/2
BASR   0  0 -1
BASI   0  0  0
SYMM -x+1/2,y+1/2,-z
BASR   0  0 -1
BASI   0  0  0
 ----- End-of-block of lines for PCR

 => Basis functions of Representation IRrep( 3) of dimension  1 contained
2 times in GAMMA
    Representation number    :  3 for Site:  2
    Number of basis functions:  2

 ----- Block-of-lines for PCR start just below this line
P -1                          <--Space group symbol for hkl generation
! Nsym   Cen  Laue Ireps N_Bas
     4     1     1    -1     2
! Real(0)-Imaginary(1) indicator for Ci
  0  0
SYMM x,y,z
BASR   1  0  0   0  1  0
BASI   0  0  0   0  0  0
SYMM -x,-y,z+1/2
BASR  -1  0  0   0 -1  0
BASI   0  0  0   0  0  0
SYMM x+1/2,-y+1/2,-z+1/2
BASR  -1  0  0   0  1  0
BASI   0  0  0   0  0  0
SYMM -x+1/2,y+1/2,-z
BASR   1  0  0   0 -1  0
BASI   0  0  0   0  0  0
 ----- End-of-block of lines for PCR

 => Basis functions of Representation IRrep( 4) of dimension  1 contained
1 times in GAMMA
    Representation number    :  4 for Site:  2
    Number of basis functions:  1

 ----- Block-of-lines for PCR start just below this line
P -1                          <--Space group symbol for hkl generation
! Nsym   Cen  Laue Ireps N_Bas
```

```
     4     1     1    -1     1
! Real(0)-Imaginary(1) indicator for Ci
  0
SYMM x,y,z
BASR   0  0  1
BASI   0  0  0
SYMM -x,-y,z+1/2
BASR   0  0  1
BASI   0  0  0
SYMM x+1/2,-y+1/2,-z+1/2
BASR   0  0  1
BASI   0  0  0
SYMM -x+1/2,y+1/2,-z
BASR   0  0  1
BASI   0  0  0
 ----- End-of-block of lines for PCR

 => Basis functions of Representation IRrep( 5) of dimension  1 contained
1 times in GAMMA
    Representation number    :  5 for Site:  2
    Number of basis functions:  1

 ----- Block-of-lines for PCR start just below this line
P -1                          <--Space group symbol for hkl generation
! Nsym   Cen  Laue Ireps N_Bas
     4     1     1    -1     1
! Real(0)-Imaginary(1) indicator for Ci
  0
SYMM x,y,z
BASR   0  0  1
BASI   0  0  0
SYMM -x,-y,z+1/2
BASR   0  0 -1
BASI   0  0  0
SYMM x+1/2,-y+1/2,-z+1/2
BASR   0  0 -1
BASI   0  0  0
SYMM -x+1/2,y+1/2,-z
BASR   0  0  1
BASI   0  0  0
 ----- End-of-block of lines for PCR

 => Basis functions of Representation IRrep( 6) of dimension  1 contained
2 times in GAMMA
    Representation number    :  6 for Site:  2
    Number of basis functions:  2

 ----- Block-of-lines for PCR start just below this line
P -1                          <--Space group symbol for hkl generation
! Nsym   Cen  Laue Ireps N_Bas
     4     1     1    -1     2
! Real(0)-Imaginary(1) indicator for Ci
  0  0
SYMM x,y,z
BASR   1  0  0   0  1  0
BASI   0  0  0   0  0  0
SYMM -x,-y,z+1/2
BASR   1  0  0   0  1  0
BASI   0  0  0   0  0  0
SYMM x+1/2,-y+1/2,-z+1/2
```

```
BASR   1  0  0   0 -1  0
BASI   0  0  0   0  0  0
SYMM -x+1/2,y+1/2,-z
BASR   1  0  0   0 -1  0
BASI   0  0  0   0  0  0
 ----- End-of-block of lines for PCR

 => Basis functions of Representation IRrep( 7) of dimension  1 contained
1 times in GAMMA
    Representation number    :  7 for Site:  2
    Number of basis functions:  1

 ----- Block-of-lines for PCR start just below this line
P -1                          <--Space group symbol for hkl generation
! Nsym   Cen  Laue Ireps N_Bas
     4     1     1    -1     1
! Real(0)-Imaginary(1) indicator for Ci
  0
SYMM x,y,z
BASR   0  0  1
BASI   0  0  0
SYMM -x,-y,z+1/2
BASR   0  0 -1
BASI   0  0  0
SYMM x+1/2,-y+1/2,-z+1/2
BASR   0  0  1
BASI   0  0  0
SYMM -x+1/2,y+1/2,-z
BASR   0  0 -1
BASI   0  0  0
 ----- End-of-block of lines for PCR

 => Basis functions of Representation IRrep( 8) of dimension  1 contained
2 times in GAMMA
    Representation number    :  8 for Site:  2
    Number of basis functions:  2

 ----- Block-of-lines for PCR start just below this line
P -1                          <--Space group symbol for hkl generation
! Nsym   Cen  Laue Ireps N_Bas
     4     1     1    -1     2
! Real(0)-Imaginary(1) indicator for Ci
  0  0
SYMM x,y,z
BASR   1  0  0   0  1  0
BASI   0  0  0   0  0  0
SYMM -x,-y,z+1/2
BASR   1  0  0   0  1  0
BASI   0  0  0   0  0  0
SYMM x+1/2,-y+1/2,-z+1/2
BASR  -1  0  0   0  1  0
BASI   0  0  0   0  0  0
SYMM -x+1/2,y+1/2,-z
BASR  -1  0  0   0  1  0
BASI   0  0  0   0  0  0
 ----- End-of-block of lines for PCR
```

A.2.2 BasIreps k = (0,0.5,0.5) file for $SrLn_2O_4$ materials

```
   ------------------------------
   Output of BasIREPS for FullProf
   ------------------------------
   The group of lines starting with the symbol of space groups and
   finishing with the last keyword BASI, may be pasted into the PCR file

                 X       Y       Z           for site:  1
 -> Nd_1    :   0.4334  0.1170  0.2500  : (x,y,z)
 -> Nd_2    :  -0.4334 -0.1170  0.7500  : (-x,-y,z+1/2)
 -> Nd_3    :   0.9334  0.3830  0.2500  : (x+1/2,-y+1/2,-z+1/2)
 -> Nd_4    :   0.0666  0.6170 -0.2500  : (-x+1/2,y+1/2,-z)

 => Basis functions of Representation IRrep( 1) of dimension  2 contained
3 times in GAMMA
    Representation number    :  1 for Site:  1
    Number of basis functions:  6

 ----- Block-of-lines for PCR start just below this line
P -1                          <--Space group symbol for hkl generation
! Nsym   Cen  Laue Ireps N_Bas
     4     1     1    -1     6
! Real(0)-Imaginary(1) indicator for Ci
  0  0  0  0  0  0
SYMM x,y,z
BASR   1  0  0   0  1  0   0  0  1   0  0  0   0  0  0   0  0  0
BASI   0  0  0   0  0  0   0  0  0  -1  0  0   0 -1  0   0  0  1
SYMM -x,-y,z+1/2
BASR   0  0  0   0  0  0   0  0  0  -1  0  0   0 -1  0   0  0 -1
BASI   1  0  0   0  1  0   0  0 -1   0  0  0   0  0  0   0  0  0
SYMM x+1/2,-y+1/2,-z+1/2
BASR   1  0  0   0 -1  0   0  0 -1   0  0  0   0  0  0   0  0  0
BASI   0  0  0   0  0  0   0  0  0  -1  0  0   0  1  0   0  0 -1
SYMM -x+1/2,y+1/2,-z
BASR   0  0  0   0  0  0   0  0  0  -1  0  0   0  1  0   0  0  1
BASI   1  0  0   0 -1  0   0  0  1   0  0  0   0  0  0   0  0  0
 ----- End-of-block of lines for PCR

 => Basis functions of Representation IRrep( 2) of dimension  2 contained
3 times in GAMMA
    Representation number    :  2 for Site:  1
    Number of basis functions:  6

 ----- Block-of-lines for PCR start just below this line
P -1                          <--Space group symbol for hkl generation
! Nsym   Cen  Laue Ireps N_Bas
     4     1     1    -1     6
! Real(0)-Imaginary(1) indicator for Ci
  0  0  0  0  0  0
SYMM x,y,z
BASR   1  0  0   0  1  0   0  0  1   0  0  0   0  0  0   0  0  0
BASI   0  0  0   0  0  0   0  0  0  -1  0  0   0 -1  0   0  0  1
SYMM -x,-y,z+1/2
BASR   0  0  0   0  0  0   0  0  0  -1  0  0   0 -1  0   0  0 -1
BASI   1  0  0   0  1  0   0  0 -1   0  0  0   0  0  0   0  0  0
SYMM x+1/2,-y+1/2,-z+1/2
BASR  -1  0  0   0  1  0   0  0  1   0  0  0   0  0  0   0  0  0
BASI   0  0  0   0  0  0   0  0  0   1  0  0   0 -1  0   0  0  1
SYMM -x+1/2,y+1/2,-z
BASR   0  0  0   0  0  0   0  0  0   1  0  0   0 -1  0   0  0 -1
BASI  -1  0  0   0  1  0   0  0 -1   0  0  0   0  0  0   0  0  0
```

----- End-of-block of lines for PCR

A.2.3 BasIreps k = (0,0,0.33) file for $SrLn_2O_4$ materials

```
   ------------------------------
   Output of BasIREPS for FullProf
   ------------------------------
   The group of lines starting with the symbol of space groups and
   finishing with the last keyword BASI, may be pasted into the PCR file

                X       Y       Z           for site:  1
 -> Er1_1   :   0.4220  0.1180  0.2500  : (x,y,z)
 -> Er1_2   :  -0.4220 -0.1180  0.7500  : (-x,-y,z+1/2)
 -> Er1_3   :   0.0780  0.6180  0.7500  : (-x+1/2,y+1/2,z+1/2)
 -> Er1_4   :   0.9220  0.3820  0.2500  : (x+1/2,-y+1/2,z)

 => Basis functions of Representation IRrep( 1) of dimension  1 contained
3 times in GAMMA
    Representation number    :  1 for Site:  1
    Number of basis functions:  3

 ----- Block-of-lines for PCR start just below this line
P -1                          <--Space group symbol for hkl generation
! Nsym   Cen  Laue Ireps N_Bas
     4     1     1    -1     3
! Real(0)-Imaginary(1) indicator for Ci
  0  0  0
SYMM x,y,z
BASR   2  0  0   0  2  0   0  0  2
BASI   0  0  0   0  0  0   0  0  0
SYMM -x,-y,z+1/2
BASR  -1  0  0   0 -1  0   0  0  1
BASI   1.7321  0.0000  0.0000   0.0000  1.7321  0.0000   0.0000  0.0000 -
1.7321
SYMM -x+1/2,y+1/2,z+1/2
BASR   1  0  0   0 -1  0   0  0 -1
BASI  -1.7320  0.0000  0.0000   0.0000  1.7320  0.0000   0.0000  0.0000
1.7320
SYMM x+1/2,-y+1/2,z
BASR  -2  0  0   0  2  0   0  0 -2
BASI   0  0  0   0  0  0   0  0  0
 ----- End-of-block of lines for PCR

 => Basis functions of Representation IRrep( 2) of dimension  1 contained
3 times in GAMMA
    Representation number    :  2 for Site:  1
    Number of basis functions:  3

 ----- Block-of-lines for PCR start just below this line
P -1                          <--Space group symbol for hkl generation
! Nsym   Cen  Laue Ireps N_Bas
     4     1     1    -1     3
! Real(0)-Imaginary(1) indicator for Ci
  0  0  0
SYMM x,y,z
BASR   2  0  0   0  2  0   0  0  2
BASI   0  0  0   0  0  0   0  0  0
SYMM -x,-y,z+1/2
BASR  -1  0  0   0 -1  0   0  0  1
BASI   1.7321  0.0000  0.0000   0.0000  1.7321  0.0000   0.0000  0.0000 -
1.7321
SYMM -x+1/2,y+1/2,z+1/2
BASR  -1  0  0   0  1  0   0  0  1
```

```
BASI   1.7320  0.0000  0.0000   0.0000 -1.7320  0.0000   0.0000  0.0000 -
1.7320
SYMM x+1/2,-y+1/2,z
BASR   2  0  0   0 -2  0   0  0  2
BASI   0  0  0   0  0  0   0  0  0
 ----- End-of-block of lines for PCR

 => Basis functions of Representation IRrep( 3) of dimension  1 contained
3 times in GAMMA
    Representation number    :  3 for Site:  1
    Number of basis functions:  3

 ----- Block-of-lines for PCR start just below this line
P -1                          <--Space group symbol for hkl generation
! Nsym   Cen  Laue Ireps N_Bas
     4     1     1    -1     3
! Real(0)-Imaginary(1) indicator for Ci
  0  0  0
SYMM x,y,z
BASR   2  0  0   0  2  0   0  0  2
BASI   0  0  0   0  0  0   0  0  0
SYMM -x,-y,z+1/2
BASR   1  0  0   0  1  0   0  0 -1
BASI  -1.7320  0.0000  0.0000   0.0000 -1.7320  0.0000   0.0000  0.0000
1.7320
SYMM -x+1/2,y+1/2,z+1/2
BASR   1  0  0   0 -1  0   0  0 -1
BASI  -1.7320  0.0000  0.0000   0.0000  1.7320  0.0000   0.0000  0.0000
1.7320
SYMM x+1/2,-y+1/2,z
BASR   2  0  0   0 -2  0   0  0  2
BASI   0  0  0   0  0  0   0  0  0
 ----- End-of-block of lines for PCR

 => Basis functions of Representation IRrep( 4) of dimension  1 contained
3 times in GAMMA
    Representation number    :  4 for Site:  1
    Number of basis functions:  3

 ----- Block-of-lines for PCR start just below this line
P -1                          <--Space group symbol for hkl generation
! Nsym   Cen  Laue Ireps N_Bas
     4     1     1    -1     3
! Real(0)-Imaginary(1) indicator for Ci
  0  0  0
SYMM x,y,z
BASR   2  0  0   0  2  0   0  0  2
BASI   0  0  0   0  0  0   0  0  0
SYMM -x,-y,z+1/2
BASR   1  0  0   0  1  0   0  0 -1
BASI  -1.7320  0.0000  0.0000   0.0000 -1.7320  0.0000   0.0000  0.0000
1.7320
SYMM -x+1/2,y+1/2,z+1/2
BASR  -1  0  0   0  1  0   0  0  1
BASI   1.7320  0.0000  0.0000   0.0000 -1.7320  0.0000   0.0000  0.0000 -
1.7320
SYMM x+1/2,-y+1/2,z
BASR  -2  0  0   0  2  0   0  0 -2
BASI   0  0  0   0  0  0   0  0  0
 ----- End-of-block of lines for PCR
```

```
                X       Y       Z           for site:  2
 -> Er2_1   :   0.4130  0.6180  0.2500  : (x,y,z)
 -> Er2_2   :  -0.4130 -0.6180  0.7500  : (-x,-y,z+1/2)
 -> Er2_3   :   0.0870  1.1180  0.7500  : (-x+1/2,y+1/2,z+1/2)
 -> Er2_4   :   0.9130 -0.1180  0.2500  : (x+1/2,-y+1/2,z)

 => Basis functions of Representation IRrep( 1) of dimension  1 contained
3 times in GAMMA
    Representation number    :  1 for Site:  2
    Number of basis functions:  3

 ----- Block-of-lines for PCR start just below this line
P -1                          <--Space group symbol for hkl generation
! Nsym   Cen  Laue Ireps N_Bas
     4     1     1    -1     3
! Real(0)-Imaginary(1) indicator for Ci
  0  0  0
SYMM x,y,z
BASR   2  0  0   0  2  0   0  0  2
BASI   0  0  0   0  0  0   0  0  0
SYMM -x,-y,z+1/2
BASR  -1  0  0   0 -1  0   0  0  1
BASI   1.7321  0.0000  0.0000   0.0000  1.7321  0.0000   0.0000  0.0000 -
1.7321
SYMM -x+1/2,y+1/2,z+1/2
BASR   1  0  0   0 -1  0   0  0 -1
BASI  -1.7320  0.0000  0.0000   0.0000  1.7320  0.0000   0.0000  0.0000
1.7320
SYMM x+1/2,-y+1/2,z
BASR  -2  0  0   0  2  0   0  0 -2
BASI   0  0  0   0  0  0   0  0  0
 ----- End-of-block of lines for PCR

 => Basis functions of Representation IRrep( 2) of dimension  1 contained
3 times in GAMMA
    Representation number    :  2 for Site:  2
    Number of basis functions:  3

 ----- Block-of-lines for PCR start just below this line
P -1                          <--Space group symbol for hkl generation
! Nsym   Cen  Laue Ireps N_Bas
     4     1     1    -1     3
! Real(0)-Imaginary(1) indicator for Ci
  0  0  0
SYMM x,y,z
BASR   2  0  0   0  2  0   0  0  2
BASI   0  0  0   0  0  0   0  0  0
SYMM -x,-y,z+1/2
BASR  -1  0  0   0 -1  0   0  0  1
BASI   1.7321  0.0000  0.0000   0.0000  1.7321  0.0000   0.0000  0.0000 -
1.7321
SYMM -x+1/2,y+1/2,z+1/2
BASR  -1  0  0   0  1  0   0  0  1
BASI   1.7320  0.0000  0.0000   0.0000 -1.7320  0.0000   0.0000  0.0000 -
1.7320
SYMM x+1/2,-y+1/2,z
BASR   2  0  0   0 -2  0   0  0  2
BASI   0  0  0   0  0  0   0  0  0
 ----- End-of-block of lines for PCR
```

```
 => Basis functions of Representation IRrep( 3) of dimension  1 contained
3 times in GAMMA
    Representation number    :  3 for Site:  2
    Number of basis functions:  3

 ----- Block-of-lines for PCR start just below this line
P -1                           <--Space group symbol for hkl generation
! Nsym   Cen  Laue Ireps N_Bas
     4     1     1    -1     3
! Real(0)-Imaginary(1) indicator for Ci
  0  0  0
SYMM x,y,z
BASR   2  0  0   0  2  0   0  0  2
BASI   0  0  0   0  0  0   0  0  0
SYMM -x,-y,z+1/2
BASR   1  0  0   0  1  0   0  0 -1
BASI  -1.7320  0.0000  0.0000   0.0000 -1.7320  0.0000   0.0000  0.0000
1.7320
SYMM -x+1/2,y+1/2,z+1/2
BASR   1  0  0   0 -1  0   0  0 -1
BASI  -1.7320  0.0000  0.0000   0.0000  1.7320  0.0000   0.0000  0.0000
1.7320
SYMM x+1/2,-y+1/2,z
BASR   2  0  0   0 -2  0   0  0  2
BASI   0  0  0   0  0  0   0  0  0
 ----- End-of-block of lines for PCR

 => Basis functions of Representation IRrep( 4) of dimension  1 contained
3 times in GAMMA
    Representation number    :  4 for Site:  2
    Number of basis functions:  3

 ----- Block-of-lines for PCR start just below this line
P -1                           <--Space group symbol for hkl generation
! Nsym   Cen  Laue Ireps N_Bas
     4     1     1    -1     3
! Real(0)-Imaginary(1) indicator for Ci
  0  0  0
SYMM x,y,z
BASR   2  0  0   0  2  0   0  0  2
BASI   0  0  0   0  0  0   0  0  0
SYMM -x,-y,z+1/2
BASR   1  0  0   0  1  0   0  0 -1
BASI  -1.7320  0.0000  0.0000   0.0000 -1.7320  0.0000   0.0000  0.0000
1.7320
SYMM -x+1/2,y+1/2,z+1/2
BASR  -1  0  0   0  1  0   0  0  1
BASI   1.7320  0.0000  0.0000   0.0000 -1.7320  0.0000   0.0000  0.0000 -
1.7320
SYMM x+1/2,-y+1/2,z
BASR  -2  0  0   0  2  0   0  0 -2
BASI   0  0  0   0  0  0   0  0  0
 ----- End-of-block of lines for PCR
```

A.2.4 BasIreps k = (0,0,0.42) file for $SrLn_2O_4$ materials

```
   ------------------------------
   Output of BasIREPS for FullProf
   ------------------------------
   The group of lines starting with the symbol of space groups and
   finishing with the last keyword BASI, may be pasted into the PCR file

                X       Y       Z           for site:  1
 -> Gd1_1   :   0.4220  0.1180  0.2500  : (x,y,z)
 -> Gd1_2   :  -0.4220 -0.1180  0.7500  : (-x,-y,z+1/2)
 -> Gd1_3   :   0.0780  0.6180  0.7500  : (-x+1/2,y+1/2,z+1/2)
 -> Gd1_4   :   0.9220  0.3820  0.2500  : (x+1/2,-y+1/2,z)

 => Basis functions of Representation IRrep( 1) of dimension  1 contained
3 times in GAMMA
    Representation number    :  1 for Site:  1
    Number of basis functions:  3

 ----- Block-of-lines for PCR start just below this line
P -1                          <--Space group symbol for hkl generation
! Nsym   Cen  Laue Ireps N_Bas
     4     1     1    -1     3
! Real(0)-Imaginary(1) indicator for Ci
  0  0  0
SYMM x,y,z
BASR   4.0211  0.0000  0.0000   0.0000  4.0211  0.0000   0.0000  0.0000
4.0211
BASI   0  0  0   0  0  0   0  0  0
SYMM -x,-y,z+1/2
BASR  -1  0  0   0 -1  0   0  0  1
BASI   3.8947  0.0000  0.0000   0.0000  3.8947  0.0000   0.0000  0.0000 -
3.8947
SYMM -x+1/2,y+1/2,z+1/2
BASR   1  0  0   0 -1  0   0  0 -1
BASI  -3.8947  0.0000  0.0000   0.0000  3.8947  0.0000   0.0000  0.0000
3.8947
SYMM x+1/2,-y+1/2,z
BASR  -4.0211  0.0000  0.0000   0.0000  4.0211  0.0000   0.0000  0.0000 -
4.0211
BASI   0  0  0   0  0  0   0  0  0
 ----- End-of-block of lines for PCR

 => Basis functions of Representation IRrep( 2) of dimension  1 contained
3 times in GAMMA
    Representation number    :  2 for Site:  1
    Number of basis functions:  3

 ----- Block-of-lines for PCR start just below this line
P -1                          <--Space group symbol for hkl generation
! Nsym   Cen  Laue Ireps N_Bas
     4     1     1    -1     3
! Real(0)-Imaginary(1) indicator for Ci
  0  0  0
SYMM x,y,z
BASR   4.0211  0.0000  0.0000   0.0000  4.0211  0.0000   0.0000  0.0000
4.0211
BASI   0  0  0   0  0  0   0  0  0
SYMM -x,-y,z+1/2
BASR  -1  0  0   0 -1  0   0  0  1
BASI   3.8948  0.0000  0.0000   0.0000  3.8948  0.0000   0.0000  0.0000 -
3.8948
```

```
SYMM -x+1/2,y+1/2,z+1/2
BASR  -1  0  0   0  1  0   0  0  1
BASI   3.8948  0.0000  0.0000   0.0000 -3.8948  0.0000   0.0000  0.0000 -
3.8948
SYMM x+1/2,-y+1/2,z
BASR   4.0211  0.0000  0.0000   0.0000 -4.0211  0.0000   0.0000  0.0000
4.0211
BASI   0  0  0   0  0  0   0  0  0
 ----- End-of-block of lines for PCR

 => Basis functions of Representation IRrep( 3) of dimension  1 contained
3 times in GAMMA
    Representation number    :  3 for Site:  1
    Number of basis functions:  3

 ----- Block-of-lines for PCR start just below this line
P -1                          <--Space group symbol for hkl generation
! Nsym   Cen  Laue Ireps N_Bas
     4     1     1    -1     3
! Real(0)-Imaginary(1) indicator for Ci
  0  0  0
SYMM x,y,z
BASR   4.0211  0.0000  0.0000   0.0000  4.0211  0.0000   0.0000  0.0000
4.0211
BASI   0  0  0   0  0  0   0  0  0
SYMM -x,-y,z+1/2
BASR   1  0  0   0  1  0   0  0 -1
BASI  -3.8947  0.0000  0.0000   0.0000 -3.8947  0.0000   0.0000  0.0000
3.8947
SYMM -x+1/2,y+1/2,z+1/2
BASR   1  0  0   0 -1  0   0  0 -1
BASI  -3.8947  0.0000  0.0000   0.0000  3.8947  0.0000   0.0000  0.0000
3.8947
SYMM x+1/2,-y+1/2,z
BASR   4.0211  0.0000  0.0000   0.0000 -4.0211  0.0000   0.0000  0.0000
4.0211
BASI   0  0  0   0  0  0   0  0  0
 ----- End-of-block of lines for PCR

 => Basis functions of Representation IRrep( 4) of dimension  1 contained
3 times in GAMMA
    Representation number    :  4 for Site:  1
    Number of basis functions:  3

 ----- Block-of-lines for PCR start just below this line
P -1                          <--Space group symbol for hkl generation
! Nsym   Cen  Laue Ireps N_Bas
     4     1     1    -1     3
! Real(0)-Imaginary(1) indicator for Ci
  0  0  0
SYMM x,y,z
BASR   4.0211  0.0000  0.0000   0.0000  4.0211  0.0000   0.0000  0.0000
4.0211
BASI   0  0  0   0  0  0   0  0  0
SYMM -x,-y,z+1/2
BASR   1  0  0   0  1  0   0  0 -1
BASI  -3.8948  0.0000  0.0000   0.0000 -3.8948  0.0000   0.0000  0.0000
3.8948
SYMM -x+1/2,y+1/2,z+1/2
BASR  -1  0  0   0  1  0   0  0  1
```

```
BASI   3.8948  0.0000  0.0000   0.0000 -3.8948  0.0000   0.0000  0.0000 -
3.8948
SYMM x+1/2,-y+1/2,z
BASR  -4.0211  0.0000  0.0000   0.0000  4.0211  0.0000   0.0000  0.0000 -
4.0211
BASI   0  0  0   0  0  0   0  0  0
 ----- End-of-block of lines for PCR
                X       Y       Z           for site:  2
 -> Gd2_1   :   0.4130  0.6180  0.2500  : (x,y,z)
 -> Gd2_2   :  -0.4130 -0.6180  0.7500  : (-x,-y,z+1/2)
 -> Gd2_3   :   0.0870  1.1180  0.7500  : (-x+1/2,y+1/2,z+1/2)
 -> Gd2_4   :   0.9130 -0.1180  0.2500  : (x+1/2,-y+1/2,z)

 => Basis functions of Representation IRrep( 1) of dimension  1 contained
3 times in GAMMA
    Representation number    :  1 for Site:  2
    Number of basis functions:  3

 ----- Block-of-lines for PCR start just below this line
P -1                          <--Space group symbol for hkl generation
! Nsym   Cen  Laue Ireps N_Bas
     4     1     1    -1     3
! Real(0)-Imaginary(1) indicator for Ci
  0  0  0
SYMM x,y,z
BASR   4.0211  0.0000  0.0000   0.0000  4.0211  0.0000   0.0000  0.0000
4.0211
BASI   0  0  0   0  0  0   0  0  0
SYMM -x,-y,z+1/2
BASR  -1  0  0   0 -1  0   0  0  1
BASI   3.8947  0.0000  0.0000   0.0000  3.8947  0.0000   0.0000  0.0000 -
3.8947
SYMM -x+1/2,y+1/2,z+1/2
BASR   1  0  0   0 -1  0   0  0 -1
BASI  -3.8947  0.0000  0.0000   0.0000  3.8947  0.0000   0.0000  0.0000
3.8947
SYMM x+1/2,-y+1/2,z
BASR  -4.0211  0.0000  0.0000   0.0000  4.0211  0.0000   0.0000  0.0000 -
4.0211
BASI   0  0  0   0  0  0   0  0  0
 ----- End-of-block of lines for PCR

 => Basis functions of Representation IRrep( 2) of dimension  1 contained
3 times in GAMMA
    Representation number    :  2 for Site:  2
    Number of basis functions:  3

 ----- Block-of-lines for PCR start just below this line
P -1                          <--Space group symbol for hkl generation
! Nsym   Cen  Laue Ireps N_Bas
     4     1     1    -1     3
! Real(0)-Imaginary(1) indicator for Ci
  0  0  0
SYMM x,y,z
BASR   4.0211  0.0000  0.0000   0.0000  4.0211  0.0000   0.0000  0.0000
4.0211
BASI   0  0  0   0  0  0   0  0  0
SYMM -x,-y,z+1/2
BASR  -1  0  0   0 -1  0   0  0  1
```

```
BASI   3.8948  0.0000  0.0000   0.0000  3.8948  0.0000   0.0000  0.0000 -
3.8948
SYMM -x+1/2,y+1/2,z+1/2
BASR  -1  0  0   0  1  0   0  0  1
BASI   3.8948  0.0000  0.0000   0.0000 -3.8948  0.0000   0.0000  0.0000 -
3.8948
SYMM x+1/2,-y+1/2,z
BASR   4.0211  0.0000  0.0000   0.0000 -4.0211  0.0000   0.0000  0.0000
4.0211
BASI   0  0  0   0  0  0   0  0  0
 ----- End-of-block of lines for PCR

 => Basis functions of Representation IRrep( 3) of dimension  1 contained
3 times in GAMMA
    Representation number    :  3 for Site:  2
    Number of basis functions:  3

 ----- Block-of-lines for PCR start just below this line
P -1                          <--Space group symbol for hkl generation
! Nsym   Cen  Laue Ireps N_Bas
     4     1     1    -1     3
! Real(0)-Imaginary(1) indicator for Ci
  0  0  0
SYMM x,y,z
BASR   4.0211  0.0000  0.0000   0.0000  4.0211  0.0000   0.0000  0.0000
4.0211
BASI   0  0  0   0  0  0   0  0  0
SYMM -x,-y,z+1/2
BASR   1  0  0   0  1  0   0  0 -1
BASI  -3.8947  0.0000  0.0000   0.0000 -3.8947  0.0000   0.0000  0.0000
3.8947
SYMM -x+1/2,y+1/2,z+1/2
BASR   1  0  0   0 -1  0   0  0 -1
BASI  -3.8947  0.0000  0.0000   0.0000  3.8947  0.0000   0.0000  0.0000
3.8947
SYMM x+1/2,-y+1/2,z
BASR   4.0211  0.0000  0.0000   0.0000 -4.0211  0.0000   0.0000  0.0000
4.0211
BASI   0  0  0   0  0  0   0  0  0
 ----- End-of-block of lines for PCR

 => Basis functions of Representation IRrep( 4) of dimension  1 contained
3 times in GAMMA
    Representation number    :  4 for Site:  2
    Number of basis functions:  3

 ----- Block-of-lines for PCR start just below this line
P -1                          <--Space group symbol for hkl generation
! Nsym   Cen  Laue Ireps N_Bas
     4     1     1    -1     3
! Real(0)-Imaginary(1) indicator for Ci
  0  0  0
SYMM x,y,z
BASR   4.0211  0.0000  0.0000   0.0000  4.0211  0.0000   0.0000  0.0000
4.0211
BASI   0  0  0   0  0  0   0  0  0
SYMM -x,-y,z+1/2
BASR   1  0  0   0  1  0   0  0 -1
BASI  -3.8948  0.0000  0.0000   0.0000 -3.8948  0.0000   0.0000  0.0000
3.8948
```

```
SYMM -x+1/2,y+1/2,z+1/2
BASR  -1  0  0   0  1  0   0  0  1
BASI   3.8948  0.0000  0.0000   0.0000 -3.8948  0.0000   0.0000  0.0000 -
3.8948
SYMM x+1/2,-y+1/2,z
BASR  -4.0211  0.0000  0.0000   0.0000  4.0211  0.0000   0.0000  0.0000 -
4.0211
BASI   0  0  0   0  0  0   0  0  0
 ----- End-of-block of lines for PCR
```

Bibliography

[1] Stephen Blundell. *Magnetism in Condensed Matter*. OUP Oxford, 2001.

[2] Tapan Chatterji. *Neutron Scattering from Magnetic Materials*. 01 2006.

[3] É. du Trémolet de Lacheisserie, D. Gignoux, and M. Schlenker. *Magnetism Fundamentals*. Springer, 2005.

[4] C. A. de Coulomb. Premier mémoire sur l'électricité et le magnétisme. *Histoire de l'Académie Royale des Sciences*, a, 1785.

[5] Hans Christian Orsted, Karen Jelved, Andrew D. Jackson, and Ole Knudsen (translators from Danish to English). *Selected Scientific Works of Hans Christian Orsted*. 1997.

[6] A. M. Ampère. Recueil d'observations électro-dynamiques : contenant divers mémoires, notices, extraits de lettres ou d'ouvrages périodiques sur les sciences, relatifs à l'action mutuelle de deux courans électriques, à celle qui existe entre un courant électrique et un aimant ou le globe terrestre, et à celle de deux aimans l'un sur l'autre. 1822.

[7] M. Faraday. Experimental researches in electricity. 1922 1914.

[8] J. C. Maxwell. A treatise on electricity and magnetism. 1, 1873.

[9] P. Curie. Propriétés magnétiques des corps à diverses temperatures. *PhD thesis Faculté des Sciences de Paris*, 1895.

[10] Pierre Weiss and Gabriel Foex. *Le Magnétisme*. libr. Armand Colin, 1931.

[11] Gale Research. *Magnetism*. DISCOvering Science, 1996.

[12] Daniel N. Woodruff, Richard E. P. Winpenny, and Richard A. Layfield. Lanthanide single-molecule magnets. *Chemical Reviews*, 113(7):5110–5148, 2013. PMID: 23550940.

[13] Fu-Sheng Guo, Benjamin M. Day, Yan-Cong Chen, Ming-Liang Tong, Akseli Mansikkamäki, and Richard A. Layfield. Magnetic hysteresis up to 80 kelvin in a dysprosium metallocene single-molecule magnet. *Science*, 362(6421):1400–1403, 2018.

[14] H. T. Diep, editor. *Frustrated Spin Systems*. World Scientific, Singapore, 2005.

[15] J. S. Gardner, M. J. P. Gingras, and J. E. Greedan. Magnetic pyrochlore oxides. *Review of Modern Physics*, 82, 2010.

[16] J. S. Helton, K. Matan, M. P. Shores, E. A. Nytko, B. M. Bartlett, Y. Yoshida, Y. Takano, A. Suslov, Y. Qiu, J.-H. Chung, D. G. Nocera, and Y. S. Lee. Spin dynamics of the spin-1/2 kagome lattice antiferromagnet $ZnCu_3(OH)_6Cl_2$. *Phys. Rev. B*, 98:107204, 2007.

[17] O.A. Petrenko, C. Ritter, M. Yethiraj, and D. McK Paul. Investigation of the low-temperature spin-liquid behavior of the frustrated magnet gadolinium gallium garnet. *Physical Review Letters*, 80, 1998.

[18] Y. Zhou, K. Kanoda, and T-K Ng. Quantum spin liquid states. *Reviews Of Modern Physics*, 89, 2017.

[19] S. T. Bramwell and M. J. P Gingras. Spin ice state in frustrated magnetic pyrochlore materials. *Science*, 294:1495–1501, 2001.

[20] Charles Kittel. *Introduction to Solid State Physics*. Wiley, 8 edition, 2004.

[21] W. Selke. The ANNNI model - theoretical analysis and experimental application. *Physics Reports (Review Section of Physics Letters)*, 170:213–264, 1998.

[22] R. Moessner, S. L. Sondhi, and P. Chandra. Phase diagram of the hexagonal lattice quantum dimer model. *Physical Review B*, 64, 2001.

[23] Hans-Conrad zur Loye, Qingbiao Zhao, Daniel E. Bugarisa, and W. Michael Chancea. 2H-perovskite related oxides: Synthesis, structures, and predictions. *CrystEngComm*, 14:23–39, 2012.

[24] H. Karunadasa, Q. Huang, B. G. Ueland, J. W. Lynn, P. Schiffer, K. A. Regan, and R. J. Cava. *Phys. Rev. B*, 71:144414, 2005.

[25] O. A. Petrenko, O. Young, D. Brunt, G. Balakrishnan, P. Manuel, D. D. Khalyavin, and C. Ritter. Evolution of spin correlations in $SrDy_2O_4$ in an applied magnetic field. *Phys. Rev. B*, 95:104442, 2017.

[26] N Gauthier, B Prévost, A Amato, C Baines, V Pomjakushin, A D Bianchi, R J Cava, and M Kenzelmann. Evidence for spin liquid ground state in $SrDy_2O_4$ frustrated magnet probed by $\mu SR. Journal of Physics : Conference Series$, 828(1) : 012014, 2017.

[27] N. Gauthier, A. Fennell, B. Prévost, A.-C. Uldry, B. Delley, R. Sibille, A. Désilets-Benoit, H. A. Dabkowska, G. J. Nilsen, L.-P. Regnault, J. S. White, C. Niedermayer, V. Pomjakushin, A. D. Bianchi, and M. Kenzelmann. Absence of long-range order in the frustrated magnet $SrDy_2O_4$ due to trapped defects from a dimensionality crossover. *Phys. Rev. B*, 95:134430, 2017.

[28] N. Gauthier, A. Fennell, B. Prévost, A. Désilets-Benoit, H. A. Dabkowska, O. Zaharko, M. Frontzek, R. Sibille, A. D. Bianchi, and M. Kenzelmann. Field dependence of the magnetic correlations of the frustrated magnet $SrDy_2O_4$. *Phys. Rev. B*, 95:184436, 2017.

[29] O. Young, L. C. Chapon, and O. A. Petrenko. Low temperature magnetic structure of geometrically frustrated $SrHo_2O_4$. *J. Phys.: Conf. Ser.*, 391:012081, 2012.

[30] O. Young, A. R. Wildes, P. Manuel, B. Ouladdiaf, D. D. Khalyavin, G. Balakrishnan, and O. A. Petrenko. Highly frustrated magnetism in $SrHo_2O_4$: Coexistence of two types of short-range order. *Phys. Rev. B*, 88:024411, 2013.

[31] B. Z. Malkin, S. I. Nikitin, I. E. Mumdzhi, D. G. Zverev, R. V. Yusupov, I. F. Gilmutdinov, R. Batulin, B. F. Gabbasov, A. G. Kiiamov, D. T. Adroja, O. Young, and O. A. Petrenko. Magnetic and spectral properties of the multisublattice oxides $SrY_2O_4 : Er^{3+}$ and $SrEr_2O_4$. *Phys. Rev. B*, 92:094415, 2015.

[32] T. J. Hayes, O. Young, G. Balakrishnan, and O. A. Petrenko. *J. Phys. Soc. Japan*, 84:024708, 2012.

[33] T. J. Hayes, G. Balakrishnan, P. P. Deen, P. Manuel, L. C. Chapon, and O. A. Petrenko. *Phys. Rev. B*, 84:174435, 2011.

[34] A. Fennell, V. Y. Pomjakushin, A. Uldry, B. Delley, B. Prévost, A. Désilets-Benoit, A. D. Bianchi, R. I. Bewley, B. R. Hansen, T. Klimczuk, R. J. Cava, and M. Kenzelmann. *Phys. Rev. B*, 89:224511, 2014.

[35] D. L. Quintero-Castro, B. Lake, M. Reehuis, A. Niazi, H. Ryll, A. T. M. N. Islam, T. Fennell, S. A. J. Kimber, B. Klemke, J. Ollivier, V. G. Sakai, P. P. Deen, and H. Mutka. *Phys. Rev. B*, 86:064203, 2012.

[36] B. F. Decker and J. S. Kasper. *Acta Cryst.*, 10:332, 1957.

[37] O. A. Petrenko, G. Balakrishnan, N. R. Wilson, S. de Brion, E. Suard, and L. C. Chapon. *Phys. Rev. B*, 78:184410, 2008.

[38] E. Hasan and B. W. Southern. Monte carlo study of a geometrically frustrated rare-earth magnetic compound: $SrGd_2O_4$. *Phys. Rev. B*, 96:094407, 2017.

[39] A. A. Aczel, L. Li, V. O. Garlea, J.-Q. Yan, F. Weickert, M. Jaime, B. Maiorov, R. Movshovich, L. Civale, V. Keppens, and D. Mandrus. Magnetic ordering in the frustrated j1-j2 ising chain candidate $BaNd_2O_4$. *Phys. Rev. B*, 90:134403, 2014.

[40] A.A. Aczel, L. Li, V.O. Garlea, J.-Q. Yan, F. Weickert, V. S. Zapf, R. Movshovich, M. Jaime, P. J. Baker, V. Keppens, and D. Mandrus. Spin-liquid ground state in the frustrated j_1-j_2 zigzag chain system $BaTb_2O_4$. *Phys. Rev. B*, 92:041110, 2015.

[41] Bobby Prévost. Université de Montréal PhD Thesis. 2013.

[42] F. Heidrich-Meisner, I. A. Sergienko, A. E. Feiguin, and E. R. Dagotto. Universal emergence of the one-third plateau in the magnetization process of frustrated quantum spin chains. *Phys. Rev. B*, 75:064413, 2007.

[43] Kouichi Okunishi and Takashi Tonegawa. Fractional S^z excitation and its bound state around the 1/3 plateau of the S=1/2 ising-like zigzag XXZ chain. *Physical Review B*, 68, 2003.

[44] Kouichi Okunishi and Takashi Tonegawa. Fractional s^z excitation and its bound state for the S=1/2 antiferromagnetic zigzag spin chain in a magnetic field. *arXiv:cond-mat*, 2005.

[45] Oleg A Starykh. Unusual ordered phases of highly frustrated magnets: a review. *Reports On Progress In Physics*, 78, 2015.

[46] J. Wosnitza. Frustrated magnets in high magnetic fields—selected examples. *Reports On Progress In Physics*, 79, 2016.

[47] U. Nowak and A. Hucht. Monte Carlo simulation of Ising models with dipole interaction. *Journal of Applied Physics*, 76:6341–6343, 1994.

[48] E. Stryjewski and N. Giordano. Metamagnetism. *Advances in Physics*, 26(5):487–650, 1977.

[49] G. L. Squires. *Introduction to the Theory of Thermal Neutron Scattering*, volume c. Dover Publisher, 1966.

[50] D. S. Sivia. *Elementary scattering theory: For x-ray and neutron users*. 2011.

[51] Roger Pynn. *Neutron Scattering: A Primer*. 1990.

[52] Monte B. Boisen, Jr., and G. V. Gibbs. A derivation of the 32 crystallographic point groups using elementary group theory. *American Mineralogist*, 61:145–165, 1976.

[53] Zbigniew Dauter and Mariusz Jaskolski. How to read (and understand) volume a of international tables for crystallography: an introduction for nonspecialists. *Journal of Applied Crystallography*, 43:1150–1171, 2010.

[54] IUCr. *International Tables for Crystallography, Volume A: Space Group Symmetry*. International Tables for Crystallography. Kluwer Academic Publishers, Dordrecht, Boston, London, 5. revised edition edition, 2002.

[55] Juan Rodríguez-Carvajal. Recent advances in magnetic structure determination by neutron powder diffraction. *Physica B: Condensed Matter*, 192(1):55 – 69, 1993.

[56] R. B. Von Dreele, J. D. Jorgensen, and C. G. Windsor. Rietveld refinement with spallation neutron powder diffraction data. *Journal of applied crystallography*, 15:581–589, 1982.

[57] Navid Qureshi. Mag2pol: a program for the analysis of spherical neutron polarimetry, flipping ratio and integrated intensity data. *Journal of applied crystallography*, 52, 2019.

[58] P. Coppens. *Crystallographic Computing*, pages 255 – 270, 1979.

[59] P. Coppens, L. Leiserowitz, and D. Rabinovich. Calculation of absorption corrections for camera and diffractometer data. *Acta Cryst.*, 18:1035, 1965.

[60] C. R. Groom, I. J. Bruno, M. P. Lightfoot, and S. C. Ward. The cambridge structural database. *Acta Cryst.*, 72:171–179, 2016.

[61] Anubhav Jain, Shyue Ping Ong, Geoffroy Hautier, Wei Chen, William Davidson Richards, Stephen Dacek, Shreyas Cholia, Dan Gunter, David Skinner, Gerbrand Ceder, and Kristin a. Persson. The Materials Project: A materials genome approach to accelerating materials innovation. *APL Materials*, 1(1):011002, 2013.

[62] J. R. Stewart, P. P. Deen, K. H. Andersen, H. Schober, J.-F. Barthélémy, J. M. Hillier, A. P. Murani, T. Hayes, and B. Lindenau. Disordered materials studied using neutron polarization analysis on the multi-detector spectrometer, D7. *J. Appl. Cryst.*, 42:69–84, 2009.

[63] O. Young, G. Balakrishnan, M. R. Lees, and O. A. Petrenko. Magnetic properties of geometrically frustrated $SrGd_2O_4$. *Phys. Rev. B*, 90:094421, 2014.

[64] O. Young. The University of Warwick PhD Thesis. 2013.

[65] O. J. Schumann. Cologne Laue Indexation Program (CLIP). http://clip4.sourceforge.net/.

[66] Institut Laue-Langevin. OrientExpress. https://www.ill.eu/users/instruments/instruments-list/orientexpress/description/instrument-layout/.

[67] QuantumDesign. Physical property measurement system. *Heat Capacity Option User's Manual*, 2000.

[68] Paul Barnes, Simon Jacques, and Martin Vickers. Powder diffraction. *Birkbeck College, University of London.*

[69] Institut Laue-Langevin. D20. https://www.ill.eu/users/instruments/instruments-list/d20/description/instrument-layout/.

[70] Institut Laue-Langevin. D7. https://www.ill.eu/users/instruments/instruments-list/d7/description/instrument-layout/.

[71] Institut Laue-Langevin. D4. https://www.ill.eu/users/instruments/instruments-list/d4/description/instrument-layout/.

[72] Institut Laue-Langevin. D9. https://www.ill.eu/users/instruments/instruments-list/d9/description/instrument-layout/.

[73] Institut Laue-Langevin. D10. https://www.ill.eu/users/instruments/instruments-list/d10/description/instrument-layout/.

[74] S. G. Tresvyatskii, V. N. Pavlikov, and L. M. Lopato. Phase transformations in the Nd_2O_3-SrO system. *Inorg. Mater.*, 6:33–36, 1970.

[75] Winnie Wong-Ng. Powder diffr. *Powder Diffr.*, 10, 1995.

[76] Hanskarl Müller-Buschbaum. Hochtemperatur-festkörperchemie: Der niederdruck-hochfrequenz- plasmabrenner: Synthese stabiler und metastabile oxometallate der lanthanoide. *WILEY-VCH*, pages 369–383, 2006.

[77] B. A. Frandsen, X. Yang, and S. J. L. Billinge. Magnetic pair distribution function analysis of local magnetic correlations. *Acta Crystallographica*, A70:3–11, 2014.

[78] Haifeng Li, Cong Zhang, Anatoliy Senyshyn, Andrew Wildes, Karin Schmalzl, Wolfgang Schmidt, Martin Boehm, Eric Ressouche, Binyang Hou, Paul Meuffels, Georg Roth, and Thomas Bruckel. Incommensurate antiferromagnetic order in the manifoldly-frustrated $SrTb_2O_4$ with transition temperature up to 4.28 k. *Frontiers in Physics*, 2(42), 2014.

[79] H.-F. Li, B. Hou, A. Wildes, A. Senyshyn, K. Schmalzl, W. Schmidt, C. Zhang, T. Bruckel, and G. Roth. Absence of magnetic ordering in the ground state of a $SrTm_2O_4$ single crystal. *J. Mater. Chem. C*, 3(7658), 2015.

[80] A. E. Miller, F. J. Jelinek, K. A. Gschneidner Jr, and B. C. Gerstein. Low-temperature magnetic behavior of several oxides of gadolinium. *The Journal of Chemical Physics*, 55:6, 1971.

[81] G. R. Stewart, J. A. Barclay, and W. A. Steyert. The specific heat of c-phase Gd_2O_3. *Solid State Communications*, 29:17–19, 1979.

[82] H. R. Child, R. M. Moon, L. J. Raubenheimer, and W. C. Koehler. The paramagnetic form factor of gadolinium. *Journal of Applied Physics*, 38, 1967.

[83] R. M. Moon and W. C. Koehler. Magnetic properties of Gd_2O_3. *Physical Review B*, 11:1609–1622, 1975.

[84] G. Balakrishnan, T. J. Hayes, O. A. Petrenko, and D. M^{c}K Paul. *J. Phys.: Condens. Matter*, 21:012202, 2009.

[85] Simon Cotton. *Lanthanide and Actinide Chemistry.* Wiley, 2006.

[86] O. Young, O. A. Petrenko, and N. Q. Qureshi. *ILL experimental report, 5-41-700.*

[87] Varley F. Sears. Neutron scattering lengths and cross sections. *Neutron News*, 3:29–37, 1992.

[88] OriginLab Northampton (MA).

[89] Youichi Murakami and Sumio Ishihara. *Resonant X-Ray Scattering in Correlated Systems.* Springer, Berlin, Heidelberg, 2017.

[90] N. Qureshi. Rplot is a simple program to visualize d10 (and other ill single-crystal diffractometers) raw data, 2018.

[91] R. L. McGreevy and L. Pusztai. Reverse monte carlo simulation: A new technique for the determination of disordered structures. *Molecular Simulation*, 1(6):359–367, 1988.

[92] Joseph A M Paddison, J Ross Stewart, and Andrew L Goodwin. spinvert: a program for refinement of paramagnetic diffuse scattering data. *J. Phys.: Condens. Matter*, 25(45):454220, 2013.